Advanced single molecule fluorescent tools to reveal spatiotemporal multi-molecular interactions in living cells

PhD Thesis

Nicolás Mateos Estévez

April 2023

Supervised by:

Prof. Dr. María F. García-Parajo (Supervisor)

Dr. Juan A. Torreño-Piña (Co-Supervisor)

ICFO - Institut de Ciències Fotòniques

UPC - Universitat Politècnica de Catalunya

Abstract

The spatiotemporal organisation and compartmentalisation of molecules in living cells is crucial to regulate cell function. Dysregulation in how molecules dynamically explore their environment and interact with other molecules can lead to disease and death. Therefore, understanding the nature of these dynamic interactions is pivotal in cell biology studies. Fluorescence light microscopy is the preferred approach to perform the necessary biophysical studies and it has led to major findings in the field. Nevertheless, spatial and temporal studies are typically conducted separately due to technical limitations. Moreover, quantitative imaging and novel analysis toolboxes are required to address new questions in the field. The aim of this thesis is three-fold: (1) develop and implement novel algorithms to analyse super-resolution microscopy data to study the spatial organisation of a variety of proteins at the plasma membrane of cells; (2) develop a novel methodology to study the spatiotemporal organisation of receptors at the plasma membrane of cells based on high-density single particle tracking; and (3) apply our novel methodology in a multi-colour scheme to study the compartmentalisation of DC-SIGN and its multi-component interactions with CD44 and Galectin 9 during viral engagement.

In Chapter 1, we overview how cells are compartmentalised from the intra-cellular organisation to how the cell membrane is compartmentalised by multiple organisers acting most probably in synergy. Also, in Chapter 1, we review the main fluorescence microscopy techniques used in the field of cell biology to study the spatiotemporal organisation of molecules in cells. In Chapter 2, we present the analyses that we have performed to super-resolution microscopy techniques such as stimulated emission depletion (STED) and stochastic optical reconstruction microscopy (STORM). We have used these techniques to elucidate the spatial organisation of proteins at the plasma membrane such as Siglec-1, integrins or PRL-3. We have implemented state-of-the-art algorithms into our analysis workflow to resolve the biological inquiries of our research. In Chapter 3, we change gears and present our novel methodology to analyse high-density single particle tracking, which consists on generating high-density maps (HiDenMaps). In this chapter, we specify the

technical requirements to obtain a faithful representation on how molecules explore space. In Chapter 4, we study CD44 which is a transmembrane protein extremely interesting because it can interact with the underlying cortical actin and the extracellular milieu. Moreover, it is thought to act as a key actor in the spatiotemporal compartmentalisation of the plasma membrane for third receptors that do not interact directly with actin. In this Chapter, we have used HiDenMaps to elucidate the hierarchical organisation of CD44 at the plasma membrane of living cells. In Chapter 5, we present a palette of analysis tools to further quantify the patterns revealed by HiDenMaps and resolve the temporal dynamics of these patterns. Moreover, our work reveals a multi-scale organisation of CD44 ranging from fast single molecules dynamics with a mesoscale dynamic compartmentalisation. In Chapter 6, we present a functional study on viral capture by DC-SIGN in immature dendritic cells. We extended our HiDenMap methodology to a multi-colour scheme to study the multi-component interactions of DC-SIGN with CD44 and Galectin 9 during viral engagement. Importantly, we demonstrate the existence of DC-SIGN/CD44/Galectin 9 tripartite pre-docking platform that enhances the successful engagement of HIV-1 and SARS-CoV-2 virus-like particles in immature dendritic cells. Finally, in Chapter 7 we summarise the main results of this thesis and highlight future directions of our research.

Resumen

La organización espacio-temporal y compartimentalización de moléculas en células vivas es crucial para regular múltiples funciones celulares. La desregulación en cómo las moléculas exploran dinámicamente su entorno e interactúan con otras moléculas puede llevar a una gran variedad de enfermedades e incluso a la muerte. Por lo tanto, comprender la naturaleza de estas interacciones dinámicas es fundamental en los estudios de biología celular. Durante muchos años, la microscopía de fluorescencia ha sido el enfoque preferido para visualizar dinámicamente los componentes moleculares de las células con alto contraste y de manera no invasiva. Además, el surgimiento de la microscopía de super-resolución basada en fluorescencia y la detección de fluorescencia de moléculas individuales ha revolucionado los campos de la microscopía y también la biología. Ha proporcionado detalles sin precedentes sobre la organización dinámica de las moléculas en células vivas, y en particular, a nivel de la membrana plasmática. Desafortunadamente, debido a limitaciones técnicas asociadas con estas novedosas técnicas, los estudios temporales y espaciales se realizan por separado. Además, aunque los microscopios de super-resolución están disponibles en la mayoría de los laboratorios, el análisis cuantitativo de los datos proporcionados por estas técnicas sigue siendo extremadamente desafiante. Por lo tanto, se requiere el desarrollo de nuevas herramientas de análisis para lograr un verdadero entendimiento en el campo de la biología celular.

El objetivo de esta tesis ha sido abordar algunos de estos desafíos actuales. En particular, nos hemos enfocado en: (1) desarrollar e implementar algoritmos innovadores para analizar los datos de microscopía de super-resolución para estudiar la organización espacial a escala nanométrica de una variedad de proteínas en la membrana plasmática de las células; (2) desarrollar una metodología innovadora basada en el seguimiento de partículas individuales de alta densidad (multicolor) para estudiar la organización espacio-temporal a múltiples escalas de diferentes biomoléculas en la membrana plasmática; y (3) aplicar nuestra metodología innovadora para abordar dos preguntas principales en el campo de la biología celular: a) el papel del citoesqueleto de actina y el

medio extracelular para modular la organización espacio-temporal del receptor transmembrana CD44, y b) el papel de CD44 y Galectina 9 en la modulación de la capacidad de DC-SIGN para capturar virus en células del sistema inmunológico. En conjunto, esta tesis ha proporcionado herramientas sofisticadas que van más allá de los métodos actuales de visualización basados en moléculas individuales. Además, hemos estudiado cómo las células regulan la compartimentalización (en espacio y tiempo) de componentes moleculares para orquestar la función celular.

En el Capítulo 1, revisamos el papel de la compartimentalización celular en general con énfasis en la membrana celular, que está compartimentada por múltiples organizadores que actúan probablemente en sinergia. También, en el Capítulo 1, revisamos las principales técnicas de microscopía de fluorescencia utilizadas en el campo de la biología celular para estudiar esta organización espacio-temporal. En particular, nos centramos en la microscopía de super-resolución y los métodos de fluorescencia de moléculas individuales. En el Capítulo 2, presentamos los análisis que hemos realizado en imágenes de microscopía de super-resolución, en particular, la depleción por emisión estimulada (STED) y la microscopía de reconstrucción óptica estocástica (STORM). Hemos implementado algoritmos de vanguardia en nuestro flujo de trabajo de análisis para abordar diferentes preguntas biológicas de nuestra investigación. Combinando estas técnicas con nuestras herramientas de análisis, hemos abordado la organización espacial de diferentes proteínas en la membrana plasmática como Siglec-1, integrinas y PRL-3.

En el Capítulo 3, presentamos una metodología novedosa desarrollada durante esta tesis para analizar datos de seguimiento de partículas individuales en alta densidad (HD-SPT). El método consiste en generar mapas de alta densidad (HiDenMaps) a partir de las posiciones identificadas de moléculas en miles de imágenes de SPT. Describimos en detalle nuestro nuevo método y especificamos los requisitos técnicos para obtener una representación fiel de cómo las moléculas exploran el espacio mediante HiDenMaps. En el Capítulo 4, describimos la primera aplicación de HiDenMaps para esclarecer la organización jerárquica de la proteína transmembrana CD44 en la membrana plasmática de células vivas. Nos enfocamos en CD44 debido a su capacidad para interactuar tanto con la actina cortical subyacente como con el medio extracelular. Cabe destacar que se cree que CD44 actúa como un actor clave regulando la compartimentalización espacio-temporal de la membrana plasmática para otros receptores que no interactúan directamente con la actina. Combinando HiDenMaps con transferencia de energía de resonancia de fluorescencia (FRET), hemos demostrado que CD44 forma nanoagregados en la membrana plasmática de diferentes células. Además, revelamos que su organización tanto a nivel nano- y meso- escala está regulada el citoesqueleto de actina cortical.

En el Capítulo 5, presentamos una gama de herramientas de análisis para cuantificar patrones espaciales en la difusión de receptores en la membrana revelados por HiDenMaps y para resolver sus dinámicas temporales. Utilizando estas herramientas, nuestro trabajo desvela una organización multiescalar de CD44 que va desde la dinámica de moléculas individuales hasta una compartimentalización dinámica a nivel mesoscópico. La dinámica descubierta en los mapas de difusión probablemente corresponde a las diferentes escalas temporales de remodelado del citoesqueleto cortical de actina. En el Capítulo 6, presentamos un estudio biofísico sobre la captura viral mediada por el receptor de reconocimiento del patógeno, DC-SIGN, en células inmaduras dendríticas del sistema inmunitario. Extendimos nuestra metodología HiDenMap a un esquema multicolor para estudiar interacciones multicomponente entre DC-SIGN, CD44 y Galectina 9 durante la interacción con los virus. Adicionalmente, demostramos la existencia de plataformas tripartitas de pre-amarre de DC-SIGN/CD44/Galectina-9 que mejoran el éxito de la interacción de los virus HIV-1 y SARS-CoV-2. Finalmente, en el Capítulo 7, resumimos los resultados principales de esta tesis y destacamos las futuras direcciones de nuestra investigación.

Table of Contents

Chapter 1

Spatiotemporal organisation of molecules in cell biology and fluorescence optical microscopy techniques to study them

The spatiotemporal organisation and compartmentalisation of molecules in living cells are highly important to regulate cell function. Visualising and understanding the role of this dynamic organisation requires the use of non-invasive microscopy techniques that can access the relevant spatiotemporal scales, down to the molecular level and with milli-second temporal resolution. In this chapter, we first overview the multiple levels of spatiotemporal compartmentalisation of proteins and molecules in living cells. We mainly focus on the cell membrane of living cells, which has been the subject of study of this thesis. Then, we review different fluorescence-based optical microscopy approaches since they are the preferred tools to investigate the spatiotemporal organisation of proteins in cells. We present the state-of-the-art microscopy techniques to study the nanoscale organisation of molecules as well as how dynamic information on the diffusion of molecules can be retrieved.

1.1 Spatiotemporal organisation of molecules in living cells

Cells are the basic unit of life and are an exquisite piece of machinery that makes life possible. Cellular functions are achieved through the spatiotemporal compartmentalisation of multiple components. In fact, cells are organised into membrane-bound compartments, called organelles. Different cellular functions take place within these organelles, from DNA transcription in the nucleus, protein synthesis at the endoplasmic reticulum, energy generation at the mitochondria, protein glycosylation and export from the Golgi apparatus, … All these cellular functions take place in well-defined compartments(1). Nevertheless, not all compartmentalisation takes place within membrane-bound compartments. In fact, liquid-liquid phase separation (LLPS) has recently been proposed as a physical mechanism to transiently compartmentalise biomolecules in membrane-less compartments(2–5). The cell membrane is particularly interesting because it separates the interior of the cell from its extracellular surroundings and it has multiple roles beyond that of being a simple physical barrier: it is involved in signalling pathways between the cell and its environment, it carries sensing processes, it is in-charge of the selective transport of ions, molecules, etc(6). All these processes are performed by a myriad of different proteins and other molecules found on the cell membrane. Not surprisingly, the cell membrane is a complex fluid consisting on a phospholipid bilayer with embedded proteins and other molecules (cholesterol, glycolipid and peripheral proteins).

Understanding the cell membrane organisation has been a pivotal quest in the field of cell biology to comprehend how proteins and lipids are dynamically compartmentalised in health and disease. The first level of compartmentalisation is explained by the lipid raft hypothesis(7–9). Lipid rafts are cholesterol-enriched and sphingolipid-enriched nanodomains which also contain signalling proteins such as glycosylphosphatylinositol-anchored proteins (GPI-AP, (7, 10, 11)). Lipid rafts nanodomains are short-lived and dynamic and there is still quite some controversy in the field regarding their existence (12). In fact, it has been proposed that GPI-AP aggregation is not due to lipid rafts but rather orchestrated by short-lived “actin-asters” (short myosin-driven actin filaments), which also is a controversial mechanism in the field(13, 14).

A second level of compartmentalisation of the plasma membrane is due to the cortical actin cytoskeleton which is in close vicinity of the inner leaflet of the membrane. This model was first proposed by Michael Sheetz based on diffusion studies of proteins on the cell membrane of red blood cells(15) four decades ago. Later, Kusumi’s Lab gain further insights onto how cortical actin could compartmentalise the plasma membrane of cells hindering the diffusion of receptors(16). From their observations they referred to the cortical actin as membrane cytoskeleton fences. According to their model, proteins at the plasma membrane sense the underlying cortical actin and they are confined within corrals (~30-250 nm compartments) which hinder their long-range diffusion at the plasma membrane. Since the actin cytoskeleton is not static but dynamic, fluctuations in the cortical actin would lead to proteins to “hop” between compartments(17). Moreover, they proposed the existence of transmembrane proteins that could “anchor” to the underlying cortical actin and would act as pickets forming the corrals and hindering the diffusion of other proteins(18–21).

A third level of compartmentalisation of the plasma membrane is provided by the extracellular matrix (ECM). The ECM is a complex fuzzy coating consisting on sugars, carbohydrates, collagen fibres, etc. that interconnect glycoproteins at the plasma membrane and serve as a platform for cells to interact with their environment(22, 23). The ECM poses another level of complexity into the organisation of the plasma membrane molecules since it is a local organiser of proteins. A clear example is the so-called galectin lattice, which interconnects glycoproteins at the plasma membrane of cells to create a network with multiple functions(24).

Finally, a fourth level of compartmentalisation is given by protein-protein interactions that could lead to their clustering at the plasma membrane(25). Proteins can form nano-clusters that could then interact with lipid rafts (26), or other external organisers such as cortical actin (27)or, the ECM(28).

Importantly, all these mechanisms are thought to act in synergy to compartmentalise the plasma membrane in a hierarchical manner(29). A canonical example of this complex synergy is the spatiotemporal organisation of CD44, a transmembrane protein that can bind to cortical actin, to extracellular matrix components such as galectins and hyaluronan acid, and even, it has been proposed to interact with lipid rafts(21, 30, 31). Elucidating the mechanisms that lead to compartmentalisation of specific components of the plasma membrane is therefore of paramount importance to determine how compartmentalisation influences their function.

1.2 Optical microscopy to investigate the spatiotemporal organisation of biomolecules in living cells

Light is the preferred tool to study the spatiotemporal organisation of molecules in living cells by the cell biology community. The reasons are obvious: light is not invasive and it is fully compatible with living specimens.

The development of optical microscopy starts many centuries ago when Ptolemy observed how water bends light. In fact, it was in the 1st century AD that Seneca used a flask of water to magnify small letters, i.e. creating the first magnifier. Later, in the 13th century in Italy, the first high-quality silicate glass lenses were manufactured, allowing to produce the first lenses to be worn as glasses. It was not until the end of the 16th century when Zacharias and Hans Janssen combined several lenses within a tube to obtain a higher magnification than single lenses. This was a breaking point in history because it meant that new optical instruments could be built by combining lenses. From this point, Galileo Galilei built his *occholiolino* in 1609 and together with his colleague Giovanni Faber, termed the word microscope (from the Greek words *micron* (small) and *skopien* (to view)). The next breaking point in the use of microscopy was the discovery of the basic unit of life, the cell, by Robert Hooke in the 17th century, using a microscope to observe cork. Nevertheless, one of the most important scientists and pioneer in microbiology is Antonie Van Leeuwenhoek, who using his own microscopes observed bacteria, yeast cells and blood cells amongst other microscopic specimens for the first time in human history. The development of the optical microscope has been ever evolving to the date, with novel technologies and more sophisticated equipment.

However, the study of cell biology does not stand alone with optical microscopy itself. Another key discovery that led to major breakthroughs in the field was fluorescence and the biochemistry tools that allow to label specific proteins.

1.2.1 **Fluorescence microscopy**

Fluorescence is the spontaneous emission of photons by an excited molecule after absorbing light. Molecules have multiple energetic states, the main ones are electronic energetic states ($S_{0, 1, 2, ...}$) and vibronic states within each electronic energy state. Typically, molecules are found in their ground energy state, S_0, and upon photon excitation they will get excited to a higher state if the energy of the photon is high enough. Once in the excited state, multiple energetic transitions can take place. First, a fast vibronic relaxation, where the molecule relaxes from the excited vibronic state to the corresponding electronic state in a non-radiative way (no emission of photons). When the molecule is at the lowest excited electronic state, S_1, it can either decay back to the ground state, S_0, emitting a photon (fluorescence), decay in a non-radiative way (not emitting a photon) or if the electrons change their spin, decay to the triplet state (T_1) via intersystem crossing. At the triplet state, it can decay to the ground state via emission of photons (phosphorescence) or in a non-radiative manner. The wavelength of the excitation photon, λ_{exc}, is shorter than the fluorescence wavelength, λ_{fluor}, because of the energy loss during the energetic transitions. The shift in wavelength is known as the Stokes shift. Moreover, the wavelength of phosphorescence is even longer than the one of fluorescence and the lifetime, i.e., the time it stays at the triplet state before decaying, is also much longer (in the order of milliseconds) as compared to fluorescence which typically occurs in the nanosecond time scale. All these processes are depicted in the Jablonski diagram (Figure 1.1). Fluorescent molecules (fluorophores) can undergo this cycle a limited number of times (10^6-10^8 times) before photobleaching occurs(32). Thus, fluorophores emit a certain number of photons, their photon budget (~10^4-10^7 photons), before being permanently photobleached.

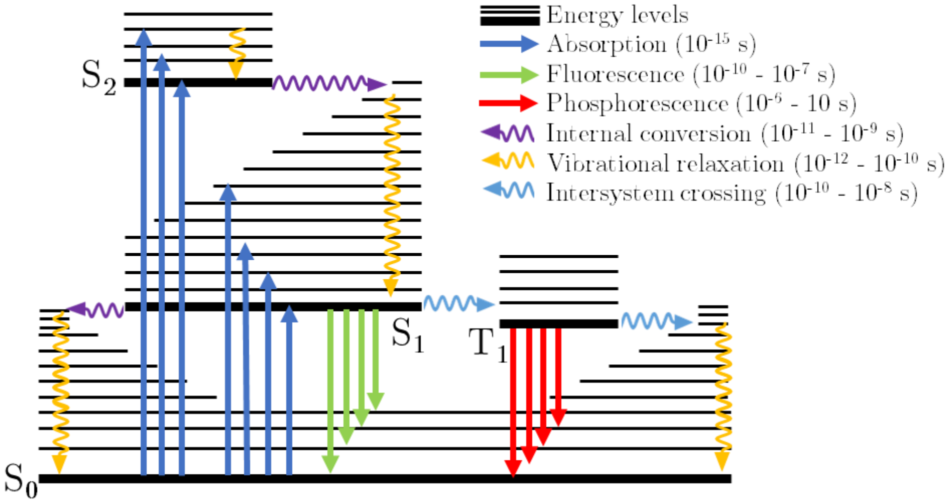

Figure 1.1 A Jablonski diagram depicts the energetic states of a molecule and the transitions that can occur upon light absorption (blue straight arrow). The energy levels, which can be electronic (thick line) or vibronic (thin line), are depicted as black horizontal lines with energy increasing vertically. The transitions between energy states can be either radiative (fluorescence or phosphorescence) or non-radiative (internal conversion, vibrational relaxation and intersystem crossing). The typical timescales of the processes are shown in the legend. Figure adapted from Edinburg instruments.

Fluorescence microscopy relies on the use of fluorescent probes to generate an image that provides superior contrast as compared to the simple absorption of light by the specimen. For the incorporation of fluorescence contrast, one mainly needs two separate units: a specific module to label the molecule of interest and, a fluorophore that emits fluorescence and enables the visualisation of the molecule of interest. In terms of fluorophores, the most commonly used are fluorescent proteins, fluorescent dyes and quantum dots. Fluorescent proteins, such as the green fluorescent protein (GFP; (33, 34)) and derivatives(35), are very interesting because they can be genetically encoded to directly tag the molecule of interest and are especially suitable to study intracellular processes. Fluorescent dyes (organic and synthetic) are versatile fluorophores that can be used to easily label any kind of molecule. However, organic dyes, suffer from low photostability and low brightness which limits their application for certain studies. More recently, a new family of organic dyes have emerged as powerful fluorescent probes for fluorescence microscopy studies due to their superior performance, Janelia dyes (36, 37). Finally, quantum dots (QD) are semiconductor nanocrystals whose emission wavelength is tuned by their size. They are extremely useful in multi-colour applications because of their broad absorption and narrow emission spectra (38, 39). Moreover, when excited at low-to-moderate excitation powers, they are extremely bright, stable and highly resistant to photodissociation(39). However, QDs are bulky when bioconjugated to make them compatible with live cell imaging.

In order to tag the fluorophores to the biomolecule of interest, there are mainly three approaches. The first approach is *immunolabelling* which uses antibodies (or subunits, such as nanobodies or single-chain antibodies) to tag the specific molecule. Antibodies can be fluorescently label with fluorescent dyes and quantum dots using proper bio-conjugation protocols. The second approach is *genetic tagging* which covalently labels the molecule of interest with a fluorescent protein. Genetic tagging is especially interesting for live cell experiments and it is extremely precise. However, overexpression of the targeted molecule and the size of fluorescent proteins poses a challenge. The third approach consists on using self-labelling protein tags such as SNAP-tag (40), /HALO-tag (41) tag and CLIP-tag (42). These tags are fused to the molecule of interest and then they can be fluorescently labelled with fluorescent dyes. These techniques are becoming very popular in the field due to the advent of the Janelia dyes, which are highly photostable. However, the main limitation as with genetic tagging is the overexpression of the tagged molecule. Overall, given the fact that each type of fluorophore and labelling modules have advantages and drawbacks, experimentalists need to survey which is the most convenient labelling approach for their specific biological question.

The most basic optical implementation of fluorescence microscopy relies on the use of a light source at a given wavelength to excite the fluorophores, a filter to spectrally separate the emission of the fluorescent photons from the excitation ones and a detector to collect the fluorescence photons being emitted by the sample. Although extremely simple and powerful, a main limitation of the first fluorescence microscopes was the background noise originated from the fluorescence signal coming from molecules out of the plane of interest. This background noise resulted into blurred images. Confocal microscopy was born to resolve this problem by focusing the excitation laser into a single point in the sample and using a pinhole in the optical detection path to remove out-of-focus fluorescence (32). Confocal microscopy is a point-by-point illumination technique that creates images by performing line scans in the field of view with an axial resolution of roughly the excitation wavelength. Additionally, using confocal microscopy we can perform 3D imaging by moving the sample in the Z direction and creating a z-stack. Nowadays, confocal microscopy is one of the most widely used fluorescence microscopy techniques due to its versatility and simplicity. Moreover, it is possible to perform multi-colour imaging choosing properly the fluorophores and using different detection filters and laser lines (or super-continuum white light sources).

Total internal reflection fluorescence (TIRF) microscopy is another technique widely used in the field of cell biology specially for membrane dynamics studies. In TIRF, an evanescent wave is generated at the interface between the glass and the medium where cells are, by total reflection of the excitation laser. This is accomplished by focusing the laser at the back-focal plane of the objective and not at the centre of the objective (it would be EPI illumination) but displaced towards the edge (Figure 1.2). A high numerical aperture (NA) objective allows that the incidence angle of the excitation light into the sample reaches the critical value needed to have the total internal reflection and to generate an evanescent field within the sample. The evanescent field only penetrates $\sim 200\,nm$, so that only fluorophores at this range in the sample are excited and not those deeper within the cell. TIRF provides great signal-to-background ratios but studies are limited to the basal membrane of cells or to the cytosol close to the membrane.

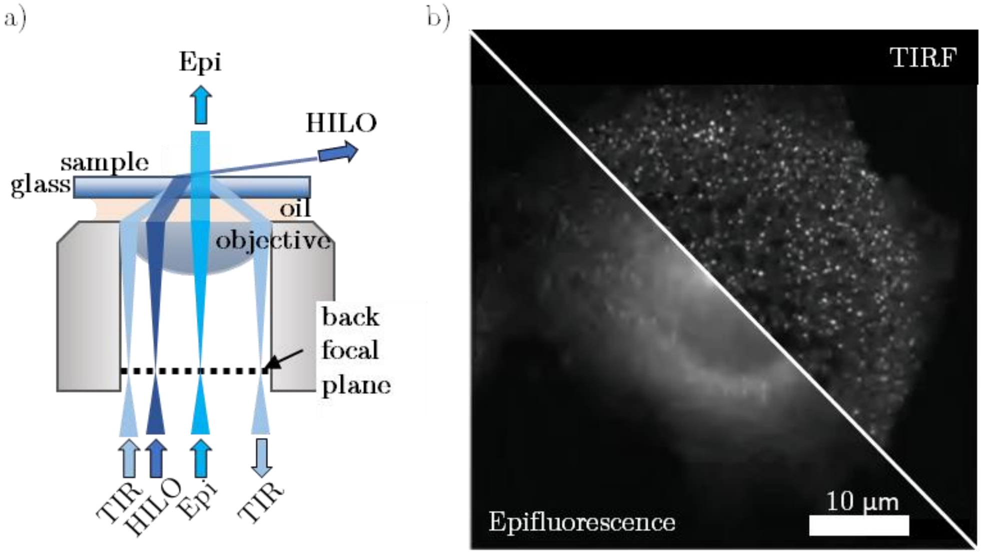

Figure 1.2 TIRF illumination provides better signal-to-background than Epifluorescence. a) Different excitation schemes including TIR, HILO and Epi, in which the laser is focused at the back focal plane but at different positions with respect to the centre of the objective. Adapted from Manzo and Garcia-Parajo (43). b) Clathrin-light chain tagged with GFP and imaged in Epifluorescence (bottom left triangle) and TIRF (top right triangle). Image adapted from Rao et al. (44).

Highly inclined and laminated optical (HILO) sheet illumination can be implemented if the laser is not fully displaced to the edge of the objective (45). With HILO, we can illuminate the sample with a rather thin ($\sim 1\ \mu m$) sheet of light that enables to study regions inside the cell, beyond that of the cell membrane. However, the imaging is still limited to a certain depth of the cell and the signal-to-background ratio is worse than for TIRF due to the thickness of the sheet.

1.2.2 Diffraction limit of light

Despite the revolution that fluorescence microscopy meant to the field of cell biology, it suffers from a major drawback: the diffraction limit of light. According to Abbe's limit(46), two objects cannot be resolved if they are closer than:

$$d \approx \frac{\lambda}{2 \cdot NA} \tag{1.1}$$

where λ is the wavelength of the excitation light, and NA is the numerical aperture of the objective. This limit arises because a light source (fluorophore) that emits light on the sample is imaged as a diffraction limited spot and due to the optical properties of the setup, it is imaged as an Airy disk. Considering typical objectives and visible light used to excite photons, the diffraction limit of light is roughly $\sim 200 - 300\, nm$. Therefore, we cannot resolve small proteins (1-10 nm in size) in crowded regions as the plasma membrane or any other region of the cell. Confocal microscopy, epi-fluorescence microscopy and TIRF are all techniques that suffer from diffraction despite their improvement in terms of SNR. Aside from the limited spatial resolution afforded by these techniques, its impact is particularly troublesome in studies focussed on determining interactions or proximity between different biomolecules. This is because what it would appear to spatially colocalise by means of one of these diffraction limited techniques, might in fact be spatially separated by distances smaller that the diffraction limit. These artefactual results would thus bias the conclusions from such studies.

1.2.3 **Super-resolution microscopy**

As already mentioned, the diffraction limit of light is an obstacle to study finer structures and to better resolve the spatial organisation of molecules in cell biology and requires the use of super-resolution techniques that overcome diffraction. In the last 15 years, a multitude of such super-resolution approaches have been implemented and applied to different cellular contexts. Below, we summarise the main working principle of the most notable ones.

1.2.3.1 Near-field optical microscopy (NSOM)

A sophisticated optical technique to break the diffraction limit is near-field scanning optical microscopy (NSOM). In this technique, excitation is done through a sub-wavelength aperture on the tip of a glass fibre that creates an evanescent field confined both laterally and axially. The imaging is performed by raster scanning the sample with the probe in close vicinity (few nm) from the surface using a feedback-loop similar to the one used for atomic force microscopy (AFM) imaging (47) (Figure 1.3a). The resolution achieved by NSOM depends on the aperture size, and it is typically between 50-100 nm (48–50).

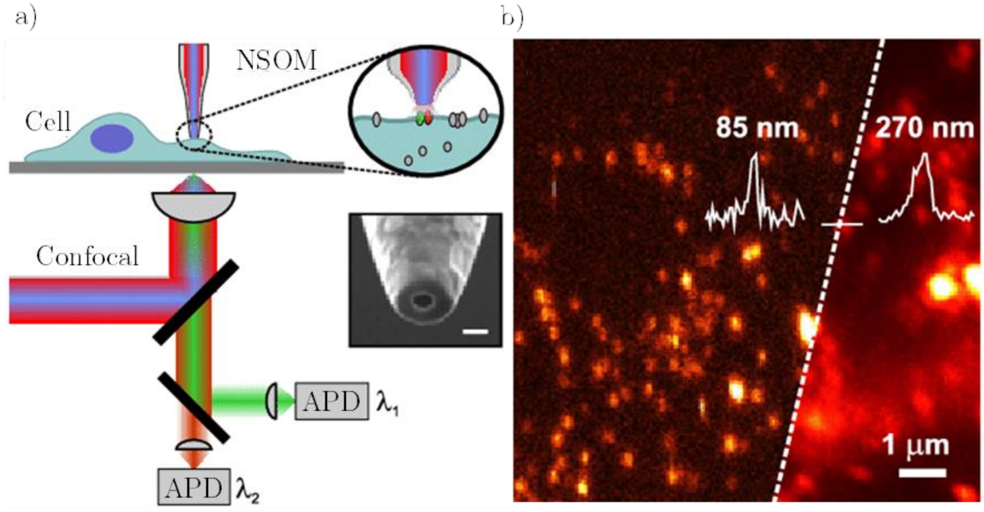

Figure 1.3 Working principle of NSOM and improved spatial resolution. a) The NSOM probe is built on a confocal microscope. The probe raster scans the sample and excites locally the fluorophores at each step. An electron microscopy image shows the used tip by Van Zanten et al. The scale bar is 100 nm. b) LFA-1 nanocluster imaging with NSOM (left) and confocal (right). A line profile is drawn over the same cluster demonstrating the improved spatial resolution of NSOM (85 nm) with respect to confocal (270 nm). Adapted from Van Zanten et al. (11)

NSOM has given insights into the spatial organisation of different receptors at the plasma membrane of cells(11, 50) (Figure 1.3b). Despite the great capabilities of NSOM, the studies are limited to the surface of cells and also, technically, it is a very complex approach to implement.

1.2.3.2 Structured illumination microscopy (SIM)

Structured illumination microscopy (SIM) is a technique that pushes the diffraction limit and allows an increase in resolution to ~100 nm(51, 52). SIM uses structured illumination to excite the sample with well-controlled illumination patterns. Since the molecules of interest are not homogenously distributed on the space but are within sub-diffraction patterns themselves, the detected emission consists on Moiré fringes. These fringes arise from the combination of the structured illumination and the pattern of fluorophores at the sample. Then, the illumination pattern is rotated and displaced to generate multiple images, each containing a different Moiré fringe. Since the used structured excitation pattern is known beforehand, using Fourier inverse transform it is possible to recover the pattern of fluorophores, a.k.a. the distribution of molecules of interest.

SIM is a fast imaging technique, with low excitation intensity and compatible with 3D imaging, which is ideal for live cell imaging. Moreover, it is compatible with any fluorophore. However, it is also technically complex, in particular the reconstruction of the final image, and its modest increase in terms of spatial resolution still limits its broad applicability for studying the spatial organisation of molecules with nanometre resolution.

1.2.3.3 Single molecule localisation microscopy (SMLM)

According to Abbe's diffraction limit, two fluorescent particles cannot be resolved if they are closer than the diffraction of light. But, what if they emit at different moments in time? If first a molecule emits light and then the other, both molecules can be localised unambiguously. Single molecule localisation microscopy (SMLM) techniques rely on using the temporal component to resolve molecules that are very close in space and to localise them accurately.

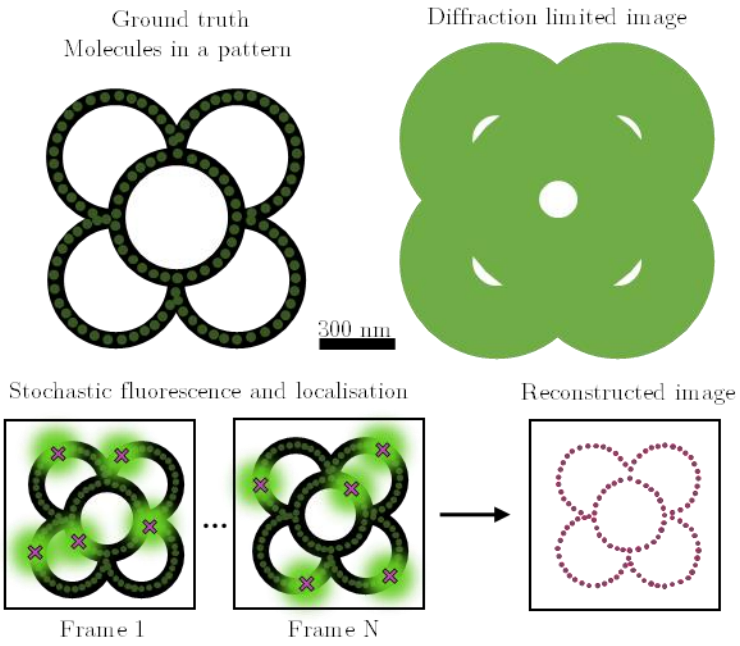

Figure 1.4 Working principle for SMLM techniques. Molecules are located in a given pattern very close to each other. Using conventional fluorescence microscopy, the pattern is barely visible due to the diffraction limit of light. However, if the molecules are made to fluoresce stochastically (or with photoactivation) and sequentially, at each frame only a subset of molecules emit light and

the centre of mass position can be determined by fitting a 2D gaussian. This process is repeated thousands of times (N>1000) until a faithful reconstruction of the image can be performed.

The advent of photo-activatable and photo-switchable dyes was the trigger for for the advent of SMLM techniques which occurred almost simultaneously: photoactivated localisation microscopy (PALM, (53)), stochastic optical reconstruction microscopy (STORM, (54)) and fluorescence photoactivated localisation microscopy (fPALM, (55)) were born and reported in 2006. All SMLM techniques share the same working principle despite the technical difference on how they accomplish the turning of the ON (bright) and the OFF (dark, not emitting) states of individual fluorophores (Figure 1.4). In SMLM a small subset of fluorophores is turned ON so that the distance between them is larger than the diffraction limit of light ($\lambda/2NA$). Since any point source (i.e. a fluorescence emitter) acquired with an optical microscope appears as a diffraction limited Airy disk, the central lobe is fitted to a 2D spatial gaussian and the centre of mass can be determined with very high accuracy, a few nanometres. This process of turning ON a subset of fluorophores and localising them in space is performed sequentially over thousands of frames until all of the fluorophores have been localised. Then, using the acquired localisations, the final super-resolution image is reconstructed.

The main difference between STORM and PALM relies on the fluorescent probes used in each case. STORM uses photoswitchable dyes and certain buffers containing oxygen scavengers, redox chemicals and glucose to control the ON-OFF states. On the other hand, PALM uses photoactivatable or photoconvertible fluorescent proteins that can be genetically encoded.

In the case of STORM, at the beginning of the experiment, all fluorophores are in their bright state (ON) emitting fluorescence. The first step consists on bringing all the fluorophores from the ON state to the OFF state by exciting the sample with high laser powers at the proper wavelength. In the presence of photoswitching buffers, dark states become stable for several seconds before the fluorophores decay back to the singlet ground state by reacting with residual oxygen(56). Thus, in the photoswitching buffer also oxygen scavengers are added to avoid this unspecific decay to a ground state where the fluorophore can be excited and emit fluorescence. Finally, the photoswitching of these fluorophores from the OFF state to the ON state in a controlled manner can be achieved either using an activator dye (STORM)(54, 57) or without it (as in direct STORM, dSTORM)(58, 59). In either case, fluorescent dyes are stochastically turned ON from the OFF state and emit fluorescence, which is then detected. Importantly, the transition between ON and OFF states is reversible in photoswitchable dyes, which means that a single fluorophore can undergo multiple times this process and blink many times(60).

In the case of PALM, photoconvertible and photoactivatable fluorescent proteins are used. Both photoactivation and photoconversion are irreversible processes. Photoactivatable fluorophores are activated (from OFF to ON) with a UV light ($\lambda_{OFF \to ON} = 405\, nm$) and imaged with a longer wavelength which will return the fluorophores from the ON to the OFF emitting state (60). In this case, the ability to localise individual molecules relies on the fact that not all of the fluorescence proteins are simultaneously activated with the activation laser, just a small subset. Photoconvertible fluorophores on the other hand, can switch from emitting in one wavelength to another wavelength upon radiation with the appropriate excitation light. For instance, Eos can be photoconverted to emit in the green or in the red by UV radiation(61, 62).

An alternative SMLM technique, that does not rely on photoswitching, photactivation or photoconversion, is point accumulation in nanoscale topography (PAINT) (63). PAINT relies on freely diffusing fluorescent dyes that interact with the target protein with certain kinetic rates of binding and unbinding. When the fluorescent dyes are bound to the target molecule, they will get excited by the excitation laser and will emit fluorescence. Once the dye gets unbound from the target molecule, excitation will not occur and therefore no emission of fluorescence. DNA-PAINT is the most well-known variant of PAINT where fluorescently labelled single strands of DNA are used to target the protein of interest and to perform the imaging (64, 65). A powerful application of DNA-PAINT is the fact that one can engineer the DNA single strands to target different molecules and by imaging sequentially it has been possible to perform multiplexed imaging of 124 colours successfully(66).

1.2.3.4 Stimulated emission depletion (STED)

Stimulated emission depletion (STED) microscopy is a super-resolution microscopy technique based on the precise control of the fluorophore's photo-physics to break the diffraction limit of light(67, 68). STED exploits the transitions between energetic states of fluorophores to control which fluorophores emit fluorescence and which do not. When a molecule is at the lowest excited state (S_1, Figure 1.5a) one can de-excite the molecule down to the ground state by stimulated emission. This is done by illuminating the excited molecule with a red-shifted STED laser, forcing the molecule to decay emitting a photon of the same wavelength as the stimulated excitation. In order to exploit this property to achieve super-resolution, in STED microscopy two lasers are combined. The first laser provides the excitation for the molecules using a gaussian beam as it is standard in confocal. The second laser is the STED laser (or depletion laser) which is doughnut-shaped and overlaps with the excitation laser. Therefore, at the centre of the doughnut, molecules are excited and will emit fluorescence normally (Figure 1.5b). However, at the ring of the doughnut, molecules undergo stimulated emission which is filtered at the detection path. As for the case of confocal microscopy, STED is a point-by-point scanning technique. By controlling the intensity of the STED laser, one can readily tune the size, *d*, of the resultant, effective spot and thus increase the spatial resolution:

$$d \approx \frac{\lambda}{NA \cdot \sqrt{\left(1+\frac{I}{I_S}\right)}}, \tag{1.2}$$

Where NA is the numerical aperture of the objective, I is the STED intensity and I_S is the saturation intensity (which accounts for the absorption cross-section of the molecule and lifetimes). The measured dependence of the effective excitation diameter, i.e., spatial resolution is shown in Figure 1.5b, bottom panel.

Nowadays, STED is a powerful technique widely used to study cellular structures(69), protein clusters(70, 71), DNA organisation(72, 73), etc. Additionally, STED is compatible with multi-colour imaging and allows colocalisation studies between different molecules. However, STED also suffers from some drawbacks. First, the STED laser powers required are high (I_{STED} ~ 1-10 MW/cm^2, (74)) which makes live cell imaging highly challenging. Indeed, live cell STED experiments have poorer resolution since lower excitation STED powers are used to preserve cell viability. Thus, for the best performance in terms of resolution most researchers work with fixed cells. Second, the choice of fluorophores is critical because working at such high laser powers induces photobleaching. Therefore, the development of bright and photostable fluorophores is crucial for STED microscopy. In fact, new fluorescent dyes require less powerful STED laser powers opening the door to STED live cell imaging. Third, optically, the STED set-up is a complex system because of the laser engineering required to (1) create the doughnut shape with a wave-plate and (2) align it properly to fully overlap with the excitation laser.

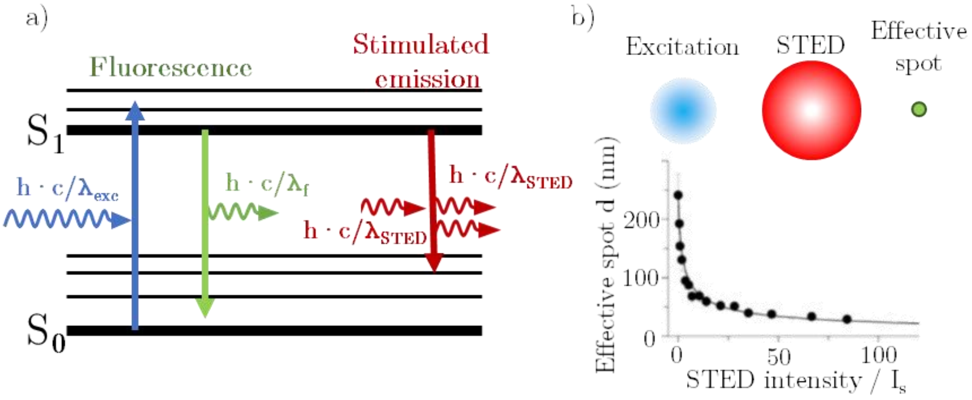

Figure 1.5 Working principle of STED microscopy. a) Jablonski diagram for STED showing how stimulated depletion takes place. b) Top: showing how the excitation and STED laser illuminate the sample and the effective excitation spot. Bottom: how the effective excitation spot diametre decreases with increasing STED laser intensity. Adapted from Eggeling et al. (74).

1.2.4 Microscopy techniques to assess temporal information

Super-resolution techniques suffer from poor temporal resolution, which limits the study of dynamic processes in living cells. Therefore, to access temporal information of diffusing molecules a different set of techniques are used by the community.

1.2.4.1 Fluorescence Recovery After Photobleaching (FRAP)

Fluorescence recovery after photobleaching (FRAP) consists on photobleaching an area of the cell using a high intensity laser and measuring the recovery of fluorescence as function of time by incoming diffusing fluorescent molecules. By monitoring the time that takes to recover the fluorescence in the area, one can measure the ensemble mobility of the fluorescently labelled molecules as well as the fraction of mobile molecules (Figure 1.6).

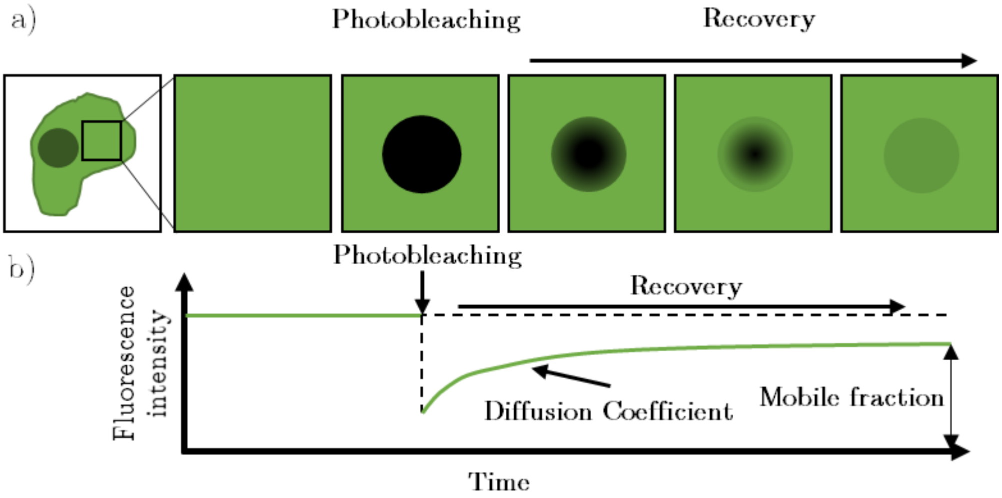

Figure 1.6 Fluorescence Recovery After Photobleaching (FRAP) working principle. a) A given region of the cell is photobleached using a high intensity laser and then the fluorescence recovers over time in the photobleached area. Green denotes fluorescence and black the photobleached area not emitting fluorescence. b) The fluorescence intensity is measured throughout the process and the diffusion coefficient of the ensemble diffusing molecules (mobile fraction) can be retrieved. Adapted from (75).

FRAP was one of the first techniques used in cell biology to measure diffusions and it became even more popular when it became possible to express GFP-labelled proteins(76–79). However, the main disadvantage of using FRAP is that one cannot observe the dynamics of individual molecules and just have a measure of the whole ensemble of labelled molecules.

1.2.4.2 Fluorescence correlation spectroscopy (FCS)

Fluorescence correlation spectroscopy (FCS) is another powerful technique that allows to have access to the temporal information of fluorescently labelled molecules (80–82). In FCS, the fluorescence intensity fluctuations of molecules diffusing through an illumination volume as a function of time is measured (Figure 1.7a). Usually the illumination volume consists on a confocal excitation volume but FCS has also been combined with STED and NSOM to obtain diffusion information in the nanoscale (83, 84). For the analysis, the time traces are auto-correlated with different time-lags and from the autocorrelation curve it is possible to fit parameters such as the diffusion coefficient and the number of molecules among other parameters (Figure 1.7b).

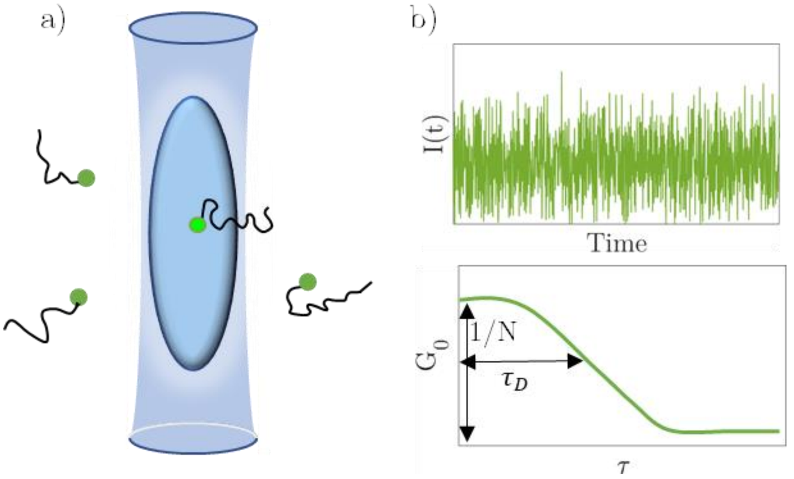

Figure 1.7 Working principle of Fluorescence Correlation Spectroscopy (FCS). a) Molecules diffuse through the excitation volume and emit fluorescence which is detected as a function of time. b) Time traces of fluorescence are recorded and the autocorrelation function is computed form them. From the autocorrelation function (G_0), one can obtain the diffusion and the number of molecules.

1.2.4.3 Single particle tracking (SPT)

Single particle tracking (SPT) is another impressive technique that combines high spatial and temporal resolution. In SPT single molecules are located with nanometric precision and tracked over time to generate trajectories that can be further analysed. Figure 1.8a shows how SPT works from acquisition to tracking. First, sparsely labelled molecules are imaged during hundreds (or thousands) of frames at high frame rates. In the processing step, all molecules are localised at each frame of the movie. Since any point source (i.e. a fluorescence emitter) acquired with an optical microscope appears as a diffraction limited Airy disk, the central lobe is fitted to a 2D spatial gaussian. The centroid position is then determined from the gaussian fitting of each fluorescent spot. The localisation precision on the determination of the centroid position is typically 10-30 nm, and it is affected by the background noise, the number of detected photons and other sources of noise. Moreover, the localisation accuracy is the difference between the emitters actual position and the determined centroid. SPT has great capabilities and algorithms typically localise single molecules with nanometre accuracy. Once the molecules are localised at each frame, the next step is to link the localisation from frame to frame in order to build trajectories. For this step, low labelling is crucial because it simplifies the reconnection, and the reconnection algorithms merely need to connect nearest-neighbours within frames. However, more sophisticated algorithms have emerged to account for the blinking of fluorophores, missed localisations, possibility of particles crossing each other, etc (85–88). In fact, after reconnection, there must be a cross-check from the user to ensure that all trajectories retrieved have been successfully reconnected to avoid artefacts. Once the trajectories are generated and checked, one can extract large amount of information from them: instantaneous velocity, diffusion, confinement zones, turning angles, … All these parameters allow to understand how single molecules explore the space and dynamically interact with their environment and with other molecules. The mean square displacement (MSD) is one of the most commonly used analysis to quantify the trajectories obtained with SPT. The MSD describes how the molecule explores the space in average as a function of the time lag. The MSD for a single trajectory is calculated as follows:

$$MSD\left(t_{lag} = m\Delta \mathrm{t}\right) = \frac{1}{N-m} \cdot \sum_{i=1}^{N-m} [\boldsymbol{x}(t_i + m\Delta t) - \boldsymbol{x}(t_i)]^2 \tag{1.3}$$

Here, $\mathbf{x}$ denotes the space vector containing the spatial coordinates ($\mathbf{x}$ = {x,y,z}) and N is the total number of frames of the trajectory. The MSD curve as a function of t_{lag} has different slopes (Figure 1.8b) depending on the type of motion of the studied molecule that arise from single molecule interactions with its surroundings (43, 89–91).

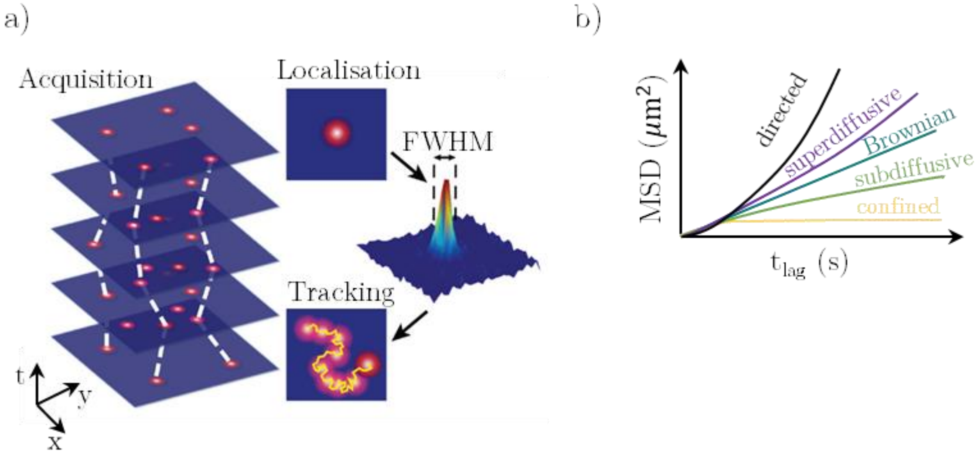

Figure 1.8 Principle of Single Particle Tracking (SPT). a) Schematic representation on the working principle of SPT. During acquisition sparsely labelled molecules (red dots) are recorded as a function of time generating hundreds (or thousands) of images. During the localisation step, the centre of mass position of each fluorescent molecule is retrieved. The localisation accuracy ultimately depends on the full-width at half-maximum (FWHM) of the emitter Airy disk, the number of collected photons from the emitters and the different sources of noise. After localising all the fluorescent molecules as a function of time, reconnection is done by linking the localisations between consecutive frames to generate trajectories. Adapted from Manzo and Garcia-Parajo (43). b) The mean-square displacement (MSD) plot as a function of lag time has different behaviours depending on the diffusing nature of the studied trajectories.

One of the challenges of SPT is the photostability of fluorescent probes used to label the molecules of interest. Ideally, one would like to have long trajectories in order to compute the MSD in a robust manner without noise, and be able to study how a single molecule explores different regions of space. Traditional organic dyes suffer from low photostability, high photobleaching and low brightness, which pushed researchers to use other types of fluorophores to perform SPT. For studies at the plasma membrane of cells, QDs have been used to overcome the limitations of traditional fluorescent dyes due to their great photo-physical properties(92, 93). However, using QDs for intracellular studies is challenging and prone to artefacts, albeit some groups have proven to be possible(93, 94). Another less popular approach is the use of gold-colloidal particles that scatter light and allow to track the molecules for several minutes with extremely high temporal resolution (μs regime) (16). Nonetheless, because they are not fluorescence, their applications are limited to single-colour experiments and they are rather large which might hinder the diffusion of molecules(95). Finally, the recent advent of more photostable and bright fluorescent dyes such as the Janelia dyes(36, 37) allow for good performance in SPT and because of their small size they are ideal to study the dynamics both at the plasma membrane and at the interior of the cell.

Despite the potential and importance of SPT in the field of cell biology, the technique suffers from low statistics. As the number of trajectories obtained per experiment is low, SPT requires to perform many replicates in order to collect enough statistics. In the light of this limitation, high-density single particle tracking (HD-SPT) is emerging as a powerful approach to obtain large number of trajectories from single cell experiments and derive spatial information from the trajectories. Deeper insights into HD-SPT are given in Chapters 3, 4 and 5 of this thesis.

1.3 Current challenges in the field

Understanding the spatiotemporal organisation of molecules in the cell is intrinsically linked to the evolution of the microscopy techniques herein described. Gaining access to the nanoscale by means of super-resolution microscopy allowed to resolve structures and image clusters of proteins beyond what was ever possible with traditional fluorescence microscopy. In fact, super-resolution techniques have been applied to study many different components in cells: nuclear pores(96), chromatin substructures(97, 98), centrioles (99, 100), Golgi apparatus(101, 102), the endoplasmic reticulum(103), plasma membrane receptors (28, 71), etc. and the amount of research is exponentially growing. Unfortunately, super-resolution microscopy suffers from poor temporal resolution limiting the studies to either fixed cells or imaging very slow dynamics. To gain access to the temporal information and dynamics in cell biology a set of techniques have developed being FRAP, FCS and SPT the most commonly used. These techniques have provided great insights onto the dynamics in cell biology: lipid diffusion(76), DNA(104), membrane receptors(105), etc. But these techniques fail to give a comprehensive understanding on the ensemble spatial organisation of molecules. Therefore, when one wants to elucidate the spatiotemporal organisation of a receptor or molecule with high temporal and spatial resolutions, one finds itself in a crossroad: either one can get high spatial resolution using super-resolution microscopy or access the temporal information using FRAP, FCS or SPT. This poses a major bottleneck to real quantitative cell biology studies because ideally one would like to have a full understanding on how molecules dynamically explore their surroundings with high temporal and spatial resolutions.

In the light of this void, current research is conducted to bridge between both families of techniques and to reach a compromise between spatial and temporal resolutions. A fascinating new field of hybrid methodologies is emerging where super-resolution microscopy techniques are combined with other techniques. Some examples are STED-FCS(106), sptPALM(107), universal PAINT (uPAINT)(108), live cell STED(109), … Our goal is to contribute to this field with the development of novel methodologies.

1.4 Concept of the thesis

In this thesis we aim to push the limits of what is currently possible and contribute to the field of quantitative cell biology and fluorescence microscopy with new tools to understand the spatiotemporal organisation of proteins. We have developed novel analysis tools for quantitative super-resolution imaging. Moreover, we propose a novel methodology to bridge between super-resolution microscopy techniques and temporal techniques by using high-density single particle tracking. In this first Chapter we have reviewed most current models of spatiotemporal organisation in the field of cell membrane biology as well as a state-of-the-art overview on the fluorescence microscopy tools. In Chapter 2, we focus on quantitative super-resolution STED and STORM microscopy, showing newly developed algorithms during the span of the thesis. In Chapter 3, we present a novel methodology that takes advantage of high-density SPT, that we called high-density maps (HiDenMaps). We explain the technical requirements in HD-SPT to have faithful HiDenMaps that describe the full spatial exploration of molecules. In Chapter 4, we apply HiDenMaps to study the spatiotemporal organisation of CD44, a transmembrane receptor that interacts both with the extracellular matrix and cortical actin. In Chapter 5, we present a set of analysis tools to further exploit the information encoded in HiDenMaps and study different temporal scales in actin-driven plasma membrane compartmentalisation. In Chapter 6, we extend our HiDenMap methodology to a multi-colour scheme and we study virus infection of immature dendritic cells. We show that the dynamic establishment of pre-docking platforms constituted by tripartite proteins ensures the successful engagement of viruses on the plasma membrane. Finally, in Chapter 7, we highlight the main findings of our research and provide new avenues for further research in the field.

1.5 References

1. B. Alberts, D. Bray, K. Hopkin, A. D. Johnson, *Essential Cell Biology - Alberts - Third Edition* (2010).
2. S. F. Banani, H. O. Lee, A. A. Hyman, M. K. Rosen, Biomolecular condensates: Organizers of cellular biochemistry. *Nat. Rev. Mol. Cell Biol.* **18** (2017).
3. C. P. Brangwynne, *et al.*, Germline P granules are liquid droplets that localize by controlled dissolution/condensation. *Science (80-.).* **324** (2009).
4. A. A. Hyman, C. A. Weber, F. Jülicher, Liquid-liquid phase separation in biology. *Annu. Rev. Cell Dev. Biol.* **30** (2014).
5. Y. Shin, C. P. Brangwynne, Liquid phase condensation in cell physiology and disease. *Science (80-.).* (2017) https:/doi.org/10.1126/science.aaf4382.
6. R. Phillips, Jane Kondev, Julie Theriot, Hernan Garcia, *Physical Biology of the Cell*, 2nd Ed. (Garland Science, 2012).
7. K. Simons, D. Toomre, Lipid rafts and signal transduction. *Nat. Rev. Mol. Cell Biol.* **1** (2000).
8. D. Lingwood, K. Simons, Lipid rafts as a membrane-organizing principle. *Science* **327**, 46–50 (2010).
9. G. van Meer, E. H. Stelzer, R. W. Wijnaendts-van-Resandt, K. Simons, Sorting of sphingolipids in epithelial (Madin-Darby canine kidney) cells. *J. Cell Biol.* **105** (1987).
10. P. Sharma, *et al.*, Nanoscale Organization of Multiple GPI-Anchored Proteins in Living Cell Membranes. *Cell* **116** (2004).
11. T. S. Van Zanten, *et al.*, Hotspots of GPI-anchored proteins and integrin nanoclusters function as nucleation sites for cell adhesion. *Proc. Natl. Acad. Sci. U. S. A.* **106** (2009).
12. E. Sevcsik, G. J. Schütz, With or without rafts? Alternative views on cell

membranes. *BioEssays* **38**, 129–139 (2016).

13. K. Gowrishankar, *et al.*, Active remodeling of cortical actin regulates spatiotemporal organization of cell surface molecules. *Cell* **149** (2012).
14. A. Chaudhuri, B. Bhattacharya, K. Gowrishankar, S. Mayor, M. Rao, Spatiotemporal regulation of chemical reactions by active cytoskeletal remodeling. *Proc. Natl. Acad. Sci. U. S. A.* **108** (2011).
15. M. P. Sheetz, Membrane skeletal dynamics: Role in modulation of red cell deformability, mobility of transmembrane proteins, and shape. *Semin. Hematol.* **20**, 175–188 (1983).
16. A. Kusumi, *et al.*, Paradigm shift of the plasma membrane concept from the two-dimensional continuum fluid to the partitioned fluid: High-speed single-molecule tracking of membrane molecules. *Annu. Rev. Biophys. Biomol. Struct.* (2005) https:/doi.org/10.1146/annurev.biophys.34.040204.144637.
17. T. Fujiwara, K. Ritchie, H. Murakoshi, K. Jacobson, A. Kusumi, Phospholipids undergo hop diffusion in compartmentalized cell membrane. *J. Cell Biol.* **157** (2002).
18. A. Kusumi, *et al.*, Dynamic organizing principles of the plasma membrane that regulate signal transduction: Commemorating the fortieth anniversary of singer and nicolson's fluid-mosaic model. *Annu. Rev. Cell Dev. Biol.* **28** (2012).
19. Z. Kalay, T. K. Fujiwara, A. Otaka, A. Kusumi, Lateral diffusion in a discrete fluid membrane with immobile particles. *Phys. Rev. E - Stat. Nonlinear, Soft Matter Phys.* **89** (2014).
20. N. Morone, *et al.*, Three-dimensional reconstruction of the membrane skeleton at the plasma membrane interface by electron tomography. *J. Cell Biol.* **174** (2006).
21. S. A. Freeman, *et al.*, Transmembrane Pickets Connect Cyto- and Pericellular Skeletons Forming Barriers to Receptor Engagement. *Cell* **172**, 305-317.e10 (2018).
22. M. J. Paszek, *et al.*, Scanning angle interference microscopy reveals cell dynamics at the nanoscale. *Nat. Methods* **9**, 825–827 (2012).
23. W. L. Barnes, Fluorescence near interfaces: the role of photonic mode density. *J. Mod. Opt.* **45**, 661–699 (1998).
24. O. B. Garner, L. G. Baum, Galectin-glycan lattices regulate cell-surface glycoprotein organization and signalling in *Biochemical Society Transactions*, (2008) https:/doi.org/10.1042/BST0361472.
25. M. F. Garcia-Parajo, A. Cambi, J. A. Torreno-Pina, N. Thompson, K. Jacobson, Nanoclustering as a dominant feature of plasma membrane organization. *J. Cell Sci.* **127** (2014).
26. K. G. N. Suzuki, *et al.*, GPI-anchored receptor clusters transiently recruit Lyn and Gα for temporary cluster immobilization and Lyn activation: Single-molecule tracking study 1. *J. Cell Biol.* **177** (2007).

27. K. Jaqaman, *et al.*, Cytoskeletal control of CD36 diffusion promotes its receptor and signaling function. *Cell* **146** (2011).

28. J. A. Torreno-Pina, *et al.*, Enhanced receptor-clathrin interactions induced by N-glycan-mediated membrane micropatterning. *Proc. Natl. Acad. Sci.* **111**, 11037–11042 (2014).

29. P. Lajoie, J. G. Goetz, J. W. Dennis, I. R. Nabi, Lattices, rafts, and scaffolds: domain regulation of receptor signaling at the plasma membrane. *J. Cell Biol.* **185** (2009).

30. H. Ponta, L. Sherman, P. A. Herrlich, CD44: From adhesion molecules to signalling regulators. *Nat. Rev. Mol. Cell Biol.* (2003) https:/doi.org/10.1038/nrm1004.

31. S. Donatello, *et al.*, Lipid raft association restricts CD44-ezrin interaction and promotion of breast cancer cell migration. *Am. J. Pathol.* **181** (2012).

32. J. B. Pawley, <italic>Handbook of Biological Confocal Microscopy, Second Edition</italic>. *Opt. Eng.* **35** (1996).

33. O. Shimomura, F. H. Johnson, Y. Saiga, Extraction, Purification and Properties of Aequorin, a Bioluminescent Protein from the Luminous Hydromedusan,Aequorea. *J. Cell. Comp. Physiol.* **59** (1962).

34. R. Y. Tsien, THE GREEN FLUORESCENT PROTEIN. *https://doi-org.sire.ub.edu/10.1146/annurev.biochem.67.1.509* **67**, 509–544 (2003).

35. N. C. Shaner, P. A. Steinbach, R. Y. Tsien, A guide to choosing fluorescent proteins. *Nat. Methods* **2** (2005).

36. J. B. Grimm, *et al.*, Bright photoactivatable fluorophores for single-molecule imaging. *Nat. Methods* **13** (2016).

37. J. B. Grimm, T. A. Brown, B. P. English, T. Lionnet, L. D. Lavis, "Synthesis of Janelia Fluor HaloTag and SNAP-tag ligands and their use in cellular imaging experiments" in *Methods in Molecular Biology*, (2017).

38. X. Michalet, *et al.*, Quantum dots for live cells, in vivo imaging, and diagnostics. *Science (80-.).* **307** (2005).

39. M. Bruchez, M. Moronne, P. Gin, S. Weiss, A. P. Alivisatos, Semiconductor nanocrystals as fluorescent biological labels. *Science (80-.).* **281** (1998).

40. A. Keppler, *et al.*, A general method for the covalent labeling of fusion proteins with small molecules in vivo. *Nat. Biotechnol.* **21** (2003).

41. G. V. Los, *et al.*, HaloTag: A novel protein labeling technology for cell imaging and protein analysis. *ACS Chem. Biol.* **3** (2008).

42. A. Gautier, *et al.*, An Engineered Protein Tag for Multiprotein Labeling in Living Cells. *Chem. Biol.* **15** (2008).

43. C. Manzo, M. F. Garcia-Parajo, A review of progress in single particle tracking: From methods to biophysical insights. *Reports Prog. Phys.* (2015) https:/doi.org/10.1088/0034-4885/78/12/124601.

44. T. C. Rao, T. J. Nawara, A. L. Mattheyses, "Live-Cell Total Internal Reflection

Fluorescence (TIRF) Microscopy to Investigate Protein Internalization Dynamics" in *Methods in Molecular Biology*, (2022).

45. M. Tokunaga, N. Imamoto, K. Sakata-Sogawa, Highly inclined thin illumination enables clear single-molecule imaging in cells. *Nat. Methods* **5** (2008).
46. E. Abbe, Beiträge zur Theorie des Mikroskops und der mikroskopischen Wahrnehmung. *Arch. für Mikroskopische Anat.* **9**, 413–468 (1873).
47. F. De Lange, *et al.*, Cell biology beyond the diffraction limit: Near-field scanning optical microscopy. *J. Cell Sci.* **114** (2001).
48. N. F. Van Hulst, J. A. Veerman, M. F. García-Parajó, L. Kuipers, Analysis of individual (macro)molecules and proteins using near-field optics. *J. Chem. Phys.* **112** (2000).
49. M. F. García-Parajó, *et al.*, Near-field fluorescence microscopy: An optical nanotool to study protein organization at the cell membrane. *Nanobiotechnology* **1** (2005).
50. B. I. De Bakker, *et al.*, Nanoscale organization of the pathogen receptor DC-SIGN mapped by single-molecule high-resolution fluorescence microscopy. *ChemPhysChem* **8** (2007).
51. W. Lukosz, Optical Systems with Resolving Powers Exceeding the Classical Limit II. *J. Opt. Soc. Am.* **57** (1967).
52. M. G. L. Gustafsson, Surpassing the lateral resolution limit by a factor of two using structured illumination microscopy. *J. Microsc.* **198** (2000).
53. E. Betzig, *et al.*, Imaging intracellular fluorescent proteins at nanometer resolution. *Science (80-.).* (2006) https:/doi.org/10.1126/science.1127344.
54. M. J. Rust, M. Bates, X. Zhuang, Sub-diffraction-limit imaging by stochastic optical reconstruction microscopy (STORM). *Nat. Methods* **3** (2006).
55. S. T. Hess, T. P. K. Girirajan, M. D. Mason, Ultra-high resolution imaging by fluorescence photoactivation localization microscopy. *Biophys. J.* (2006) https:/doi.org/10.1529/biophysj.106.091116.
56. S. Van De Linde, *et al.*, Direct stochastic optical reconstruction microscopy with standard fluorescent probes. *Nat. Protoc.* **6** (2011).
57. M. Bates, T. R. Blosser, X. Zhuang, Short-range spectroscopic ruler based on a single-molecule optical switch. *Phys. Rev. Lett.* **94** (2005).
58. M. Heilemann, E. Margeat, R. Kasper, M. Sauer, P. Tinnefeld, Carbocyanine dyes as efficient reversible single-molecule optical switch. *J. Am. Chem. Soc.* **127** (2005).
59. M. Heilemann, *et al.*, Subdiffraction-resolution fluorescence imaging with conventional fluorescent probes. *Angew. Chemie - Int. Ed.* **47** (2008).
60. M. Lelek, *et al.*, Single-molecule localization microscopy. *Nat. Rev. Methods Prim.* **1** (2021).
61. B. Turkowyd, D. Virant, U. Endesfelder, From single molecules to life: microscopy at the nanoscale. *Anal. Bioanal. Chem.* **408** (2016).

62. S. Wang, J. R. Moffitt, G. T. Dempsey, X. S. Xie, X. Zhuang, Characterization and development of photoactivatable fluorescent proteins for single-molecule-based superresolution imaging. *Proc. Natl. Acad. Sci. U. S. A.* **111** (2014).
63. A. Sharonov, R. M. Hochstrasser, Wide-field subdiffraction imaging by accumulated binding of diffusing probes. *Proc. Natl. Acad. Sci. U. S. A.* **103** (2006).
64. R. Jungmann, *et al.*, Multiplexed 3D cellular super-resolution imaging with DNA-PAINT and Exchange-PAINT. *Nat. Methods* (2014) https:/doi.org/10.1038/nmeth.2835.
65. J. Schnitzbauer, M. T. Strauss, T. Schlichthaerle, F. Schueder, R. Jungmann, Super-resolution microscopy with DNA-PAINT. *Nat. Protoc.* (2017) https:/doi.org/10.1038/nprot.2017.024.
66. O. K. Wade, *et al.*, 124-Color Super-resolution Imaging by Engineering DNA-PAINT Blinking Kinetics. *Nano Lett.* **19** (2019).
67. S. W. Hell, J. Wichmann, Breaking the diffraction resolution limit by stimulated emission: stimulated-emission-depletion fluorescence microscopy. *Opt. Lett.* (1994) https:/doi.org/10.1364/ol.19.000780.
68. T. A. Klar, S. Jakobs, M. Dyba, A. Egner, S. W. Hell, Fluorescence microscopy with diffraction resolution barrier broken by stimulated emission. *Proc. Natl. Acad. Sci. U. S. A.* (2000) https:/doi.org/10.1073/pnas.97.15.8206.
69. M. Spiess, *et al.*, Active and inactive β1 integrins segregate into distinct nanoclusters in focal adhesions. *J. Cell Biol.* **217** (2018).
70. K. I. Willig, S. O. Rizzoli, V. Westphal, R. Jahn, S. W. Hell, STED microscopy reveals that synaptotagmin remains clustered after synaptic vesicle exocytosis. *Nature* **440** (2006).
71. C. Manzo, *et al.*, The neck region of the C-type lectin DC-SIGN regulates its surface spatiotemporal organization and virus-binding capacity on antigen-presenting cells. *J. Biol. Chem.* **287** (2012).
72. F. Persson, *et al.*, Fluorescence nanoscopy of single DNA molecules by using stimulated emission depletion (STED). *Angew. Chemie - Int. Ed.* **50** (2011).
73. Z. Cseresnyes, U. Schwarz, C. M. Green, Analysis of replication factories in human cells by super-resolution light microscopy. *BMC Cell Biol.* **10** (2009).
74. C. Eggeling, K. I. Willig, S. J. Sahl, S. W. Hell, Lens-based fluorescence nanoscopy. *Q Rev Biophys* **48**, 178–243 (2015).
75. C. V. Carman, Overview: Imaging in the study of integrins. *Methods Mol. Biol.* **757** (2011).
76. D. Axelrod, *et al.*, Lateral motion of fluorescently labeled acetylcholine receptors in membranes of developing muscle fibers. *Proc. Natl. Acad. Sci. U. S. A.* (1976) https:/doi.org/10.1073/pnas.73.12.4594.
77. D. Axelrod, D. E. Koppel, J. Schlessinger, E. Elson, W. W. Webb, Mobility measurement by analysis of fluorescence photobleaching recovery kinetics.

Biophys. J. (1976) https:/doi.org/10.1016/S0006-3495(76)85755-4.

78. J. Lippincott-Schwartz, N. Altan-Bonnet, G. H. Patterson, Photobleaching and photoactivation: Following protein dynamics in living cells. *Nat. Rev. Mol. Cell Biol.* **4** (2003).
79. E. A. J. Reits, J. J. Neefjes, From fixed to FRAP: Measuring protein mobility and activity in living cells. *Nat. Cell Biol.* (2001) https:/doi.org/10.1038/35078615.
80. E. Haustein, P. Schwille, Fluorescence correlation spectroscopy: Novel variations of an established technique. *Annu. Rev. Biophys. Biomol. Struct.* **36** (2007).
81. E. L. Elson, Fluorescence correlation spectroscopy: Past, present, future. *Biophys. J.* **101** (2011).
82. S. A. Kim, K. G. Heinze, P. Schwille, Fluorescence correlation spectroscopy in living cells. *Nat. Methods* **4** (2007).
83. C. Eggeling, *et al.*, Direct observation of the nanoscale dynamics of membrane lipids in a living cell. *Nature* (2009) https:/doi.org/10.1038/nature07596.
84. C. Manzo, T. S. Van Zanten, M. F. Garcia-Parajo, Nanoscale fluorescence correlation spectroscopy on intact living cell membranes with NSOM probes. *Biophys. J.* (2011) https:/doi.org/10.1016/j.bpj.2010.12.3690.
85. A. Sergé, N. Bertaux, H. Rigneault, D. Marguet, Dynamic multiple-target tracing to probe spatiotemporal cartography of cell membranes. *Nat. Methods* (2008) https:/doi.org/10.1038/nmeth.1233.
86. K. Shafique, M. Shah, A noniterative greedy algorithm for multiframe point correspondence. *IEEE Trans. Pattern Anal. Mach. Intell.* **27** (2005).
87. W. J. Godinez, K. Rohr, Tracking multiple particles in fluorescence time-lapse microscopy images via probabilistic data association. *IEEE Trans. Med. Imaging* **34** (2015).
88. K. Jaqaman, *et al.*, Robust single-particle tracking in live-cell time-lapse sequences. *Nat. Methods* **5** (2008).
89. M. J. Saxton, K. Jacobson, Single-particle tracking: Applications to membrane dynamics. *Annu. Rev. Biophys. Biomol. Struct.* **26** (1997).
90. S. Wieser, G. J. Schütz, Tracking single molecules in the live cell plasma membrane-Do's and Don't's. *Methods* **46** (2008).
91. D. Krapf, Mechanisms Underlying Anomalous Diffusion in the Plasma Membrane. *Curr. Top. Membr.* **75** (2015).
92. M. Dahan, *et al.*, Diffusion Dynamics of Glycine Receptors Revealed by Single-Quantum Dot Tracking. *Science (80-.).* **302** (2003).
93. F. Pinaud, S. Clarke, A. Sittner, M. Dahan, Probing cellular events, one quantum dot at a time. *Nat. Methods* **7** (2010).
94. J. Janczura, *et al.*, Identifying heterogeneous diffusion states in the cytoplasm by a hidden Markov model. *New J. Phys.* **23** (2021).

95. M. P. Clausen, B. Christoffer Lagerholm, The Probe Rules in Single Particle Tracking. *Curr. Protein Pept. Sci.* **12** (2011).
96. A. Löschberger, *et al.*, Super-resolution imaging visualizes the eightfold symmetry of gp210 proteins around the nuclear pore complex and resolves the central channel with nanometer resolution. *J. Cell Sci.* **125** (2012).
97. B. J. Beliveau, *et al.*, Single-molecule super-resolution imaging of chromosomes and in situ haplotype visualization using Oligopaint FISH probes. *Nat. Commun.* **6** (2015).
98. A. N. Boettiger, *et al.*, Super-resolution imaging reveals distinct chromatin folding for different epigenetic states. *Nature* **529** (2016).
99. S. Lawo, M. Hasegan, G. D. Gupta, L. Pelletier, Subdiffraction imaging of centrosomes reveals higher-order organizational features of pericentriolar material. *Nat. Cell Biol.* **14** (2012).
100. N. Olivier, D. Keller, P. Gönczy, S. Manley, Resolution Doubling in 3D-STORM Imaging through Improved Buffers. *PLoS One* **8** (2013).
101. Y. Wakana, *et al.*, The er cholesterol sensor scap promotes carts biogenesis at er–golgi membrane contact sites. *J. Cell Biol.* **220** (2021).
102. R. S. Erdmann, *et al.*, Super-resolution imaging of the Golgi in live cells with a bioorthogonal ceramide probe. *Angew. Chemie - Int. Ed.* **53** (2014).
103. S. H. Shim, *et al.*, Super-resolution fluorescence imaging of organelles in live cells with photoswitchable membrane probes. *Proc. Natl. Acad. Sci. U. S. A.* **109** (2012).
104. D. Magde, E. Elson, W. W. Webb, Thermodynamic fluctuations in a reacting system measurement by fluorescence correlation spectroscopy. *Phys. Rev. Lett.* (1972) https:/doi.org/10.1103/PhysRevLett.29.705.
105. V. Levi, E. Gratton, Exploring dynamics in living cells by tracking single particles. *Cell Biochem. Biophys.* **48** (2007).
106. A. Honigmann, *et al.*, Scanning STED-FCS reveals spatiotemporal heterogeneity of lipid interaction in the plasma membrane of living cells. *Nat. Commun.* **5**, 5412 (2014).
107. S. Manley, *et al.*, High-density mapping of single-molecule trajectories with photoactivated localization microscopy. *Nat. Methods* (2008) https:/doi.org/10.1038/nmeth.1176.
108. G. Giannone, *et al.*, Dynamic superresolution imaging of endogenous proteins on living cells at ultra-high density. *Biophys. J.* (2010) https:/doi.org/10.1016/j.bpj.2010.06.005.
109. V. Westphal, *et al.*, Video-rate far-field optical nanoscopy dissects synaptic vesicle movement. *Science (80-.).* **320** (2008).

Chapter 2

Quantitative super-resolution imaging

The advent of new super-resolution fluorescence microscopy techniques has provided access to the spatial organisation of molecules in intact cells with unprecedented resolutions. The new kind of data provided by these images has revealed details never anticipated and thus has opened up new questions regarding how these molecules organise in space, whether and how they interact with other molecules in their immediate surrounding, and ultimately, how this organisation impacts their function. However, addressing these questions in a truly quantitative fashion requires the development of novel ways to visualise and analyse the data. In this chapter, we focus on several approaches to quantitatively analyse stimulated emission depletion (STED) super-resolution images and single molecule localisation microscopy (SMLM) data. Moreover, we show how these analyses have contributed to a better understanding of the spatial organisation of different receptor proteins located at the plasma membrane of intact cells.

This work has been partially published as:

1. Enric Gutiérrez-Martínez, Susana Benet, **Nicolas Mateos**, Itziar Erkizia, Jon Ander Nieto-Garai, Maier Lorizate, Carlo Manzo, Felix Campelo, Nuria Izquierdo-Useros, Javier Martinez-Picado, Maria F. Garcia-Parajo, “Actin-regulated Siglec-1 nanoclustering influences HIV-1 capture and virus-containing compartment formation in dendritic cells”, *eLife, second revision*

2. Sarah Keary, **Nicolas Mateos**, Felix Campelo, and Maria F. Garcia-Parajo, “Differential activation and mesoscale organisation of integrin nanoclusters in focal adhesions”, *in preparation*

3. Pablo Lujan, Pablo Rios, **Nicolas Mateos**, Hans-Michael Müller, Christian Lüchtenborg, Timo Sachsenheimer, Britta Brügger, Maria F. Garcia-Parajo, Felix Campelo, Walter Nickel, and Maja Köhn, “Phosphatase of regenerating liver-3 enhances clathrin-mediated endocytosis by PI(4,5)P2 dephosphorylation”, *in preparation.*

2.1 Motivation

The advent of fluorescence microscopy has been a game-changer in cell biology research. It has allowed to image cells in a non-invasive manner and together with the development of new fluorescent probes it has been possible to virtually tag any protein of interest. A milestone in fluorescence microscopy has been the invention of super-resolution (SR) microscopy techniques that overcome the diffraction limit of light. As discussed in Chapter 1, the most widely used SR approaches are stimulated emission depletion (STED) and single molecule localisation microscopy (SMLM) methods such as STORM (stochastic optical reconstruction microscopy) and PALM (photoactivated localisation microscopy)(1–5). These SRs approaches have enabled the study of the spatial organisation of proteins with unprecedented high resolutions. However, these new SR techniques require the development of novel analysis tools in order to provide truly quantitative information on the images obtained.

Quantitative analyses of SR images are far beyond trivial and demand enormous care because they are prone to pitfalls and artefacts (reviewed in (6–8)). Thus, SR microscopy requires proper calibrations and controls to ensure reliable results. Moreover, it is crucial that the experiments are performed methodologically maintaining constant the imaging conditions, labelling strategies, fluorescent probes, etc for the same set of experiments.

In the case of STED, the analytical tools needed to quantify the images should in principle be rather simple because the images generated contain true fluorescence information (i.e., intensity, spectral and even lifetime information). Yet, in practice, STED analysis is challenging. For instance, one of the most straightforward analysis that one can perform in STED images is counting the number of biomolecules (stoichiometry) in the fluorescent spots by directly linking the fluorescent signal to the number of emitters. Although this approach is very powerful, deriving stoichiometric information on STED images requires proper modelling of the detected photon statistics and careful experimental imaging (8). In our lab, we have implemented an algorithm to derive stoichiometric information from STED images(9–11) and in this chapter we show our latest results using this methodology to study the nanoclustering of a membrane receptor expressed on cells of the immune system.

In the case of SMLM images, they consist on discrete single molecule localisation maps, and thus, it might be tempting to count the number of localisations to derive the stoichiometry of a given nanocluster. However, this approach can lead to major artefacts because a single fluorophore can reappear multiple times during the acquisition time leading to multiple localisations (amongst other plausible sources of artefacts, (6, 12–14)). Nevertheless, if one considers all the possible sources of artefacts, it is likely to make an estimate on the number of molecules per cluster by performing the proper statistics(15–17). Another line of quantification refers to studying the spatial organisation of nanoclusters by performing colocalisation analysis. At the birth of SMLM techniques, super-resolution images were obtained by voxelating the space and counting the number of localisations within each voxel to generate intensity-like images(18). These images were then processed similarly to confocal, TIRF or STED images and used typical colocalisation analysis such as the Pearson's or the Manders' coefficients (18, 19). However, this approach kind of takes away the fun and the enormous potential of having single molecule data. In the past decade, new methods have emerged to perform localisation-based colocalisation using different strategies and giving better insights in SMLM(20–23). In this chapter, we will exploit the data from STORM imaging to quantify our experiments using state-of-the-art algorithms for SMLM.

The aim of this chapter is to present the reader with novel algorithms to quantify SR images. We focus on STED microscopy and more extensively in STORM analysis. We have implemented algorithms published by other Labs and have also developed novel algorithms based in MATLAB. Using these advanced algorithms, we show some of our latest findings in the context of different biological questions.

2.2 Spatial organisation of the transmembrane receptor Siglec-1 in dendritic cells

2.2.1 **Motivation**

A great advantage of STED is that one can rely on the fluorescence intensity obtained in the images and provide a quantitative view on the stoichiometry of molecules in nanoclusters by performing the proper modelling and statistics. In this section, we focus on studying a receptor on the plasma membrane of immune cells which is crucial for the recognition of HIV-1.

Dendritic cells (DCs) are a specialised group of leukocytes that play an essential role in the innate and adaptive immunity through their function as antigen presenting cells (see Chapter 6 for a more detailed explanation, Ref (24)). Amongst other viruses and pathogens DCs recognise HIV-1 viruses and capture them. In the case of immature DC (iDCs), the recognition of HIV-1 is mainly performed by the receptor DC-SIGN(25); while in the case of mature DC (mDCs), it has been shown that the recognition and capture of HIV-1 is mostly mediated by the receptor Siglec-1(26, 27). Since Siglec-1 takes over DC-SIGN in mDCs, we wanted to ascertain if, aside from the different expression levels of these receptors, there is a different spatial organisation of Siglec-1 in iDCs compared to mDCs that could impact in the capture capacity of the receptor.

We thus used STED microscopy to map the spatial organisation of Siglec-1 in DCs. We discovered that Siglec-1 forms nanoclusters on mDCs, while on iDC Siglec-1 remains mostly randomly organised. We quantified the nanoclusters by means of the number of molecules within the clusters, their size and the nearest-neighbour distance between nanoclusters in iDCs and mDCs. In this Chapter we show a small part of a larger thorough study performed by Dr. Enric Gutiérrez-Martínez *et al.* in our group(28).

2.2.2 **Methods**

2.2.2.1 Determining the number of molecules per nanocluster in STED microscopy

To define the area of Siglec-1 individual spots, STED images were processed using Fiji to apply a subtraction of the background and a Gaussian blur filter (sigma radius 1) followed by a difference of Gaussian (smaller/greater sigma 1:3). Then an intensity threshold was used to create binary masks of the individual spots from which we obtain the mean intensity values per each spot within the original images. Thereafter, we used a MATLAB custom code to fit the distribution of intensities of individual spots from antibodies on glass to a lognormal function (f1).

$$f_1(I) = \frac{1}{\sqrt{2\pi}\,\sigma I}\, e^{-\frac{(\ln I-\mu)^2}{2\sigma^2}} \tag{2.1}$$

This model corresponds to the expected theoretical distribution for the intensity corresponding to the detection of a single fluorescent emitter (29–31). The intensity values obtained from spots on glass were used to define the µ (mean) and σ (standard deviation) of the lognormal distribution, through its fit to a linear combination of N = 2 functions. These parameters were used as a single molecule reference to define the stoichiometry of the fluorescence of Siglec-1 receptors in the cells measured under identical experimental conditions (10, 32).

The intensity histograms of Siglec-1 spots on cell samples showed higher intensities and broader distributions than the antibodies on glass, indicative of nanoclustering and of a mixture of different populations of nanoclusters composed by a different number of molecules (Figure 2.1). To calculate the probability distribution of molecules per spot, the intensity histograms of Siglec-1 spots on cells was fitted to a model distribution g_N (I) composed of a linear combination of functions as described in (9).

$$g_N(I) = \sum_{n=1}^{N} \alpha_n \cdot f_n(I) \tag{2.2}$$

Where f_n shows the intensity distribution of a spot containing n receptors, and α_n is the relative weight of this distribution so that, $\sum_n^N \alpha_n = 1$, being N the maximum number of receptors (in our analysis 12) (30). We considered that the distribution for a spot containing n receptors could be obtained recursively as

$$f_n = f_{n-1} \otimes f_1 \tag{2.3}$$

where $\otimes$ represents the convolution of the intensity distribution lognormal functions for n= 1,2,...,12 (10, 30, 31).

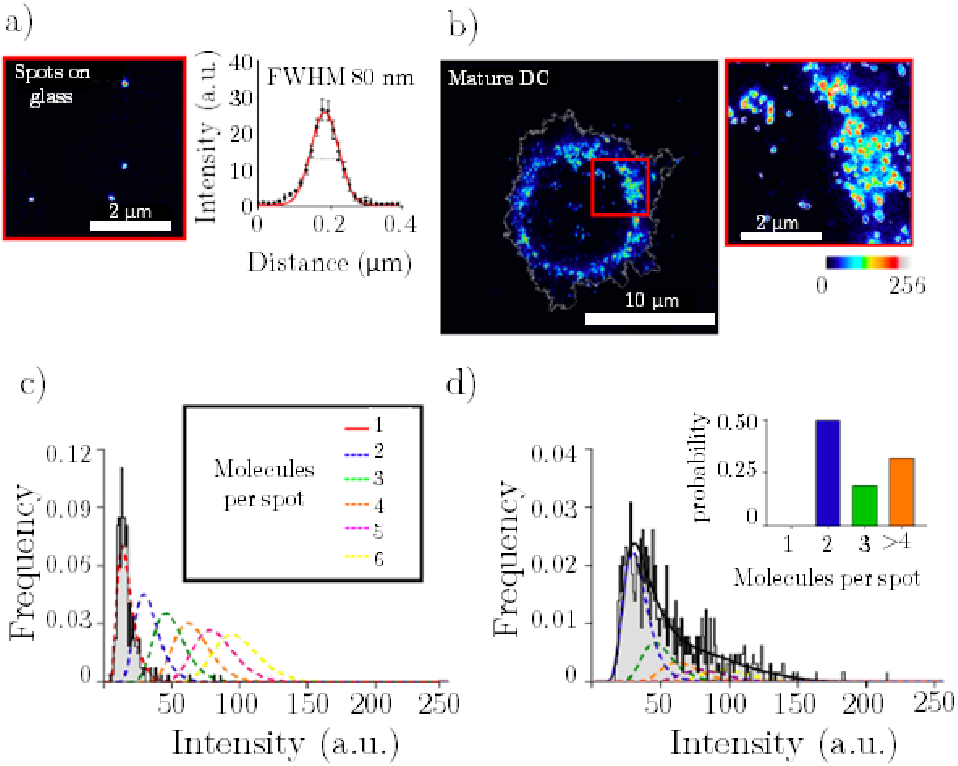

Figure 2.1 Distribution of intensities of spots on glass and of siglec-1 in mDCs. a) STED image of siglec-1 antibodies non-specifically adhered to glass and labelled with secondary antibody Fab-Atto488 and the gaussian fit of the intensity per spot (left). b) STED image of siglec-1 on mDCs with a zoom-in region of interest (right). c) Histogram of spot intensities for spots on glass with the lognormal fit of the experimental data (black line and shaded region). The dashed lines correspond to the calculated intensity distribution functions for different number of molecules per spot. d) Histogram of spot intensity distribution for the representative image shown in panel

b. The inset shows the fitted probabilities of the number of molecules per spot for the representative figure. Figure adapted from Gutierrez-Martinez et al. (28).

2.2.3 **Results**

2.2.3.1 DC activation induces the formation of Siglec-1 nanoclusters

The trans-infection capacity of DCs correlates with the expression levels of Siglec-1, which are increased upon cell activation with (lipopolysaccharide) LPS or (interpheron) IFN (26, 27). However, the spatial organisation of Siglec-1 receptors in resting or activated DCs is not yet known. To address whether DC maturation alters Siglec-1 distribution in the plasma membrane, we first examined the nanoscale organisation of Siglec-1 by STED microscopy in iDCs and LPS-treated DCs (mDCs) differentiated from peripheral blood monocytes (PBMCs) (Figure 2.2a). With a lateral resolution of ~ 80 nm, we discriminated individual Siglec-1 fluorescent spots on the cell surface and measured their peak intensities. To quantify the number of Siglec-1 molecules per spot in the plasma membrane of iDC and mDC we relied on the intensity obtained from individual antibodies (Abs) on glass, corresponding to single molecules (9). LPS-mediated DC maturation induced a higher fraction (~ 57% vs. ~37%) of Siglec-1 dimers and small nanoclusters with > 3 molecules/spot as compared to iDCs, where Siglec-1 was mainly found as monomers (~57% vs. ~22%) (Figure 2.2a,b). The increase in the average number of molecules per spot also coincided with an average increase in spot sizes (Figure 2.2c) and a significant increase in the proximity of Siglec-1 spots on mDCs as compared to iDCs (Figure 2.2d). These results thus indicate that Siglec-1 forms nanoclusters on activated mDCs, whereas its organisation is more random in non-activated iDCs.

To rule out possible artefacts during fixation and labelling of Siglec-1, we proceeded to image Siglec-1 in mDCs using different fixation protocols and labelling approaches. The summary of the results is shown in Figure 2.3. First, we performed the labelling with full chain antibodies and fixed the samples with 4% paraformaldehyde (PFA) (Figure 2.3a). These are the same conditions as to the ones used for Figure 2.2. Second, we used single-chain antibodies to label siglec-1 and fixed the samples with 4% PFA (Figure 2.3b). In this case, we rule out any possible protein aggregation due to the full-chain antibodies. Finally, we used single-chain antibodies and we modified the fixation protocol by using 4% PFA + 0.2% GA (glutaraldehyde) (Figure 2.3c). Analysis on multiple STED images in all three conditions showed no difference in terms of nanoclustering capacity of Siglec-1, ruling out any potential artefacts due to sample fixation or labelling conditions.

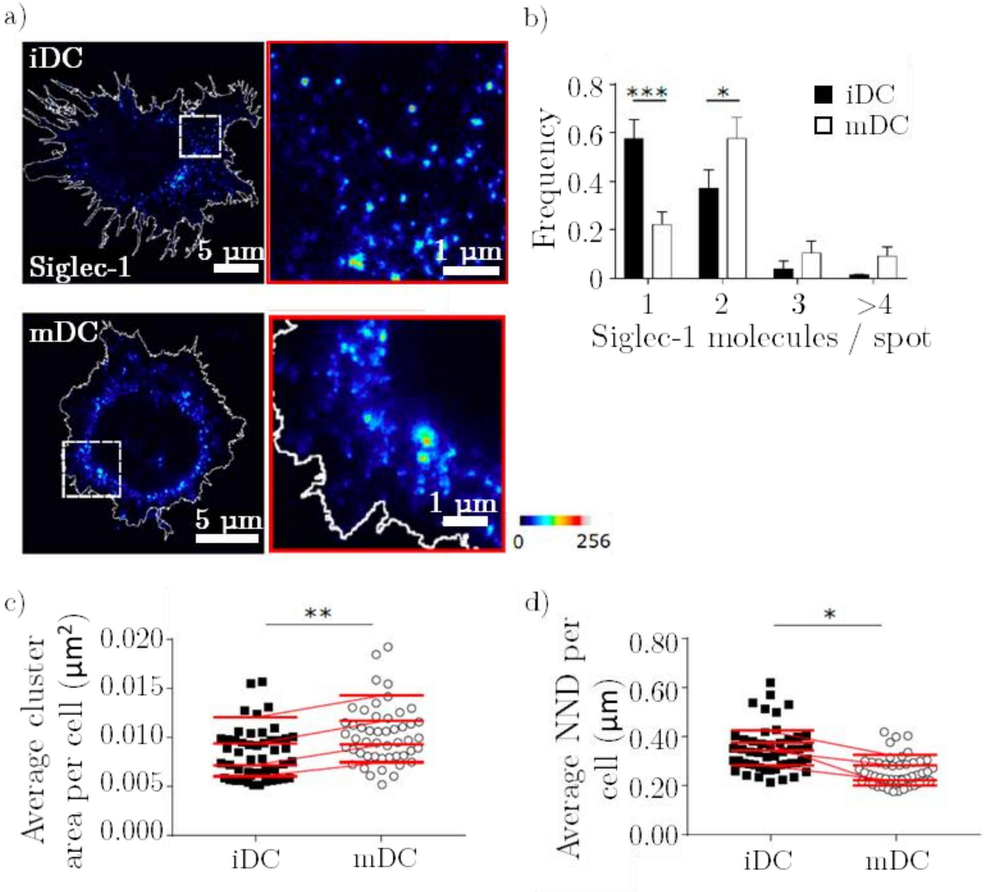

Figure 2.2 Siglec-1 distribution at the plasma membrane of dendritic cells. a) Representative STED images of Siglec-1 at the plasma membrane of iDCs (top) and mDCs (bottom). The image at the right corresponds to the enlarged region-of-interest highlighted by the white box on the left images. The pseudo-colour code denotes the intensity of siglec-1 signal from monomers (blue) to nanoclusters (red). b) Frequency of the number of Siglec-1 molecules per spot in iDCs (black) and mDCs (white). Bars represent the mean and the errors bars represent the standard deviation of the mean of 3 different donors (with minimum 9 cells/donor and condition). The statistical test is a two-way ANOVA with multiple comparison Bonferroni tests. c) Average Siglec-1 spot area per cell. d) Nearest-neighbour distance (NND) between Siglec-1 spots per cell. In c) and d), each symbol corresponds to a single cell, red lines are the mean value per donor (4 donors, 9 cells/cell type). Paired T-test analysis was performed in c) and d). Figure adapted from Gutiérrez-Martínez et al. (28).

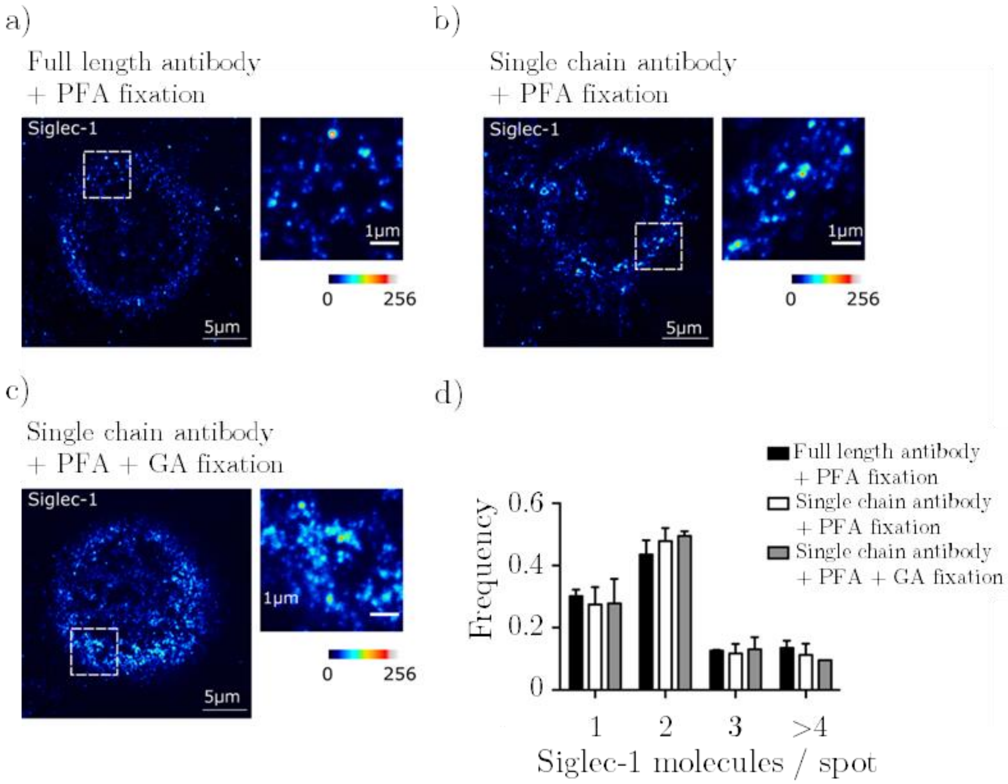

Figure 2.3 Control measurements to discard artefacts on the clustering of Siglec-1 in mDCs. Representative Siglec-1 STED images in: a) mDC fixed with 4% PFA and Siglec-1 labelled with full-length antibodies. b) mDC fixed with 4% PFA and Siglec-1 labelled with single-chain antibodies. c) mDC fixed with 4% PFA + 0.2% GA and Siglec-1 labelled with single-chain antibodies. d) Quantification on the number of Siglec-1 molecules per cluster for the three conditions (a-c), showing no significant difference between them.

Therefore, these experiments show a difference in the spatial organisation of Siglec-1 in mDCs as compared to iDCs. In iDCs, most of Siglec-1 appear as monomers while in mDCs, Siglec-1 clusterises in a larger extend. Considering that nanoclustering is essential in the functional performance of many receptors(33), it becomes clear why in mDCs Siglec-1 is the canonical receptor in HIV-1 capture and not DC-SIGN.

2.3 Quantitative STORM analysis to elucidate the spatial organisation of proteins

In this section we focus on the analysis tools that we have implemented and developed during the span of this thesis for STORM data. Because in our Lab we perform studies on proteins at the plasma membrane of cells, STORM is a great asset. We have implemented already existing algorithms to quantify our data such as studying the clusters of localisations, but we have also developed new algorithms. In this section, we show how we have implemented these algorithms to solve different biological questions and how these analyses have enabled us to learn more about the spatial organisation of different proteins at the plasma membrane.

2.3.1 **Density-based spatial clustering of applications with noise (DBSCAN)**

DBSCAN is a widely used algorithm in the field of SMLM in order to define clusters of localisations(34). The algorithm requires to define two parameters: the radial distance, r, and the minimum number of neighbour localisations, N_{min}, within the radial distance. The working principle of DBSCAN is schematically depicted in Figure 2.4a. Let's consider a set of localisations obtained with any SMLM technique and we define a certain radius, r, and a minimum number of neighbours, N_{min}. The algorithm starts by taking one localisation randomly from the data set, L_k, defining a circle centred at that localisation and counting the number of localisations within the circle, N_k. There are two options: 1) the number of localisations is smaller than the threshold, $N_k < N_{min}$, or, 2) the number of localisations is equal or greater than the threshold, $N_k \geq N_{min}$. In the first scenario, the localisation L_k is classified temporally as noise. Therefore, another localisation is randomly picked and the process is repeated. In the second scenario, the localisation is classified as a core point or seed of the cluster and we proceed to study what happens with the neighbouring localisations of L_k, $L_{k,j}$. For each $L_{k,j}$ the process is repeated and the localisations will be classified as core points or border points depending on whether they fulfil the requirements (number of neighbouring localisations within the circle) or not. Importantly, the border points do belong to the cluster but if let's say some localisations were neighbours of this border point, the algorithm doesn't continue analysing them at this stage. It could be that a localisation that initially was considered to be noise, it was actually a border point. Since the algorithm has to run over all the localisations, it will re-visit that localisation but as a connectivity process from another cluster. Once the algorithm ends, those unconnected localisations to any clusters (not core nor border points) are classified as noise.

The main downfalls of DBSCAN are the sensitivity to the density of localisations and the background(35). Moreover, it requires the researcher's input to determine the parameters and it is often challenging to account for cell to cell variability in expression levels of the protein of interest. Moreover, determining the radius and the minimum number of localisations is a task that must be performed cautiously. Taking too large radiuses can merge independent clusters into a single large cluster. Moreover, if the minimum number of localisations is too small, then the condition to include localisations into a growing cluster is too lax and will overestimate the number of clusters. As a rule of thumb, one must consider how many localisations a single fluorophore can report (performing controls with spots on glass). Ultimately, the human eye is the best tool to find and recognise patterns, clusters, etc. Thus, the parameters chosen must deliver clusters that are similar as the ones visually recognised by the human eye for all the samples studied.

As an example on how DBCAN works, we have analysed a STORM image of CD44, a transmembrane protein, at the plasma membrane of iDCs (Figure 2.4b). We have used the DBSCAN parameters of r=25 nm and Nmin = 20 points to detect the clusters in the image on the left. The output of DBSCAN is shown on the right of Figure 2.4b colour-coding the clusters to tell them apart. Finally, we have computed the cluster area of the detected clusters for CD44 at the plasma membrane of immature DCs (Figure 2.4c).

Despite its potential drawbacks, DBSCAN is one of the most commonly used techniques in order to determine the cluster of localisations. Once the clusters are defined, a whole palette of analysis can be performed in order to obtain quantitative information such as the cluster area or the number of localisations per cluster. Additionally, more sophisticated analysis can be performed as for example nearest-neighbour distributions, colocalisation analysis or distances to a given structure. In the following section, we present some methods that we have implemented to extract the most out of the cluster information obtained from DBSCAN.

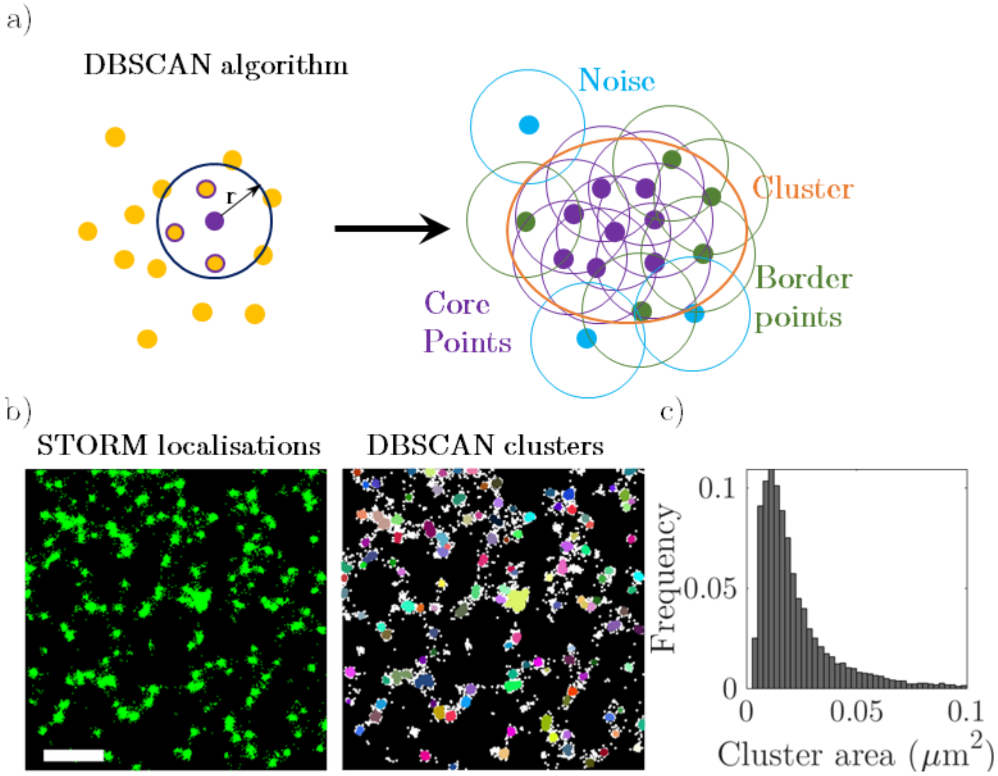

Figure 2.4 Working principle of DBSCAN. a) If we have a set of localisations, we need to define a radius, r, and a minimum number of neighbours, N_{min}. We take a random localisation, in the figure depicted as the purple point on the left. Then, a circle of radius r is drawn and those localisations falling within the circle (yellow with purple edge), the neighbours, are counted. If the number of neighbours is equal or larger to N_{min}, then the purple point is considered to belong to the core of the cluster and the process propagates throughout the neighbours (arrow towards the right picture). In this case, N_{min} was set to 3. The connectivity propagates while the neighbour condition is fulfilled (purple points), when is no longer fulfilled, then those localisations are considered as border points (in green). Moreover, those localisations that do not fulfil at all the conditions, are tagged as noise (light blue). Adapted from Pageon et al. (36). b) Raw STORM localisations of CD44 at the plasma membrane of an iDC (left) and the clusters detected using DBSCAN with r=25 nm and Nmin = 20 points. On the right, the detected clusters colour-coded randomly. The scalebar is 1 µm. c) Quantification of the cluster area for CD44 at the plasma membrane.

2.3.2 Spatial organisation of integrins in focal adhesions

Focal adhesions are highly dense structures that allow the cells to interact with their environment by adhering to the substrate, the extracellular matrix (ECM). One of the key components in focal adhesions are integrins, heterodimeric transmembrane receptors consisting on an alpha and a beta subunit(37, 38). Integrins engage specifically to their ligands on the ECM and to the actin cytoskeleton on the cytosolic region via adaptor proteins such as paxillin, vinculin, focal adhesion kinase, kindlin,… (39–42). Moreover, integrins are sensitive to mechanical changes in their environment such as the stiffness of the substrate and act as mechano-sensing receptors for the cell(38).

In our lab we have vast experience on the study of integrins, such as LFA-1, using single molecule techniques(32, 43–45). More recently, Dr Sarah Keary in our group has performed an exquisite and thorough PhD dissertation unravelling the lateral spatial organisation of integrins and key adaptor proteins at focal adhesions of fibroblasts using STORM. STORM microscopy is an excellent technique to explore the lateral nanoscale organisation of proteins in focal adhesions because it relies on TIRF, which only excites a very thin section of the basal membrane of cells where focal adhesions are located.

Together with Dr Keary, we have developed a wide range of analysis tools in order to quantify the organisation of integrins and adaptor proteins in focal adhesions (46). Herein, we explain how we quantified the spatial organisation of nanoclusters with respect to an external structure, the focal adhesion. We focused on two proteins: the integrin $\alpha_5\beta_1$ and an adaptor protein, paxillin. Both proteins were imaged using dual-colour STORM.

For the analysis, a binary mask of the focal adhesions was first manually-selected from the raw dual-colour STORM data. Then, using MATLAB, we defined the edges of the different focal adhesions using morphological operations on the binary mask (Figure 2.5a, blue boundaries). Second, the clusters of $\alpha_5\beta_1$ and paxillin were identified using DBSCAN with a radius of 20 nm and N_{min} of 3 localisations. Later, those identified clusters with less than 10 localisations were removed. The centre-of-mass (CoM) of the detected clusters were plotted on the top of the binary mask (Figure 2.5b). If one zooms into a focal adhesion, one can visualise note that $\alpha_5\beta_1$ appears more at the periphery of the focal adhesion while Paxillin seems more homogeneously distributed (Figure 2.5c). In order to validate quantitatively our observations, we measured the nearest neighbour distance (nnd) from the CoM to the nearest edge of the focal adhesion.

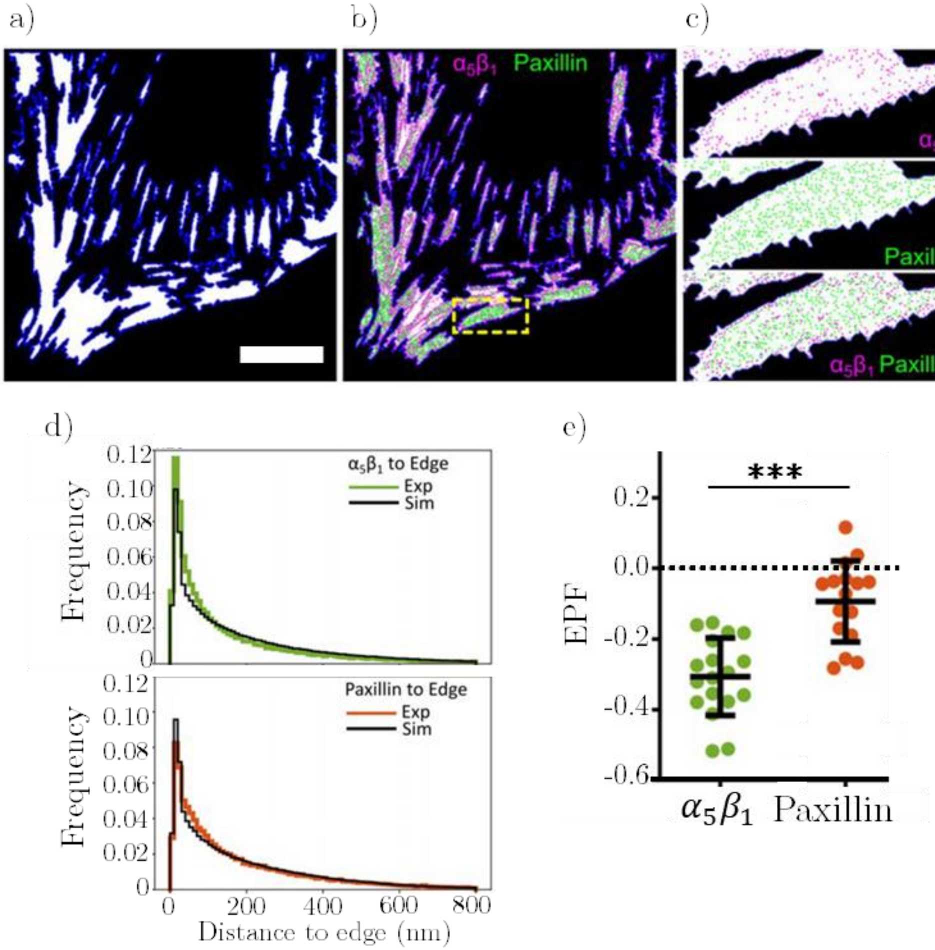

Figure 2.5 Quantifying the lateral spatial organisation of integrin $\alpha_5\beta_1$ and paxillin in focal adhesions imaged in STORM. a) Binary mask of the manually-selected focal adhesions with the edges detected by MATLAB. b) Centre of mass position of the detected clusters of integrin $\alpha_5\beta_1$ and paxillin overlaid on the mask of figure (a). c) Zoom-in of the yellow box in image (b). On the top, the CoM positions of integrin $\alpha_5\beta_1$, in the middle for paxillin and the bottom both together. d) Histograms of the distance to the focal adhesion edge, for the clusters of integrin $\alpha_5\beta_1$ (top) and paxillin (bottom). In black solid line, the histograms for simulated randomly distributed clusters. e) Edge proximity factor (EPF) per cell inside focal adhesions for integrin $\alpha_5\beta_1$ and paxillin. Statistical significance test with one-way ANOVA test ($p<0.001$). The scalebar is 10 µm. Figure adapted from Dr Sarah Keary's thesis (46)

In order to assess whether the distance-to-edge distributions found for experimental data are relevant and differ from randomly distributed clusters, we developed an *in-silico* simulated routine consisting of the following steps:

1) *Identify the clusters within each focal adhesion.* The first step consists on segmenting the clusters that fall inside focal adhesions and pairing each cluster to their focal adhesion. After this step, we have a list of clusters (for both proteins) for each focal adhesion.
2) *Randomly distributing the same number of clusters accounting for their physical size.* The second step consists on randomly placing the same number of clusters as the experimentally detected ones inside the focal adhesion. However, since the detected clusters are well-segregated, we need to include a non-overlapping condition for the randomly distributed clusters, thus, accounting for their size. We approximate clusters to be circles, of a given radius ($r = \sqrt{\frac{Area}{pi}}$) and we compute the edge-to-edge distance between the clusters finding the k nearest-neighbours and subtracting their radii:

$$\boldsymbol{d^{i,k}}_{edge-to-edge} = \boldsymbol{nnd}_k - \boldsymbol{r}_i - \boldsymbol{r}_{i,k}, \tag{2.4}$$

Where $\boldsymbol{nnd}_k$ is the nearest-neighbour distance of the k-nearest-neighbours, r_i is the radius of the cluster of interest and $\boldsymbol{r}_{i,k}$ are the radiuses of those nearest neighbour clusters. The bold typing is because we define this equation as vectors of multiple neighbours. If the distance is smaller than 0, then it means that the clusters overlap. Therefore, we reject those nearest-neighbours with negative edge-to-edge distance and they will be randomly thrown again until no overlapping occurs. The process of randomly distributing the clusters is performed in a two-step fashion accounting for the size. First, the larger clusters (the 20% of clusters with largest areas) are randomly placed ensuring that no overlapping occurs. Second, the smaller clusters (remaining 80% of clusters) are thrown keeping the larger clusters fixed and always checking the no-overlap condition. The reason for splitting the distribution of clusters between large and small cluster is because of the high-density of detected clusters and the small sizes of focal adhesions. If we place all the clusters simultaneously, we find that the number of large clusters rejected at each iteration is large and after each iteration there is less space where large clusters can fit. Importantly, the no-overlapping condition is only performed for the clusters of the same protein.

3) *Placement of the last 10 clusters.* At each iteration of the routine, a certain number of clusters are rejected, Nrej, which are the ones that will be randomly placed at the following iteration. However, we found that when the Nrej is equal or less than 10 clusters, it becomes more efficient to place the remaining clusters one by one. To do so, we randomly place 1000 clusters within the focal adhesion, all with the same cluster radius. We find which of those 1000 clusters satisfy the no-overlapping condition (distance > 0) with the already placed clusters and we pick one of those. We repeat this cycle until no rejected clusters remain.
4) *Repeat the process 10 times.* To ensure a close-to-theoretical random distribution of clusters to the edge of the focal adhesion, we iterate the whole process 10 times and compute the distance to the edge of the adhesion for each iteration.

Finally, we plotted the distance to the focal adhesion edge for all the experimental and simulated clusters for the integrin $\alpha_5\beta_1$ and paxillin (Figure 2.5d). Despite the similarities between the experimental and simulated distributions, we can observe subtle (statistically significant) differences for the integrin distribution compared to the simulated distribution. Analytically, it makes sense that the randomly distributed clusters appear to be close to the edge. If we think of a focal adhesion as an ellipse, we can draw concentric rings of the same width, Δr, from the edge to the centre. The area of outer rings is larger than the rings closer to the centre. Therefore, the number of clusters that can allocate outer rings is larger at the edge than the centre of the focal adhesion. Nevertheless, the subtle differences in the distributions between experimental and simulated can be significant. In order to measure the deviation from random and to compare how the proteins are spatially distributed with respect to each other, we calculated what we termed as the edge proximity factor (EPF). The EPF is calculated by subtracting the median values of experimental and simulated distance to edge distributions and normalised by the median value of the simulated data:

$$EPF = \frac{\widetilde{d_{edge}^{exp}} - \widetilde{d_{edge}^{sim}}}{\widetilde{d_{edge}^{sim}}} \tag{2.5}$$

The results for the integrin $\alpha_5\beta_1$ and paxillin are shown in Figure 2.5e. Negative values of the EPF means that the median experimental distance to the edge is closer to the edge than the expected from the randomly distributed clusters. From this, we clearly see that integrin $\alpha_5\beta_1$ is significantly closer to the edge than paxillin, revealing a preferential location of this integrin towards the edge of the adhesions(46).

2.3.3 1st rank Voronoi tessellation of localisations

Voronoi tessellation is becoming a popular method in SR-SMLM data analysis due to its unique properties(22, 23, 47). The Voronoi tessellation consists on partitioning the space using seeds (localisations) and generating a Voronoi cell for each seed. The Voronoi cells have the unique property that any point within the cell is closer to the corresponding seed than to any other seed. Because of this, if the seeds are densely packed, the corresponding Voronoi area of the cell is smaller than if the seeds are more sparsely located. This can be extrapolated to the nearest neighbours and if all the seeds are densely packed in a region of space, all those areas will be small. Accordingly, in less crowded regions, the areas will be larger. Levet et al. have implemented the Voronoi tessellation in the analysis of SR-SMLM to study clusters by separating the localisations into low and high density fractions and then either running DBSCAN on the high-density localisations or perform colocalisation analysis between two channels (23, 47). In fact, using the 1st rank Voronoi density to remove low-density localisations prior to running the DBSCAN algorithm is more efficient because low-density localisation (i.e. noise) are removed. This is especially interesting for datasets with a large number of localisations.

The 1st rank Voronoi tessellation consists on assigning a density value to each individual localisation considering the vicinity of nearest-neighbour localisations. Given a set of N localisations, (herein called seeds), $s_{k,k\in[1,N]}$, we perform a Voronoi tessellation of the space such that each seed, s_i, belongs within a polygon, P_i, of area A_i. The 1st rank neighbours of seed s_i are those seeds whose polygons share an edge with seed s_i. The concept behind computing the rank 1 Voronoi density is to calculate the density accounting also for the areas of the 1st rank neighbours (Figure 2.6a, see also Chapter 5 for a more detailed explanation).

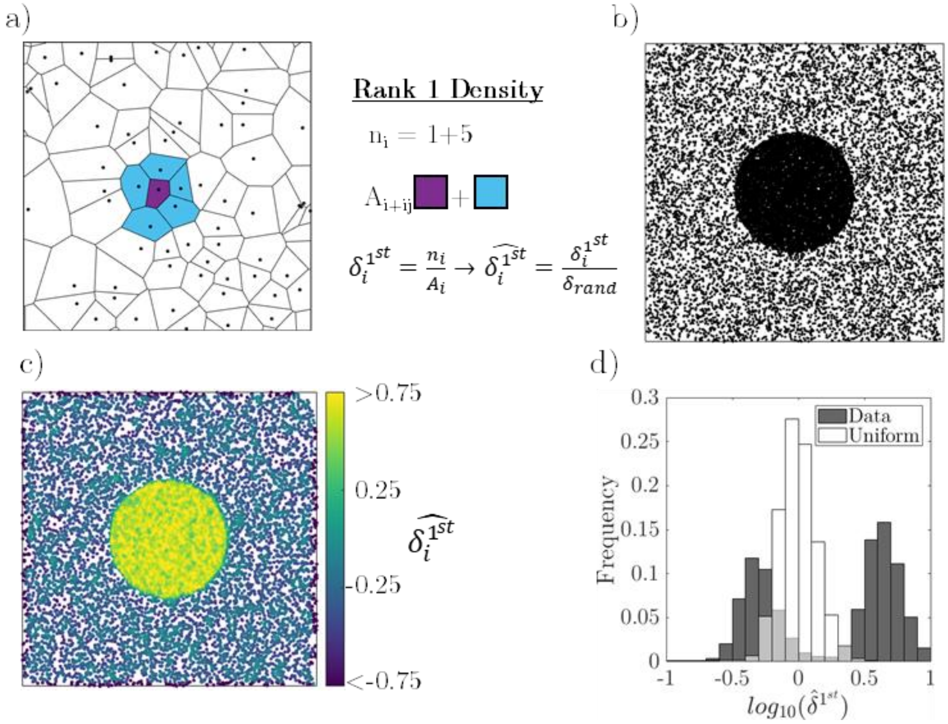

Figure 2.6 1st Rank Voronoi tessellation of localisations. a) Schematic example on how the Rank 1 Voronoi density is computed for the localisation within the purple area. The cyan areas correspond to the first neighbours to the localisation of interest. b) *In-silico* generated localisations clustered as a circle and noise localisations around. c) The same localisations as in (b) but colour-coding them with their 1st rank Voronoi density values. d) The distribution of 1st rank Voronoi densities (in logarithmic scales) for the *in-silico* cluster and the same number of localisations uniformly distributed in space.

To demonstrate the potential of using the 1st rank Voronoi density and to validate the performance of our algorithm, we reproduced the *in-silico* datasets presented by Levet et al. (47). We have *in-silico* simulated a circular cluster (radius = 3 pixels) and random localisations on a 10-by-10 pixels grid (Figure 2.6b). Then, we computed the 1st rank Voronoi density for these localisations and plotted them in a scatter plot colour-coding the localisations according to their normalised 1st rank Voronoi density, $\hat{\delta}_i^{1^{st}}$. Those localisations within the circle have higher densities than the ones randomly distributed outside the cluster (Figure 2.6c). In fact, if we plot the distribution of normalised 1st rank Voronoi densities for the data in Figure 2.6b and for the exact same number of localisations uniformly random distributed, we observe a clear difference (Figure 2.6c). While the uniformly distributed data has a monomodal distribution, the data of the circular cluster has a bimodal distribution. The first population (left peak) belongs to randomly distributed points and the second population (right peak) to the clustered localisations.

Therefore, we can use this methodology to segment the SR-SMLM localisations into high-density and low-density fractions. In principle, low-density localisations will arise from spontaneous emission and noise during acquisition, while the high-density localisations arise from clusters and structures. In order to segment the data, we use the 1st rank Voronoi density distribution of uniformly distributed and take the 99% value of the cumulative density function (CDF).

2.3.4 **Inter-cluster distance**

Once the clusters are defined using DBSCAN, one can proceed to obtain relevant information as the inter-cluster distance between clusters of different proteins in multi-colour SR-SMLM, such as dual-colour STORM. The inter-cluster distance is a valuable parameter because it allows to measure the distance between different protein species and also to quantify the fraction of colocalising clusters.

We have used dual-colour STORM to study the spatial organisation of the phosphatase of regenerating liver-3 (PRL-3) with respect to clathrin-coated pits (CCPs). PRL-3 is involved in promoting tumour progression and metastasis with poor prognosis(48–50). PRL-3 interacts directly with integrins β1 and focal adhesion kinases regulating the contact between focal adhesions and the extracellular matrix and, ultimately, inducing cell migration(51, 52). Moreover, the recycling of integrins (internalisation) is a clathrin-mediated endocytosis (CME) process. For CME to occur, first clathrin coated pits need to be formed by recruiting adaptor proteins which enable clathrin polymerisation and eventual CCP formation, a process that is called nucleation. Within a broader study on the plausible role or PRL-3 in CME, we evaluated the recruitment of PRL-3 to CCPs using dual-colour STORM. We studied over-expressed wild-type (WT) PRL-3 and a hyperactive PRL-3 mutant (E50R), which slows down CCP maturation.

First, the STORM raw data was processed using Insight3 software to retrieve the localisations and to correct for drift and channel cross-talk(53). The resulting STORM images for WT and Mutant PRL-3 together with Clathrin are shown in Figure 2.7(a, b). We then segmented the area to be analysed into 4-by-4 µm^2 regions of interest (ROIs). Next, we filtered out isolated random localisations using the 1st rank Voronoi tessellation and removed the low-density fraction of localisations. Subsequently, the DBSCAN algorithm was used to identify clusters using the following parameters:

Table 2.1 DBSCAN parameters used to identify the clusters of localisations for PRL-3 and Clathrin after a thorough screening of possible radiuses and minimum number of points.

	Clathrin	PRL-3
Radius (nm)	52.8	64.3
Nmin	20	10

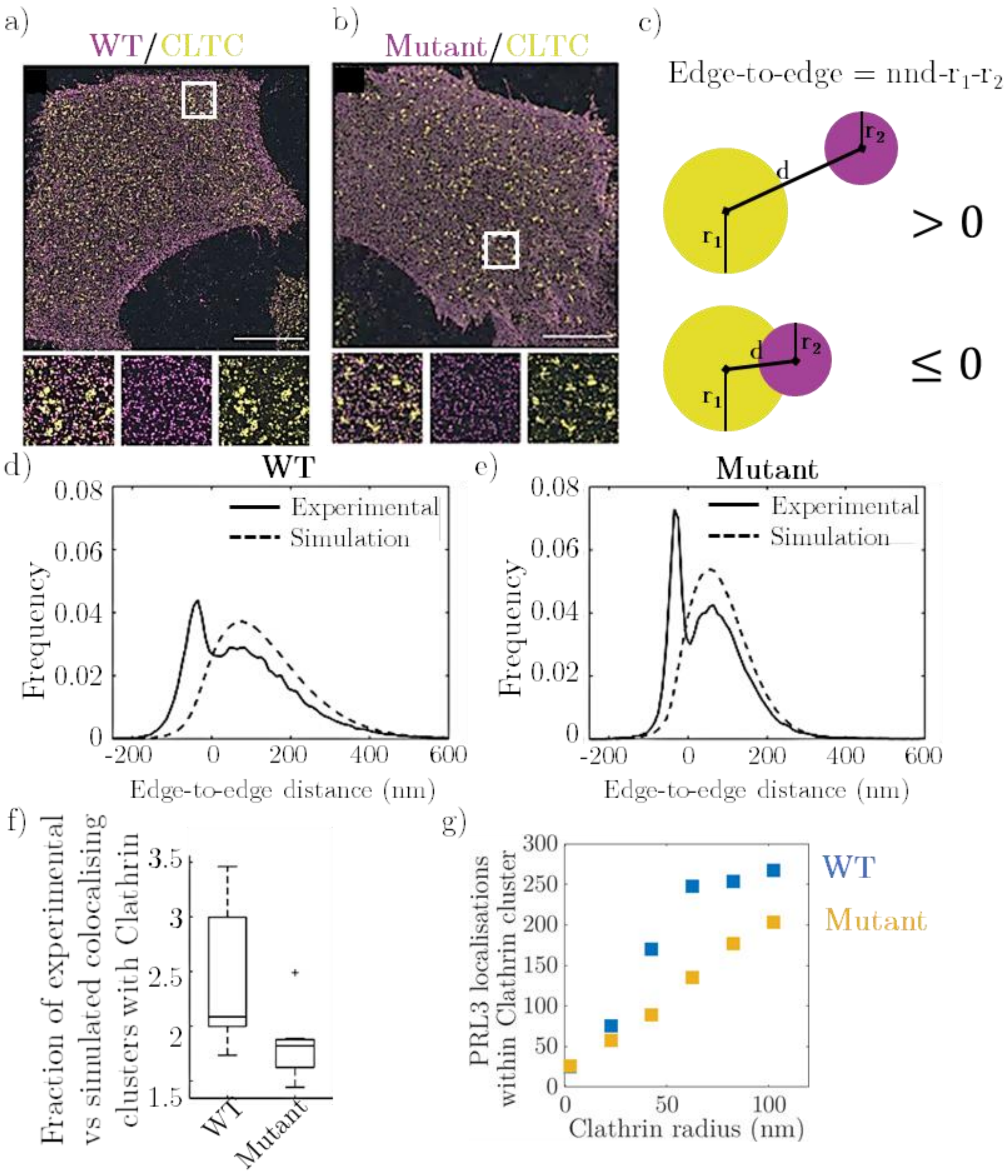

Figure 2.7 Recruitment of PRL-3 to Clathrin coated pits. Reconstructed two-colour STORM images of the plasma membrane of HeLa cells over-expressing 3xFlag-PRL-3 (WT) (a) and 3xFlag-PRL-3 E50R (Mutant) (b). The PRL-3 constructs are in purple and clathrin coated pits, labelled via the light chain (CLTC) in yellow. For both images, we show enlarged ROIs below the main image which show the merged (left), PRL-3 (middle) and clathrin (right). The scalebar is 10 µm. c) Schematic representation on how the edge-to-edge distance between a clathrin nanocluster (yellow) and the nearest PRL-3 construct nanocluster (purple) is computed. *d* is the distance between the centre-of-mass positions of the clusters and r_1 and r_2 are the radii of the

clathrin and PRL-3 constructs respectively. The top illustration depicts non-overlapping clusters (edge-to-edge distance > 0) and the bottom illustration depicts overlapping clusters (edge-to-edge distance ≤ 0). d) Edge-to-edge distance histogram for the experimental WT (solid line) and randomly distributed clusters (simulated, dashed line). e) Edge-to-edge distance histogram for the experimental Mutant (solid line) and randomly distributed clusters (simulated, dashed line). f) Boxplot plot of the ratio between experimental and simulated fractions of nanoclusters colocalising (edge-to-edge distance < 15 nm) with clathrin clusters. g) Number of localisations of PRL-3 within clathrin clusters as a function of the clathrin cluster radius. Unpublished data.

Having identified the clusters, we then proceeded to compute the edge-to-edge distance between PRL-3 clusters and clathrin. We computed the centre-of-mass position for each cluster and calculated the cluster area. By approximating the clusters to circles, we obtained an effective radius, r_i for each cluster. To determine the edge-to-edge distance, we measured the nearest-neighbour distance (nnd) between the centre-of-mass positions of neighbouring clusters and subtracted the radii of both clusters from the nnd (Figure 2.7c). Considering the STORM localisation accuracy (~30 nm), we considered that those clusters with edge-to-edge distances smaller than 15 nm (half the localisation accuracy) were overlapping clusters. Interestingly, the edge-to-edge distance can give negative values if the clusters are partially overlapping. Additionally, we performed simulations to estimate the degree of overlap expected from uniformly distributed clusters. Such simulations consisted on taking the same number of PRL-clusters and their sizes, and reshuffling them in the 4-by-4 μm^2 ROIs. Importantly, the simulated random clusters cannot overlap between them, so once the clusters are placed in the ROI, the edge-to-edge distance is calculated between nearest-neighbours. In the case of overlapping (distance < 15 nm), then those clusters are removed and thrown randomly again. Since clathrin is the reference protein to compare the spatial organisation with, the clathrin clusters remained unaltered. Finally, we computed the edge-to-edge distance between the randomly distributed PRL-3 clusters with respect to clathrin clusters. Compared to the edge-to-edge distance of randomly placed clusters, the experimental data clearly show a higher degree of overlapping, indicating a preferential organisation of PRL-3 clusters towards being close to clathrin coated pits (Figure 2.7d,e). To ascertain any difference between the WT and the mutant, we computed the ratio between the percentage of overlapping clusters in experimental and simulated data (Figure 2.7f) and the number of PRL-3 localisations within clathrin clusters as a function of the clathrin cluster radius (Figure 2.7g). This methodology thus allowed us to quantitively show an increased colocalisation between PRL-3 and clathrin coated pits as compared to the mutant. Since the mutant slows down CCP maturation, the growth of CCP and recruitment of PRL-3 to them is hampered, which is consistent with less colocalisation between the mutant and clathrin compared to the WT PRL-3 which is properly recruited to CCPs

2.3.5 1st rank Voronoi tessellation--based colocalisation analysis

Despite the potential applications of using DBSCAN to detect clusters and perform colocalisation analysis as we have presented above, DBSCAN can be challenging to implement. For instance, in datasets that contain clusters of localisations of very different sizes, when clusters are too close together, the expression levels of the proteins are high, then, it becomes difficult to use DBSCAN to identify clusters. In the light of these challenges, different types of localisation-based colocalisation analysis have emerged(20–23, 54). All of these methods provide new approaches to quantify the degree of colocalisation between the different channels in dual-colour SMLM images. During the span of this research, we have implemented these alternative algorithms in MATLAB for our analysis. The Clus-DoC (Cluster Degree of Colocalisation) algorithm (21)combines DBSCAN with the degree of colocalization (DoC) algorithm by Malkusch et al (20). The ClusterVisu algorithm uses Voronoi cell areas obtained from the Voronoi tessellation to remove noisy localisations(22). However, as we have shown above, using the 1st rank Voronoi density is more reliable to account for local densities, so we switch to the algorithms proposed by Levet et al. (23, 47). Finally, we implemented in MATLAB the Coloc-Tesseller colocalisation algorithm presented by Levet *et al* for our analysis(23, 47). The advantage of this algorithm is that it is quasi-automated (only the threshold in the CDF has to be fixed, see also previous section on Voronoi tessellation). Moreover, the algorithm gives a single value per each analysed ROI, which is convenient and easier.

The Coloc-Tesseller relies on pairing localisations of each channel and generating pair-density histograms. The pairing is performed using the unique properties of Voronoi cells: if we have a set of Voronoi cells generated from a set of localisations (from channel A), the space is segmented such that any point within a cell is closer to the seed that generated the Voronoi cell than to any other point. Therefore, we can pair the localisations of channel B with the localisations of channel A by placing them on their respective Voronoi density cells. This pairing is done taking channel A as reference first, and then channel B (see Ref. (23) for further details). Moreover, we assign to each localisation their 1st rank Voronoi density (per channel), so once we pair the localisations of each channel we can correlate their 1st rank Voronoi densities. In other words, we can determine if a localisation of channel B that is in a cluster (high density) is paired with a high-density localisation of channel A (thus, colocalising in high-density regions). Or, it can happen that a high-density localisation in A is paired to a low-density localisation in B, which leads to anti-correlation. Finally, from these correlated density values one can compute the Manders Coefficient (M) and the Spearman Rank (S) correlation to quantify the correlations. The Spearman Rank measures the monotonicity between two ranked variables and quantifies the strength of the interaction between these variables(55, 56). These quantifications are performed always from one protein with respect to the other, so that two values are in fact obtained per coefficient.

To demonstrate the sensitivity of this approach, we have simulated clusters of localisations in two channels and the quantifications (Figure 2.8). We show three conditions in which the clusters are separated at different distances d, from the centre of mass (with d = 0, 50 and 125 nm). When the clusters fully overlap, both correlation coefficients are close to 1, denoting high correlation (Figure 2.8a). When the clusters partially overlap, both Manders and Spearman Rank rapidly decrease their value (Figure 2.8b). In the case of not overlapping clusters, the Manders is 0 while the Spearman Rank becomes negative, which denotes anticorrelation (Figure 2.8c). The advantage of using this approach is that the quantification is performed in an automated manner without any required input from the user. For further details in the algorithm, refer to Levet *et al.* (23).

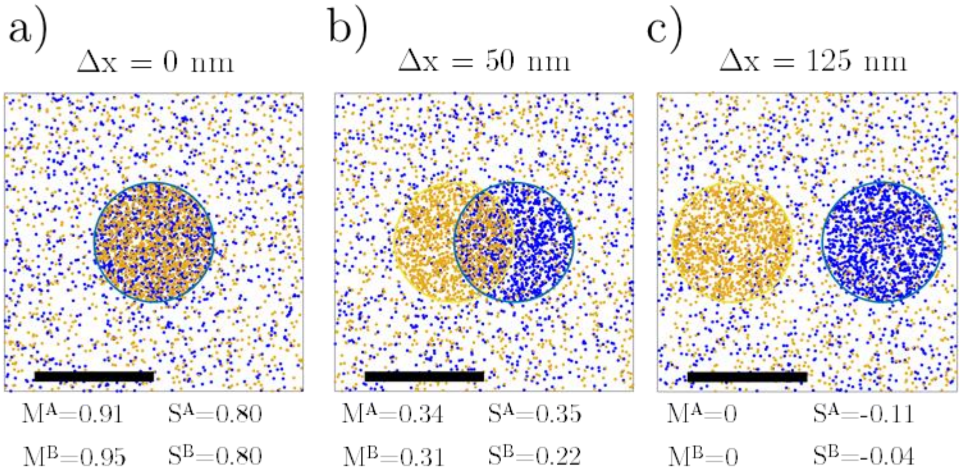

Figure 2.8 Voronoi-based colocalisation analysis of two-colour simulated data. Channel A (yellow) and channel B (blue) simulate two circular clusters, both with added noise. The centres of the clusters are fully overlapping (a), partially-overlapping separated by 50 nm (b) and separated a distance of 125 nm (c). The Manders (M) and Spearman Rank (S) correlation coefficients are shown below the simulated data. The scalebar is 125 nm.

We have implemented this algorithm to further study the colocalisation of PRL-3 with clathrin coated pits (Figure 2.9). Consistent with our previous results shown in Figure 2.7, we find that WT PRL-3 colocalises to a higher extent with clathrin than the mutant PRL-3 (Figure 2.9a,b). Moreover, clathrin coated pits seem to also have a preferential colocalisation with WT PRL-3 as compared to the mutant (Figure 2.9c,d).

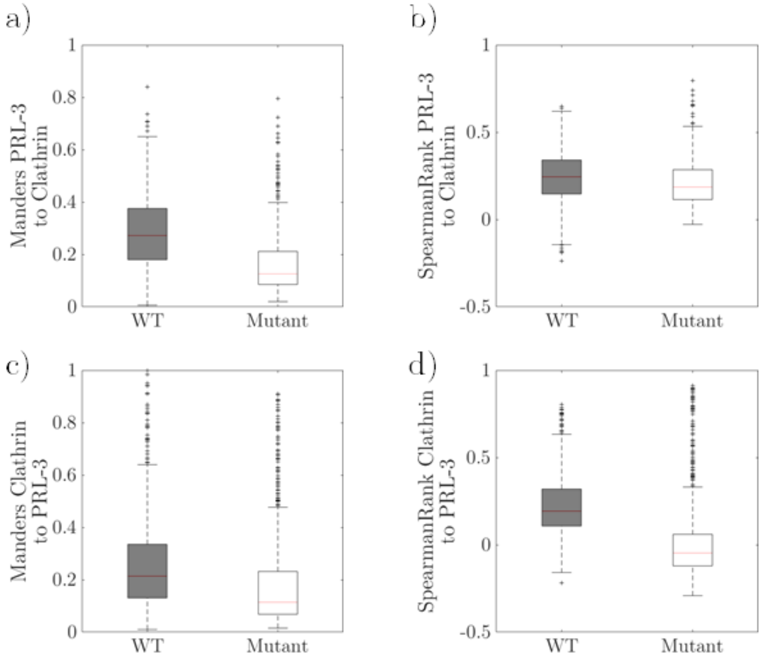

Figure 2.9 Colocalisation analysis of PRL-3 constructs with Clathrin coated pits. a) Manders coefficient of PRL-3 with respect to Clathrin. b) Manders coefficient of Clathrin with respect to PRL-3. c) Spearman rank coefficient of PRL-3 with respect to Clathrin. b) Spearman rank coefficient of Clathrin with respect to PRL-3. The median of the distribution is depicted with the red line and outliers with black crosses. The distributions are significantly different ($p<10^{-3}$) running a Kruskal Wallis analysis.

2.4 Discussion

During this research thesis, we have developed and implemented state-of-the-art algorithms to analyse super-resolution microscopy data. We have implemented an automated analysis to quantify the number of molecules per cluster in STED images and developed a GUI (graphical-user interface) in MATLAB to allow an easy interaction of the fellow researchers with the analysis. Nevertheless, STORM analysis has evolved to be a heavy part of the implemented algorithms to analyse datasets of fellow group members. Most of the research that we have performed lately in the lab has involved studying proteins at the plasma membrane of cells and we required of novel, state-of-the-art, analyses to quantify our observations. Together, we have worked on finding new ways to crunch the data and find solutions to our questions. Although extremely challenging at times, herein we have presented a palette of algorithms and tools that have enabled us to push the knowledge of the field. We have gained further understanding on multiple fields, for instance in the organisation of focal adhesions or the interactions of phosphatases with clathrin coated pits. In addition to these two studies, we have also applied these algorithms in other studies which are not included in this thesis such as the role of Galectin-1 in cancer fibroblasts (unpublished results) and the study of RNA polymerase II (Pol II) transcriptional condensates within the nucleus of living cells (unpublished results).

Regarding our STORM data, we can classify the analyses performed into cluster-based analysis and non-cluster colocalisation analysis. The advantage of working with algorithms such as DBSCAN that enable to identify clusters of localisations is that it provides a more tangible visualisation of the data. Also, the quantifications deliver a more physical understanding such as the nearest-neighbour distribution, distances to the edge of structures (such as focal adhesions), cluster area, etc. Regarding the colocalisation analysis presented in this chapter, we have used two distinct approaches for the same dataset. First, we have presented an analysis based on clusters defined with DBSCAN. Considering the well-defined clusters of PRL-3 and clathrin, this approach is preferred because it enables studying overlap of clusters and provide a more physical measure of colocalisation. Nevertheless, as we have mentioned, defining the parameters for DBSCAN is non-trivial and one needs to be very careful when choosing the radius and the minimum number of points. Second, we have shown an alternative approach that is quasi-automated to quantify the colocalisation based on Voronoi tessellation. The advantage of using this approach is the fact that one can quantify colocalisation without having to define parameters for DBSCAN. In the case of datasets with a heterogeneous distribution of cluster sizes and densely packed clusters which are difficult to segment properly, this approach is better suited. In fact, we have used Voronoi based colocalisation analysis to study transcriptional condensates in the nucleus because the sizes of the condensates vary between cells and within the nucleus (unpublished data). Moreover, the expression levels of the PolII vary from cell to cell. In this case, using DBSCAN is less than ideal because one would have to change the parameters from cell to cell to define the clusters.

In summary, depending on the nature of the data to be analysed one can use different tools to study colocalisation. If the dataset consists on well-defined clusters of localisations and separated enough, using DBSCAN is the perfect choice because one can perform multiple quantifications based on the clusters, as we have shown here. On the other hand, if the dataset consists on clusters with various sizes, very close between them and/or with high expression levels, then using the Voronoi based colocalisation is the most advantageous approach to quantify the colocalisation. Finally, if the dataset consists on well-defined clusters but with some background (i.e., sparse localisations arising from unspecific blinking during acquisition), then it could be interesting to combine both approaches. In this case, one could first use the Voronoi tessellation to segment the localisations between high and low regions and then run the DBSCAN algorithm on the high-density regions.

Despite the challenges of STORM imaging and data analysis, if done properly and carefully, the data analysis of STORM imaging is engaging and attractive due to its potential.

2.5 References

1. S. W. Hell, J. Wichmann, Breaking the diffraction resolution limit by stimulated emission: stimulated-emission-depletion fluorescence microscopy. *Opt. Lett.* (1994) https:/doi.org/10.1364/ol.19.000780.
2. T. A. Klar, S. Jakobs, M. Dyba, A. Egner, S. W. Hell, Fluorescence microscopy with diffraction resolution barrier broken by stimulated emission. *Proc. Natl. Acad. Sci. U. S. A.* (2000) https:/doi.org/10.1073/pnas.97.15.8206.
3. M. J. Rust, M. Bates, X. Zhuang, Sub-diffraction-limit imaging by stochastic optical reconstruction microscopy (STORM). *Nat. Methods* **3** (2006).
4. E. Betzig, *et al.*, Imaging intracellular fluorescent proteins at nanometer resolution. *Science (80-.).* (2006) https:/doi.org/10.1126/science.1127344.
5. S. T. Hess, T. P. K. Girirajan, M. D. Mason, Ultra-high resolution imaging by fluorescence photoactivation localization microscopy. *Biophys. J.* (2006) https:/doi.org/10.1529/biophysj.106.091116.
6. N. Durisic, L. L. Cuervo, M. Lakadamyali, Quantitative super-resolution microscopy: Pitfalls and strategies for image analysis. *Curr. Opin. Chem. Biol.* **20** (2014).
7. D. Baddeley, J. Bewersdorf, Biological Insight from Super-Resolution Microscopy: What We Can Learn from Localization-Based Images. *Annu. Rev. Biochem.* **87** (2018).
8. J. Keller-Findeisen, S. J. Sahl, S. W. Hell, “Quantifying molecule numbers in STED/RESOLFT fluorescence nanoscopy” in *Topics in Applied Physics*, (2020).
9. L. Martínez-Muñoz, *et al.*, Separating Actin-Dependent Chemokine Receptor Nanoclustering from Dimerization Indicates a Role for Clustering in CXCR4 Signaling and Function. *Mol. Cell* **70** (2018).
10. J. A. Torreno-Pina, *et al.*, The actin cytoskeleton modulates the activation of iNKT cells by segregating CD1d nanoclusters on antigen-presenting cells. *Proc. Natl. Acad. Sci. U. S. A.* **113** (2016).
11. C. Manzo, *et al.*, The neck region of the C-type lectin DC-SIGN regulates its surface spatiotemporal organization and virus-binding capacity on antigen-presenting cells. *J. Biol. Chem.* **287** (2012).
12. S. H. Lee, J. Y. Shin, A. Lee, C. Bustamante, Counting single photoactivatable fluorescent molecules by photoactivated localization microscopy (PALM). *Proc. Natl. Acad. Sci. U. S. A.* **109** (2012).
13. P. Annibale, S. Vanni, M. Scarselli, U. Rothlisberger, A. Radenovic, Quantitative Photo Activated Localization Microscopy: Unraveling the effects of photoblinking. *PLoS One* **6** (2011).
14. P. Annibale, S. Vanni, M. Scarselli, U. Rothlisberger, A. Radenovic, Identification of clustering artifacts in photoactivated localization microscopy. *Nat. Methods* **8** (2011).

15. P. Sengupta, *et al.*, Probing protein heterogeneity in the plasma membrane using PALM and pair correlation analysis. *Nat. Methods* **8** (2011).
16. P. Sengupta, T. Jovanovic-Talisman, J. Lippincott-Schwartz, Quantifying spatial organization in point-localization superresolution images using pair correlation analysis. *Nat. Protoc.* **8** (2013).
17. S. L. Veatch, *et al.*, Correlation functions quantify super-resolution images and estimate apparent clustering due to over-counting. *PLoS One* **7** (2012).
18. S. Bolte, F. P. Cordelières, A guided tour into subcellular colocalization analysis in light microscopy. *J. Microsc.* **224** (2006).
19. E. M. M. Manders, J. Stap, G. J. Brakenhoff, R. Van Driel, J. A. Aten, Dynamics of three-dimensional replication patterns during the S-phase, analysed by double labelling of DNA and confocal microscopy. *J. Cell Sci.* **103** (1992).
20. S. Malkusch, *et al.*, Coordinate-based colocalization analysis of single-molecule localization microscopy data. *Histochem. Cell Biol.* **137** (2012).
21. S. V. Pageon, P. R. Nicovich, M. Mollazade, T. Tabarin, K. Gaus, Clus-DoC: A combined cluster detection and colocalization analysis for single-molecule localization microscopy data. *Mol. Biol. Cell* **27** (2016).
22. L. Andronov, I. Orlov, Y. Lutz, J. L. Vonesch, B. P. Klaholz, ClusterViSu, a method for clustering of protein complexes by Voronoi tessellation in super-resolution microscopy. *Sci. Rep.* **6** (2016).
23. F. Levet, *et al.*, A tessellation-based colocalization analysis approach for single-molecule localization microscopy. *Nat. Commun.* (2019) https:/doi.org/10.1038/s41467-019-10007-4.
24. J. Banchereau, R. M. Steinman, Dendritic cells and the control of immunity. *Nature* **392** (1998).
25. T. B. H Geijtenbeek, *et al.*, The Netherlands in the lymphoid tissues (Grouard and Clark, 1997; Row-§ Skirball Institute of BioMolecular Medicine land-Jones. *Cell* **100**, 587–597 (2000).
26. N. Izquierdo-Useros, *et al.*, Siglec-1 Is a Novel Dendritic Cell Receptor That Mediates HIV-1 Trans-Infection Through Recognition of Viral Membrane Gangliosides. *PLoS Biol.* **10** (2012).
27. W. B. Puryear, *et al.*, Interferon-Inducible Mechanism of Dendritic Cell-Mediated HIV-1 Dissemination Is Dependent on Siglec-1/CD169. *PLoS Pathog.* **9** (2013).
28. E. Gutiérrez-Martínez, *et al.*, Actin-regulated Siglec-1 nanoclustering influences HIV-1 capture and virus-containing compartment formation in dendritic cells. *bioRxiv*, 2022.04.28.489919 (2022).
29. F. Cella Zanacchi, *et al.*, ADNAorigami platform for quantifying protein copy number in super-resolution. *Nat. Methods* **14** (2017).
30. M. Moertelmaier, M. Brameshuber, M. Linimeier, G. J. Schütz, H. Stockinger, Thinning out clusters while conserving stoichiometry of labeling. *Appl. Phys.*

Lett. **87** (2005).

31. T. Schmidt, Local stoichiometries determined by counting individual molecules. *Anal. Chem.* **68** (1996).
32. T. S. Van Zanten, *et al.*, Hotspots of GPI-anchored proteins and integrin nanoclusters function as nucleation sites for cell adhesion. *Proc. Natl. Acad. Sci. U. S. A.* **106** (2009).
33. M. F. Garcia-Parajo, A. Cambi, J. A. Torreno-Pina, N. Thompson, K. Jacobson, Nanoclustering as a dominant feature of plasma membrane organization. *J. Cell Sci.* **127** (2014).
34. M. Ester, H.-P. Kriegel, J. Sander, X. Xu, A Density-Based Algorithm for Discovering Clusters in Large Spatial Databases with Noise in *Proceedings of the 2nd International Conference on Knowledge Discovery and Data Mining*, (1996).
35. H. Deschout, *et al.*, Precisely and accurately localizing single emitters in fluorescence microscopy. *Nat. Methods* **11**, 253–66 (2014).
36. S. V. Pageon, *et al.*, Functional role of T-cell receptor nanoclusters in signal initiation and antigen discrimination. *Proc. Natl. Acad. Sci. U. S. A.* **113** (2016).
37. J. W. Tamkun, *et al.*, Structure of integrin, a glycoprotein involved in the transmembrane linkage between fibronectin and actin. *Cell* **46** (1986).
38. J. Z. Kechagia, J. Ivaska, P. Roca-Cusachs, Integrins as biomechanical sensors of the microenvironment. *Nat. Rev. Mol. Cell Biol.* **20** (2019).
39. M. C. Brown, J. A. Perrotta, C. E. Turner, Identification of LIM3 as the principal determinant of paxillin focal adhesion localization and characterization of a novel motif on paxillin directing vinculin and focal adhesion kinase binding. *J. Cell Biol.* **135** (1996).
40. M. Theodosiou, *et al.*, Kindlin-2 cooperates with talin to activate integrins and induces cell spreading by directly binding paxillin. *Elife* **5** (2016).
41. L. Zhu, *et al.*, Structural Basis of Paxillin Recruitment by Kindlin-2 in Regulating Cell Adhesion. *Structure* **27** (2019).
42. M. Soto-Ribeiro, *et al.*, β1D integrin splice variant stabilizes integrin dynamics and reduces integrin signaling by limiting paxillin recruitment. *J. Cell Sci.* **132** (2019).
43. A. Cambi, *et al.*, Organization of the integrin LFA-1 in nanoclusters regulates its activity. *Mol. Biol. Cell* **17** (2006).
44. I. K. Piechocka, *et al.*, Shear forces induce ICAM-1 nanoclustering on endothelial cells that impact on T-cell migration. *Biophys. J.* **120** (2021).
45. A. Sosa-Costa, *et al.*, Lateral mobility and nanoscale spatial arrangement of chemokine-activated α4β1 integrins on T cells. *J. Biol. Chem.* **291** (2016).
46. S. Keary, "Spatiotemporal organisation of protein nanoclusters in adhesion complexes," Universitat Politècnica de Catalunya. (2022) (January 11, 2023).
47. F. Levet, *et al.*, SR-Tesseler: A method to segment and quantify localization-

based super-resolution microscopy data. *Nat. Methods* (2015) https:/doi.org/10.1038/nmeth.3579.

48. K. Guzinska-Ustymowicz, A. Pryczynicz, PRL-3, An Emerging Marker of Carcinogenesis, Is Strongly Associated with Poor Prognosis. *Anticancer. Agents Med. Chem.* **11** (2012).
49. P. Rios, X. Li, M. Köhn, Molecular mechanisms of the PRL phosphatases. *FEBS J.* **280** (2013).
50. S. Hardy, *et al.*, Physiological and oncogenic roles of the PRL phosphatases. *FEBS J.* **285** (2018).
51. M. Foy, O. Anézo, S. Saule, N. Planque, PRL-3/PTP4A3 phosphatase regulates integrin β1 in adhesion structures during migration of human ocular melanoma cells. *Exp. Cell Res.* **353** (2017).
52. L. Peng, *et al.*, Identification of integrin α1 as an interacting protein of protein tyrosine phosphatase PRL-3. *Biochem. Biophys. Res. Commun.* **342** (2006).
53. B. Huang, W. Wang, M. Bates, X. Zhuang, Three-Dimensional Super-Resolution Reconstruction Microscopy. *Science (80-.).* **319** (2008).
54. J. Rossy, E. Cohen, K. Gaus, D. M. Owen, Method for co-cluster analysis in multichannel single-molecule localisation data. *Histochem. Cell Biol.* **141** (2014).
55. T. D. Gauthier, Detecting Trends Using Spearman's Rank Correlation Coefficient. *Environ. Forensics* **2**, 359–362 (2001).
56. J. H. Zar, Spearman Rank Correlation. *Encycl. Biostat.* (2005) https:/doi.org/10.1002/0470011815.B2A15150 (February 2, 2023).

Chapter 3

High-Density Single Particle Tracking to generate spatiotemporal exploration maps on the cell membrane

Molecules in living cells are dynamically compartmentalised in space and time, with the smallest scales going down to the molecular level. Importantly, this organisation regulates many of the cell functions. Since dysregulation in how molecules explore the space and interact with their environment leads to a large variety of diseases, understanding their spatiotemporal behaviour is key in cell biology. Unfortunately, due to technical limitations, spatial and temporal studies at the nanoscale are mostly conducted separately. High-density single particle tracking (HD-SPT) has recently emerged as a powerful technique to bridge between super-resolution approaches and standard SPT to investigate the spatiotemporal organisation of molecules with extreme sensitivity and selectivity. In this Chapter, we introduce a novel concept to exploit HD-SPT acquired data in order to generate high-density maps (HiDenMaps). We stablish the technical requirements to generate HiDenMaps that allow us to go beyond already existing methods. We show the versatility of the method and provide guidelines on how to reconstruct faithful HiDenMaps that deliver exquisite information on how molecules dynamically explore their environment from the nano- to the meso-scale in few seconds.

3.1 Introduction

The spatiotemporal organisation and compartmentalisation of molecules in living cells are highly important to regulate cell function(1–4). Dysregulation in the way that molecules dynamically explore the space and/or interact with other molecular partners can lead to disease and even death. Therefore, understanding the nature of these dynamic interactions is pivotal in cell biology studies. However, spatial and temporal studies are typically conducted separately due to technical limitations.

Super-resolution single molecule localisation microscopy (SR-SMLM) techniques such as PALM (5, 6), STORM (7) or PAINT(8, 9), enable the study of the nanoscale spatial organisation of molecules at high labelling densities. These SR-SMLM techniques rely effectively on reducing the number of emitting fluorophores so that the distance between emitting probes is larger than Abbe's diffraction limit(10). PALM and STORM rely on the stochastic "on/off" switching of fluorescent probes to artificially reduce the number of fluorescent molecules at a given time allowing their detection and localisation at the single molecule level. PAINT relies on the chemical binding kinetics of fluorophores: freely diffusing fluorophores are too fast to be detected but once the fluorophores attach reversibly to the target structure, they become immobile so that they can be detected and localised at the single molecule level. Overall, in SR-SMLM, at these artificially induced sparse fluorophore conditions, the centre of mass position can be determined with nanometre precision. This procedure of "on/off" switching or reversible binding is repeated thousands of times and over thousands of frames until the localisation positions of virtually all the molecules labelling the sample are mapped and used to reconstruct a full image of the structure under study with nanometric localisation accuracy. In this way, SR-SMLM methods allow for an effective increased spatial resolution and the study of the full ensemble of proteins. However, as SR-SMLM techniques still suffer from poor temporal resolution, imaging is commonly performed on fixed cells precluding dynamic studies at relevant temporal scales. Moreover, the applicability of SR-SMLM, in particular STORM, is limited due to the need of photo-switchable fluorescent probes and the use of blinking buffers (which are not compatible with live cell imaging and challenges multi-colour imaging). Moreover, quantitative analysis of STORM images is challenging and the results might be biased due to labelling density and sample preparation protocols.

To gain access to temporal information, several fluorescence-based optical techniques have been developed over the past years (11–17). FRAP(11), FCS(12) and STED-FCS(13) reveal temporal information on the average dynamics of molecules over small regions of the sample (typically the diffraction limited spot in the case of FRAP and standard FCS, and sub-diffraction regions in the case of STED-FCS). Although these techniques have high temporal resolution since they rely on the use of fast point detectors, they cannot be easily implemented to resolve the spatial heterogeneity present in most cellular processes. A well-known and simple to implement technique is single particle tracking (SPT) which provides similar localisation accuracy as SR-SMLM at an increased millisecond temporal resolution. SPT is based on imaging the motion of sparsely labelled fluorescent molecules over multiple frames. Each molecule is localised with nanometric precision and the localisations are reconnected between frames. Once the trajectory is retrieved, one can access the dynamic information of each individual molecule (diffusion, velocity, trapping, etc.) as a function of space and time (18). An advantage of SPT is the availability of small labelling probes and labelling strategies, including the use of autofluorescent proteins. However, the main limitation of standard SPT is the poor statistics obtained from single experiments. In order to localise individual molecules and track them accurately in time, only a small population of molecules can be labelled. Therefore, the number of experiments required to have enough statistics becomes large. Moreover, since each individual trajectory maps only a small region of its surrounding (limited by the fluorophore photobleaching), correlating molecular diffusion to its environment becomes highly challenging.

More recently, high-density SPT (HD-SPT) has emerged as a powerful approach which bridges technically between SR-SMLM and SPT to increase the statistics on the number of trajectories that can be obtained in a single experiment(19). The first methodology proposed to obtain more trajectories per experiment is sptPALM(20), which relies on the use photo-activatable fluorescent probes (21, 22). As in the case of PALM, one can reduce the effective labelling density by stochastically activating a small subset of fluorescent probes allowing for single particle tracking. Once those fluorescent probes have photobleached, a new subset is stochastically activated and imaged. This process is repeated many times until enough trajectories are retrieved. The main disadvantage of sptPALM is the need to use photo-activatable/convertible proteins which need to be transfected and expressed together with the protein of interest. Generally, this means that the proteins are overexpressed, leading to non-physiological conditions. Moreover, the photo-physics and poor photo-stability of autofluorescent proteins limit the length of the obtained trajectories. Recently, new photo-activatable/convertible dyes based on Janelia fluorophores that overcome the disadvantages of autofluorescent proteins in terms of over-expression and photo-stability but, unfortunately, their use is still far from routine(23–25). Another approach to generate HD-SPT datasets is universal points-accumulation-for-imaging-in-nanoscale-topography (uPAINT) (26). uPAINT is based on stochastic labelling of molecules at the plasma membrane by having a constant pool of fluorescent probes (tagged with the ligand) on the medium while imaging in TIRF (total internal reflection fluorescence) or HILO (highly inclined and laminated optical sheet) configurations. Fluorescent probes not bound to their biomolecule will diffuse too fast to be detected. And thus, only those fluorescent probes that are bound to the biomolecule at the plasma membrane are tracked. Since the concentration of fluorescent probes is low, the amount of labelled proteins at a given point is low enabling point reconnection and tracking. Fluorescent probes can be tracked until they either photobleach or dissociate from the studied biomolecule. The limitation of uPAINT is that only plasma membrane studies can be conducted. Overall, HD-SPT can be a valuable approach to get more trajectories from single experiments, increasing the statistics as compared to standard SPT. However, recording hundreds of trajectories on the same cell still requires long acquisition times in the order of minutes which will wash-out any fast dynamics of the environment.

Here, we propose an alternative approach that combines the advantages of SR-SMLM and standard SPT: live cell imaging, single molecule localisation accuracy, dynamic information at the nano- and meso- scale and simplicity. In this chapter we show how we can easily explore the whole plasma membrane of living cells using high density maps (HiDenMaps) generated for HD-SPT data and what parameters are required for a faithful representation of the images.

3.2 Materials and Methods

3.2.1 Supported Lipid Bilayers (SLB) preparation.

No.1 Coverslips (CS 25R/ 64-0705, Warner Instruments), were sonicated with Hellmanex III (0.5%) for 40 min followed by 5M KOH for 10 min. The glass was washed extensively in MilliQ after each treatment. The glass was then dried under N_2 and stored in a desiccator until further use. Just before making the bilayer, a coverslip was taken out of the desiccator, a cylindrical chamber (made from a cut PCR tube) was stuck on to the coverslip with transparent UV glue. The coverslip was then place in an Ozone/UV cleaner for 15 min after which it was washed with PBS. Small Unilamellar Vesicles with DOPC(98%) and NiNTA-DGS(2%) were prepared in advance according to the protocols mentioned in (32). 2uL of 4mM SUVs were added to the chambers and were incubated for 15 min. Unbound vesicles were washed off with buffer. The coverslip was incubated with 0.1mg/ml of beta-Casein for 10 min to block the exposed surfaces where vesicles did not form a bilayer which was subsequently washed off. HSE-RA(A SNAP tagged version of the construct HYE-R579A used in (32)) was used as a bilayer marker. HSE-RA has a Deca-His tag which allows it to bind to the Nickel containing lipids on the bilayer. It has a SNAP tag for visualisation, which was labelled with JF-549. HSE-RA was added to the bilayer at a final concentration of 100 picomolar and allowed to bind for 40 min before washing it off. PCA/PCD/Trolox described in (33) were added at 4mM, 125nM and 2mM respectively to reduce photobleaching and triplet state transitions.

3.2.2 CD44 labelling on immature dendritic cells

Peripheral blood mononuclear cells (PBMC) were harvested from the buffy coat interface after using Ficoll-Hypaque gradient (Alere Technologies AS) on HIV-1 seronegative donor leukocytary layer. The monocytes were then isolated by plastic adherence for 1h. Immature dendritic cells (iDCs) were obtained after culturing the monocytes in complete RPMI supplemented with 1,000 IU/ml granulocyte-macrophage colony-stimulating factor (GM-CSF) and interleukin-4 (IL-4) (both from R&D) for six days and replacing media and cytokines every two days. Experiments were conducted at day 6. For CD44 labelling, we generated single chain antibodies using the antibody G44-26 (BD-Biosciences), biotinylated them and conjugated with streptavidin QDot 605 (Thermofisher).

3.2.3 **STORM imaging**

Day 6 human immature dendritic cells (iDCs) were plated on an eight-well plate Lab-Teck #1 at a density of 50.000 cells/well. Cells were incubated at 37°C for 1h before fixation with 4% PFA in PBS for 15 min at room temperature. After fixation, samples were blocked using 3% wt/vol bovina serum albumin (BSA) in PBS during 30 min at room temperature. Cells were labelled with primary antibody rabbit-antihuman CD44 (HPA005785, Sigma-Aldrich) at a concentration of 5 µg/ml for 1 hour at room temperature. The corresponding secondary antibody, an anti-rabbit antibody, was tagged in-house with Alexa Fluor 647 (Invitrogen) as reporter and Alexa Fluor 405 as an activator. We incubated the secondary antibody for 1 hour at room temperature. The STORM buffer used was the same as in (28, 34): Glox solution (40 mg/ml Catalase [Sigma Aldrich], 0.5 mg/ml glucose oxidase, 10% glucose in PBS) and MEA 10 mM (Cysteamine MEA [Sigma-Aldrich; #30070-50G] in 360 mM Tris-HCl).

3.2.4 **Supported Lipid Bilayer Imaging.**

The SLBs were imaged on a Nikon Ti-E microscope body equipped with a motorised TIRF arm (from Nikon) with a 100x, 1.45NA objective. Agilent (MLC-300) laser combiner was used with a 561 nm laser line, giving 9 mW at the back focal plane. Images were acquired on Prime95B sCMOS camera at frame rate of 100 Hz for 2 min.

3.2.5 **Monte Carlo *in-silico* simulations of molecules diffusing with Brownian motion.**

We performed Monte Carlo simulations of Brownian diffusing molecules with diffusion coefficient D in 2D. We define a square imaging region consisting of L=256 pixels (100 nm per pixel). To avoid edge effects, we randomly place 1500 molecules in a 356-by-356 pixels grid, but our imaging region consists on the 256-by256 pixels in the centre of the simulation. The total observation time is set to 1000 seconds and the frame rate to 100 Hz. To account for the diffusion, at each temporal step molecules are displaced according to a normal distribution $\delta xy \sim N(0, \sqrt{2 \cdot dt \cdot D})$. While diffusing, molecules cannot interact with each other. In the case of results showing slower frame rates than 100 Hz, we have down-sampled the data from the 100 Hz. With this, we are capable of generating multiple sub frame rate simulations from a fast simulation. Moreover, we only perform one simulation at a high labelling density (ρ~1.18 molecules/µm^2) and then remove molecules to obtain lower labelling densities.

3.2.6 **Expected observation time to explore 90% of the ROI's area**

We run a simulation for each diffusion coefficient condition (D = [0.001, 0.01, 0.1, 1, 10] µm^2/s) at a high labelling density (ρ~1.18 molecules/µm^2) for a total observation time of 1000 seconds. However, for some conditions we estimated that we would need ~10^4-10^6 seconds to explore 90% of space. In order to derive these long observation times, we first computed the curve explored space vs observation time. Then, we fitted the curve using MATLAB's function "*linearinterp*" and extrapolated the curve until it would hit the 90% boundary.

3.2.7 **Cluster analysis for STORM and HiDenMap datasets**

We used the DBSCAN algorithm (35) to determine the clusters of localisations for STORM and HiDenMap datasets (see also Chapter xx for more details). For the STORM data, we used an epsilon of 50 nm and 50 as the minimum number of points. For the HiDenMap data, we used an epsilon of 100 nm and 12 as the minimum number of points. We used the *dbscan* function in MATLAB.

3.3 Results

3.3.1 **Generation of high-density single molecule maps (HiDenMaps).**

Our approach is similar to HD-SPT, i.e., the protein of interest is labelled at high density conditions, typically two orders of magnitude higher than for standard SPT. At each image frame, we localise single molecules with nanometre precision. However, in contrast to standard SPT where the centre-of-mass position of individual molecules are reconnected in time to build up trajectories, here we simply collapse all the recorded localisations into a single image, similar to SR-SMLM methods. The resulting high-density map (HiDenMap) thus contains all the localisation positions of individual molecules as they dynamically explore the space (Figure 3.1). While the localisation accuracy of the HiDenMaps are similar to those of SR-SMLM, the temporal resolution is given by the camera framerate, typically tens of milliseconds. For a sufficiently long observation time and high labelling conditions, a HiDenMap resembles that of a SR-SMLM image, with similar spatial resolution but acquired in living cells and in only a few hundreds of seconds. Importantly, the HiDenMap encodes both spatial and temporal information that report on the motion of molecules and their interactions with the environment.

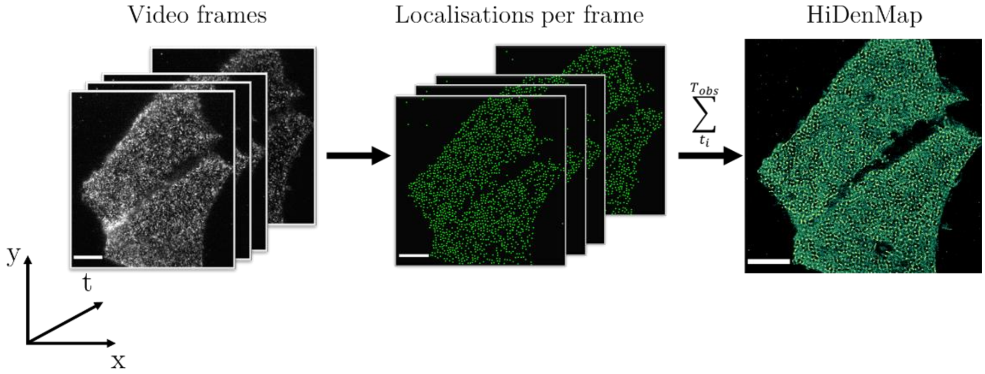

Figure 3.1 Schematic on how HiDenMaps are generated. Individual fluorescent molecules are localised at each frame of the video and collapsed into a single image, the HiDenMap. Scale bar is 10 µm.

Generating a HiDenMap is straightforward and experimentally simple. However, one needs to account for several technical requirements in order to generate a faithful representation of how the molecule of interest dynamically explores its surrounding.

3.3.2 Technical requirements for the generation of reliable HiDenMaps

We investigated how multiple parameters (labelling density, imaging frame rate, observation time and fluorophore diffusion coefficient) affect the generated HiDenMaps. To assess the influence of these parameters we performed *in-silico* simulations of particles diffusing in a Brownian fashion in 2D with a mean diffusion coefficient of 0.1 µm²/s. Our hypothesis is that the resulting HiDenMaps of Brownian diffusion should reveal a homogeneous image since molecules can explore the whole space without constraints. Nevertheless, if the technical settings are not chosen properly, it might be that we do not observe such homogeneous HiDenMap. To qualitatively illustrate the effect of labelling density (ρ), frame rate and observation time, we have represented four HiDenMaps, colour-coding the localisations by occurrence time (purple localisations appeared at initial times and yellow, at later times) (Figure 3.2).

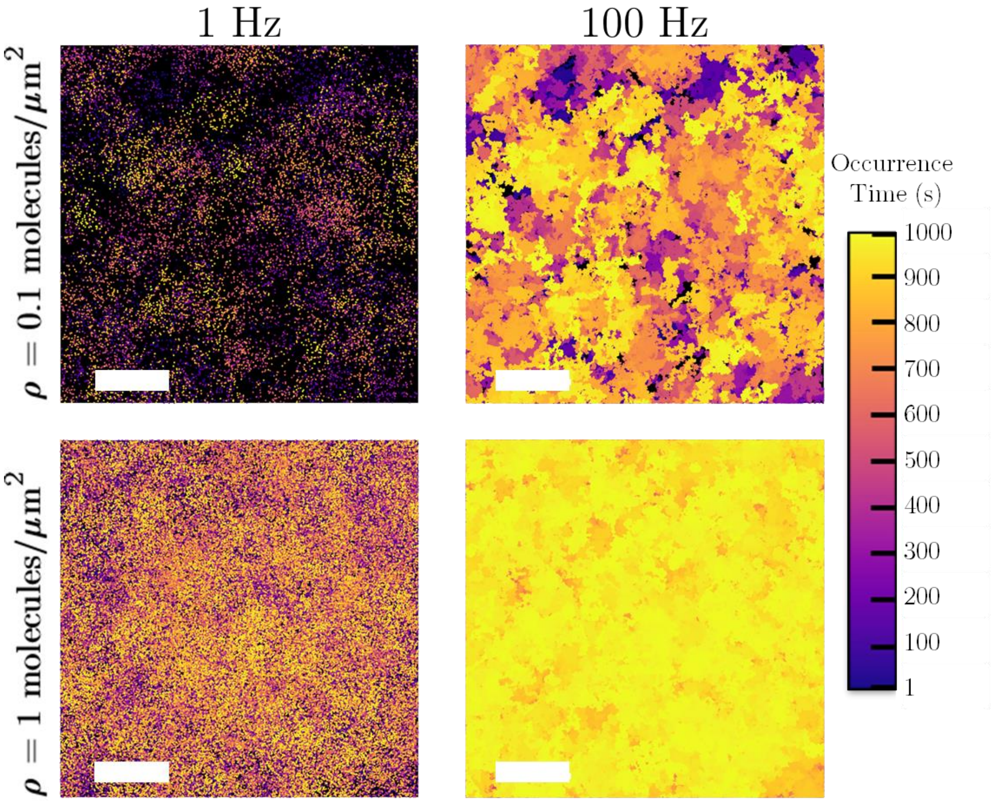

Figure 3.2 HiDenMap images of in-silico simulations of molecules diffusing in a Brownian fashion at D=0.1 µm²/s at two labelling densities (0.1 molecules/µm² (top row) and 1 molecule/µm² (bottom row) and two frame rates (1Hz -1st column- and 100 Hz -second column-). Localisations are colour-coded according to the occurrence time. Scale bar is 2 µm.

On the one hand, for a sparse labelling density, (ρ = 0.1 molecules/µm²) similar to the one used in standard SPT and a slow frame rate (1 Hz), the HiDenMap appears mostly empty after an observation time of 1000 seconds. Increasing the camera frame to 100 Hz and collecting localisations during 1000 seconds leads to an almost full HiDenMap. Nevertheless, imaging for 1000 seconds at 100 Hz framerate is unrealistic with typical fluorophores or fluorescent proteins due to their limited photon budget and photostability. Additionally, the high excitation powers needed to record enough photons from individual molecules at an integration time of 10 ms (i.e., camera framerate of 100Hz) for such long periods of time increase the chances of cell phototoxicity.

On the other hand, at high labelling densities (ρ = 1 molecule/µm^2) and a slow frame rates (1 Hz), the whole space has been explored in 1000 seconds. But, again, imaging for 1000 seconds is experimentally challenging. In contrast, at high labelling densities and at fast frame rates (100 Hz), a homogeneous exploration of the full space is achieved in roughly 100-200 seconds. Thus, from these simulations, it is clear that faithful HiDenMaps can be best generated by working at high labelling densities (but still at levels in which single molecules can be discriminated individually) and by imaging at fast frame rates.

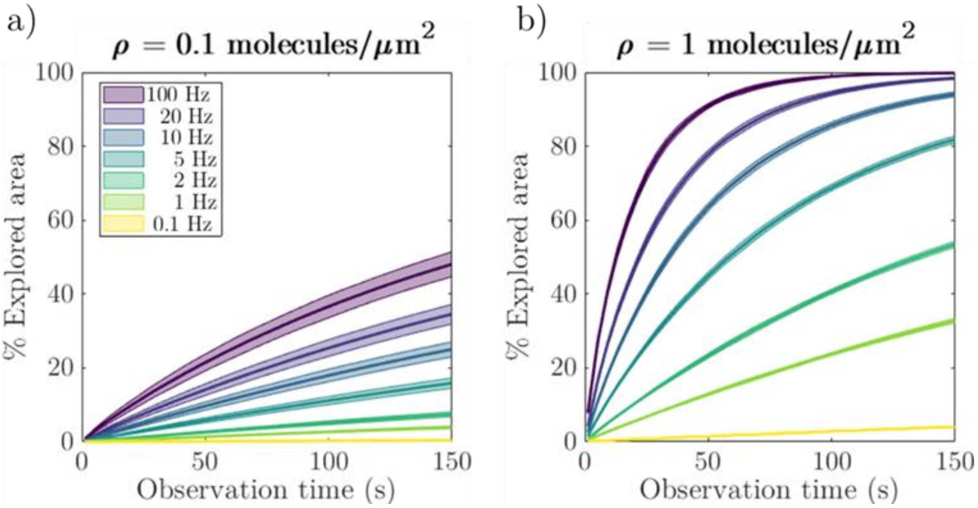

Figure 3.3 Percentage of explored area by molecules diffusing in 2D in a Brownian fashion at D = 0.1 µm^2/s and at different frame rates (0.1, 1, 2, 5, 10, 20, 100 Hz). a) Labelling density of 0.1 molecules/µm^2. b) Labelling density of 1 molecule/µm^2.

To quantitively show these results, we calculated the percentage of explored area as a function of observation time for two labelling densities and different acquisition frame rates (Figure 3.3). To compute the percentage of the explored area, we binned regions of interest (ROIs) of 10-by-10 µm into 25 nm squared pixels and counted how many pixels had localisations at each given observation time.

As expected, at low labelling densities, the observed explored area barely reaches to 50% after imaging for 150 seconds at 100 Hz. At slower frame rates, the explored area decreases significantly. We have restricted to 150 seconds to account for the photobleaching of fluorophores, since imaging for longer periods of time with typical fluorophores is not possible, besides the phototoxicity. At high labelling density, the whole space is explored in 100 seconds when imaging at a frame rate of 100 Hz. Moreover, imaging at slower frame rates of 20 Hz or even 10 Hz can reveal a full homogenous HiDenMap.

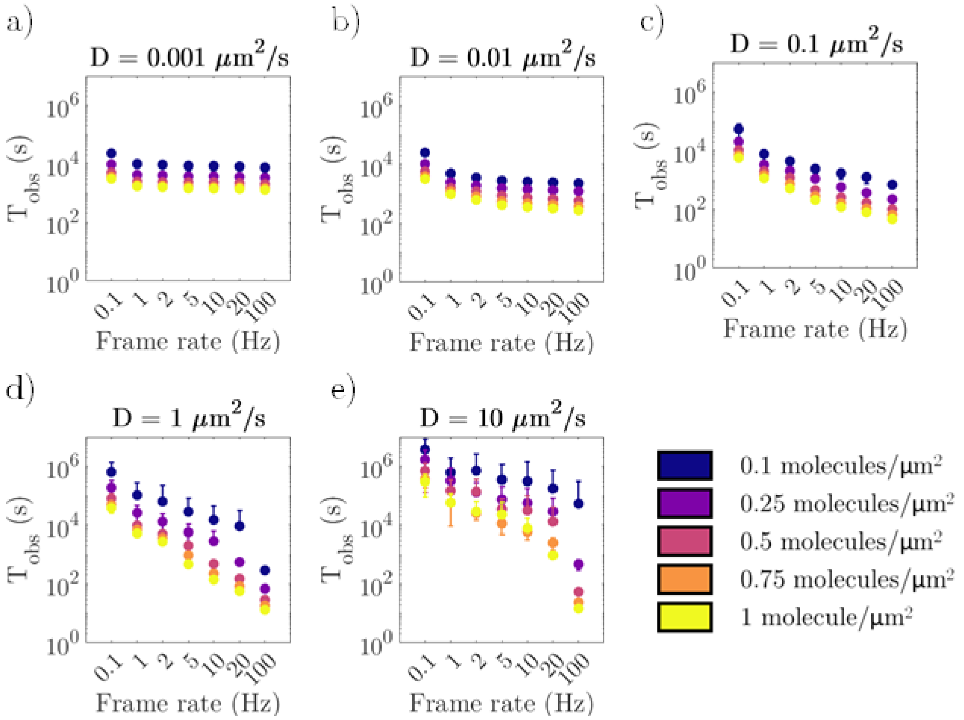

Figure 3.4 Expected observation time required to observe 90% of the area explored, for varying labelling densities as a function of the frame rate, with molecules diffusing at different diffusion coefficients (D=0.01, 0.1, 1 and 10 μm²/s)

Next, we investigated the effect of molecular diffusion on the exploration of space. We performed *in-silico* simulations of Brownian motion at different diffusion coefficients (D = 0.001, 0.01, 0.1, 1, 10 μm²/s) and computed the expected observation time required to explore 90% of the ROI (Figure 3.4). For each diffusion coefficient we also investigated the effect of the imaging frame rate and the labelling densities. In the case of slowly diffusing molecules (D~0.001 µm^2/s, Figure 3.4a) the main parameter allowing to observe more area explored is the labelling density rather than the frame rate (this is valid for frame rates $\geq 1\,Hz$), i.e., the higher the labelling density the shorter the observation time. At fixed labelling densities, the time required to observe 90% of the area explored is essentially constant for all the frame rates faster than 0.1 Hz.

As we increase the diffusion coefficient of the molecules, the role of the frame rate becomes more important. For a diffusion coefficient of 0.01 µm^2/s, we would need to image at least at 5 Hz (rather slow) and at high labelling densities (Figure 3.4b) to effectively reduce the observation time which in turn, remains essentially constant regardless of the frame rate used. For faster diffusion coefficients (D ≥ 0.1 µm^2/s), increasing the frame rate reduces the estimated observation time (Figure 3.4c-e). At these diffusion coefficients, working at frame rates > 20 Hz and high labelling densities ($\rho \geq$ 0.75 molecules/µm^2) allow to explore the whole space in less than 100 seconds. Finally, for fast diffusion coefficients (D ∈ [1,10] µm^2/s) the estimated observation times decay fast both with increasing frame rate and labelling density. Interestingly, for very fast diffusing molecules, the estimated time required to observe 90% of the area explored at frame rates slower than 20 Hz is longer than for slow diffusing molecules. This effect results from the temporal under sampling, i.e., although the molecules explored the full space, we only sample at specific points missing all the data in between.

To better illustrate the effect of the diffusion coefficient, we plotted the same data as above but separating the curves according to the labelling density ($\rho =$ 0.1, 0.25, 0.5, 0.75, 1 molecules/µm^2) (Figure 3.5).

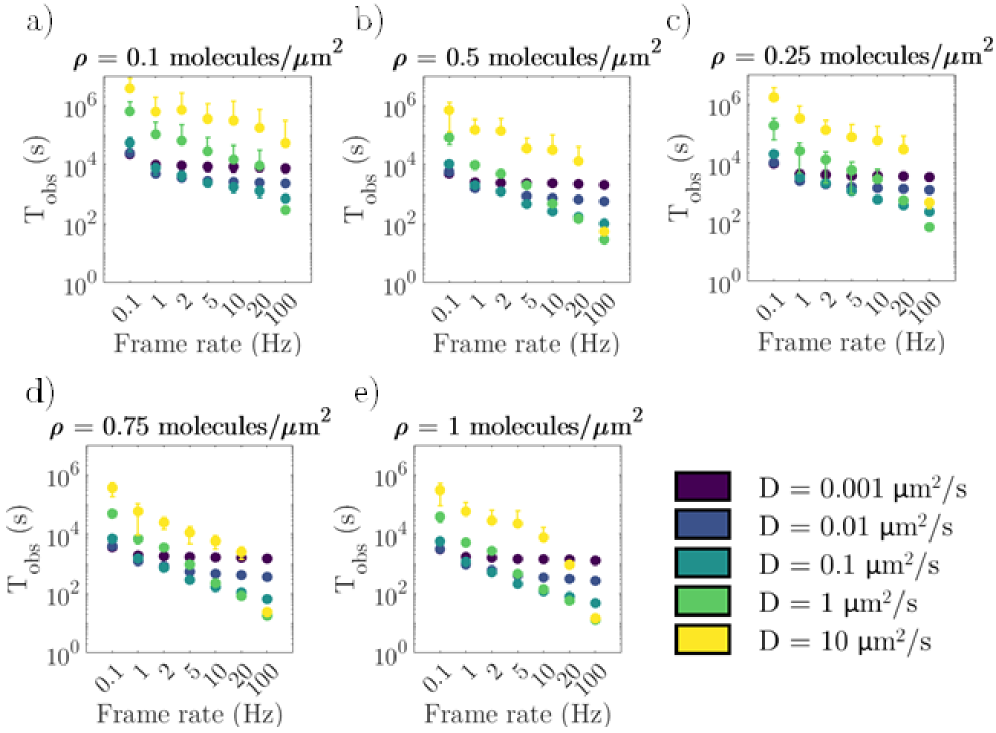

Figure 3.5 Expected observation time required to observe 90% of the area explored, for varying diffusion coefficients (D=0.01, 0.1, 1 and 10 µm^2/s) as a function of the frame rate, at different labelling densities (ρ = 0.1, 0.25, 0.5, 0.75 and 1 molecules/ µm^2).

As mentioned above, the estimated observation time for an exploration of 90% of space is longer for fast diffusing molecules than for slower diffusing at slow frames rates. This is of course an artefact of the imaging and shows the importance of working at high frame rates (>20 Hz) especially for fast diffusing molecules. Additionally, these results reflect how critical is to work at high labelling densities ($\rho \sim$ 1 molecule/µm^2) in order to have a faithful representation on how molecules explore the space.

Overall, the crucial requirements to obtain reliable HiDenMaps are high labelling densities (between 0.75 and 1 molecules/µm^2) and fast frame rates (above to 20 Hz and preferably 100 Hz). Moreover, this methodology is especially suitable for molecules with diffusion coefficients between D = 0.01 and 0.1 µm^2/s. Slower diffusing molecules can also be studied with our methodology but at the expense of retrieving a lower fraction of the space visited during a given observation time window. Importantly, the parameters obtained from our simulations in terms of labelling density, camera frame rates, molecular diffusion coefficients and observation times are all compatible with single molecule imaging of most receptors on the cell membrane using standard labelling probes. Therefore, the use of HiDenMaps should provide unique information on how receptors explore the cell membrane with high spatial and temporal resolution.

3.3.3 **HiDenMaps in experimental data, is everything Brownian?**

We have shown that *in-silico* simulations of diffusing molecules exhibiting Brownian motion reveal a homogeneous HiDenMap exploring the full space. To validate these simulations, we performed experiments on supported lipid bilayers containing Nickel-chelating lipids to anchor His-SNAP-EzrRA recombinant protein labelled with JF549-SNAP. This system serves as an *in-vitro* control of Brownian diffusing proteins with a $D_{1\text{-}4}$ of ~1 $\mu m^2/s$. The HiDenMap of the lipid bilayer system renders a homogeneous map (Figure 3.6, 1st and 2nd columns) consistent with the *in-silico* simulations of Brownian motion. In addition, we could also observe the effect of down-sampling the frame rate. The original data was recorded at a frame rate of 100 Hz (2nd column) and we down-sampled it to 33.33 Hz by dropping two out of three frames. As observed, both HiDenMaps are homogeneous regardless of the effective frame rate used. Nevertheless, and in full agreement with our simulations, increasing the frame rate results in an increased coverage of the space.

We then performed experiments on live mouse embryonic fibroblasts (MEFS) labelling the receptor CD44. CD44 is a type II transmembrane adhesion receptor that can interact both with the intracellular cortical actin and with multiple molecules of the extracellular matrix(27). Since the reported diffusion coefficient of CD44 is rather low ($D_{1\text{-}4}$~0.048 $\mu m^2/s$ (28, 29)), we first performed *in-silico* simulations of proteins diffusing randomly with the same characteristic diffusion coefficient as CD44. Using a frame rate of 33.3 Hz and 30 nM labelling density, the *in-silico* generated HiDenMap exhibits a homogeneous uniform distribution of localisations with most of the space being explored at 75-100 seconds (Figure 3.6, 3rd column). Thus, these simulations indicate that under realistic experimental settings we should be able to map with single molecule sensitivity and nanometric accuracy how CD44 dynamically explores the cell membrane.

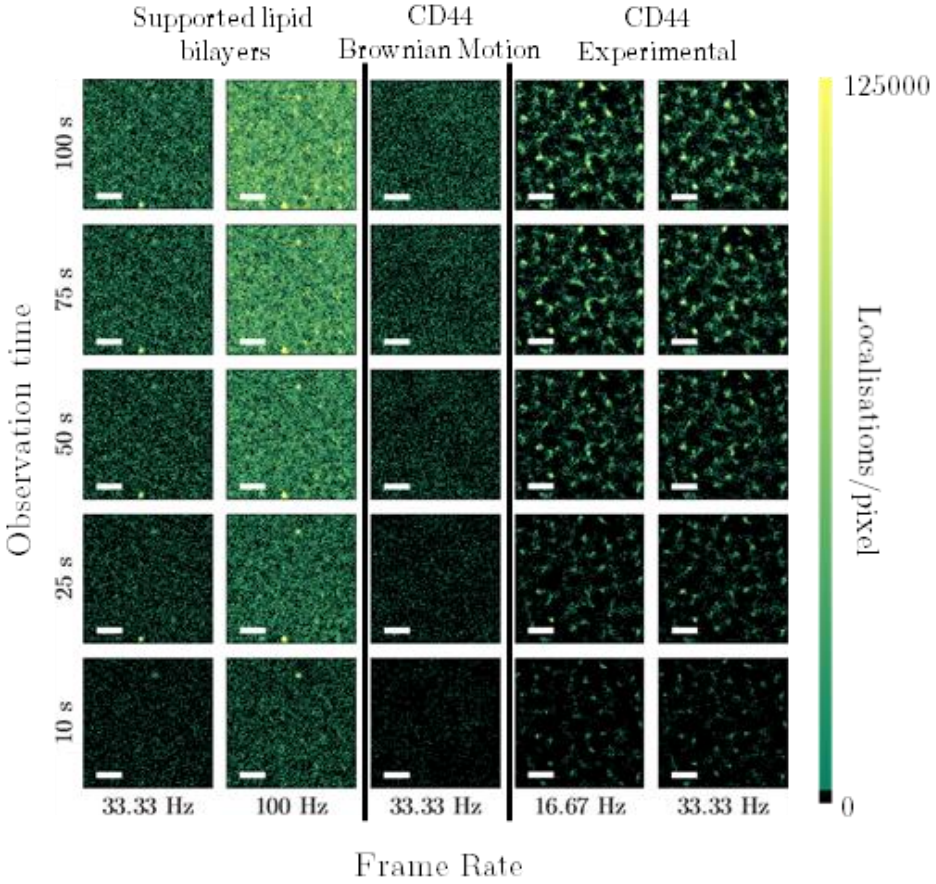

Figure 3.6 HiDenMaps at multiple observation times (10, 25, 50, 75 and 100 seconds) and different frame rates for supported lipid bilayers (1st and 2nd columns), Brownian motion in-silico simulation of CD44 (3rd column) and experimental CD44 in MEFs for two different camera frame rates (4th and 5th columns). Scale bar is 1 µm.

Remarkably, the HiDenMaps obtained experimentally differ dramatically from the *in-silico* simulations (Figure 3.6, 4th and 5th columns). Rather than a homogenous exploration of the space, the HiDenMaps of CD44 reveal patterns in the diffusion of the receptor, which are built over time as one can infer from the different observation times. Increasing the frame rate from 16.67 Hz to 33.33 Hz does not result in a more homogeneous HiDenMap, but instead, it enriches the patterns that are being built. These results clearly indicate that CD44 diffusion is far from homogeneous and suggest that CD44 strongly interacts with its surrounding environment at the nano- and meso-scale (~ 1μm), describing diffusion patterns as the receptor explores the plasma membrane. In Chapters 4 and 5 of this thesis we present detailed insights on the biophysical origin of these patterns.

3.3.4 Exploring the nanoscale spatial organisation of molecules using HiDenMaps

The single molecule localisations of HiDenMaps encode both spatial and temporal information. We can thus access different spatial scales by tuning the observation times. Integrating over long periods of time (~100 s range) will provide access on the mesoscale organisation of the proteins, whereas integrating for short periods of time (~1 s range) reveals nanoscale information.

In order to assess the potential of HiDenMaps to investigate processes at the nanoscale, we compared super-resolution images taken by STORM and HiDenMaps (integrating for 1 seconds) of CD44 at the plasma membrane of immature dendritic cells (Figure 3.7). It is important to note that whereas STORM imaging was performed on fixed cells using secondary antibodies for CD44 labelling, the HiDenMaps were generated from single molecule imaging in living cells using single chain-antibodies. The STORM image was generated by collecting 1.930.700 single molecule localisations while the HiDenMap contains 36.842 localisations. The lower number of localisations on the HiDenMap results in part from the lower labelling density used to generate the map as compared to the full labelling required for STORM, but most importantly, they arise because of the short integration time used (1 s) as compared to the STORM image which is generated by collecting single molecule localisations over 45 min. Despite this difference in terms of the number of localisations, the two images look remarkably similar. In both cases, we observe nanoclusters of localisations as well as some wiggles, albeit the sources of localisations are very different. Indeed, the STORM image is a snapshot of the protein distribution at one time point because the sample is fixed. The HiDenMap results from integrating 1 second (with a frame rate of 30 Hz), and shows how the labelled proteins have diffused over that period of time.

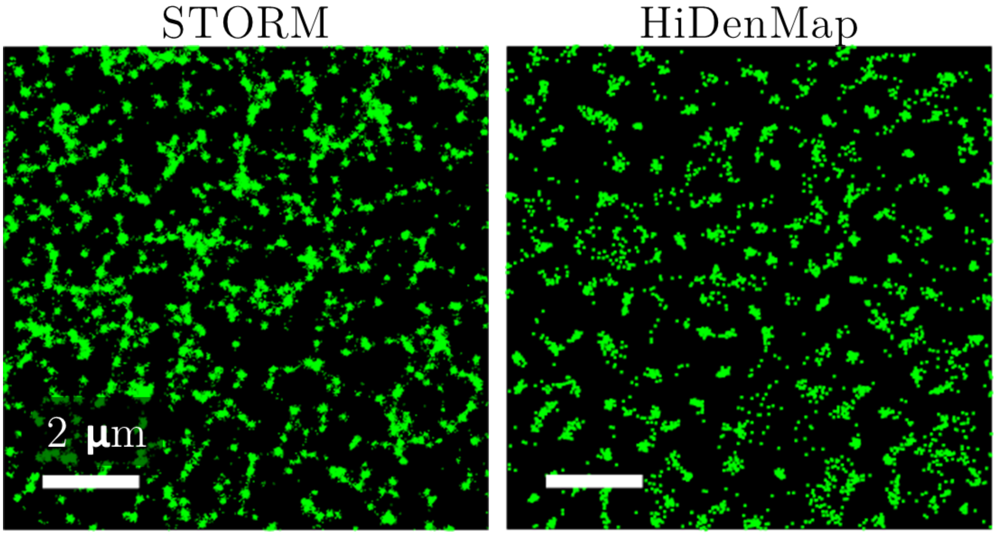

Figure 3.7 Nanoscale spatial organisation of CD44 using STORM (left) and HiDenMaps (right) with an integration time of 1 second at a frame rate of 30 Hz.

To provide a more quantitative basis for the interpretation of both images, we took both images, detected clusters of localisations using the DBSCAN algorithm (as described in Chapter 2) and quantified both, the cluster area and the cluster radius (Figure 3.8). Despite the similarity of the distributions, they are statistically different. Nevertheless, the median values of both the cluster areas are similar; the median area for the STORM image is $A_{STORM} = 0.0169$ µm^2 and the median area of the HiDenMap is $A_{HiDenMap} = 0.0160$ µm^2. Moreover, assuming the clusters to be circles, then the radius of the clusters for STORM have a median radius of 73 nm while the ones for the HiDenMaps have a median radius of 71 nm.

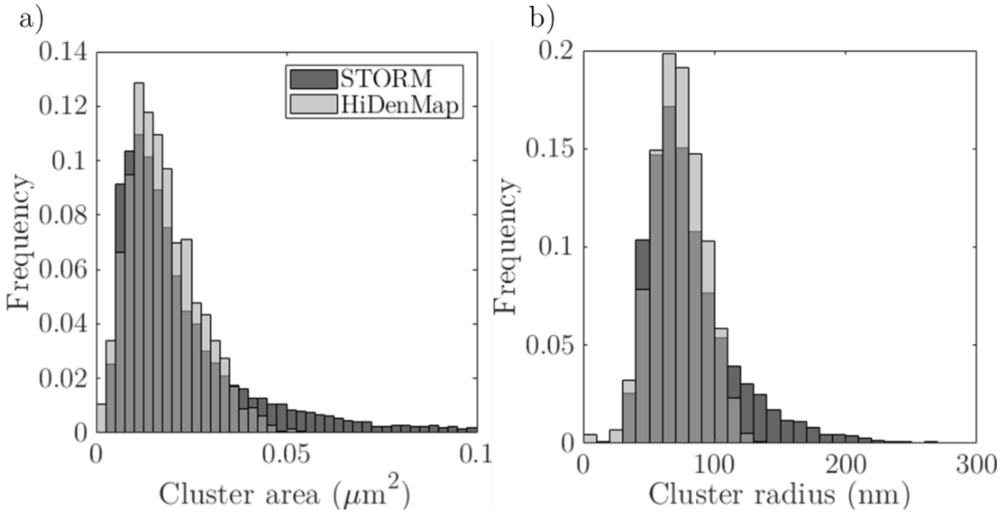

Figure 3.8 Quantification of STORM and HiDenMap images of CD44 on immature dendritic cells. a) Cluster area in µm^2 and, b) Approximated cluster radius assuming clusters to be circles. We analysed 8 cells for the STORM data and 11 cells for the HiDenMap data.

Therefore, although STORM and HiDenMaps are different techniques, we can access the nanoscale organisation of molecules using HiDenMaps with short integration times. Of course, one could argue that the nanoclusters detected by STORM and HiDenMap arise from different biological mechanisms. One the one hand, the nanoclusters detected in the STORM images arise from the spatial clustering of proteins. On the other hand, the nanoclusters in the HiDenMap data are clusters of localisations of probably a single or few proteins diffusing in a confined region of the cell membrane.

3.4 Discussion

Understanding the spatiotemporal organisation of receptors at the plasma membrane of cells is crucial to elucidate their functions. However, spatial and temporal studies are typically conducted separately. On the one hand, super-resolution (SR) microscopy techniques are focused on revealing the spatial organisation of receptors, sacrificing temporal information because either cells are fixed or it takes too long to perform the imaging. On the other hand, single particle tracking (amongst other techniques) is focused on studying the dynamics of single receptors, but only mapping a sparse number of molecules which results in low statistics. Recently, HD-SPT has emerged as a powerful technique to obtain more trajectories and therefore more statistics from single experiments by either using stochastic emission(20) or stochastic labelling(26). However, the temporal framework is in the order of minutes, which limits the study of fast dynamics for instance at the plasma membrane of living cells. In this work, we propose a novel methodology based on single molecule fluorescence live cell imaging with high-labelling density (but sub-saturating conditions) to generate high density maps (HiDenMaps) and bridge between both approaches.

HiDenMaps consist on generating super-resolution single molecule localisation images with temporal information encoded. In this Chapter we have performed a thorough study on the parameters in order to obtain a faithful exploration map. We have focused on how to adjust a proper imaging frame rate and observation time considering the diffusion coefficient of the studied protein. Our methodology relies on generating localisation-based exploration maps, which do not require of any reconnection. Therefore, we can simplify greatly our experimental settings and work at higher labelling concentrations as far as we can still detect single molecules.

We have performed *in-silico* simulations of Brownian motion to determine how would molecules explore space randomly. As we had initially expected, the resulting HiDenMaps of these simulations reveal a homogeneous exploration of the space. We translated our *in-silico* simulations towards *in-vitro* measurements of Brownian motion by studying proteins embedded in lipid bilayers which reveal the same homogeneous exploration. An interesting finding of our work is the emergence of diffusion patterns for receptors that interact with their plasma membrane environment. Therefore, HiDenMaps are sensitive to heterogeneities of the environment that proteins can feel during their diffusion on the membrane. Because of the temporal scales of our measurements, we can potentially access different dynamics of the proteins just by studying the HiDenMap as we will see in the next chapters. Certainly, this simple methodology that consists on localising single molecules at each frame and collapsing them into a HiDenMap already unlocks a novel view on how molecules dynamically explore the space.

Moreover, we have shown that we can also investigate the nanoscale organisation of a receptor such as CD44 by tuning the integration time of our obtained HiDenMap. We have compared a STORM image obtained for CD44 on immature dendritic cells with a HiDenMap composed of single CD44 localisations collected during an observation time of only 1 second. We quantified the nanoclusters of proteins in STORM and those from the HiDenMaps and retrieve similar values in terms of median nanocluster area and radius. Although the biological mechanism leading to the emergence of these nanoclusters might be different, the HiDenMaps provide dynamic information at the nanoscale in short times. This is also quite astonishing if we consider the imaging time required for each method; a STORM image can take easily 30 minutes, while the HiDenMap to reveal this information takes 1 second. Moreover, in STORM cells are fixed while in HiDenMaps, cells are alive.

The HiDenMap methodology can be extended to other cellular contexts besides the plasma membrane. For instance, we have used HiDenMaps to study progesterone receptor (PR) transcription factor condensates in the nucleus of living cells(31). Indeed, using HiDenMaps we observed an accumulation of PR in nanoscale hotspots upon hormone treatment compared to the control in which no hotspots were visible. The emergence of these hotspots originate from the formation of PR condensates within the nucleus(31).

In the next chapter we will focus on exploiting HiDenMaps to its maximum by developing new algorithms to quantify them. We will investigate the patterns of CD44 and how other molecules also reveal diffusion patterns that arise from their interactions with their environment.

3.5 References

1. S. J. Singer, G. L. Nicolson, The fluid mosaic model of the structure of cell membranes. *Science (80-.).* **175**, 720–731 (1972).
2. M. F. Garcia-Parajo, A. Cambi, J. A. Torreno-Pina, N. Thompson, K. Jacobson, Nanoclustering as a dominant feature of plasma membrane organization. *J. Cell Sci.* **127** (2014).
3. S. F. Banani, H. O. Lee, A. A. Hyman, M. K. Rosen, Biomolecular condensates: Organizers of cellular biochemistry. *Nat. Rev. Mol. Cell Biol.* **18** (2017).
4. B. Alberts, D. Bray, K. Hopkin, A. D. Johnson, *Essential Cell Biology - Alberts - Third Edition* (2010).
5. S. T. Hess, T. P. K. Girirajan, M. D. Mason, Ultra-high resolution imaging by fluorescence photoactivation localization microscopy. *Biophys. J.* (2006) https:/doi.org/10.1529/biophysj.106.091116.
6. E. Betzig, *et al.*, Imaging intracellular fluorescent proteins at nanometer resolution. *Science (80-.).* (2006) https:/doi.org/10.1126/science.1127344.
7. M. J. Rust, M. Bates, X. Zhuang, Stochastic optical reconstruction microscopy (STORM) provides sub-diffraction-limit image resolution. *Nat Meth* (2006) https:/doi.org/10.1038/nmeth929.
8. R. Jungmann, *et al.*, Multiplexed 3D cellular super-resolution imaging with DNA-PAINT and Exchange-PAINT. *Nat. Methods* (2014) https:/doi.org/10.1038/nmeth.2835.
9. J. Schnitzbauer, M. T. Strauss, T. Schlichthaerle, F. Schueder, R. Jungmann, Super-resolution microscopy with DNA-PAINT. *Nat. Protoc.* (2017) https:/doi.org/10.1038/nprot.2017.024.
10. E. Abbe, Beiträge zur Theorie des Mikroskops und der mikroskopischen Wahrnehmung. *Arch. für Mikroskopische Anat.* **9**, 413–468 (1873).
11. D. Axelrod, D. E. Koppel, J. Schlessinger, E. Elson, W. W. Webb, Mobility measurement by analysis of fluorescence photobleaching recovery kinetics. *Biophys. J.* (1976) https:/doi.org/10.1016/S0006-3495(76)85755-4.
12. D. Magde, E. Elson, W. W. Webb, Thermodynamic fluctuations in a reacting system measurement by fluorescence correlation spectroscopy. *Phys. Rev. Lett.* (1972) https:/doi.org/10.1103/PhysRevLett.29.705.
13. C. Eggeling, *et al.*, Direct observation of the nanoscale dynamics of membrane lipids in a living cell. *Nature* (2009) https:/doi.org/10.1038/nature07596.
14. C. Manzo, T. S. Van Zanten, M. F. Garcia-Parajo, Nanoscale fluorescence correlation spectroscopy on intact living cell membranes with NSOM probes. *Biophys. J.* (2011) https:/doi.org/10.1016/j.bpj.2010.12.3690.
15. A. Kusumi, Y. Sako, M. Yamamoto, Confined lateral diffusion of membrane receptors as studied by single particle tracking (nanovid microscopy). Effects of calcium-induced differentiation in cultured epithelial cells. *Biophys. J.* **65** (1993).

16. M. J. Saxton, K. Jacobson, Single-particle tracking: Applications to membrane dynamics. *Annu. Rev. Biophys. Biomol. Struct.* **26** (1997).
17. M. J. Saxton, Lateral diffusion in an archipelago. Single-particle diffusion. *Biophys. J.* **64** (1993).
18. C. Manzo, M. F. Garcia-Parajo, A review of progress in single particle tracking: From methods to biophysical insights. *Reports Prog. Phys.* (2015) https:/doi.org/10.1088/0034-4885/78/12/124601.
19. J. B. Sibarita, High-density single-particle tracking: Quantifying molecule organization and dynamics at the nanoscale. *Histochem. Cell Biol.* (2014) https:/doi.org/10.1007/s00418-014-1214-1.
20. S. Manley, *et al.*, High-density mapping of single-molecule trajectories with photoactivated localization microscopy. *Nat. Methods* (2008) https:/doi.org/10.1038/nmeth.1176.
21. R. Ando, H. Hama, M. Yamamoto-Hino, H. Mizuno, A. Miyawaki, An optical marker based on the UV-induced green-to-red photoconversion of a fluorescent protein. *Proc. Natl. Acad. Sci. U. S. A.* **99** (2002).
22. G. H. Patterson, J. Lippincott-Schwartz, A photoactivatable GFP for selective photolabeling of proteins and cells. *Science (80-.).* **297** (2002).
23. J. B. Grimm, *et al.*, A general method to improve fluorophores for live-cell and single-molecule microscopy. *Nat. Methods* **12** (2015).
24. J. B. Grimm, *et al.*, Bright photoactivatable fluorophores for single-molecule imaging. *Nat. Methods* **13** (2016).
25. J. B. Grimm, T. A. Brown, B. P. English, T. Lionnet, L. D. Lavis, “Synthesis of Janelia Fluor HaloTag and SNAP-tag ligands and their use in cellular imaging experiments” in *Methods in Molecular Biology*, (2017).
26. G. Giannone, *et al.*, Dynamic superresolution imaging of endogenous proteins on living cells at ultra-high density. *Biophys. J.* (2010) https:/doi.org/10.1016/j.bpj.2010.06.005.
27. H. Ponta, L. Sherman, P. A. Herrlich, CD44: From adhesion molecules to signalling regulators. *Nat. Rev. Mol. Cell Biol.* (2003) https:/doi.org/10.1038/nrm1004.
28. P. Sil, *et al.*, Dynamic actin-mediated nano-scale clustering of CD44 regulates its meso-scale organization at the plasma membrane. *Mol. Biol. Cell* (2020) https:/doi.org/10.1091/mbc.E18-11-0715.
29. S. A. Freeman, *et al.*, Transmembrane Pickets Connect Cyto- and Pericellular Skeletons Forming Barriers to Receptor Engagement. *Cell* **172**, 305-317.e10 (2018).
30. W. H. Kruskal, W. A. Wallis, Use of Ranks in One-Criterion Variance Analysis. *J. Am. Stat. Assoc.* **47** (1952).
31. G. Muñoz-Gil, *et al.*, Stochastic particle unbinding modulates growth dynamics and size of transcription factor condensates in living cells. *Proc. Natl. Acad. Sci.*

U. S. A. **119**, e2200667119 (2022).

32. D. V. Köster, *et al.*, Actomyosin dynamics drive local membrane component organdtion in an in vitro active composite layer. *Proc. Natl. Acad. Sci. U. S. A.* **113**, E1645–E1654 (2016).
33. C. E. Aitken, R. A. Marshall, J. D. Puglisi, An oxygen scavenging system for improvement of dye stability in single-molecule fluorescence experiments. *Biophys. J.* **94**, 1826–1835 (2008).
34. P. A. Gómez-García, E. T. Garbacik, J. J. Otterstrom, M. F. Garcia-Parajo, M. Lakadamyali, Excitation-multiplexed multicolor superresolution imaging with fm-STORM and fm-DNA-PAINT. *Proc. Natl. Acad. Sci. U. S. A.* (2018) https:/doi.org/10.1073/pnas.1804725115.
35. M. Ester, H.-P. Kriegel, J. Sander, X. Xu, A Density-Based Algorithm for Discovering Clusters in Large Spatial Databases with Noise in *Proceedings of the 2nd International Conference on Knowledge Discovery and Data Mining*, (1996).

Chapter 4

HiDenMaps reveal nano- and meso-organisation of the CD44 transmembrane receptor in living cells

Transmembrane adhesion receptors at the cell surface, such as CD44, are often equipped with modules to interact with the extracellular matrix (ECM) and the intracellular cytoskeletal machinery. CD44 has been recently shown to compartmentalise the membrane into domains by acting as membrane pickets, facilitating the function of signalling receptors. While spatial organisation and diffusion studies of membrane proteins are usually conducted separately, here we exploit HiDenMaps in combination with fluorescence resonance energy transfer anisotropy measurements to investigate the nano- and meso-scale organization of CD44 in living cells. We combine observations of organisation and diffusion by using high spatiotemporal resolution imaging on living cells to reveal a hierarchical organisation of CD44. Our results show that CD44 is present in a meso-scale meshwork pattern where it exhibits enhanced confinement and is enriched in nanoclusters of CD44 along its boundaries. This nanoclustering is orchestrated by the underlying cortical actin dynamics. Interaction with actin is mediated by specific segments of CD44 intracellular domain. This influences the organisation of the protein at the nano-scale, generating a selective requirement for formin over Arp2/3-based actin-nucleation machinery. The extracellular domain and its interaction with elements of ECM do not influence CD44 meso-scale organisation, but may serve to reposition the meshwork with respect to the ECM. Taken together, our results capture the hierarchical nature of CD44 organisation at the cell surface, with active cytoskeleton-templated nanoclusters localised to a meso-scale meshwork pattern.

This work has been published as Parijat Sil*, Nicolas Mateos*, Sangeeta Nath, Sonja Buschow, Carlo Manzo, Kenichi G. N. Suzuki, Takahiro Fujiwara, Akihiro Kusumi, Maria F. Garcia-Parajo, and Satyajit Mayor, "Dynamic actin-mediated nano-scale clustering of CD44 regulates its meso-scale organization at the plasma membrane", *Molecular Biology of the Cell* 31(7) (2020). *Equally contributing authors.

4.1 Motivation

Heterogeneity in the distribution of membrane proteins and lipids is becoming an increasingly appreciated paradigm in the context of the organisation of molecules at the plasma membrane (1). This regulated, non-random distribution of membrane proteins, such as signalling receptors, is implicated in their molecular function and signalling output (2). The advent of super-resolution microscopy and breakthroughs in single molecule techniques has revolutionised our understanding of cellular organisation at the molecular level (3–5). The major goal from such techniques has traditionally been to obtain detailed descriptions of protein clustering, cluster sizes, or intermolecular distances. However, these super-resolution techniques are often technically demanding, and associated invasive sample preparation methods are fraught with criticism for being non-physiological. Additionally, although such studies of membrane constituents inform us on the organisational details at the molecular level, there have been fewer efforts to understand the organisation and dynamics of proteins at larger spatial scales, to ascertain whether there exists any spatial hierarchy in membrane protein organisation.

Studies of the membrane organisation of many transmembrane receptors such as TCRs, EGFR, E-cadherin, GPCRs, or chemokine receptors such as CXCR-4 have advanced our understanding of changes at the nano-scale due to receptor dimerisation or oligomerisation (~2–40 nm) in the presence or absence of the cognate ligand (6–12). At the same time, studies elucidating the inhomogeneous diffusion behaviour of membrane proteins such as transferrin receptors (13) or CD44 (14) have revealed the presence of compartments in the cell membrane at a larger length scale (approximately a few hundred nanometres), templated by the underlying cytoskeletal meshwork. The potential hierarchy in the nature of organisation of membrane proteins has been speculated in the past based on evidences from clustering and diffusion studies of different proteins (15). It is likely that a unified study of diffusion and organisation interrogating the distribution of a particular membrane protein at different spatial scales will provide information of any underlying hierarchy in spatial scales of organisation.

Type-1 transmembrane proteins are a major and abundant class of integral membrane proteins that span three distinct environments: the extracellular space, transmembrane, and cytoplasmic milieu. The lymphocyte homing receptor CD44, is a type I transmembrane protein involved in cell-matrix adhesion (16). It has a heavily glycosylated extracellular domain (ECD) that ensures binding to extracellular lectins such as galectins, besides being able to bind to its ligand hyaluronic acid (HA) as well as other components of the extra cellular matrix (ECM) such as fibronectin and osteopontin (16, 17). Previous studies have shown that the ECD of CD44 is clustered by Galectin-3, which in turn also binds glycosphingolipids and is important for the endocytosis of the protein by a clathrin-independent pathway (18, 19). Additionally, HA binding has been shown to influence the dynamics of the protein at the plasma membrane (14, 19). The juxtamembrane O-glycosylation site and the transmembrane region with two putative palmitoylation sites confer the ability on the protein to partition into detergent-resistant membrane fractions or cholesterol-enriched domains on the plasma membrane (20, 21).

At the intracellular side, the relatively short 70 amino acid–long cytoplasmic tail of CD44 interacts with multiple cytoskeletal adaptor proteins. The association of the protein with ezrin has been shown to be important for T-cell migration in interstitial spaces of endothelial cells (22). The interaction with ezrin also influences the protein's ability to act as membrane picket in macrophages providing a functional partitioning of the FcγRIIA at the plasma membrane and facilitating its phagocytic function in macrophages (14). Ankyrin binding has been shown to be important for HA binding by CD44 (23). A proteomic analysis of the interacting partners of the CD44 cytoplasmic tail has also revealed an interaction with other cytoskeletal adaptors such as vinnexin, IQGAP1 and talin1 (24). The modularity of these potential cytoskeletal interactions in the tail of CD44 via its multiple cytoskeletal adaptor binding sites opens up possibilities to study how they may independently regulate organisation and turnover of the protein at the cell surface.

Thus, the diverse structural attributes of CD44 impart this receptor with the ability to be influenced by extracellular interactions, membrane composition, and the actin cytoskeleton. Hence, it also provides an ideal platform to uncover general principles of how such molecules are organised at varying length scales, determined by distinct modes of interaction in the different milieu and also the interplay between these length scales. Nevertheless, studies so far have not systematically investigated the role of the different structural domains of the protein in the organisation and dynamics of the liganded, as well as the native unliganded receptor on the membrane, at multiple spatial scales.

In this study, we have exploited various imaging methods in living cells to characterise the organisation of CD44 at the single molecule level over multiple spatiotemporal scales. High-density single particle tracking (HD-SPT) allowed us to capture the dynamics of CD44, at both the nano- and meso-scale levels. We define nano-scale organisation as being built of individual molecules brought together within an ~10-nm scale and meso-scale as domains ~100 nm–<1 μm in scale. By means of interleaved homo-Forster's resonance energy transfer (FRET)-based anisotropy and high-density maps (HiDenMaps), we show that the meso-scale organisation of CD44 is significantly associated with its nanoclusters. Overall, our data provide evidence for a hierarchical organisation of CD44, wherein each layer of organisation is determined by distinct interactions of the receptor.

4.2 Materials and Methods

4.2.1 **Plasmids, cell lines, and antibodies**

CD44-GFP, CD44ECDTm-GFP, and CD44TmICD-GFP cloned in p-EGFP N1 vector were gifts from Rob Parton at the University of Queensland, Australia. SNAP- and FR-tagged CD44 constructs were designed and cloned into a lentiviral pHR transfer backbone and cloned between MluI and BamHI/NotI sites using the Gibson Assembly method. All constructs were sequenced and verified using appropriate primers. SNAP CD59 GPI was obtained from Addgene (Addgene #50374). Cell line-expressing FR-CD44TmICD and FR-CD44Tm were generated by transfecting and selecting transfected cells by staining for FR-expressing cells with anti-FR MOV19 antibody using fluorescence-assisted cell sorting. CHO cells were cultured in Ham's F12 media (HiMedia, Mumbai, India); MCF-7, COS-7 (African green monkey kidney cells), and MEFs were cultured in DMEM high glucose (Gibco, 21720-024). The media was supplemented with fetal bovine serum (FBS) (Gibco, 16000044) and a cocktail of penicillin, streptomycin, and l-glutamine (Sigma; G1146-100 ml). MEFS, COS-7, or CHO cells were seeded sparsely and grown for 2 d on 35-mm cell culture dishes fitted with a glass bottom coverslip for imaging. Cells were transfected with the different CD44 plasmids, 12–16 h before imaging, using FuGENE 6 Transfection Reagent (E2692; Promega).

4.2.2 **Antibody labelling and expression level estimation**

Endogenous and overexpressed CD44 on the cell surface in the different cell lines, plated on cover slip bottom 35-mm dishes, after 2 d of plating, were labelled using IM7 antibody (14-0441-82; eBioscience) on ice for 1 h followed by incubation with anti-Rat secondary antibody tagged to Alexa 633 (A21094; Life Technologies) on ice for 1 h. The antibodies were diluted in 10% FBS containing culture media (DMEM). The cells were washed and imaged in HEPES buffer and imaged using a 20× objective on a spinning-disk microscope. Mean intensity from ROIs drawn around cells was quantified using ImageJ.

4.2.3 **Actomyosin perturbation**

Formin perturbation was carried out using 10–25 µM SMI-FH2 (Calbiochem; Cat. No. S4826-5MG) for 15 min–1 h based on experimental requirement.

4.2.4 **STORM sample preparation and imaging**

CHO cells were plated on an eight-well Lab-Tek #1 chamber slide system (Nunc) at a density of 30,000 cells/well. Cells were incubated at 37°C for 24 h. After incubation, the samples were fixed with 4% paraformaldehyde in phosphate-buffered saline (PBS) at room temperature for 20 min. After fixation, blocking solution (3% wt/vol bovine serum albumin in PBS) was applied for 30 min. Cells were labelled with rat-anti-mouse–anti-CD44 primary antibody (Clone KM114; BD Pharmingen #558739) at a concentration of 5 µg/ml for 1 h at room temperature. The corresponding secondary antibody (anti-rat) was tagged with Alexa Fluor 647 (Invitrogen) as a reporter and with Alexa Fluor 405 as an activator. The secondary antibody was incubated for 1 h at room temperature. Cells were stored in 1% PFA in PBS. The STORM buffer used was the same as that of Gómez-García et al. (25): Glox solution (40 mg/ml

Catalase [Sigma Aldrich], 0.5 mg/ml glucose oxidase, 10% glucose in PBS) and MEA 10 mM (Cysteamine MEA [Sigma-Aldrich; #30070-50G] in 360 mM Tris-HCl). The imaging for STORM on endogenous CD44 from top surface in CHO cells is from one experiment.

To study the nearest-neighbour distribution (NND) of clusters, we identified the clusters of localisations based on intensity (i.e., high density of localisations) and determined the position of the centre of mass. With this information, we calculate the NND for the experimental set. For the simulations, we take the same identified clusters (keeping their size) and reshuffle them in space. We repeat this process many times (100×) to get more robust information on the simulated NND.

4.2.5 **Live cell imaging for fluorescence emission anisotropy and HiDenMap experiments**

All live cell imaging was interchangeably carried out, based on requirement, in one of the following setups: 1) Total internal reflection fluorescence (TIRF) microscope setup was equipped with Nikon Eclipse Ti body; a 100×, 1.45NA Nikon oil objective; photometrics Evolve EMCCD cameras; an Agilent laser combiner MCL400 (Agilent Technologies) whose 488, 561, and 640 nm excitation wavelengths were used as necessary; and μ Manager for image acquisition. 2) TIRF microscope setup was equipped with Nikon TE2000 body; a 100×, 1.49NA Nikon oil objective; EMCCD Cascade 512 cameras (Photometrics, Tuscon, AZ); a home-built laser combiner equipped with 488 and 561 nm lasers; and Metamorph/µManager for image acquisition. Wherever necessary, live imaging was performed in a temperature-controlled stage-top incubator chamber with immersion thermostat, ECO Silver, from Lauda Brinkmann.

4.2.6 **Fluorescence emission anisotropy measurements**

We measure emission anisotropy of our protein of interest by labelling them with GFP, which is suitable for fluorescence anisotropy measurement to report on Homo-FRET (26, 27). Cells were treated with 50–100 µg/l cycloheximide in complete media for 2.5–3 h prior to imaging for anisotropy measurement of GFP-based constructs, in order to prevent signal from GFP from the ER/Golgi-based internal pool contaminating the fluorescence signal from the plasma membrane pool. This is in accordance with anisotropy measurements of GFP-tagged membrane proteins conducted in Major's lab in the past (28). Cells were imaged in HEPES buffer containing 2 mg/ml glucose on an inverted TIRF microscope using a polarised excitation light source. Emission was split into orthogonal polarisation components using a polarisation beam splitter and collected simultaneously by two EM-CCD cameras to detect polarisation of emitted fluorescence. Fluorescence emission anisotropy measurements were interchangeably carried out, based on requirements, in one of the dual camera-equipped imaging systems described before. Steady-state fluorescence emission anisotropy was calculated as elaborated in Ghosh et al. (27). The absolute value of anisotropy is a function of the effective numerical aperture of the imaging system (27). Since the effective numerical aperture is determined by the combinatorial effect of individual lenses in the light path of the microscope system, the absolute anisotropy value of the same protein varied from one system to another. Also, since the different experiments reported here have been conducted over several years, absolute values of anisotropy for the same constructs would have varied based on the status of the optics in a given microscope system. Hence, the measurements typically contained an internal control for sensitivity of anisotropy change, which was generally a measurement of the extent of anisotropy change between the wild-type CD44-GFP and CD44ECDTm-GFP (or CD44-TmICD-GFP and CD44-Tm-GFP).

4.2.7 Fluorescence anisotropy image analysis

Image analysis was carried out using the imaging software: ImageJ or Metamorph. Fluorescence emission anisotropy of GFP-tagged proteins was calculated using images from the two cameras, which were individually background corrected, and the perpendicular image was additionally G-Factor corrected (27) to rectify effects of inherent polarisation bias of the imaging system. Regions of interest (ROIs) of size 20 × 20 or 30 × 30 pixels were drawn to sample the cell membrane, and anisotropy values from these regions were obtained. Anisotropy maps were generated after aligning the images from the two cameras and calculating pixelwise anisotropy value as described in (27) using a custom code written in MATLAB (MathWorks, Natick, MA). For data plotting, intensity was binned for appropriate intensity range, and each data point represents mean, and an error bar represents SD of anisotropy corresponding to the intensity bin. We ensured that data comparisons were done between conditions across similar intensity ranges. Intensity range chosen was decided based on different microscope properties, especially the bit depth and noise levels of the cameras.

4.2.8 **Labelling of SNAP-tagged CD44 membrane receptors**

MEFS, COS-7, or CHO cells were seeded sparsely and grown for 2 days on 35-mm cell culture dishes fitted with a glass coverslip at the bottom. Cells were transfected with the different SNAP-tagged CD44 plasmids 16–18 h prior to the experiment using FuGENE 6 Transfection Reagent. Labelling was done with SNAP tag-specific photo-stable fluorescent probes, SNAP Alexa 546, SNAP-surface 549 (λ ex/ λ em: 560/575 nm, purchased from New England Biolabs, Ipswich, MA), or JF646-SNAP ligand (λ ex/ λ em: 646/664 nm) by incubating for 10 min at 37°C using a dilution of 50–100 nM (for HiDenMap experiments) with 10% serum containing F12 medium and then washed extensively with glucose-M1 buffer (150 mM NaCl, 5 mM KCl, 1 mM CaCl2, 1 mM MgCl2, 20 mM HEPES, pH 7.3; supplemented with d-glucose at 2 mg/ml) to get rid of free dyes. The dyes were chosen to ensure they are spectrally different from GFP with minimum bleed-through. Dual colour labelling was done with JF549-cpSNAP ligand (λ ex/ λ em: 549/571 nm) and JF646-SNAP ligand (λ ex/ λ em: 646/664 nm) fluorophores by incubating for 10 min at 37°C with F12 serum medium at mixed concentrations of 50 and 150 nM for the respective dyes. Singly or dually labelled cells were subsequently washed and imaged at 37°C in the presence of HEPES buffer containing 2 mg/ml glucose.

4.2.9 **Generation of high-density maps (HiDenMaps)**

HiDenMaps were generated from movies (1000 frames, 100 Hz) recorded in TIRF mode, as explained in the previous section, using sub-saturating labelling conditions (50–100 nM). Identification of single molecules essentially corresponds to the identification of individual fluorescent spots at each given time frame. For this, we apply two criteria: First, the spots should have a size that is limited by diffraction, that is, this corresponds to the point-spread function (PSF) of the microscope. Second, the intensity of each spot should be higher than the surrounding background. The localisation precision of each individual spot is given by the number of counts on that spot, which in the case of our videos corresponds to ~20 nm. The spatial (x, y) coordinates of the labelled membrane receptors (for each of the constructs investigated) were thus retrieved from each frame using a MATLAB routine based on that of Crocker and Grier (29), with subpixel accuracy. Finally, all the receptor coordinates of all frames were collapsed into a single image, the so-called HiDenMap. With this approach, one not only can access the nano-scale organisation of the labelled receptor but also can access the mesoscale organisation without the need of reconnecting trajectories (see Chapter 3 and ref (30)). Experiments to obtain HiDenMaps of the receptor and the mutants have been conducted at least twice in MEFs and once in COS-7 cells. Formin perturbation and mesoscale organisation imaging has been done at least twice and the represented experiment here is done in COS-7 cells. SNAP-CD44-GFP HiDenMap in CHO cells and GPI mesoscale organisation experiment has been conducted once.

4.2.10 **Analysis of the HiDenMaps**

Since the HiDenMaps are generated from localisations obtained as a function of time, their evolution is dynamic. Therefore, we restricted our analysis to time windows of 2 s by collapsing all the localisations from sequential 20 frames into a single, less crowded HiDenMap image. Confinement areas were identified using the MATLAB routine DBSCAN (density-based spatial clustering of applications with noise) with settings ($\varepsilon = 1.0$ and MinPts = 10, see Chapter 2 for further details). Finally, we defined the confinement area as the area occupied by a cluster of localisations.

For the time-evolution analysis of the meso-scale domains, the time windows correspond to 2 s, that is, 20 frames. Initially, clusters are defined at the time window 0 (frames within f0 and f0 + 19). Since we slide the window through the HiDenMap, at each time window we move 100 ms in the HiDenMap.

4.2.11 **Analysis of the interleaved anisotropy and HiDenMaps**

To compare the HiDenMaps with the anisotropy images, we performed interleaved anisotropy imaging together with high-density SPT generating one anisotropy image before starting SPT, a second anisotropy at frame 500 of the SPT recording, and a final one once the SPT recording was finished (after frame

1000). To reduce temporal variations on both the anisotropy and the HiDenMaps, we focused on anisotropy images at the corresponding frame 500 of the SPT movie. The anisotropy image was divided into small ROIs (22 × 22 pixels, with a pixel size of 106 nm). This was done in order to select only those regions where the plasma membrane is completely flat and therefore the anisotropy arises exclusively from the lateral distribution of the labelled receptors. In addition to this, for each ROI, we classified each pixel of the anisotropy map into three groups: low anisotropy (Low A), median anisotropy (Medium A), and high anisotropy (High A).

We then took the localisations between frames 480 and 520 of the SPT movie and generated a HiDenMap for each of the ROIs. We identified the clusters of localisations using the MATLAB routine DBSCAN with settings ($\varepsilon = 1.0$ and MinPts = 10). With the localisations belonging to clusters, we assigned to each of them an anisotropy value corresponding to their location in the anisotropy ROI and classified them within the three groups. Simultaneously, we randomly distributed the same number of localisations on the anisotropy ROIs and also assigned their corresponding anisotropy value and posterior classification. Comparative anisotropy-HiDenMap analysis has been done from an experiment with COS-7 cells where localisation and GFP-based FRET information was obtained using dual cameras at specific intervals during acquisition of single molecule localisation time series of the SNAP tag fluorophore.

4.2.12 **Statistical analysis**

Quantification from HiDenMap experiments was tested for significance using the Kruskal–Wallis test along with the post hoc Tukey–Kramer test and the Wilcoxon sum rank test of MATLAB unless otherwise mentioned. In the figures, ns indicates no statistically significant difference between two populations. * indicates $p < 0.05$, ** indicates $p < 0.005$, *** indicates $p < 0.0005$.

4.3 Results

4.3.1 Spatiotemporal mapping of CD44 reveals a mesh-like distribution of the protein at the mesoscale

To explore the dynamics of CD44 with high spatiotemporal resolution, we utilised the standard isoform of mouse CD44 (16) tagged with a SNAP domain at the N-terminus and GFP at the C-terminus (SNAP-CD44-GFP) (Figure 4.1a). This chimeric protein can be labelled at the extracellular side using cell-impermeable benzylguanine (BG)–conjugated fluorophores that covalently link to the extracellular SNAP domain. SNAP-CD44-GFP was expressed in wild-type mouse embryonic fibroblast (MEF) cells that endogenously express CD44 as well as produce the ligand HA (31, 32) and labelled with SNAP-Alexa 546 (or BG-Alexa 546). In order to generate HiDenMaps and to ensure a faithful representation on how CD44 explores the plasma membrane we worked at high labelling densities (50-100 nM). At these densities, we guarantee high sampling frequencies of the membrane protein and yet maintaining the ability of detecting individual molecules in each single frame to determine their coordinates with subpixel accuracy (Figure 4.1b). Moreover, this density regime offers the possibility of building up a large number of localisations to construct a dynamic meso-scale HiDenMap of CD44 distribution over the entire cell membrane (Figure 4.1b).

Time-lapse images were acquired at 100 Hz for 100 s, and the spatial coordinates of identified individual molecules over multiple frames were collapsed into a single frame to obtain a time-dependent HiDenMap of the regions dynamically explored by the receptor, as described in Chapter 3. Remarkably, we found that CD44 diffusion and distribution are largely inhomogeneous, describing a clear mesh-like spatiotemporal distribution at the meso-scale (Figure 4.1b', zoomed in). This mesh results from regions frequently revisited by the receptor and/or by its temporal arrest on the cell membrane. This is in stark contrast with the distribution of *in-silico* simulated Brownian motion localisations on the plasma membrane (as shown in Chapter 2), which appears homogeneous at the same length scale. Indeed, enlarged regions of the HiDenMap generated at two different time windows and from the same area of the cell membrane, show the dynamic character of the mesh (Figure 4.1, c and c’). Most importantly, these temporally separated maps reveal sites of confinement/trapping of the receptor, which we refer as to hotspot regions, evidenced by the large number of localisations (>106 for Figure 4.1c’) occurring within regions between ~90 and 200 nm in size. Moreover, some of these hotspot regions have a long persistence time (~50–60 s, Figure 4.1, c and c’, and merged image in c’’), indicating that the receptors could be stably confined in these hotspot regions and/or transiently tethered repeatedly to the same regions.

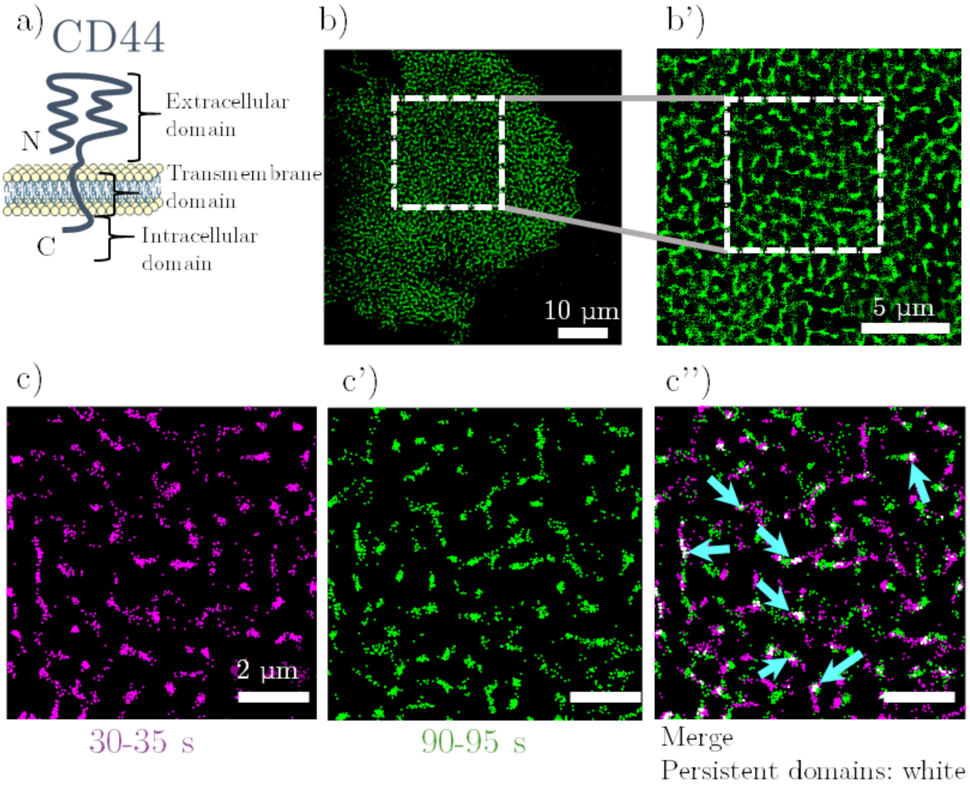

Figure 4.1 CD44 exhibits a non-random distribution at the plasma membrane at multiple spatiotemporal scales. a) Schematic of a standard isoform of CD44 showing key domains of the protein, namely, the ECD, the Tm, and the ICD. The SNAP is added at the N-terminus and the GFP is encoded at the C-terminus. b) HiDenMap of SNAP-CD44-GFP obtained at high labelling conditions (~50–100 nM); (x, y) coordinates from 1000 frames (1,354,066 localisations) collapsed in a single map with a zoomed-in region of interest (ROI) (b’). c) HiDenMap of (x, y) coordinates in the marked ROI in b from 50 consecutive frames obtained at two different experimental time windows, between 30-35 s (magenta, c) and 90-95 s (green, c’) and merged image (right, c’’). Blue arrows highlight regions of confinement, and white dots represent persistent confinement regions or sites revisited by the receptor. Adapted from Sil and Mateos et al. (33).

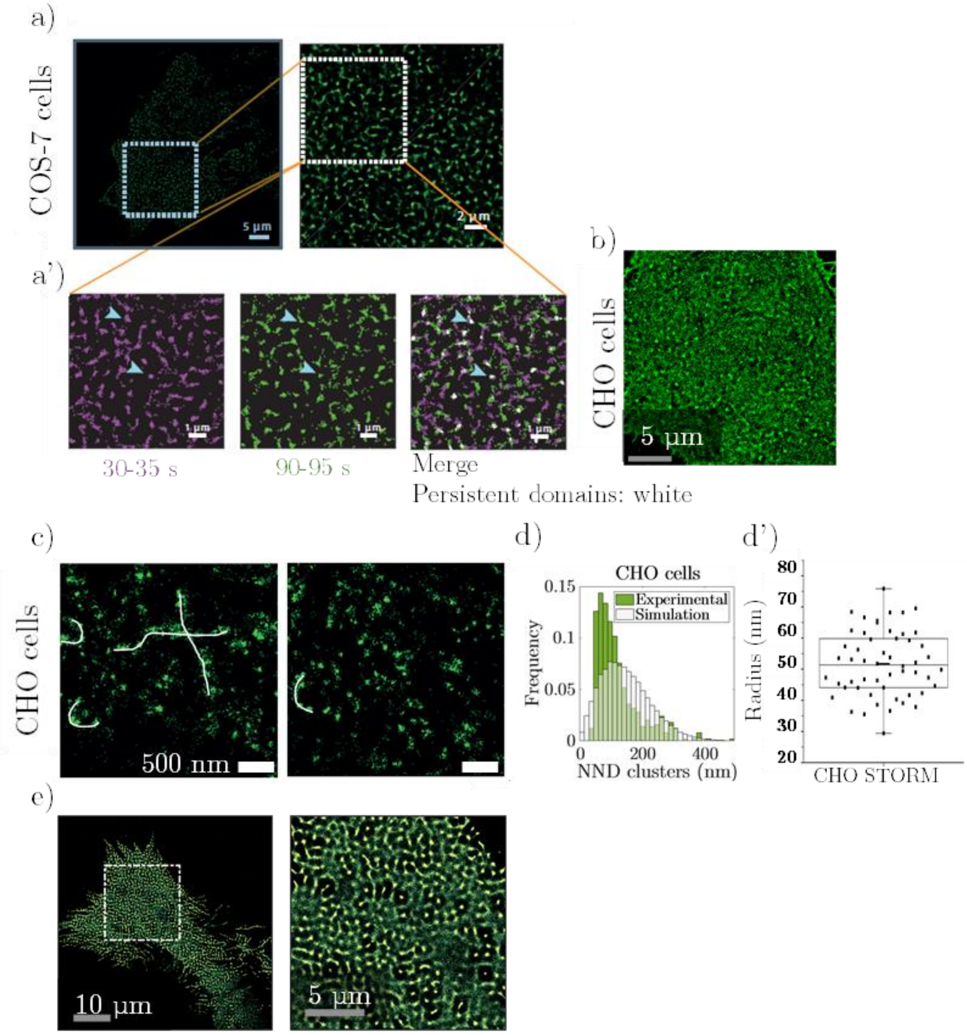

Figure 4.2 Non-random distribution of CD44. a) HiDenMap of SNAP-CD44-GFP expressed in COS-7 cells, obtained at sub-saturation labelling conditions (~50-100 nM); (x,y) coordinates obtained from 1000 frames collapsed in a single map with a zoomed-in ROI . a') HiDenMap construction of (x,y) coordinates in the marked ROI in (a) from 50 consecutive frames obtained at two different experimental time windows, between 30s-35s (magenta, left) and 90s-95s (green, centre) and merged image indicating persistent domains in white (right), also highlighted by the blue arrowheads. b) Representative HiDenMap of SNAP-CD44-GFP expressed in CHO cells. c) Representative STORM images of endogenous CD44 acquired from the top membrane in CHO cells indicating the mesh-like pattern with white dotted lines. d) Nearest neighbour distance (NND) plot of CD44 nanoclusters detected in STORM (and cluster radius d') compared to randomised simulated localisations depicting the non-random distribution of clustered CD44 at the membrane (by Wilcoxon rank sum test, p<e-18). e) HiDenMap of SNAP-CD59 GPI obtained

under similar labelling conditions as CD44 depicted at two different magnifications. Adapted from Sil and Mateos et al. (33).

Similar experiments conducted in cells that exhibit very low surface levels of endogenous CD44 (COS-7 cells; Figure 4.2, a and a') and the extracellular ligand, HA (34, 35) (CHO cells in Figure 4.2b), yielded comparable results. Together, these results indicate that CD44 is dynamically organised in a meshwork pattern on the plasma membrane. Importantly, this distribution is independent of the surface levels of endogenous proteins or the binding to its ligand HA on the extracellular side.

Since the experiments were conducted on the surface of the cell close to the coverslip, it is conceivable that the observed meso-scale pattern visualised for CD44 could be an artefact of the patterning of the membrane due to its adhesion to the cell substrate, in addition to the overexpression of the protein. To rule out the possibility that overexpression of the chimeric SNAP-tagged CD44 protein induces such a distribution, we investigated how endogenous CD44 is organised at the plasma membrane by labelling the protein using anti-CD44 antibody and performing super-resolution stochastic optical reconstruction microscopy (STORM) in fixed CHO cells (Figure 4.2c). Endogenous CD44 at non-adherent membrane of the lamella, away from the adhesion surface, also revealed a meshwork-like pattern of the protein at the meso-scale. Indeed, STORM images revealed a nano-scale clustered distribution of CD44 laid out in a non-random mesoscale mesh-like pattern (see Figure 4.2c). Nearest neighbour distance (NND) analysis on CD44 nanoclusters and cluster size of multiple STORM images further confirmed that these nanoclusters are distributed in a manner distinct from simulated randomised distribution of nanoclusters (Figure 4.2d, d'). Interestingly, we also imaged MEF cells expressing SNAP-CD59-GPI, a GPI anchored protein, unrelated to CD44. Remarkably, HiDenMaps of CD59 revealed a clear meso-scale meshwork pattern on the cell surface similar to that of CD44, suggesting a general compartmentalised state of the plasma membrane (Figure 4.2e). As a whole, the HiDenMaps and the STORM analysis suggest the formation of CD44 nanoclusters that might be organised in a meso-scale meshwork on the plasma membrane.

4.3.2 The dynamic meso-scale meshwork of CD44 is strongly related to its nanoclustering.

STORM imaging of endogenous CD44 in CHO cells as described above, as well as an earlier study (19), provide evidence for the existence of nano-scale clusters of CD44 at the plasma membrane. Moreover, CD44 exhibits spatially confined localisations that emerge as a mesh-like pattern in the HiDenMaps. Together, these observations motivated us to investigate a potential relationship between CD44 nanoclustering and its meso-scale dynamics organisation by combining HiDenMaps with homo fluorescence resonance energy transfer (FRET) microscopy (27).

Fluorescence emission anisotropy-based homo-FRET measurements probe the proximity of fluorescently tagged proteins at a molecular length scale ~Forster's radius (~5 nm for the GFP fluorophore (27)) on the living cell membrane, reporting on molecular interactions at a length scale ~10 times smaller than achievable resolution in STORM. In addition, homoFRET provides information in living cells avoiding any potential artefacts associated to cell fixation, in contrast to STORM or other super-resolution methods. Indeed, this technique has been extensively used to assess the degree of GPI-AP nanoclustering on the surface of living cells (27, 28, 36–38). Moreover, to avoid any potential artefacts associated to high expression levels of CD44 (which would artificially induce nanoclustering) or to ligand-induced nanoclustering, we used COS-7 cells as they have very low surface levels of endogenous CD44 and do not synthesise HA, a major ECM component that can bind CD44 from the extracellular side (34, 36, 37). Using homoFRET, we identified regions of low and high anisotropy in the membrane of unperturbed living COS-7 cells (Figure 4.3a). In here, regions of low anisotropy correspond to the enrichment of CD44-GFP molecules at ≤5 nm intermolecular distances, thus indicating the occurrence of CD44 nanoclustering at a steady state. These results are consistent with the STORM data and agree well with the hotspot regions observed in the HiDenMaps.

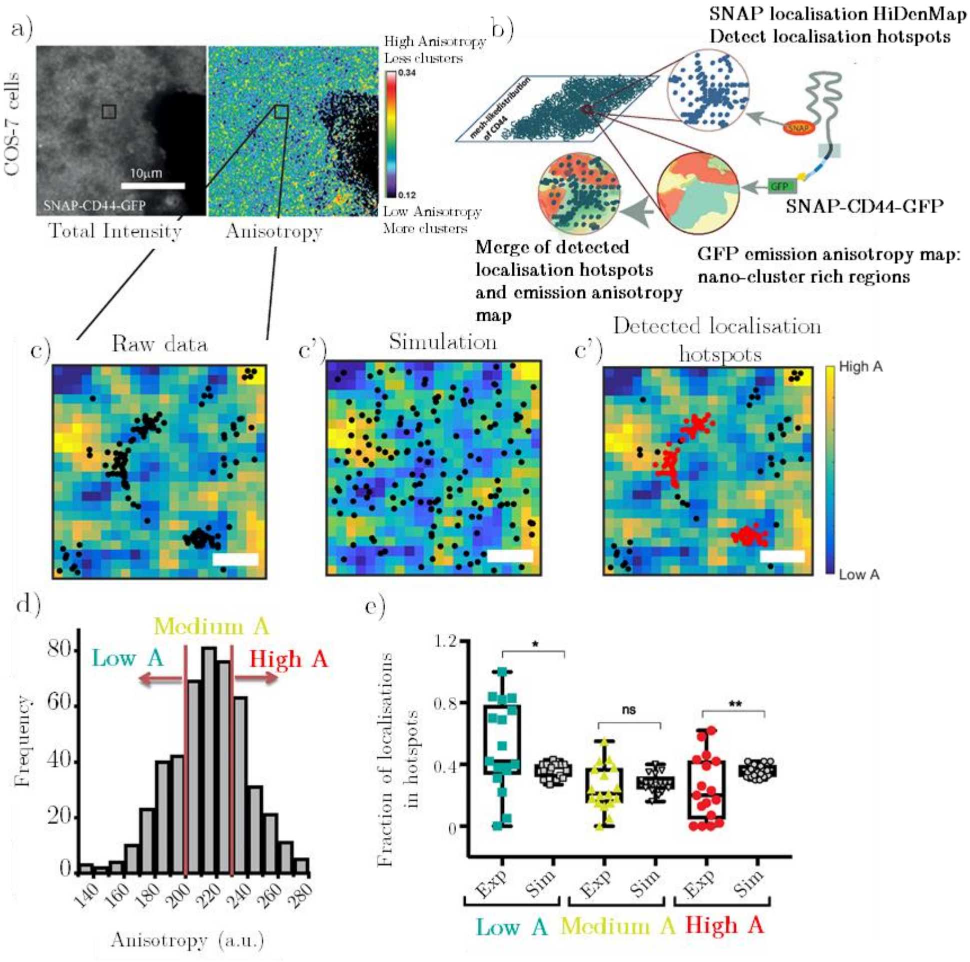

Figure 4.3 Meso-scale meshwork of CD44 colocalises with regions enriched in CD44 nanoclusters. a) Total GFP fluorescence intensity and anisotropy map of the SNAP-CD44-GFP protein expressed in COS-7 cells. Note that the anisotropy image shows regions of low anisotropy (blue) and high anisotropy (red), corresponding respectively, to regions enriched in or depleted of CD44 molecules in nano-scale proximity (CD44 nanoclusters). (b) Schematic depicting the methodology by which FRET based anisotropy maps was correlated to localisation maps obtained from high-density single molecule imaging and HiDenMap analysis. c, c, c'') Representative ROI image depicting the anisotropy map overlaid with localisations from raw HiDenMaps integrated over 40 frames (left), random localisations obtained from simulations (centre), and detected localisation hotspots (red dots) of SNAP-CD44-GFP (right). d) Histogram of the anisotropy values for the ROI shown in c. Red vertical lines indicate the thresholds chosen to classify regions of low anisotropy (Low A), medium anisotropy (Medium A), and high anisotropy (High A), where medium anisotropy is binned around the median value of anisotropy in a given ROI. (e) Fraction of detected localisations in the localisation hotpots in low, medium, and high anisotropy regions compared with simulated random localisations. Each symbol in the plot corresponds to a single ROI, and the data are obtained from at least six different cells from > 15 ROIs. Difference

between distributions has been tested using Kolmogorov–Smirnov test. Adapted from Sil and Mateos et al. (33).

To ascertain the relationship between nano- and meso-scale dynamic organisation of CD44, we expressed the SNAP-CD44-GFP construct in COS-7 cells. In this way, we could obtain FRET-based anisotropy maps from the GFP tag, interleaved with single molecule imaging from the sub-saturation labelled SNAP tag, and thus amenable for generating HiDenMaps. We selected different anisotropy ROIs and superimposed the corresponding spatial coordinates of individual molecules integrated over 40 frames (20 frames preceding and 20 frames following the anisotropy image) (Figure 4.3, b and c). We restricted our analysis to windows of 40 frames around an anisotropy image to reduce temporal variations that might occur between the anisotropy and HiDenMap (see Methods). We then identified spatially restricted enriched localisations, i.e., hotspots on the HiDenMaps, and classified these localisation hotspots according to the corresponding anisotropy value (see Methods and Figure 4.3c, c', c'', and d). A significantly higher fraction of localisation hotspots were found in regions of low anisotropy as compared to simulations of randomised localisations (Figure 4.3e). Concomitantly, such localisation hotspots were consistently depleted from the high anisotropy regions when compared with randomly dispersed localisations. Since the low anisotropy regions correspond to nanoclustering, these data strongly indicate that the meso-scale regions observed on the HiDenMaps coincide with regions of increased nano-scale clustering of the receptor. As a whole, our results reveal a multiscale organisation of CD44 on the cell membrane with the distribution of nano-scale clusters correlated to the meso-scale meshwork.

4.3.3 Meso-scale organisation of CD44 is influenced by its cytoplasmic interactions

Since CD44 nanoclustering is spatially correlated to its meso-scale distribution, we then tested whether alteration in the nanoclustering potential of different CD44 mutants would also affect their meso-scale organisation. For this, our collaborators generated the following constructs: a mutant that lacks the extracellular domain of CD44, denoted as CD44TmICD-GFP; and a mutant with a deletion of the entire intracellular domain in the CD44TmICD-GFP construct to create a transmembrane domain (Tm)-only protein, denoted as

CD44Tm-GFP. SNAP-CD44-GFP, SNAP-CD44TmICD-GFP, and SNAP-CD44Tm-GFP constructs were expressed in MEFs, exogenously labelled, and imaged at a temporal resolution of 100 Hz, as described earlier, in order to generate HiDenMaps of the different constructs (Figure 4.4, a and b). Visual inspection of the HiDenMaps already shows more tightly bound localisations in the case of the full-length receptor whereas a larger number of dispersed localisations were visually apparent on the SNAP-CD44Tm-GFP mutant. Comparison of the confinement areas revealed similar confinement strength for the full-length receptor (0.028 ± 0.013) μm^2 and the mutant lacking the extracellular domain (ECD) (0.027 ± 0.013) μm^2 (Figure 4.4, c and d), indicating that the ECD does not play a major role on the meso-scale organisation of the receptor. Consistent with these results, we did not find significant differences on the fractional number of localisations found on the meshwork between the full-length receptor (SNAP-CD44-GFP) and the mutant lacking the ECD (SNAP-CD44TmICD-GFP) (Figure 4.4e). In contrast, the mutant lacking the cytoplasmic tail as well as the ECD (SNAP-CD44Tm-GFP) exhibited larger confinement areas (0.032 ± 0.013) μm^2 (Figure 4.4, c and d) and a significantly lower number of localisations associated to the meshwork as compared with the full-length receptor (SNAP-CD44-GFP) or the mutant lacking the ECD alone (SNAP-CD44TmICD-GFP) (Figure 4.4e). We also performed similar experiments in HA-deficient COS-7 cells and obtained comparable results (Figure 4.5). As a whole these results strongly indicates that the cytoplasmic domain of CD44 mediates the tight confinement of the receptor at the plasma membrane.

We also performed simulations of random localisations and overlaid them to an experimentally obtained meshwork to obtain a “basal” fraction of localisations that are stochastically found over the meshwork (labelled as random in Figure 4.4e). Comparison with the *in silico*–generated data revealed that even in the absence of the cytoplasmic tail, the SNAP-CD44Tm-GFP mobility is somewhat constrained by this underlying mesh albeit to a much lower extent than the cytoplasmic domain containing counterparts. Therefore, our results strengthen the arguments for cytoplasmic interactions as a major player in orchestrating the nano- and meso-scale organisation of CD44. Since the cytoplasmic tail of CD44 interacts with multiple cytoskeletal adaptor proteins such as ezrin and ankyrin (22, 23, 40, 41), our results suggest that CD44 nanoclustering might be induced by its tethering to the actin cytoskeleton. This finding resonates with the recently published results of CD44 in macrophages where diffusion characteristics of the protein are affected by tethering to the cytoskeleton mediated by ezrin (14) and leads us to investigate the role of the actin cytoskeleton in the nanoclustering as well as in the meso-scale organisation of the protein.

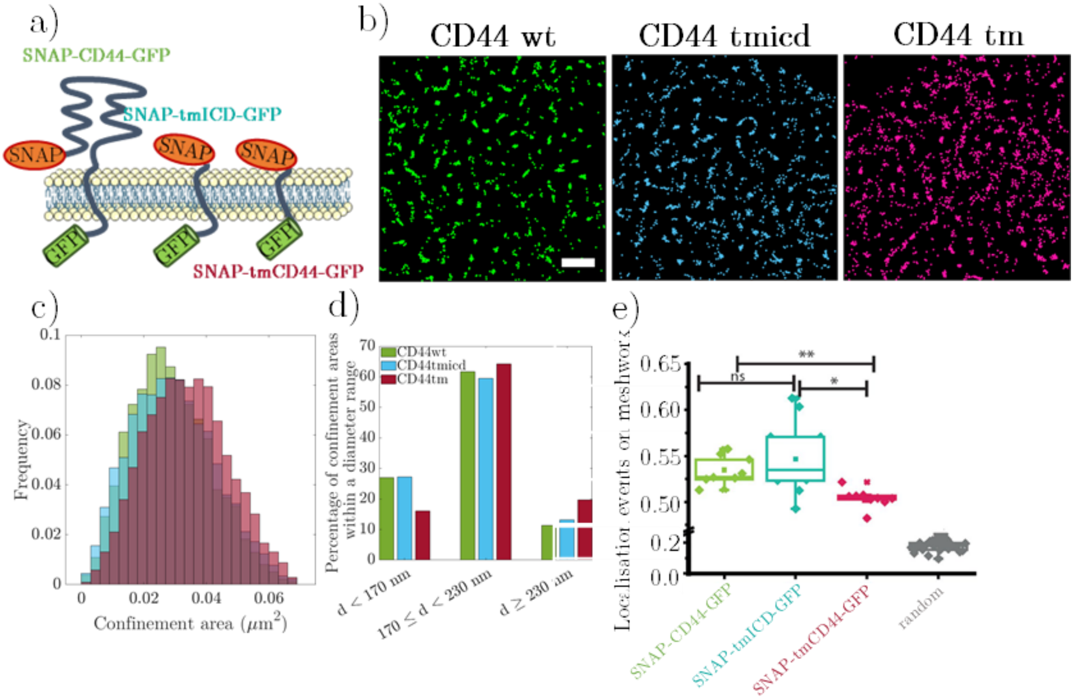

Figure 4.4 Meso-scale organisation of CD44 is determined primarily by interactions of the ICD. a) Schematic drawings of the indicated CD44 constructs. b) Representative HiDenMaps of the indicated CD44 constructs expressed in MEFs obtained from imaging at 100 Hz and accumulating the spatial coordinates of individual molecules over 2 s (20 frames). c) Quantification of the confinement areas for the different constructs during 2 s. Black lines correspond to the mean value. d) Relative fractions of confinement areas for the different constructs, classified as a function of the confinement length, i.e., d < 170 nm, 170 < d < 230 nm, or d > = 230 nm. e) Fraction of localisation events that belong to the meshwork for the different constructs and compared with the fraction of similar type of localisations measured from randomised localisations. The data are from one representative experiment. The experiment has been conducted at least twice with similar results. Data were obtained from a number of cells

expressing SNAP-CD44-GFP (8), SNAP-CD44TmICD-GFP (11), or SNAP-CD44Tm-GFP (9). Adapted from Sil and Mateos et al. (33).

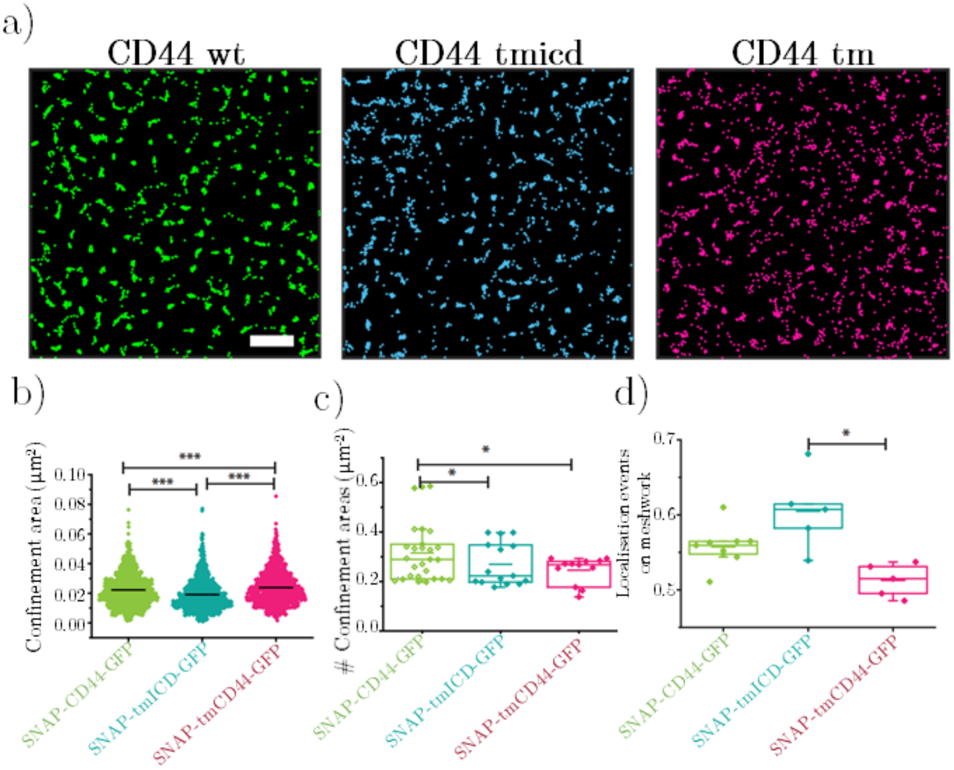

Figure 4.5 : Analysis of the meso-scale organisation of the different constructs in CD44-deficient COS-7 cells. a) HiDenMaps of the indicated SNAP tagged CD44 constructs expressed in CD44-null COS-7 cells, obtained by imaging at 50-100 nM labelling conditions, at 100 Hz and accumulating the spatial coordinates of individual molecules over 2 s period. b) Quantification of the confinement areas for the different constructs over 2 s. Black lines correspond to the mean value. c) Normalised fraction of confinement areas/area for the three different constructs. A significantly lower number of confined regions per unit area are observed in the SNAP-CD44Tm-GFP as compared to the full-length receptor or the mutant lacking the extra-cellular domain. This can also be directly inferred from the HiDenMaps where the localisations are more tightly bound for the full-length receptor and much more disperse in the case of the SNAP-CD44Tm-GFP mutant. d) Fraction of localisation events belonging to the meshwork for the wild type and the mutant construct in COS-7 cells. SNAP-CD44-GFP (n) = 9 cells; SNAP-CD44TmICD-GFP (n) = 6 cells; SNAP-CD44Tm-GFP(n)= 5 cells. Difference between distributions was tested for significance using Kruskal-Wallis and post hoc test with Tukey-Kramer. (b): SNAP-CD44-GFP & SNAP-CD44TmICD-GFP: p<e-9; SNAP-CD44-GFP & SNAP-CD44Tm-GFP: p <e-8, SNAP-CD44TmICD-GFP & SNAP-CD44Tm-GFP: p<e-9. (c): SNAP-CD44-GFP & SNAP-

CD44TmICD-GFP: $p<0.05$; SNAP-CD44-GFP & SNAP-CD44Tm-GFP: $p < 0.05$; SNAP-CD44TmICD-GFP & SNAP-CD44Tm-GFP: $p=0.997$ (ns). (d): SNAP-CD44-GFP & SNAP-CD44TmICD-GFP: $p=0.5386$ (ns); SNAP-CD44-GFP & SNAP-CD44Tm-GFP: $p = 0.0855$ (ns); SNAP-CD44TmICD-GFP & SNAP-CD44Tm-GFP: $p< 0.005$. Adapted from Sil and Mateos et al. (33).

4.3.4 Meso-scale organisation and turnover of CD44 is regulated by formin-nucleated actin dynamics

The diffusion of CD44 has been suggested to be sensitive to formin-generated actin filaments (14)since upregulation of Rho activity (which in turn regulates formin activity) influences the diffusion behaviour of CD44. To test which actin nucleation machinery is responsible for CD44 nanoclustering, we inhibited formin- and Arp2/3-mediated actin filament-nucleation activity in CHO cells using small molecule inhibitors, SMI-FH2 and CK-666, respectively (33). HomoFRET experiments performed by our collaborators showed that CD44 nanoclustering was much more sensitive to inhibition of formin nucleation as compared with Arp2/3 perturbation (33). These results indicate that formin-nucleated F-actin filaments not only influence the mobility of the receptor as reported previously (14) but importantly, also promotes its nanoclustering and, as a consequence, may also influence its meso-scale organisation.

To ascertain the effect of formin perturbation on the meso-scale meshwork, we conducted high-density SPT of SNAP-CD44-GFP in COS-7 cells before and after formin perturbation and built up HiDenMaps in both conditions. Our results show that meso-scale meshwork of CD44 is perturbed in formin-perturbed cells. Although the confinement area distribution is not significantly altered in formin-perturbed cells as compared to the vehicle (dimethylsulfoxide [DMSO])-treated cells (Figure 4.6a), the fraction of localisation events detected along the meshwork in formin-inhibited cells was significantly reduced (Figure 4.6b), which is reminiscent of the distribution of the SNAP-CD44Tm-GFP that lacks both the cytoplasmic and the exoplasmic domains and is also defective in nanoclustering.

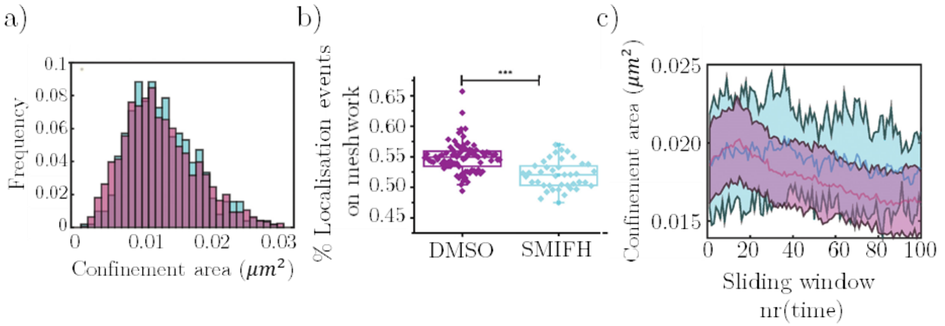

Figure 4.6 Formin-mediated actin polymerisation affects the meso-scale distribution and turnover of CD44. a) Plot depicting confinement area size of the meso-scale domains in formin-perturbed cells (cyan) compared with untreated ones (magenta). b) Fraction of localisations detected on the meshwork in control cells (DMSO) compared to formin-inhibited condition ($p < e\text{-}8$). c) Temporal evolution of meso-scale domains on control (DMSO) vs. formin inhibitor treatment. The x-axis depicts time as 2 s sliding window (depicted as frame number) and the y-axis depicts confinement area. (DMSO [n] = 12 cells, SMIFH2 [n] = 9 cells). Adapted from Sil and Mateos et al. (33).

A striking difference in the formin-inhibited cells compared with the untreated cells was in the turnover time of the meso-scale domains. Time evolution analysis of the meso-scale domains revealed that while untreated (vehicle-treated) cells exhibited a visible disassembly/reorganisation of the mesoscale domains, formin-inhibited cells exhibited a marked persistence of meso-scale domains (Figure 4.6c) during the observed time window. These results indicated that dynamic remodelling of the meso-scale meshwork is dependent on formin activity, consistent with the suggestion that formin-driven actin polymerisation is a key contributor to dynamic remodelling of the actin meshwork (42).

4.4 Discussion

CD44 has a multitude of extracellular and cytoplasmic interactions that makes it an ideal candidate for studying regulation of the organisation of a typical transmembrane protein. Here we have used non-invasive methods to study nanoclustering and dynamics of CD44 using live-cell compatible techniques such as homo-FRET imaging and SPT methods to generate spatial maps of the protein at the plasma membrane at the nano- and meso-scale. Previous studies have attempted to understand CD44 organisation by multiple approaches, from characterising graded distribution of GP-80 in motile fibroblasts (43) to super-resolution imaging wherein CD44 was found clustered at the cell membrane using STORM, and extracellular galectins were found to be responsible for their nanoclustering (19). In another study, the intracellular domain was implicated in supporting mobile clusters at the membrane based on hetero-FRET measurements, brightness number analysis, and biochemical cross-linking studies in mammalian cells (44). In a more recent study, SPT on CD44 revealed that CD44 diffusion is confined to pickets and fences and may indeed determine the corralling of other membrane proteins such as the FcγRIIA (14).

The results reported here provide a comprehensive understanding of the organisation of CD44 by combining the determination of distribution and diffusion behaviour of the protein across varying spatial scales at the plasma membrane of living cells. HiDenMap analysis (to probe the meso-scale organisation of the protein) and its correlation with anisotropy measurements (reporting on nanoclustering), for the first time, bridge the gap between SPT-based diffusion studies and the steady-state nanocluster detection method of homo-FRET. Complemented with the HiDenMap analysis of single particle localisations and nanocluster distribution in STORM images, the combination of these approaches enabled us to build a hierarchical framework for the organisation of a type-1 transmembrane protein at the plasma membrane (Figure 4.7). Together with additional experiments performed by our collaborators not shown in here but included in our joint publication (33), we found that CD44 nanoclusters depend on the actomyosin machinery. CD44 actomyosin templated nanoclusters spatially enrich the receptors along a mesoscopic meshwork pattern, laid down by frequent localisations of the protein at the plasma membrane. These nanoclusters resemble actomyosin-based clusters observed for model transmembrane proteins with actin-binding domains (45, 46).

The correlation between nano-scale and meso-scale organisation of the protein reported in this Chapter reconciles the apparent heterogeneity in diffusion modes retrieved when performing SPT of CD44 (14, 33). From our meso-scale organisation and SPT studies reported in Ref. 33, the regions on the membrane where the receptors are transiently confined/ temporarily arrested correspond to regions of increased receptor localisation as well as potentially localisation hotspots. These regions have an area ~100–300 nm, outlining a fragmented meshwork-like pattern. Moreover, the timescale of turnover of localisation hotspots (Figure 4.6c) corresponds to the timescale of transient confinement of single molecules of CD44 (~few < 3 s (33)). Thus, the receptor transiently associates with such regions and eventually unbinds to diffuse again, often guided by the underlying actin cytoskeleton-laid fences, until it encounters another suitable site at the membrane-cytoskeleton interface to be arrested again. Thus, we propose that our localisation hotspots could correspond to the picket fences described earlier (47, 48).

To ascertain whether actin dynamics-driven mechanisms could template the nano- and the meso-scale organisation of CD44, we investigated the role of formin nucleation-based actin polymerisation. As nanoclustering of CD44 is lost on formin perturbation, we also observe concomitant lowering of the CD44 localisations detected on the underlying meshwork. This is reminiscent of the Tm of CD44 (CD44Tm-GFP) that cannot bind to actin. Additionally, the meso-scale domain turnover is remarkably slowed down. This is consistent with previous studies that implicate the role of formin activity in the turnover of the underlying cortical actin meshwork (42). These findings lead us to an important conclusion: the meso-scale spatiotemporal meshwork of CD44 arises as a consequence of the association of CD44 with the underlying actin cortex, and it is likely that the formin-mediated actin nucleation and turnover of the cortical actin meshwork contribute to the pool of dynamic actin necessary to template the nanoclustering of the protein as proposed previously (45). This also provides a natural explanation for the enrichment of CD44 nanoclusters along the meso-scale mesh, which appears to mirror the cortical actin cytoskeleton mesh. At this time, it should be noted that further experiments are necessary to prove the relationship between the cortical actin meshwork and the mesoscale meshwork of CD44.

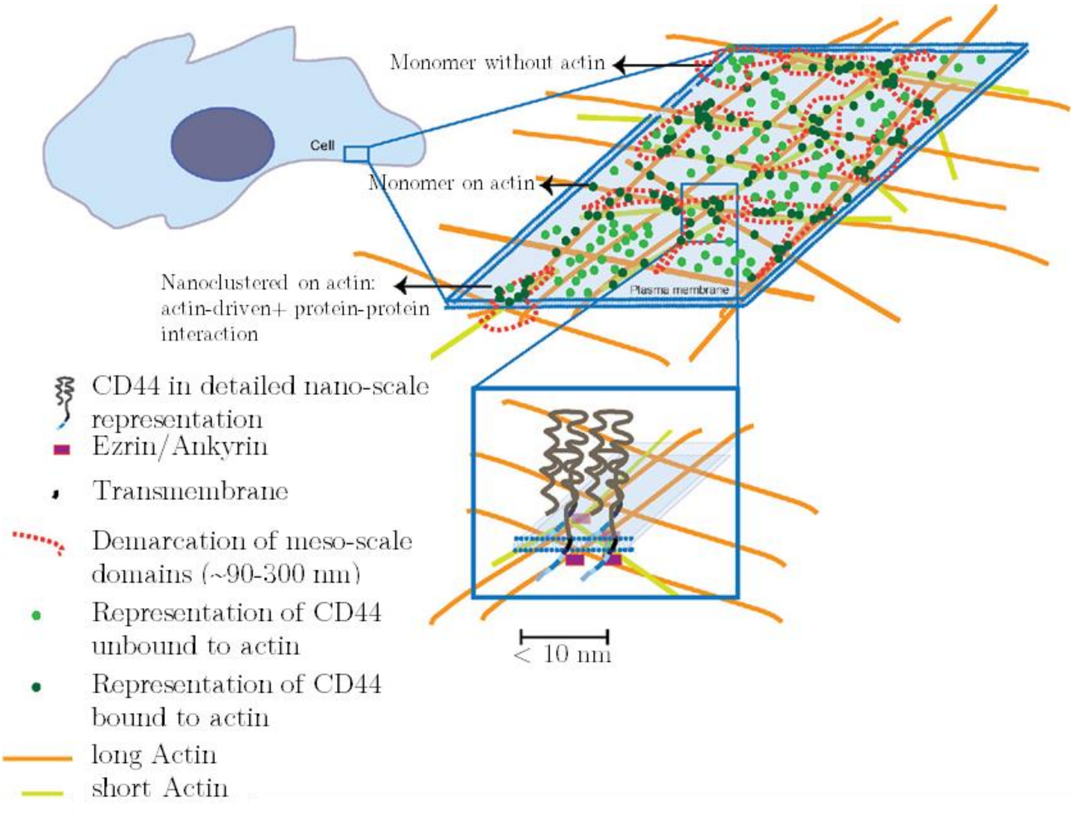

Figure 4.7 Proposed model for plasma membrane organisation of CD44. In the cell membrane a ROI is outlined to show the distribution of monomers as well as clusters of CD44 receptors. Nanoclustered receptors are shown coupled to actin cytoskeletal elements by adaptors such as ezrin/ankyrin (see zoomed-in nanocluster) interspersed with unattached CD44 molecules. The clusters of receptors are depicted as being driven by the action of formin polymerised actin filaments and myosin driven actin motility (molecules not depicted in the schematic). The meso-scale domains are CD44 localisation hotspots identified in our experiment that are characterised by their close association with nanoclusters of the protein. The emerging meso-scale meshwork of the cell membrane receptor (depicted by the orange dotted line) may reflect the cytoskeletal meshwork juxtaposed to the plasma membrane. Adapted from Sil and Mateos et al. (33).

Nanoclustering of CD44 is also abrogated on removal of the cytoplasmic domain of CD44 (33). This finding is further supported by cytoskeletal sensitivity of nanoclustering of the protein. The sensitivity of CD44 nanoclustering particularly to formin and ezrin perturbation is well aligned with the changes in CD44 diffusion on similar perturbations, observed in SPT recently (14). In that study, formin- and ezrin-mediated picketing function of CD44 had been implicated in regulating FcγRIIA dynamics and function in phagocytosis.

Involvement of similar molecular machinery in nanoclustering, as reported here, strongly suggests that the picketed CD44 receptors are nanoclustered by the underlying dynamic actin filaments generated as a consequence of formin-driven actin polymerisation, and driven by myosin activity.

In this study, we have attempted to gain insights into specific interactions mediated by the ECD and ICD of CD44 in determining its diffusion and organisation at the cell membrane. We find a strong correlation between nanoclustering potential and the tethering strength for the different truncation mutants of CD44 at the cell surface. Although removal of the ECD has little effect on the confinement radius of CD44, removal of the ICD from the mutant already lacking the ECD (CD44Tm-GFP) has a stronger effect on its confinement as well as localisation on the meshwork at the mesoscale (Figure 4.4e and Figure 4.5d). The ICD thus emerges as a stronger determinant for tighter confinement of CD44 at the membrane and as the domain that augments the registry of the mesoscale distribution with a meshwork pattern. Together with the result suggesting that the ECD deleted mutant still exhibits acto–myosin-sensitive nanoclustering, we believe that the meso-scale organisation is templated on an underlying cortical actin mesh and serves to orchestrate the emergence of transient nanoclusters in its proximity (33).

The meshwork pattern that we observe may have a larger significance, since SNAP-CD44Tm-GFP and SNAP-CD59-GPI, proteins that are not directly coupled to actin, also exhibit a meshwork-like appearance at the meso-scale. FcγRIIA, which cannot interact with actin but associates with a CD44 defined mesh (14), also exhibits a spatially restricted diffusion pattern and non-random diffusion at the meso-scale. This is likely to be mediated via lateral association of their membrane anchoring domains with actin-binding membrane pickets, or confinement within membrane compartments demarcated by picketing proteins. These data support the picture of a tightly coupled actin-membrane composite where even proteins that do not couple to actin are impacted by the patterning of the underlying meshwork.

With further sophistication of imaging and analysis methods, the correlation of HiDenMap and anisotropy can be studied with higher temporal resolution. While our study is currently restricted to cytoskeletal interactions of CD44, there remains scope for detailed analysis of the influence of the exo-plasmic interactions with molecules such as galectins and HA. Simultaneous imaging of signalling and cytoskeletal adaptors along with CD44 can open up possibilities for exploring potential outside-in (ligand binding can lead to signalling adaptor recruitment) as well as inside-out signalling (ankyrin binding can influence hyaluronic acid binding; (49)) at the nano- and meso-scale domains. Since CD44 is implicated in processes such as metastasis, phagocytosis, or lymphocyte rolling (41, 50–52), they provide physiologically relevant scenarios where local and global organisation of CD44 may have an impact on relevant physiological scenarios. Indeed, in Chapter 6 of this thesis we provide evidence on the coupling of CD44 and galectins to regulate the ability of a pathogen recognition receptor (DC-SIGN) to capture viruses such as HIV-1 and SARS-CoV-2 on cells of the immune system.

We believe that the spatial organisation of CD44, determined by the dynamic remodelling of the actin cytoskeleton, defines dynamic fences that partition the receptor in different regions of the cell membrane. These fences have been implicated in the phagocytic function of FcγRIIA and the endocytic capacity of DC-SIGN, which are transmembrane receptors that do not exhibit direct interaction with the actin cytoskeleton (14, 30). In conclusion, our approach and findings provide a multiscale view of organisation of a transmembrane protein at the cell membrane, revealing a hierarchical framework where actomyosin-driven nanoclusters emerge in close association with an underlying dynamically remodelling meso-scale meshwork, enabling the cells to spatiotemporally regulate receptor organisation.

4.5 References

1. E. Sezgin, I. Levental, S. Mayor, C. Eggeling, The mystery of membrane organization: Composition, regulation and roles of lipid rafts. *Nat. Rev. Mol. Cell Biol.* **18** (2017).
2. M. F. Garcia-Parajo, A. Cambi, J. A. Torreno-Pina, N. Thompson, K. Jacobson, Nanoclustering as a dominant feature of plasma membrane organization. *J. Cell Sci.* **127** (2014).
3. A. Kusumi, H. Ike, C. Nakada, K. Murase, T. Fujiwara, Single-molecule tracking of membrane molecules: Plasma membrane compartmentalization and dynamic assembly of raft-philic signaling molecules. *Semin. Immunol.* **17** (2005).
4. E. Klotzsch, G. J. Schütz, A critical survey of methods to detect plasma membrane rafts. *Philos. Trans. R. Soc. B Biol. Sci.* **368** (2013).
5. T. S. van Zanten, S. Mayor, Current approaches to studying membrane organization. *F1000Research* **4** (2015).
6. M. C. Overton, K. J. Blumer, G-protein-coupled receptors function as oligomers in vivo. *Curr. Biol.* **10** (2000).
7. S. Terrillon, M. Bouvier, Roles of G-protein-coupled receptor dimerization. *EMBO Rep.* **5** (2004).
8. E. G. Hofman, *et al.*, Ligand-induced EGF receptor oligomerization is kinase-dependent and enhances internalization. *J. Biol. Chem.* **285** (2010).
9. K. Beck-García, *et al.*, Nanoclusters of the resting T cell antigen receptor (TCR) localize to non-raft domains. *Biochim. Biophys. Acta - Mol. Cell Res.* **1853** (2015).
10. P. O. Strale, *et al.*, The formation of ordered nanoclusters controls cadherin anchoring to actin and cell-cell contact fluidity. *J. Cell Biol.* **210** (2015).
11. S. V. Pageon, *et al.*, Functional role of T-cell receptor nanoclusters in signal initiation and antigen discrimination. *Proc. Natl. Acad. Sci. U. S. A.* **113** (2016).
12. L. Martínez-Muñoz, *et al.*, Separating Actin-Dependent Chemokine Receptor Nanoclustering from Dimerization Indicates a Role for Clustering in CXCR4 Signaling and Function. *Mol. Cell* **70** (2018).
13. A. Kusumi, Y. Sako, Cell surface organization by the membrane skeleton. *Curr. Opin. Cell Biol.* **8** (1996).
14. S. A. Freeman, *et al.*, Transmembrane Pickets Connect Cyto- and Pericellular Skeletons Forming Barriers to Receptor Engagement. *Cell* **172**, 305-317.e10 (2018).
15. A. Kusumi, K. G. N. Suzuki, R. S. Kasai, K. Ritchie, T. K. Fujiwara, Hierarchical mesoscale domain organization of the plasma membrane. *Trends Biochem. Sci.* **36** (2011).
16. H. Ponta, L. Sherman, P. A. Herrlich, CD44: From adhesion molecules to signalling regulators. *Nat. Rev. Mol. Cell Biol.* (2003) https:/doi.org/10.1038/nrm1004.

17. L. T. Senbanjo, M. A. Chellaiah, CD44: A multifunctional cell surface adhesion receptor is a regulator of progression and metastasis of cancer cells. *Front. Cell Dev. Biol.* **5** (2017).
18. M. T. Howes, *et al.*, Clathrin-independent carriers form a high capacity endocytic sorting system at the leading edge of migrating cells. *J. Cell Biol.* **190** (2010).
19. R. Lakshminarayan, *et al.*, Galectin-3 drives glycosphingolipid-dependent biogenesis of clathrin-independent carriers. *Nat. Cell Biol.* (2014) https:/doi.org/10.1038/ncb2970.
20. S. P. Thankamony, W. Knudson, Acylation of CD44 and its association with lipid rafts are required for receptor and hyaluronan endocytosis. *J. Biol. Chem.* **281** (2006).
21. B. Shao, *et al.*, O-glycans direct selectin ligands to lipid rafts on leukocytes. *Proc. Natl. Acad. Sci. U. S. A.* **112** (2015).
22. P. Mrass, *et al.*, CD44 Mediates Successful Interstitial Navigation by Killer T Cells and Enables Efficient Antitumor Immunity. *Immunity* **29** (2008).
23. L. Y. W. Bourguignon, Hyaluronan-mediated CD44 activation of RhoGTPase signaling and cytoskeleton function promotes tumor progression. *Semin. Cancer Biol.* **18** (2008).
24. S. S. Skandalis, I. Kozlova, U. Engström, U. Hellman, P. Heldin, Proteomic identification of CD44 interacting proteins. *IUBMB Life* **62** (2010).
25. P. A. Gómez-García, E. T. Garbacik, J. J. Otterstrom, M. F. Garcia-Parajo, M. Lakadamyali, Excitation-multiplexed multicolor superresolution imaging with fm-STORM and fm-DNA-PAINT. *Proc. Natl. Acad. Sci. U. S. A.* (2018) https:/doi.org/10.1073/pnas.1804725115.
26. D. Sinnecker, P. Voigt, N. Hellwig, M. Schaefer, Reversible photobleaching of enhanced green fluorescent proteins. *Biochemistry* **44** (2005).
27. S. Ghosh, S. Saha, D. Goswami, S. Bilgrami, S. Mayor, "Dynamic imaging of homo-FRET in live cells by fluorescence anisotropy microscopy" in *Methods in Enzymology*, (2012).
28. P. Sharma, *et al.*, Nanoscale Organization of Multiple GPI-Anchored Proteins in Living Cell Membranes. *Cell* **116** (2004).
29. J. C. Crocker, D. G. Grier, Methods of digital video microscopy for colloidal studies. *J. Colloid Interface Sci.* **179** (1996).
30. J. A. Torreno-Pina, *et al.*, Enhanced receptor-clathrin interactions induced by N-glycan-mediated membrane micropatterning. *Proc. Natl. Acad. Sci.* **111**, 11037–11042 (2014).
31. S. Gerecht, *et al.*, Hyaluronic acid hydrogel for controlled self-renewal and differentiation of human embryonic stem cells. *Proc. Natl. Acad. Sci. U. S. A.* **104** (2007).
32. H. Siiskonen, S. Oikari, S. Pasonen-Seppänen, K. Rilla, Hyaluronan synthase 1:

A mysterious enzyme with unexpected functions. *Front. Immunol.* **6** (2015).

33. P. Sil, *et al.*, Dynamic actin-mediated nano-scale clustering of CD44 regulates its meso-scale organization at the plasma membrane. *Mol. Biol. Cell* **31**, 561–579 (2020).
34. W. Knudson, E. Bartnik, C. B. Knudson, Assembly of pericellular matrices by COS-7 cells transfected with CD44 lymphocyte-homing receptor genes. *Proc. Natl. Acad. Sci. U. S. A.* **90** (1993).
35. A. M. Shyjan, P. Heldin, E. C. Butcher, T. Yoshino, M. J. Briskin, Functional cloning of the cDNA for a human hyaluronan synthase. *J. Biol. Chem.* **271** (1996).
36. D. Goswami, *et al.*, Nanoclusters of GPI-Anchored Proteins Are Formed by Cortical Actin-Driven Activity. *Cell* **135** (2008).
37. R. Varma, S. Mayor, GPI-anchored proteins are organized in submicron domains at the cell surface. *Nature* **394** (1998).
38. S. Saha, *et al.*, Active emulsions in living cell membranes driven by contractile stresses and transbilayer coupling. *Proc. Natl. Acad. Sci. U. S. A.* **119**, e2123056119 (2022).
39. C. Yang, *et al.*, The high and low molecular weight forms of hyaluronan have distinct effects on CD44 clustering. *J. Biol. Chem.* **287** (2012).
40. T. Mori, *et al.*, Structural basis for CD44 recognition by ERM proteins. *J. Biol. Chem.* **283** (2008).
41. S. Donatello, *et al.*, Lipid raft association restricts CD44-ezrin interaction and promotion of breast cancer cell migration. *Am. J. Pathol.* **181** (2012).
42. M. Fritzsche, A. Lewalle, T. Duke, K. Kruse, G. Charras, Analysis of turnover dynamics of the submembranous actin cortex. *Mol. Biol. Cell* **24** (2013).
43. A. Ishihara, B. Holifield, K. Jacobson, Analysis of lateral redistribution of a plasma membrane glycoprotein-monoclonal antibody complex [corrected]. *J. Cell Biol.* **106** (1988).
44. Y. Wang, *et al.*, Cytoskeletal regulation of CD44 membrane organization and interactions with E-selectin. *J. Biol. Chem.* **289** (2014).
45. A. Chaudhuri, B. Bhattacharya, K. Gowrishankar, S. Mayor, M. Rao, Spatiotemporal regulation of chemical reactions by active cytoskeletal remodeling. *Proc. Natl. Acad. Sci. U. S. A.* **108** (2011).
46. K. Gowrishankar, *et al.*, Active remodeling of cortical actin regulates spatiotemporal organization of cell surface molecules. *Cell* **149** (2012).
47. K. Murase, *et al.*, Ultrafine membrane compartments for molecular diffusion as revealed by single molecule techniques. *Biophys. J.* **86** (2004).
48. T. K. Fujiwara, *et al.*, Confined diffusion of transmembrane proteins and lipids induced by the same actin meshwork lining the plasma membrane. *Mol. Biol. Cell* **27** (2016).
49. Z. Dan, L. Y. W. Bourguignon, Interaction between CD44 and the repeat

domain of ankyrin promotes hyaluronic acid-mediated ovarian tumor cell migration. *J. Cell. Physiol.* **183** (2000).
50. A. Hill, *et al.*, Cortactin underpins CD44-promoted invasion and adhesion of breast cancer cells to bone marrow endothelial cells. *Oncogene* **25** (2006).
51. M. Hanke-Roos, *et al.*, CD44 mediates the catch-bond activated rolling of HEPG2Iso epithelial cancer cells on hyaluronan. *Cell Adhes. Migr.* **11** (2017).
52. E. Vachon, *et al.*, CD44 is a phagocytic receptor. *Blood* **107** (2006).

Chapter 5

Quantitative High-Density Maps

High-density maps (HiDenMaps) obtained from high-density single particle tracking (HD-SPT) data allow to investigate how molecules dynamically explore their surroundings. In this Chapter, we present a palette of analysis tools to extract relevant quantitative information from HiDenMaps. We focused our studies on the prototypical transmembrane receptor CD44, that interacts with the underlying cortical actin cytoskeleton and the extracellular milieu. The HiDenMaps of this receptor revealed meshwork-like patterns that arise from multiple single molecule interactions with the environment. Using multiple constructs of CD44 having different affinities to bind actin, we revealed that the mesoscale dynamics of CD44 correlates with its ability to bind to actin. Moreover, we correlated the nanoscale dynamics of CD44 with its mesoscale spatiotemporal organisation. Finally, using HiDenMaps we revealed a spatiotemporal compartmentalisation at three distinct temporal scales most probably arising from the interaction of the receptor with its environment, but also importantly, from dynamic changes of the environment itself. Overall, HiDenMaps promise to become an incredibly useful tool to study the spatiotemporal organisation of molecules in living cells due to its simplicity and potential in terms of analysis.

This work has been published as **Nicolas Mateos**[†], Parijat Sil[†], Sankarshan Talluri, Satyajit Mayor, Carlo Manzo, and Maria F. Garcia-Parajo, "HiDenMaps: a biophysical tool to understand the interactions of single molecules with their environment", *in preparation*. [†]Equally contributing authors.

5.1 Introduction

The advent of high-density single particle tracking (HD-SPT) approaches has increased significantly the number of individual trajectories that could be retrieved on a single experiment (1, 2). First applications of HD-SPT by means of spt-PALM(1) (single particle tracking photo-activated localisation microscopy) have revealed the dynamics of individual integrins within and outside focal adhesions(3), contributed to the understanding of how AMPA receptors are spatiotemporally organized inside synapses(4) and provided insights on how TNF-α influences the lateral dynamics of TNF receptor I in living cells(5). These examples demonstrate the potential of HD-SPT to correlate the dynamics of single molecules with their environment and to generate a general view on how the diffusion of individual molecules depends on their surroundings.

Parallel to the development of HD-SPT, several groups started to address the issue of membrane heterogeneity and how to infer the forces applied to molecules from individual trajectory data(6, 7). Later, inference Bayesian methods found on HD-SPT the perfect source of trajectories in order to generate diffusion, force and potential-well maps of the plasma membrane(8–10). More complex analytical tools that include variational Bayesian approaches together with a hidden Markov model have been also developed to deal with the short length of the trajectories obtained by sptPALM (11). This analytical approach allows in principle to reveal multiple diffusive states and their transition rates of short single-molecule trajectories of intracellularly diffusing proteins, and it has been applied to study diffusive states of intracellular RNA (11). These works show the potential of HD-SPT data, yet, they still rely on reconnecting trajectories (which can be very short) which in turns requires the use of specific labelling, either with photo-activatable fluorescent probes as used for sptPALM, or by means of stochastic labelling used for universal point accumulation for imaging in nanoscale topography (uPAINT).

In previous chapters we have presented an alternative approach to HD-SPT analysis workflows that allows to explore the full membrane in few seconds, by generating high density maps (HiDenMaps). HiDenMaps can be generated with any standard single molecule-compatible fluorophore and the time required to record a full set of data is faster than for sptPALM and uPAINT experiments. Moreover, HiDenMaps are simple to generate and compatible with other techniques, such as fluorescence resonance energy transfer between identical fluorophores homo-FRET as shown in Chapter 4 and Ref(12). Although other groups have already generated HiDenMaps from their HD-SPT data (1, 2, 4, 9, 13, 14) they have mostly focused on generating trajectories and extracting relevant information from them.

We have already shown that HiDenMaps can readily reveal how molecules explore the space and interact with their environment. However, we have not yet demonstrated the full potential of HiDenMaps. In this chapter, we present a set of methodologies to exploit the data retrieved by HiDenMaps in the context of molecules interacting with the underlying cortical actin network. We have adapted algorithms used in super-resolution single molecule localisation microscopy (SR-SMLM) and exploited the temporal information encoded in the localisations of HiDenMaps. We have studied the spatial patterns of the transmembrane receptor CD44 which are built dynamically over time and computed multiple typical temporal scales that range from the single molecule dynamics to the mesoscale dynamics of the patterns. Moreover, we present the potential of using correlative HiDenMaps with SPT to correlate single molecule dynamics with the mesoscale spatiotemporal organisation of the molecular environment.

5.2 Materials and Methods

5.2.1 **Primary cell culture**

Human immature dendritic cells (iDCs) were obtained from the peripheral blood mononuclear cells (PBMC) from HIV-1-seronegative donors using a Ficoll-Hypaque gradient (Alere Technologies AS). The monocyte population was selected by adherence on a T75cm^2 flask for 1 hour. iDCs were obtained by culturing the monocytes in complete RPMI with 1.000 IU/ml GM-CSF (granulocyte-macrophage colony-stimulating factor) and IL-4 (interleukin-4) both from R&D for 6 days. The medium was replaced every two days with fresh GM-CSF and IL-4. Experiments were performed at day 6 from the monocyte extraction.

5.2.2 tmABD and tmRA cell preparation

TrVb1 cells (Chinese hamster ovary (CHO) cells expressing human transferrin receptor) stably expressing FR-TmEz (tmABD) or FR-TmEz*(tmRA) were cultured in Ham's-F12 media (HF-12) (HiMedia, Mumbai, India), supplemented with 10% fetal bovine serum (FBS) (GibcoTM, 16000044), cocktail of Penicillin, Streptomycin, L-Glutamine (PSG) (Sigma, G1146-100ml), Geneticin (200ug/ml) and Hygromycin (100ug/ml) at 37° C and 5% CO2. For imaging, cells were seeded on glass coverslip fitted 35mm cell culture dishes and grown in Ham's-F12 media (with PSG but without selection antibiotics) for 2 days. Cells were labelled using MOV F(ab) fragment (a generous gift from Dr. Mariangela Figini, Dipartimento di Ricerca Applicata e Sviluppo Tecnologico (DRAST), Fondazione IRCCS Istituto Nazionale dei Tumori, Milan ITALY) was conjugated with STAR-635 (Abberior ST635). MOV F(ab) specifically recognizes and binds to the FR domain of the receptor. The labelling concentration was ~50-100 nM. MOV-635 was diluted in 10% FBS containing phenol red free HF-12 and incubated at 37° C, 5% CO_2 for 5 minutes. Cells were washed and imaged in HEPES buffer containing 2mg/ml glucose, in a stage top incubator, set to 37° C.

5.2.3 Supported Lipid Bilayers composition.

No. 1 Coverslips (CS 25R/ 64-0705, Warner Instruments), were sonicated with Hellmanex III (0.5%) for 40 min followed by 5M KOH for 10 min. The glass was washed extensively in MilliQ after each treatment. The glass was then dried under N_2 and stored in a desiccator until further use. Just before making the bilayer, a coverslip was taken out of the desiccator, a cylindrical chamber (made from a cut PCR tube) was stuck on to the coverslip with transparent UV glue. The coverslip was then placed in an Ozone/UV cleaner for 15 min after which it was washed with PBS. Small Unilamellar Vesicles with DOPC (98%) and NiNTA-DGS(2%) were prepared in advance according to the protocols mentioned in (15). 2uL of 4mM SUVs were added to the chambers and were incubated for 15 min. The unbound vesicles were washed off with buffer. The coverslip was incubated with 0.1mg/ml of beta-Casein for 10 min to block the exposed surfaces where vesicles did not form a bilayer which was subsequently washed off. HSE-RA (a SNAP-tagged version of the construct HYE-R579A used in Ref. (15)) was used as a bilayer marker. HSE-RA has a Deca-His tag which allows it to bind to the Nickel containing lipids on the bilayer and a SNAP tag for visualization, which was labelled with JF-549. HSE-RA was added to the bilayer at a final concentration of 100 picomolar and allowed to bind for 40 min before washing it off. PCA/PCD/Trolox described in Ref. (16) were added at 4mM, 125nM and 2mM respectively to reduce photo-bleaching and triplet state transitions.

5.2.4 Monte Carlo *in-silico* simulations of molecules diffusing with Brownian motion.

We performed Monte Carlo simulations of 2D Brownian diffusing molecules with diffusion coefficient D. We define our imaging region to be a square of side L=256 pixels (100 nm per pixel) and to avoid edge effects, we randomly place 1500 molecules in a 356-by-356 pixels grid, with the centre being our imaging region. The total observation time is set to 1000 seconds and the frame rate to 100 Hz. For the diffusion, at each temporal step molecules are displaced according to a normal distribution $\delta xy \sim N(0, \sqrt{2 \cdot dt \cdot D})$. While diffusing, molecules cannot interact with each other. In the case of results showing slower frame rates than 100 Hz, we have down-sampled the data from the 100 Hz. With this, we are capable of generating multiple sub frame rate simulations from a fast simulation.

5.2.5 Monte Carlo *in-silico* simulations of diffusing molecules interacting with an imposed network.

These simulations add a layer of complexity to the Brownian diffusing simulations. We generate an imposed network in our simulations that molecules can interact with. The imposed network consists of a Voronoi network with 0.5 μm^2 mean patch size and a filament thickness of 10 nm (similar to actin). We define the space in the same way as for the Brownian motion simulation, as well as the number of diffusing molecules, observation time and frame rate. For the simulation itself, molecules diffuse randomly (Brownian motion with $\delta xy \sim N(0, \sqrt{2 \cdot dt \cdot D})$ within the patches of the imposed network. However, when a step δxy crosses a filament or ends on the filament, then the molecule has a certain probability, $0 < P_{bind} \leq 1$, to bind. The interaction is determined by randomly generating a number from a uniform distribution between 0 and 1. If the number is smaller than P_{bind}, then the interaction takes place. Else, the molecule proceeds with its Brownian motion. The interaction with the network consists on staying on the network for a time that is given by an exponential probability distribution with $\lambda = \tau_{inter}$. After this time, the molecule can rebind (interact again) to the network with a probability, $0 < P_{rebind} \leq 1$. If the molecule actually rebinds to the network, then it would again spend some time in the network as before. For our simulations, we studied two scenarios: either not rebinding at all or rebind with $P_{bind} = P_{rebind}$. We repeat this process for all the simulated molecules for the total observation time (1000 s) and at a frame rate of 100Hz. Finally, once all the trajectories have been generated we add white Gaussian noise to all localisations with a standard deviation of 20 nm to account for the localisation accuracy.

5.2.6 **Simultaneously obtained single particle tracking and HiDenMaps.**

We performed the experiments in CHO cells and labelled CD44 with a SNAP-tag JF560 and JF640. The imaging was performed on a home-built total internal reflection (TIRF) microscope which consists on a Nikon Eclipse Ti body and a Nikon 100X Apochromat 1.49 (NA) objective. The set-up is equipped with two high-speed CMOS camera (FASTCAM-SA1,Photron, Tokyo – Japan - (17–19)) coupled to a two-stage micro-channel plate intensifier (C8600-03, Hamamatsu Photonics, Hamamatsu, Japan) by means of an optical-fibre bundle. The imaging was performed at a frame rate of 60 Hz and an acquisition time of 90 seconds. The excitation power at the back focal plane (BFP) was of 18 mW ($\lambda_{exc} = 640\,nm$) and 13.9 mW ($\lambda_{exc} = 561\,nm$). For the set of experiments, we determined a localisation accuracy to be $\delta_{560} = 22\,nm$ and $\delta_{640} = 20\,nm$. Although we performed dual colour experiments, we did the analyses per channel.

5.2.7 **Manders coefficient formula**

The Mander's overlap coefficient (MOC) and the Mander's fractional coefficient (M_1) of the Rivers network (R) with respect to the imposed network (N) are computed as follows:

$$MOC = \frac{\sum_{i,j}(R_{i,j} * N_{i,j})}{\sqrt{\left(\sum_{i,j} R_{i,j}^2\right) \cdot \left(\sum_{i,j} N_{i,j}^2\right)}} \tag{5.1}$$

and

$$M_1 = \frac{\sum R_N}{\sum R} \tag{5.2}$$

Where, R_N refers to the pixels of R that coincide with full pixels in N(20).

5.2.8 Fitting parameters for the double exponential decay

The fitting consists on a double exponential decay with a constant term:

$$F(t) = \tilde{A}_1 e^{-t/\tau_1} + \tilde{A}_2 e^{-t/\tau_2} + B$$

We performed the fitting in MATLAB's *Curve Fitting* Tool setting the bounds of $\tilde{A}_1, \tilde{A}_2\ and\ B \in [0,1]$ and $\tau_1\ and\ \tau_2 \in [0, \infty)$. We chose '0.5' as the starting point for all the variables. The rest of parameters used for the fittings are summarised in the following table:

Table 5.1 Table summarizing the fitting options used in MATLAB for the double exponential fitting.

Algorithm	**Trust-Region**
Robust	On
Maximum iterations	10^5
Maximum number of evaluations	10^5
Minimum change in coefficients	10^{-8}
Maximum change in coefficients	10^{-2}
Termination tolerance on model value	10^{-16}
Termination tolerance on coefficient values	10^{-16}

5.2.9 **Trajectory reconnection.**

We used ImageJ plugin Trackmate (21, 22) for the detection of the single molecules (Diameter blob = 8 pixels and Threshold = 1.5). For the tracking we set used the simple LAP tracker with a maximum distance between frames of 5 pixels and we did not allow for blinking (missing frames). Overall, we obtained > 1000 trajectories for N = 9 cells.

5.2.10 **Trajectory segmentation using simultaneously obtained HiDenMaps.**

We segment the trajectories considering whether the molecule has visited a high- or low-density region of the HiDenMaps. First, we define a 1-by-1 μm^2 region of interest (ROI) around the trajectory. In order to establish if a region of the ROI has a high or low density of localisations, we have performed a 1st rank Voronoi density segmentation. For the segmentation, we took the 90% value of the cumulative distribution function of the uniformly distributed data. For each localisation in the trajectory, we count the nearest neighbours in the ROI at a maximum distance of 50 nm and we compute the ratio of high vs total. If the ratio is larger than 50%, then we assign that localisation in the trajectory to be in a high-density region. Finally, to split the trajectory between high-density and low-density, at least 3 consecutive frames must be in the same type of region to classify that segment. For each trajectory we stitch together all the partial segments to obtain, in the best case, two segments per trajectory: high density and low density.

5.2.11 **Quantification of segmented trajectories.**

Once the trajectories have been divided into high and low visited regions, we proceeded to quantify the segments by means of the apparent diffusion coefficient, $D_{1\text{-}4}$, (for segments longer than 20 frames), the instantaneous velocity and the turning angle. The turning angle refers to the angle between consecutive segments.

5.2.12 **Transient confinement zones (TCZ) and hotspot identification**

First, we identify TCZ of individual trajectories using an algorithm adapted from Simson et al. (23). Then, we correlate these TCZ with confinement regions of the HiDenMap close to the TCZ. For each trajectory with a TCZ, we determine an ROI around it (± 200 nm) on the HiDenMap and we search for high localisation-density regions (hotspots) using the 1st rank Voronoi-based tessellation. Then, if a hotspot exists, we proceed to calculate its lifetime by measuring the time it takes for the cumulative distribution function of the localisation appearances in the hotspot to go from 5% to 80%.

5.3 Results

5.3.1 **Design of algorithms to quantify HiDenMaps**

As reported in Chapter 3, when generating a HiDenMap we need to acquire single molecule data for a certain time in order to have a faithful representation on how molecules explore the space. In fact, if we acquire localisations for a short period of time, then molecules will not have sufficient time to explore the full space. The recovered HiDenMap from this short acquisition can be biased and reveal an inhomogeneous pattern even if the molecules diffuse in a Brownian fashion. The pattern simply arises because not enough localisations are recorded in time to generate a homogeneous HiDenMap. Moreover, and most importantly, when running any further analysis, it would be interesting to differentiate those localisations that arise from interactions with the environment from those that come from freely diffusing molecules. In order to tackle this question, we relied on already existing algorithms used in the field of SR-SMLM to perform cluster analysis and cleaning the data.

5.3.1.1 1st rank Voronoi filtering of localisations

Voronoi tessellation is becoming a popular method in SR-SMLM data analysis due to its unique properties. The Voronoi tessellation consists on partitioning the space using seeds (localisations) and generating a Voronoi cell for each seed. The Voronoi cells have the unique property that any point within the cell is closer to the corresponding seed than to any other seed. Because of this, if the seeds are densely packed, the corresponding Voronoi area of the cell is smaller than if the seeds are more sparsely located. This can be extrapolated to the nearest neighbours and if all the seeds are densely packed in a region of space, all those areas will be small. Accordingly, in less crowded regions, the areas will be larger. Levet et al. have implemented the Voronoi tessellation in the analysis of SR-SMLM to study clusters by segmenting the localisations into low and high density(24, 25).

Inspired by the work of Levet, we have implemented the 1st rank Voronoi tessellation algorithm in our analysis workflow to filter those localisations that arise from Brownian motion from those that originate from actual interactions with the environment. The algorithm consists of two parts; first, we compute the normalised rank 1 Voronoi density for each localisation and second, we apply a filter based on these densities.

Given a set of N seeds, $s_{k,k\in[1,N]}$, we perform a Voronoi tessellation of the space such that each seed, s_i, belongs within a polygon, P_i, of area A_i. The 1st rank neighbours of seed s_i are those seeds whose polygons share an edge with seed s_i. The concept behind computing the rank 1 Voronoi density is to calculate the density accounting also for the areas of the 1st rank neighbours.

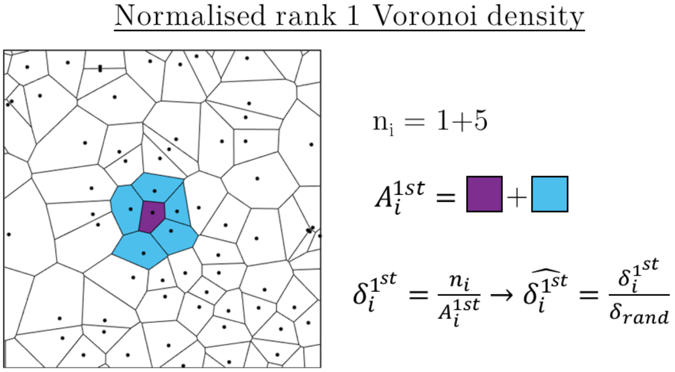

Figure 5.1 Schematic example on how the Rank 1 Voronoi density is computed for the localisation within the purple area. The cyan areas correspond to the first neighbours to the localisation of interest.

The rank 1 Voronoi density is computed as follows:

$$\delta_i^{1st} = \frac{1 + n_i^1}{A_i + \sum A_{i,j}^1} \tag{5.3}$$

Where n_i^1 corresponds to the number of 1st rank neighbours, A_i the area of the Voronoi cell for seed s_i and $A_{i,j}^1$ are the Voronoi areas of the 1st rank neighbours. Then, we normalise the density by dividing δ_i^{1st} by the mean density of uniformly distributed localisations (same number as the experimental data):

$$\hat{\delta}_i^{1^{st}} = \frac{\delta_i^{1^{st}}}{\delta_{rand}} \tag{5.4}$$

The normalisation is performed in order to centre the distribution around 0 in a logarithmic scale. Figure 5.1 shows an example on how the normalised 1^{st} rank Voronoi density is computed for the seed in the purple Voronoi cell.

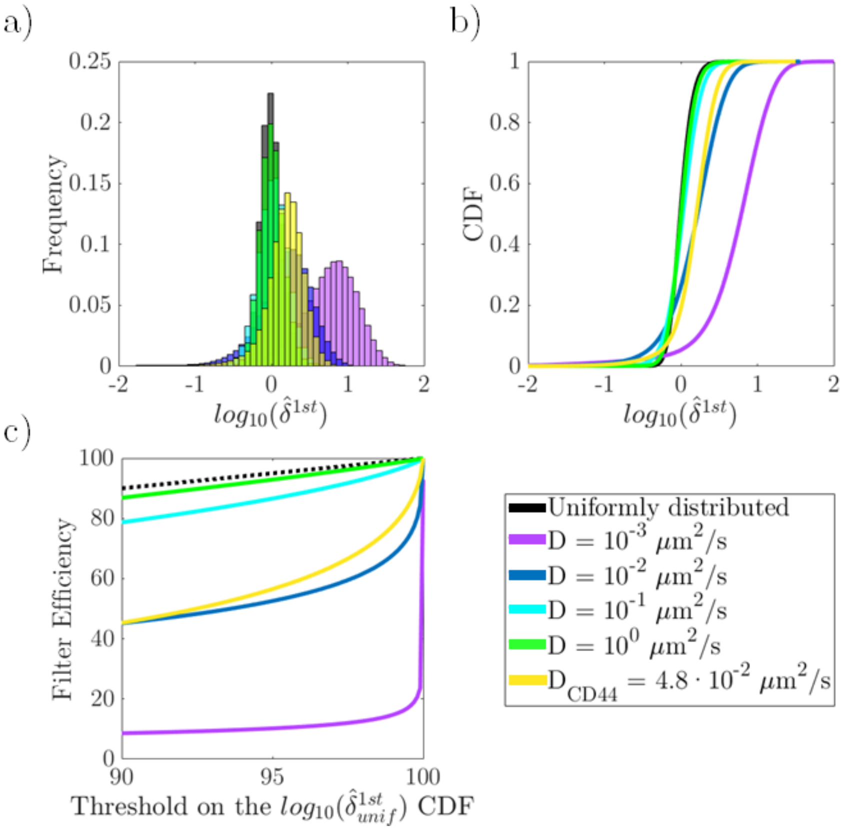

Figure 5.2 Performance of the 1st rank Voronoi density filter with in-silico simulated Brownian motion and uniformly distributed localisations. a) Distributions of the normalised 1st rank Voronoi density in logarithmic scale. b) The cumulative density function (CDF) for the normalised 1st rank Voronoi density in logarithmic scale. c) Filter efficiency as a function of the threshold on the normalised 1st rank Voronoi density from uniformly distributed data, in logarithmic scale. The dashed line is the response for the uniformly distributed data, i.e., when the horizontal and vertical coordinates are equal (x =y).

The goal is to set a threshold to determine the cut-off between high-density and low-density localisations. Ideally, for a given experimental dataset one would *in-silico* simulate Brownian motion diffusion to obtain the same number of localisations and set the threshold on that data set. However, computationally this would be very expensive and inefficient. Using uniformly distributed localisations to set the threshold is computationally more efficient and faster. To determine which is the most appropriate method to determine the threshold, we generated a set of *in-silico* simulations of Brownian diffusion with different diffusion coefficients ($D = 10^{-3}, 10^{-2}, 10^{-1}, 10^{0}\ and\ 4.8 \cdot 10^{-2}\ \mu m^2/s$). The last diffusion, $D = 4.8 \cdot 10^{-2}\ \mu m^2/s$ corresponds to the diffusion coefficient of CD44, the same protein receptor studied in Chapters 3 and 4. Figure 5.2a shows the distributions of the normalised 1st rank Voronoi densities in a logarithmic scale. For slow diffusions, $D < 10^{-2}\ \mu m^2/s$, the distributions are shifted towards the right (high densities). This is due to the slow diffusion of the molecules so that they do not explore homogenously the space and the distance between consecutive steps is small. Nevertheless, for faster diffusions, the distributions are centred around zero as it is also the case for random uniformly distributed localisations. In order to set the threshold, we computed the cumulative density function (CDF) for the normalised 1st rank Voronoi density (Figure 5.2b). We would need to work at rather high thresholds in order to be able to remove as many localisations as possible. We screened the filtering efficiency by testing thresholds on the uniformly distributed localisations from 90% up to 99.99% (Figure 5.2c). From this plot, it is clear that we need to define the threshold as the 99.99% of the CDF for the normalised 1st rank Voronoi density. To validate the performance of this algorithm as a filter to remove Brownian motion localisations, we have computed the efficiency of the filter as the percentage of localisations removed by the filter.

5.3.1.2 Rivers algorithm for in-silico pattern recognition in HiDenMaps

As shown in Chapter 4, the HiDenMaps of receptors that interact with the underlying cortical actin, such as CD44, reveal a meshwork-like pattern. These patterns originate from multiple dynamic interactions of receptors with their environment and are the finger-print on how molecules have explored the space in a non-Brownian manner. In order to study in depth the characteristics of these patterns, we developed an algorithm to reconstruct these patterns in an automated way. We have named the algorithm *Rivers* because it combines the Watershed(26–28) and the Skeletonisation(29–31) methods and it connects the patterns in HiDenMaps. Figure 5.3 shows a schematic illustration of the full pipeline that the data go through, from raw data to an *in-silico* reconstructed network.

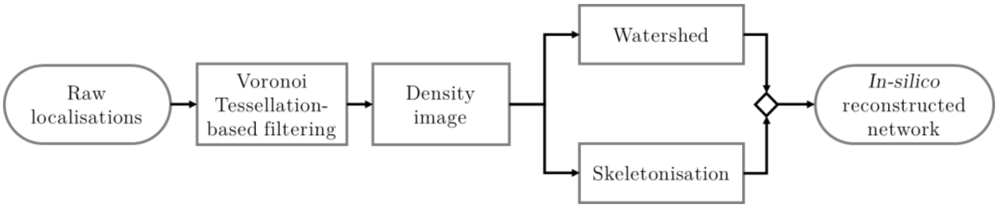

Figure 5.3 Schematic illustration of the analysis pipeline of the Rivers algorithm to generate *in-silico* reconstructed patterns from HiDenMaps. Briefly, first we take the raw localisations and apply a Voronoi tessellation-based filtering using the normalised 1st rank Voronoi density. Then, we voxel the space and generate a density image with the high-density localisations. Next, we apply two morphological transformations on the image in parallel, a Watershed and a Skeletonisation. Finally, we merge the outputs of both morphological transformations to obtain the *in-silico* reconstructed network.

The first step of the algorithm is to remove the localisations that do not contribute to the pattern, i.e., random localisations from Brownian-like motion. We apply a 1st Rank Voronoi density filter to remove these localisations. We consider the same number of localisations as in the experimental data and we distribute them uniformly in space. After computing the normalised 1st rank Voronoi density, we use the 99.99% of the CDF of the uniformly distributed localisations as the threshold for the experimental data. With this step we classify the experimental localisations into sparse ($\widehat{\delta^{1st}} < th_{99.99\%}$) and dense ($\widehat{\delta^{1st}} \geq th_{99.99\%}$). The sparse localisations arise from molecules that diffuse freely on the space whereas the dense localisations are those composing the pattern. Next, we generate a density image of the high-density localisations by defining a voxel (half of the imaging pixel size, in our case 50 nm) and counting the number of localisations per voxel. Once we have this image, we can apply different morphological operations to extract the backbone of the high-density regions of the image. Our strategy consists on applying two morphological operations independently and convoluting the results of both to obtain the reconstructed network. We apply a Watershed algorithm which connects the high-density regions by finding the centre of the regions and adding directionality to connect them(27). Unfortunately, since the Watershed also generates a network on those regions that are actually of lower density, we need to complement Watershed with another morphological operation. We chose the

Skeletonisation algorithm because it identifies the skeletons of all high-density regions(31) but it also generates smaller ramifications within the areas, which we are not interested in. When we convolute both Watershed and Skeletonisation, we obtain a clean network which removes the links between high-density regions from Watershed and the ramifications of the Skeletonisation. The final output is a binary image which contains the backbones of the high-density regions of the HiDenMaps.

To validate the performance of the algorithm, we performed *in-silico* simulations of a molecule that can freely diffuse until it encounters an imposed underlying network. When it encounters the imposed network, it can interact with the network with a given probability (see the Materials section for more detailed information on the simulations). As a negative control, we have also performed *in-silico* simulations of the same molecule diffusing with Brownian motion but not interacting with the imposed network. Figure 5.4 shows illustrations for the *in-silico* simulations mentioned above, a Brownian motion simulation ($P_{inter} = 0$, top row) and molecules interacting with the network ($P_{inter} = 1$, bottom row). The first column shows the imposed network used for the simulations and the second column corresponds to the HiDenMap resulting from integrating for 100 s. The resultant HiDenMaps are clearly different (see second column in Figure 5.4) and comparable to the HiDenMaps shown in Chapter 3 when we investigated lipid bilayers and CD44. The HiDenMap of molecules that interact with the underlying imposed network exhibit a clear pattern that is very resembling to the network. The third column is the result of running the Rivers algorithm and shows the resulting *in-silico* reconstructed network. Finally, on the fourth column we show the overlay of the previous three images. In the case of Brownian motion simulations, we do reconstruct a small network but in the overlay image we do not observe any meaningful overlap with the imposed network (no white regions). Remarkably, in the case of molecules that do interact with the imposed network, the *in-silico* reconstructed network does overlap to the imposed one to a great extent. Thus, these simulations visually show the excellent performance of our *Rivers* algorithm to *in-silico* re-construct patterns from HiDenMaps data.

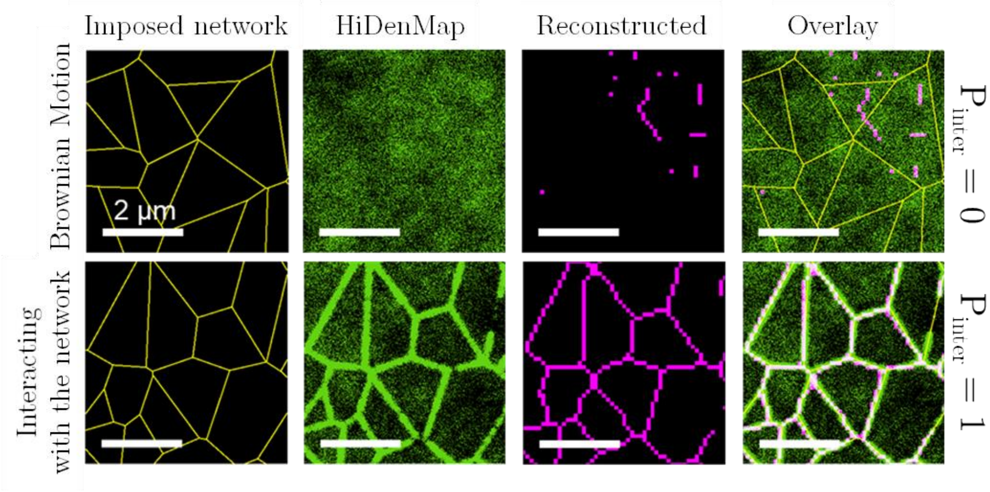

Figure 5.4 *In-silico* simulated examples for a molecule exhibiting two types of diffusing patterns (Brownian motion –top- and Interacting with a network – bottom-), with an imposed network (1st column), the obtained HiDenMap image (2nd column), the *in-silico* reconstructed pattern (3rd column) and the overlay of all the columns (4th column). The colour-code in the overlay image is conserved from the previous images, and in white we depict the overlap between the reconstructed and the imposed network. The interaction probability with the network for the two scenarios is shown on the right.

To evaluate the performance of the Rivers algorithm in a more quantitative fashion, we performed *in-silico* simulations of receptors interacting with different probabilities ($P_{inter} = [0, 0.25, 0.5, 0.75, 1]$) with the underlying imposed network. Note that the condition of $P_{inter} = 0$, refers to Brownian motion. For these simulations we set the interaction time, τ_{inter}, to 500 ms and do not allowed for molecule rebinding ($P_{rebind} = 0$), i.e., molecules will not interact and bind again to the same site of the network. Moreover, the simulations herein shown are performed for a receptor with mean diffusion coefficient of 0.05 µm^2/s, which is similar to that of CD44. Figure 5.5 summarises all the quantifications performed to evaluate the performance of the Rivers algorithm.

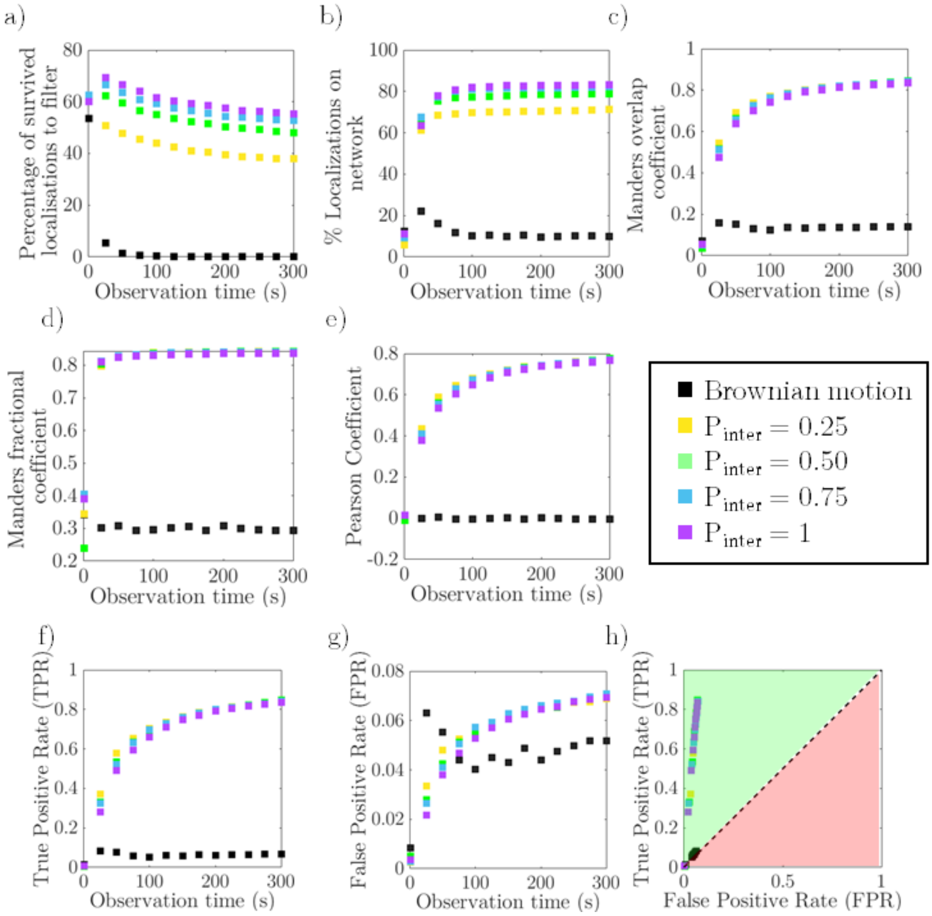

Figure 5.5 Quantifying the performance of the *Rivers* algorithm with *in-silico* simulations of Brownian motion (black) and molecules with different interaction probabilities with an imposed network (P_{inter} = 0.25, 0.50, 0.75 and 1) without rebinding. a) Percentage of localisations that survived the Voronoi-based filtering, i.e., the percentage of non-random localisations. b) Percentage of localisations on the network. b) Manders overlap coefficient (MOC) between the imposed network and the resultant Rivers pattern. d) Manders fractional coefficient (MFC) between the imposed network and the resultant Rivers pattern. e) The Pearson coefficient between the imposed network and the resultant Rivers pattern. f) The true positive rate (TPR) of the Rivers algorithm. g) The false positive rate (FPR) and the Receiver Operating Characteristic (RoC) curve h). In the ROC curve we shaded a green and red triangles referring to good and bad performance respectively. All of the parameters to quantify the performance of the Rivers algorithm are plotted as a function of the observation time.

First, we studied the percentage of localisations that survived the 1st rank Voronoi density filter (Figure 5.5a). As shown in the previous section, the efficiency of the filter with purely Brownian diffusion is excellent, removing almost all the localisations. As expected, for those simulations in which molecules do interact with an imposed network, the filtering efficiency is lower because there is a higher percentage of localisations more densely packed. Second, we quantified the percentage of localisations that fall on the reconstructed network (Figure 5.5b). Considering the high filtering efficiency for the Brownian motion case, the reconstructed network is minimal. Thus, the percentage of localisations on the network is small. On the contrary, the percentages of localisations on the network for those simulations in which molecules interact with the imposed network are much higher. In fact, the percentage scales with the probability of interacting with the network: the higher the interaction probability, the higher the percentage of localisations on the network. Next, we studied how faithful is our *Rivers*-reconstructed network compared to the imposed one. We used three indicators to measure the similarity: the Manders overlap coefficient (MOC, Figure 5.5c), the Manders fractional coefficient (M_1, Figure 5.5d)(Equation (5.2),(20)) and the Pearson coefficient (Figure 5.5e) of the reconstructed network with respect to the imposed one. For all three indicators there is a clear correlation between the reconstructed and the imposed networks for all interaction probabilities. The fact that we do not reach to a 100% is because the molecules probe stochastically the space and bind to the network randomly without fully probing the whole network within the observation window of the simulation. Remarkably, the Manders fractional coefficient is above 80% already at 50 s observation time, indicating that our algorithm is able to reconstruct the visited network with outstanding accuracy in short integration times.

Finally, we assessed the predictive capability of the Rivers algorithm by computing the true positive rate (TPR, Figure 5.5f), the false positive rate (FPR, Figure 5.5g) and the receiver-operator curve (ROC, Figure 5.5h) in a pixel-based manner. The true positive rate is the ratio between the number of pixels correctly classified as a network and the total number of pixels of the imposed network. The TPR increases as a function of observation time for all the interacting simulations. This is because as we observe for longer times, the molecules can explore more of the imposed network. For Brownian motion simulations, the TPR plateaus at 0.05 which is expected since the HiDenMaps reveal no patterns (Figure 5.5f). The false positive rate is the ratio between the number of pixels that the algorithm classifies as empty incorrectly (i.e., the imposed network exists in those pixels) and the total number of pixels classified as empty. Figure 5.5g shows an increase of the FPR for the simulations with imposed network as a function of time, plateauing at 0.07. In the case of Brownian motion simulations, the FPR decreases as a function of observation time plateauing at 0.05. Despite these tendencies, the FPRs are very small. Finally, we plot the ROC (Receiver Operating Characteristic) curve that assess the overall performance of the algorithm (Figure 5.5h). It plots the true versus the false positive rates. In the ROC curve, the x=y line serves as a divider between bad (bottom right triangle) and good (top left triangle) classifiers, and the line represents random classifiers. Moreover, the closer the points are to the top left corner of the plot the more accurate the algorithm is. For the simulations of interacting molecules, as the observation time increases, the values in the ROC curve tend towards the top left corner of the plot. On the other hand, for the Brownian motion simulations, the values fall on the x=y curve which is expected since the network is inexistent. Overall, the algorithm proves to perform remarkably well.

5.3.1.3 Unravelling characteristic temporal scales from HiDenMaps

The patterns observed in the HiDenMaps are built dynamically over time. Therefore, segmenting the HiDenMaps into time windows should allow for observing how they evolve in time, potentially revealing different dynamics. To assess different dynamic scenarios and to contrast simulated with experimental data, we performed once more *in-silico* simulations on two extreme scenarios, the first one when molecules diffuse in a purely Brownian fashion, and a second one where the molecules remain permanently trapped in the network. We then generated HiDenMaps by integrating the number of localisations during 5 seconds on different time windows (see Figure 5.6). For *in-silico* simulations of Brownian motion, the 5-second HiDenMaps reveal random exploration at different observation time points (Figure 5.6a). For *in-silico* simulations of static trapping on a network, the temporal windows show no exploration of the space since the molecules are static on the network (Figure 5.6b). Interestingly, when we compared these simulations with a 5-second HiDenMap retrieved for the experimental data on CD44 at different temporal windows, we observed a mixture of both behaviours (Figure 5.6c). Indeed, we find clusters of localisations (pointed with red arrows) which have a certain temporal persistence and they dissolve in time, as well as clusters of localisations that appear at arbitrary time windows. In addition, we also find scattered localisations which would arise from a random exploration of the space (Figure 5.6c). The way the clusters dissolve is directional since the molecules seem to move following underlying paths. This is clearly visible when collapsing all the time windows in a final HiDenMap (last column in Figure 5.6c): the multiple clusters (or hotspots of confinement) built up larger patterns in the HiDenMaps. Thus, HiDenMaps encode dynamic information on how molecules interact with their environment.

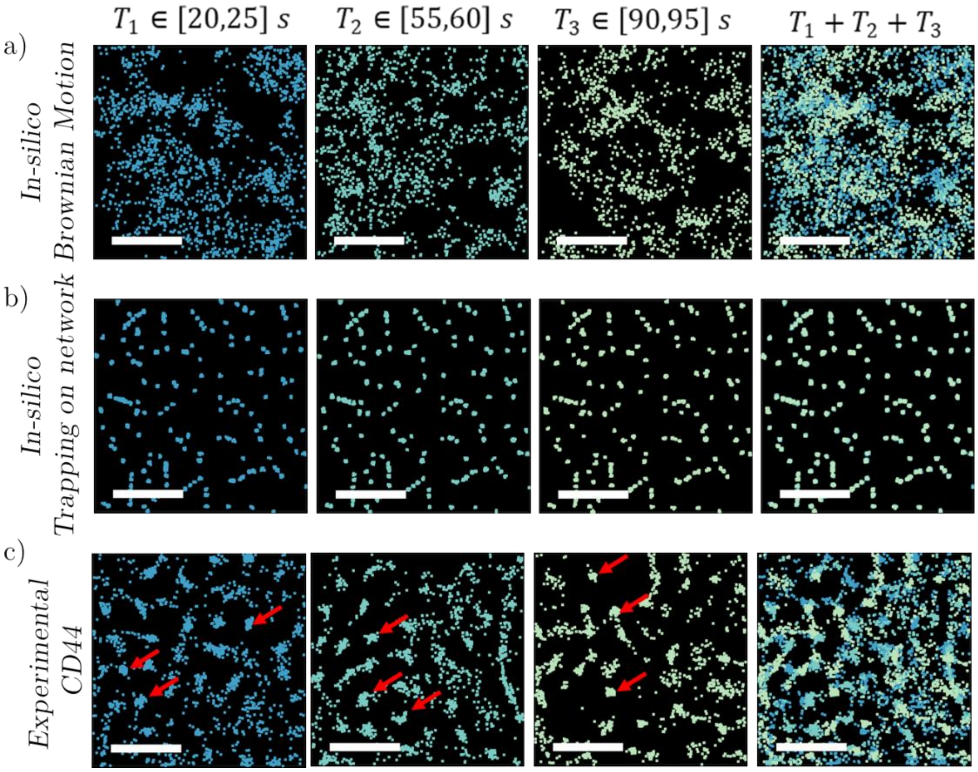

Figure 5.6 HiDenMaps of 5 s time windows during different observation times: $T \in [20,25]\ s$ (1st column), $T \in [55,60]\ s$ (2nd column) and $T \in [90,95]\ s$ (3rd column)) and the overlay of the three time windows (4rd column). The rows correspond to Brownian motion simulation (a), *in-silico* static trapping on network (b) and experimental CD44 on mouse embryonic fibroblasts (MEFs) (c). The number of localisations at each time window is the same for the three different scenarios. The scale bar is 2 µm.

To extract the temporal scales of the interaction of molecules with their environment we have developed an autocorrelation algorithm (Figure 5.7).

Considering our previous results showing that molecules interacting with their environment exhibit patterns in the HiDenMaps, our algorithm classifies the localisations depending on whether they appear on the pattern or not. First, we reconstruct the Rivers network from the HiDenMap as previously described. We then use the Rivers network as a mask in order to classify the localisations of the HiDenMap. This leads to two populations: one population of localisations of the HiDenMap that are inside the network and a second population of localisations that are outside. Second, we make a sliding time window, Δt, of 500 ms for the localisations. The length of the window results from a compromise of having to accumulate enough localisations and still be short enough so that fast dynamics are not washed out. Third, we compute the autocorrelation curve as follows:

$$G_0\left(t_{lag} = m\Delta t\right) = \frac{1}{N-m} \sum_{i=1}^{N-m} \frac{< I(\Delta t_i) * I(\Delta t_i + m\Delta t) >}{< I(\Delta t_i) > \cdot < I(\Delta t_i + m\Delta t) >} \qquad (5.5)$$

Here, $I(\Delta t_i)$ refers to the image of the i-th temporal window. To generate the images from localisations, we pixelized the space into 100 nm squared pixels and counted the number of localisations per pixel. Fourth, we normalise the curve to the first point (t_{lag} = 0 s). Finally, we fit the decay curves from the second point onwards until t_{lag} = 50 s. The fitting consists on a double exponential decay with a constant term:

$$F(t) = \tilde{A}_1 e^{-t/\tau_1} + \tilde{A}_2 e^{-t/\tau_2} + B \qquad (5.6)$$

Finally, once the fitting is performed, we rescale the amplitudes of the exponential decays as follows:

$$A_1 = \frac{\tilde{A}_1}{\tilde{A}_1 + \tilde{A}_2} \quad and \quad A_2 = \frac{\tilde{A}_2}{\tilde{A}_1 + \tilde{A}_2} \qquad (5.7)$$

We note that the autocorrelation functions are generated for both types of localisations, i.e., those that belong to the patterns and those that are outside the pattern. By doing this procedure we can thus distinguish the different interaction dynamics of the molecules as they explore the space.

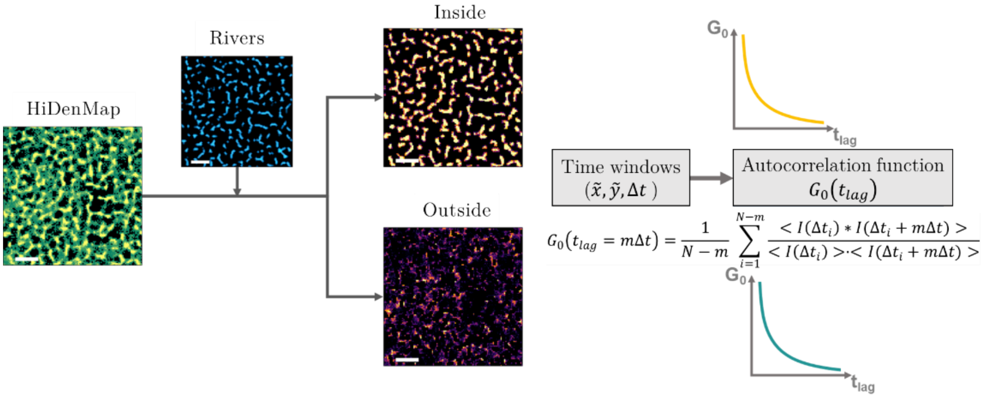

Figure 5.7 Schematic illustration on how the autocorrelation analysis is performed. From left to right: we take the HiDenMap and we apply the Rivers algorithm to generate an *in-silico* reconstructed pattern. We use the Rivers pattern as a mask to segment the localisations of the HiDenMap into inside and outside the pattern. For each set of localisations, we make time windows of 500 ms and we perform the autocorrelation function, giving two different decays.

5.3.2 **Biological insights using quantitative HiDenMaps**

5.3.2.1 Unravelling the mesoscale dynamics of actin-binding receptors

Having established a set of quantitative tools to analyse the experimentally obtained HiDenMaps, we then proceeded to investigate the spatiotemporal organisation of different membrane receptors that interact with the underlying cortical actin with distinct strengths. The first protein of study is a transmembrane actin-binding domain (tmABD) construct that consists on a tm domain with an Ezrin protein anchored to the cytosolic tail. Ezrin is a protein found on the cytosol of cells close to the plasma membrane and belongs to the group of ERM proteins (Ezrin/radixin/moesin)(32–34). ERM proteins function as linkers between transmembrane proteins such as CD44 and the actin cytoskeleton(35–37). Thus, tmABD serves as a positive control to a receptor that actively binds to cortical actin. The second protein under study is the tmRA construct, which has the same structure as tmABD but with a point mutation on the actin binding recognition domain, and thus not being able to actively bind to actin (38, 39). Nevertheless, the mutated Ezrin region can still interact with endogenous Ezrin and therefore passively sense the cortical actin.

Finally, CD44 is the most complex receptor studied since it not only binds to actin via Ezrin, but it also interacts with the extracellular matrix(40). For the experiments described below we studied CD44 on immature dendritic cells (iDCs, refer to Chapter 6 for further details) in control conditions and after treating the cells with lactose. Lactose is a β-galactosidase that competes with galectins by blocking the binding sites of glycoproteins so that galectins are not able to bind(41, 42). Therefore, lactose treatment removes the interaction of CD44 with the extracellular milieu via galectins.

In order to apply the analytical tools described above, we first evaluated the Voronoi filter efficiency in order to remove localisations that originate from random diffusion of the different proteins. For completeness and to allow a full comparison of the data, we also include the results of the lipid bilayer experiments described in Chapter 3 as well as simulations of Brownian diffusion to each set of experimental data (Figure 5.8). For the lipid bilayer data, the filter performs excellently well by removing almost 99.5% of localisations, comparable to the simulations of Brownian motion. When comparing the results of the three proteins of interest (tmRA, tmABD and CD44, with and without lactose) to their corresponding Brownian motion simulations, the number of filtered localisations is significantly less. This is because a percentage of localisations from the experimental data are identified by the Voronoi algorithm as belonging to high density regions, i.e., not random, and therefore, they are not removed by the Voronoi filter (see also section 5.3.1.1). These initial results already indicate a certain degree of non-Brownian exploration of the environment by the three different proteins of study. Moreover, although the differences between the three proteins are not statistically significant, the percentage of removed localisations is slightly higher for tmRA as compared to tmABD and CD44. These results are consistent with the fact that tmRA interacts less with actin and therefore exhibits a higher degree of random motion. Interestingly, in the case of CD44, the spread on the percentage of removed random localisations is much larger than for the other two proteins (tmRA and tmABD). This is due to the complexity of the interactions of CD44 with its environment.

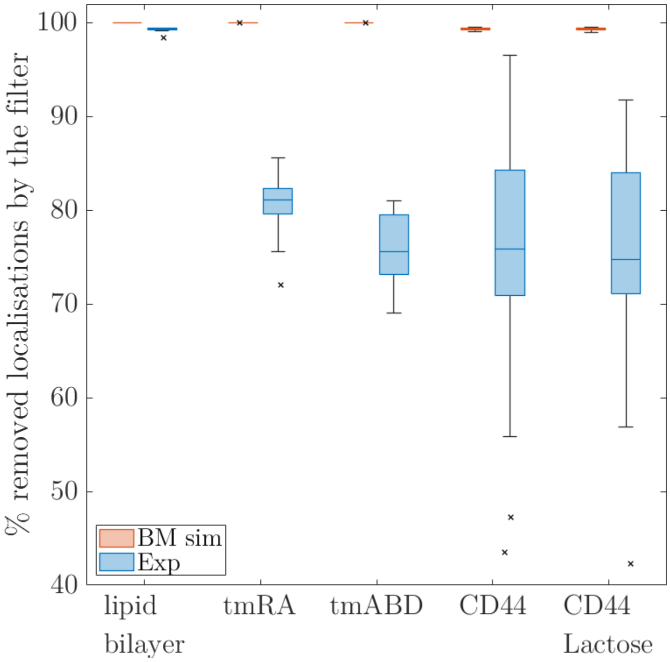

Figure 5.8 Percentage of removed localisations using the 1st rank Voronoi filter for experimenta data (blue) and the corresponding in-silico Brownian motion (BM) simulations (orange). Number of ROIs analysed: lipid bilayer (8 ROIs), tmRA (20 ROIs), tmABD (8 ROIs), CD44 (24 ROIs) and CD44 with lactose (29 ROIs). The ROIs were taken from different cells and different samples. At least from two different experimental dates.

After performing the Voronoi filtering step on the HiDenMaps, we run the Rivers algorithm, generated the reconstructed Rivers network for the three proteins of interest, classified the localisations from the experimental HiDenMaps as function of their partitioning inside or outside the Rivers network and finally generated autocorrelation functions of the localisations inside and outside the network (see section 5.2 for full details). The results of the fitting of the autocorrelation functions to a double exponential decay are shown in Figure 5.9, for localisations inside (orange) and outside (blue) the Rivers pattern, for the three proteins under study.

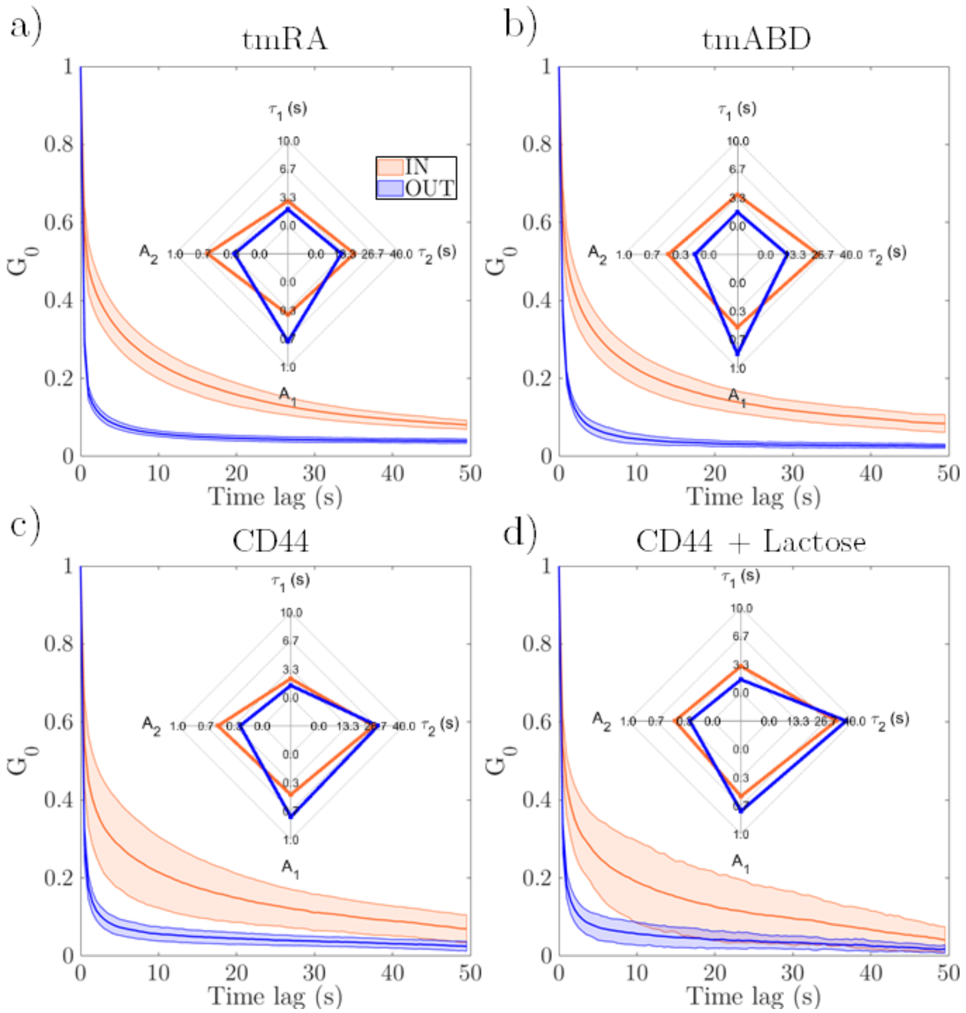

Figure 5.9 Average autocorrelation decays (G0) for tmRA (a), tmABD (b), CD44 (c) and CD44 with lactose (d). In orange we show the decay curves inside the pattern and in blue the decay curves outside the pattern. The shaded area corresponds to the standard deviation over the analysed cells while the solid line corresponds to the mean value. The insets show radar plots with the median values of the parameters retrieved from fitting the autocorrelation curves to a double exponential decay. Number of cells (and ROIs analysed per receptor): tmRA: 12 (32), tmABD 8 (16): CD44 15 (19): and CD44 with lactose: 20 (17).

The plots show the average autocorrelation decay for multiple ROIs (12-by-12 µm) in multiple cells. As expected, the curves decay very fast for those localisations outside the network (blue curves) consistent with the fact that they mainly correspond to random localisations originating from Brownian diffusion of the proteins. In contrast, the temporal decay is much longer for those localisations inside the network (orange curves), an indication of the temporal persistence of the network. The median fitted parameters to the autocorrelation curves are represented in the radar plots within the corresponding decays in Figure 5.9. The amplitudes, A_1 and A_2, correspond to the strength of the interactions, i.e., how much the receptors feel the temporal changes in the environment, with A_1 and A_2 being the amplitudes of the fast and slow decay components, respectively. Accordingly, τ_1 and τ_2 are the decay times of the fast and slow decay components, respectively. Interestingly, for both tmRA and tmABD and outside the network, the fast exponential component is predominant ($A_1>A_2$) (see Figure 5.9 a, b). In addition, for these two receptors and inside the network, the slow decay component takes a higher importance ($A_2>A_1$). In the case of CD44, the decay curves show higher variability and the changes in the radar plots, i.e., outside *vs.* inside are subtler, both in control cells and those treated with lactose (see Figure 5.9 c, d).

Figure 5.10 shows the fitted decay times and the amplitudes for all the receptors studied. Overall, we find two characteristic times in our HiDenMaps, a fast decay (τ_1~2-4 s, Figure 5.10a) and a slow decay (τ_2~10-40 s, Figure 5.10b). We find that the fast decay outside the network is shorter (~2 s) than inside (~4 s) and with reduced variability, indicating that the fast interactions of receptors outside the network are more homogeneous. Thus, outside the network, receptors have shorter and more frequent interactions with the environment (i.e., $A_1 > A_2$). Interestingly, the parameters that characterize the fast component outside the network, i.e., A_1 and τ_1 have similar magnitudes regardless of the receptor investigated, suggesting that outside the network all receptors explore and interact briefly but frequently to the environment to a similar extent (see Figure 5.10a, c). What happens with the long decay component, τ_2 outside the network? In here the difference amongst the three proteins is remarkably high (see Figure 5.10b). For both tmRA and tmABD, τ_2 is significantly shorter than for CD44, ~ 10 s compared to ~ 30 s, respectively. These results are entirely consistent with the proneness of tmRA and tmABD to selectively interact with actin and to a much lesser extent with other components of the membrane. Since the network is primarily defined by the cortical actin (as demonstrated in Chapter 4), the long-lived interactions with the environment outside the network will be less prominent and brief for these two constructs, i.e., small A_2 and short τ_2). In stark contrast, CD44 can interact both with the cortical actin as well as with many other components of the membrane, and thus the long decay component outside the network should be longer than for tmRA and/or tmABD, which is entirely consistent with our experimental observations. Interestingly, reducing the interactions of CD44 with galectins does not produce a major change on the long decay component outside the network, indicating that interactions of CD44 with other binding partners on the membrane, aside from actin and galectins, play an important role in its mesoscale dynamics. Yet, it is important to note that the strength of the long-decay interaction outside the network is smaller than for inside, i.e., A_2 outside < A_2 inside, indicating a preference for CD44 to interact with the network.

Even more interesting are the results obtained inside the network. Regarding the fast decay component, τ_1 is somewhat longer for tmABD than for the other proteins and with larger A_1 values (see Figure 5.10a, c), consistent with the fact that this construct actively interacts with cortical actin. Moreover, the τ_2 values vary significantly depending on the protein and its ability to interact with cortical actin. Indeed, the median values of τ_2 for tmRA and tmABD are 18 s and 26.3 s, respectively. These results are fully consistent with the fact that tmABD actively binds to actin, and thus longer interactions are expected as compared to the tmRA construct whose binding site to actin is mutated and its interaction with actin is only passive. Notably, CD44 has median A_2 and τ_2 similar to tmABD inside the network (Figure 5.10b, c), which further supports the notion that the pattern revealed by the HiDenMaps arises from interactions with cortical actin. The variability on the CD44 data is also large inside the network, an indication of the complex interactions of this receptor with its environment. In fact, treating the cells with lactose reduces the variability on the CD44 data (A_2 and τ_2), without significantly affecting the median values.

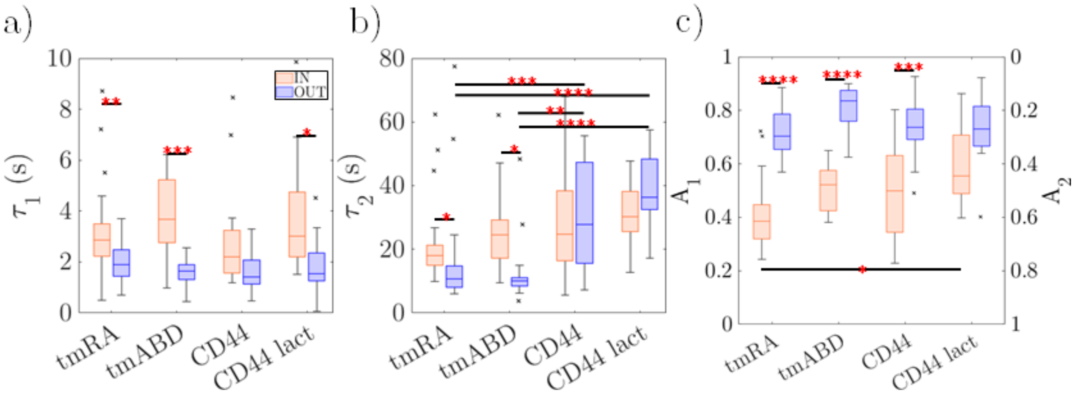

Figure 5.10 Boxplots for the fitted double exponential decays for the proteins mentioned above inside (orange) and outside (blue) the Rivers pattern. a) The fast temporal decay, τ_1. b) The slow temporal decay, τ_2. c) The normalised exponential amplitudes, A_1 (left axis) and A_2 (right axis). Statistical test performed is the non-parametric Kruskal Wallis

It is challenging to associate these two characteristic times to specific biological processes, since they could be due to interactions of the receptors with the environment, dynamic remodelling of the nano-environment, or both. Nevertheless, tmRA interacts more passively with the actin cytoskeleton but it could still be sensitive to a slowly remodelling actin. In the case of a reduced interaction with the cytoskeleton, we would expect shorter interaction times and lower interaction probabilities. In the case of tmRA, we find that A_1 is smaller and τ_1 shorter as compared to the other proteins. Moreover, the A_1 (and τ_1) values are higher (and longer) for tmABD, the construct that actively interacts with actin. Based on these results, it is tempting to speculate that the fast decay component corresponds to interaction of the receptor with the actin cytoskeleton. Regarding the long decay component, the τ_2 and A_2 values are quite similar for all the proteins, albeit slightly shorter for tmRA and with larger A_2. Since tmRA is less sensitive to actin changes, the similarity of the τ_2 and A_2 values for all the other proteins suggests that the long τ_2 component preferentially corresponds to slow remodeling of the cortical actin cytoskeleton.

5.3.2.2 Linking the nanoscale with the mesoscale temporal scales

So far, we have retrieved two very distinct temporal scales from the HiDenMaps. These timescales refer to the mesoscale dynamics of the receptors interacting with the underlying cortical actin. However, we still miss how these mesoscale dynamics are built from the nanoscale dynamics of single molecules.

HiDenMaps are a versatile approach that enables to correlate the mesoscale spatiotemporal organisation of molecules with single molecules dynamics. This is because despite the high-labelling densities (>10 nM) used to generate the HiDenMaps it is still possible to retrieve single molecule trajectories from the same data by taking advantage of photo-bleaching. When the acquisition of the data starts, the density of fluorophores is too high to track individual molecules. Nevertheless, as the acquisition continues, fluorophores will stochastically photo-bleach decreasing the effective labelling density and enabling single molecule tracking. In this way, we can obtain HiDenMaps and SPT from the same data set.

To correlate the nano- and meso-scale dynamics of receptors on the cell membrane using HiDenMaps together with SPT, we performed experiments on CHO cells and labelled CD44 with SNAP-tag JF640 at a 100 nM. Imaging was performed at a frame rate of 60 Hz and an acquisition time of 90 seconds. To avoid any crosstalk in the analysis, localisations belonging to individual trajectories were removed from the HiDenMap. Figure 5.11a shows four representative trajectories (in green) overlaid with the HiDenMap, where black areas correspond to regions not visited by the receptor. We classified the trajectories' segments according to whether the molecule had visited a high-density or a low-density localisation region (more details in Materials and Methods). The zoom-in of Figure 5.11a, shows a trajectory from an individual molecule that diffuses freely on a low-density region of the HiDenMap, then gets temporally arrested in a high-density region and finally escapes from this region to start diffusing freely again. We used this information to directly correlate the dynamics of single molecules with their dynamic environment. We quantified the segmented trajectories considering the visitation regions of the HiDenMaps (Figure 5.11b-d). Molecules in high-density regions diffused slower than when they explore low-density regions (Figure 5.11b), which correlates with their faster instant velocity on low-density regions (Figure 5.11c). Moreover, we computed the turning angle for the segmented trajectories (Figure 5.11d). The turning angle is the angle between consecutive displacements within a trajectory and provides a measure on the confinement of trajectories. If a protein is freely diffusing, we expect a homogeneous turning angle, since the molecule can move freely in any direction. In contrast, a protein having a directed motion tends to go always forward, so the turning angle plot will be shifted towards 0°. Finally, if a protein is confined in an area, it will bounce backwards when it encounters the boundary and thus the turning angle plot will be shifted towards 180°. In the case of CD44 we observe that in high density regions, the plot is more shifted towards 180° as compared to low-density regions (Figure 5.11d). Since the high-density regions in the HiDenMap correspond to the network being explored by CD44, our results thus indicate that single molecules interact with the hotspots in the HiDenMaps by a transient arrest or full confinement of CD44 in these regions.

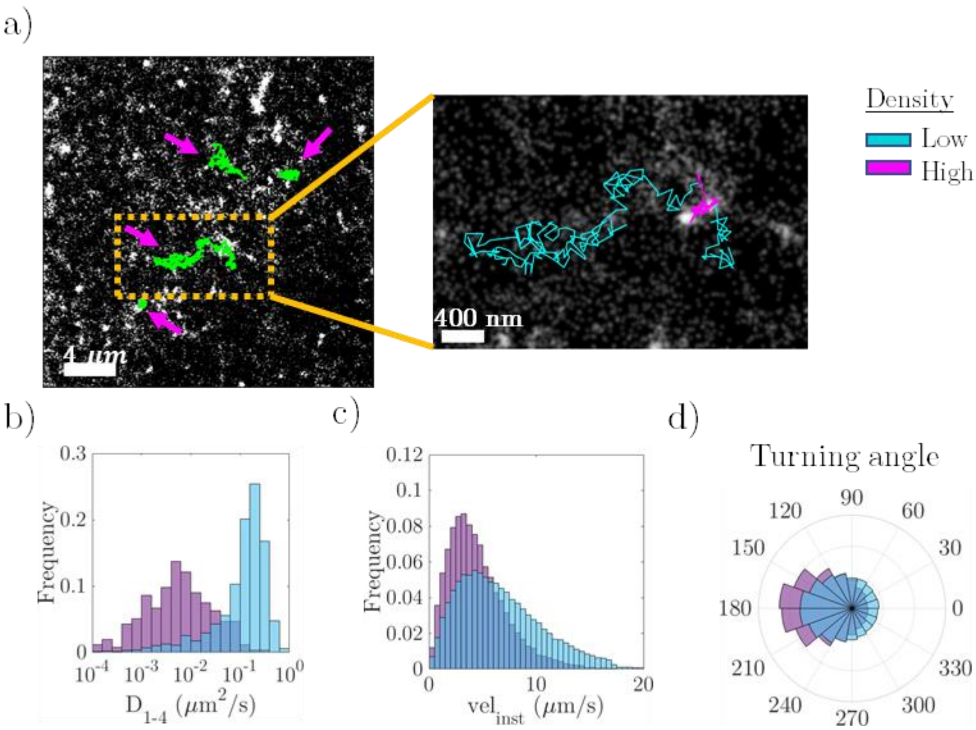

Figure 5.11 Correlative HiDenMap and SPT. a) Single molecule trajectories (in green and pointed with a magenta arrow) overlaid on a simultaneously obtained HiDenMap (left). Zoom-in of a trajectory, colour-coded as to whether the molecule visits high- or low-density localisation regions (right). b) Apparent diffusion coefficient for the segmented trajectories according to their partitioning in high- or low-density regions. c) Instant velocity and d) Turning angle between consecutive segments within a trajectory.

To better quantify these results, we investigated how the transient confinement zones (TCZ) of single molecule trajectories correlate with the HiDenMap localisation hotspots (see Materials and Methods). We classified the TCZ according to whether they occurred within hotspots or not, and quantified the TCZ arrest times, τ_{TCZ}.

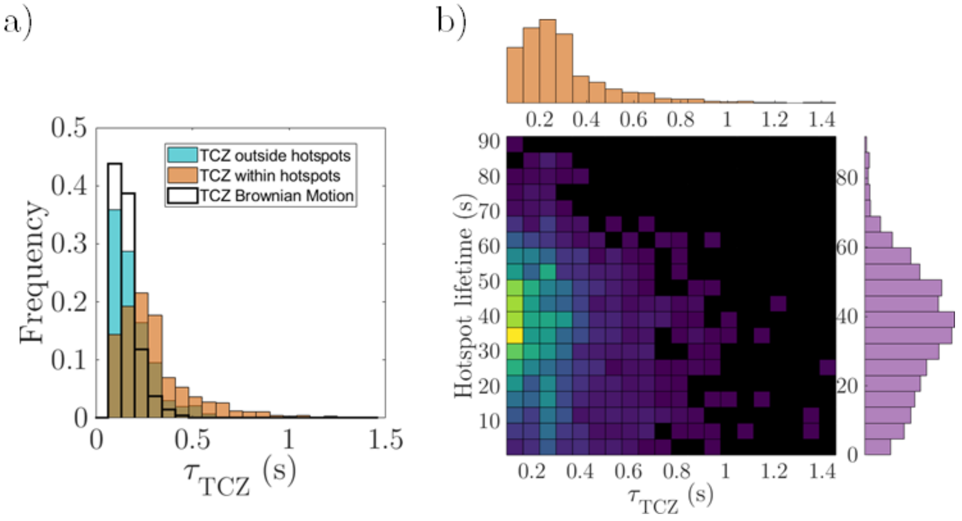

Figure 5.12 Correlating the arrest times of transient confinement zones from single molecule data with the HiDenMap. a) TCZ times for CD44 trajectories outside (cyan) and inside (orange) hotspots. The arrest times for *in*-silico simulated Brownian motion trajectories are shown in white. b) 2D histogram correlating the TCZ arrest times of single molecule trajectories (x-axis, orange) that overlap with hotspots. And the lifetime of the hotspots where the TCZ occurred (y-axis, purple).

In addition, we ran *in-silico* simulations of Brownian motion and computed the τ_{TCZ} that could be detected with our TCZ algorithm, in order to compare with the experimental data (Figure 5.12a). As expected, the distribution of τ_{TCZ} inside hotspots shows a tail towards longer confinement times as compared to the TCZ occurring outside hotspots. In addition, the TCZs outside the localisation hotspots show the same distribution of times as for the *in-silico* simulated Brownian motion trajectories to which we applied the TCZ algorithm. Thus, these results confirm that individual molecules preferentially arrest on the high-density regions described by the HiDenMaps. Finally, we correlated the transient arrest times, τ_{TCZ}, with the lifetime of the hotspots (Figure 5.12b). We took those TCZ occurring on HiDenMap hotspots and measured the lifetime of the hotspots themselves. Remarkably, we retrieve two very distinct temporal scales. The lifetime of the HiDenMap hotspots is of the same order of magnitude as τ_2, the slow time component obtained from the autocorrelation decays in the previous section. Moreover, the arrest time of single molecules, $\tau_{TCZ} \sim 250\ ms$, is an order of magnitude shorter than τ_1, the fast component in the autocorrelation decay. Together, these results reveal that CD44 transiently and dynamically interact with the hotspots of the network getting arrested for a few hundred of milliseconds, while the network itself dynamically remodels in the tens of seconds time scale. As such, HiDenMaps combined with SPT reveals dynamic molecular interactions within a dynamically changing environment.

5.4 Discussion

In this Chapter, we have presented a palette of analysis tools to study the emergence of patterns in the HiDenMaps of receptors that interact with the underlying cortical actin. First, we have adapted the algorithms by Levet et al. (24, 25) on the 1^{st} rank Voronoi density to filter the localisations arising from Brownian motion. This is especially useful in the case of studying slow molecules that would require very long acquisition times (see Chapter 3 on the technical details of HiDenMaps) and cannot be met by the experimental conditions. Using the 1^{st} rank Voronoi density as a filter, we can discriminate random diffusion and actual patterns arising from interactions of the molecules with the environment. In fact, by using the filter on experimental data we can measure the degree of randomness (Brownian motion) by computing the filter efficiency. We have observed that for those receptors that interact with the underlying cortical actin, the percentage of localisations removed is much lower than for Brownian motion simulations or the *in-vitro* Brownian motion controls (lipid bilayers).

We have developed a localisation-based pattern reconstruction algorithm, the *Rivers* algorithm, that allows to extract the diffusion patterns from HiDenMaps. We validated the performance of the Rivers algorithm by using *in-silico* simulations of molecules diffusing and interacting with an imposed network with different binding affinities. Our results show that we can reconstruct the underlying network orchestrating the spatiotemporal organisation of receptors with high fidelity. A limitation of the algorithm is that we can only reconstruct the network that has been visited and bound to by the receptors, and not the full network. Nevertheless, we can reconstruct the fraction of the network that has affected the diffusion of the tagged receptors.

The patterns arising from HiDenMaps are built dynamically over time as molecules explore the space. Such patterns are generated because of the higher persistence in time of molecules on those regions, i.e., where molecules interact stronger with their environment. Therefore, the spatiotemporal compartmentalisation experienced by the receptors differs inside and outside the patterns. We used the *Rivers* algorithm to reconstruct the underlying pattern and to classify the localisations of the HiDenMap into inside and outside the pattern for experimental data of receptors interacting with the underlying cortical actin with different strengths. We studied the mesoscale dynamics inside and outside the Rivers method by computing the autocorrelation decay to measure the temporal persistence of the mesoscale dynamics. From the double exponential decay fittings, we retrieved two very distinct temporal scales: a short lived $(\tau_1 \sim 4\,s)$ and a long lived $(\tau_2 \sim 30\,s)$. Moreover, the amplitudes of the fitted exponential decays measure the frequency and/or strength of each temporal scale. While outside the pattern the interactions are shorter lived but more frequent, inside the pattern the interactions are longer lived. These results indicate that the spatiotemporal organisation of receptors interacting with underlying cortical actin is driven by multiple temporal processes of different strengths and times.

HiDenMaps not only provide a measure on the mesoscale dynamics but we can use them to correlate single molecule dynamics with the mesoscale spatiotemporal organisation of receptors. We have performed correlative HiDenMaps and SPT from the same dataset using photo-bleaching to our advantage to reconnect trajectories at later stages of the acquisition. We have correlated the single molecule transient arrest times, τ_{TCZ}, with the localisation hotspots that appear on HiDenMaps. From this analysis we retrieve a third temporal scale in the order of ~250 ms that accounts for the interactions of single molecules with the environment. Therefore, using HiDenMaps we have been able to measure the spatiotemporal compartmentalisation at three distinct temporal scales which range from the spatial nanoscale to the mesoscale. Correlative SPT and HiDenMaps is incredibly powerful since we can directly correlate single molecule dynamics to what the ensemble of receptors is feeling simultaneously.

HiDenMaps open new frontiers in image acquisition and analysis. Although in this chapter we have focused our research on receptors interacting with cortical actin, HiDenMaps can be also applied to intracellular studies (43) or to other receptors of the plasma membrane (see Chapter 6). Additionally, the data shown in this chapter have been conducted in a single colour scheme, but HiDenMaps can be extended to multi-colour applications to study interactions between multiple proteins simultaneously (see Chapter 6).

In summary, the amount of data that can be obtained in a simple HiDenMap experiment is massive. The beauty of having localisations in space and time that reveal how molecules sense the environment is magnificent. In this chapter we have exploited the data analysis in the direction of pattern recognition and spatiotemporal correlations and dynamics, but surely, we are only grasping the tip of the iceberg in terms of analysis and applications. HiDenMaps proves to be a valuable approach due to its experimental simplicity to elucidate how single molecules interact with their environment at multiple spatiotemporal scales. Thus, it can fill the void in the field of biophysics left by the standard approaches to study the spatial and temporal organisation of molecules.

5.5 References

1. S. Manley, *et al.*, High-density mapping of single-molecule trajectories with photoactivated localization microscopy. *Nat. Methods* (2008) https:/doi.org/10.1038/nmeth.1176.
2. G. Giannone, *et al.*, Dynamic superresolution imaging of endogenous proteins on living cells at ultra-high density. *Biophys. J.* (2010) https:/doi.org/10.1016/j.bpj.2010.06.005.
3. O. Rossier, *et al.*, Integrins β 1 and β 3 exhibit distinct dynamic nanoscale organizations inside focal adhesions. *Nat. Cell Biol.* **14** (2012).
4. D. Nair, *et al.*, Super-resolution imaging reveals that AMPA receptors inside synapses are dynamically organized in nanodomains regulated by PSD95. *J. Neurosci.* **33** (2013).
5. M. Heidbreder, *et al.*, TNF-α influences the lateral dynamics of TNF receptor I in living cells. *Biochim. Biophys. Acta - Mol. Cell Res.* **1823** (2012).
6. J. B. Masson, *et al.*, Inferring maps of forces inside cell membrane microdomains. *Phys. Rev. Lett.* (2009) https:/doi.org/10.1103/PhysRevLett.102.048103.
7. S. Türkcan, J. B. Masson, Bayesian decision tree for the classification of the mode of motion in single-molecule trajectories. *PLoS One* **8** (2013).
8. J. B. Masson, *et al.*, Mapping the energy and diffusion landscapes of membrane proteins at the cell surface using high-density single-molecule imaging and bayesian inference: Application to the multiscale dynamics of glycine receptors in the neuronal membrane. *Biophys. J.* (2014) https:/doi.org/10.1016/j.bpj.2013.10.027.
9. M. El Beheiry, *et al.*, A Primer on the Bayesian Approach to High-Density Single-Molecule Trajectories Analysis. *Biophys. J.* **110** (2016).
10. N. Hoze, *et al.*, Heterogeneity of AMPA receptor trafficking and molecular interactions revealed by superresolution analysis of live cell imaging. *Proc. Natl. Acad. Sci. U. S. A.* **109** (2012).
11. F. Persson, M. Lindén, C. Unoson, J. Elf, Extracting intracellular diffusive states and transition rates from single-molecule tracking data. *Nat. Methods* **10** (2013).
12. P. Sil, *et al.*, Dynamic actin-mediated nano-scale clustering of CD44 regulates its meso-scale organization at the plasma membrane. *Mol. Biol. Cell* (2020) https:/doi.org/10.1091/mbc.E18-11-0715.
13. D. Holcman, *et al.*, Single particle trajectories reveal active endoplasmic reticulum luminal flow. *Nat. Cell Biol.* (2018) https:/doi.org/10.1038/s41556-018-0192-2.
14. P. Parutto, *et al.*, High-Throughput Super-Resolution Single Particle Trajectory Analysis Reconstructs Organelle Dynamics and Membrane Re-Organization. *SSRN Electron. J.* (2021) https:/doi.org/10.2139/ssrn.3985166.
15. D. V. Köster, *et al.*, Actomyosin dynamics drive local membrane component

organization in an in vitro active composite layer. *Proc. Natl. Acad. Sci. U. S. A.* **113**, E1645–E1654 (2016).

16. C. E. Aitken, R. A. Marshall, J. D. Puglisi, An oxygen scavenging system for improvement of dye stability in single-molecule fluorescence experiments. *Biophys. J.* **94**, 1826–1835 (2008).
17. A. C. E. Shibata, *et al.*, Archipelago architecture of the focal adhesion: Membrane molecules freely enter and exit from the focal adhesion zone. *Cytoskeleton* (2012) https:/doi.org/10.1002/cm.21032.
18. N. Hiramoto-Yamaki, *et al.*, Ultrafast Diffusion of a Fluorescent Cholesterol Analog in Compartmentalized Plasma Membranes. *Traffic* (2014) https:/doi.org/10.1111/tra.12163.
19. N. Komura, *et al.*, Raft-based interactions of gangliosides with a GPI-anchored receptor. *Nat. Chem. Biol.* (2016) https:/doi.org/10.1038/nchembio.2059.
20. J. Adler, I. Parmryd, Quantifying colocalization: The case for discarding the Manders overlap coefficient. *Cytom. Part A* **99** (2021).
21. J. Y. Tinevez, *et al.*, TrackMate: An open and extensible platform for single-particle tracking. *Methods* **115** (2017).
22. D. Ershov, *et al.*, TrackMate 7: integrating state-of-the-art segmentation algorithms into tracking pipelines. *Nat. Methods 2022 197* **19**, 829–832 (2022).
23. R. Simson, E. D. Sheets, K. Jacobson, Detection of temporary lateral confinement of membrane proteins using single-particle tracking analysis. *Biophys. J.* (1995) https:/doi.org/10.1016/S0006-3495(95)79972-6.
24. F. Levet, *et al.*, SR-Tesseler: A method to segment and quantify localization-based super-resolution microscopy data. *Nat. Methods* (2015) https:/doi.org/10.1038/nmeth.3579.
25. F. Levet, *et al.*, A tessellation-based colocalization analysis approach for single-molecule localization microscopy. *Nat. Commun.* (2019) https:/doi.org/10.1038/s41467-019-10007-4.
26. J. Serra, INTRODUCTION TO MATHEMATICAL MORPHOLOGY. *Comput. vision, Graph. image Process.* **35** (1986).
27. L. Vincent, L. Vincent, P. Soille, Watersheds in Digital Spaces: An Efficient Algorithm Based on Immersion Simulations. *IEEE Trans. Pattern Anal. Mach. Intell.* **13** (1991).
28. H. K. Hahn, M. T. Wenzel, O. Konrad-Verse, H. O. Peitgen, A minimally-interactive watershed algorithm designed for efficient CTA bone removal in *Lecture Notes in Computer Science (Including Subseries Lecture Notes in Artificial Intelligence and Lecture Notes in Bioinformatics)*, (2006).
29. L. Lam, S. W. Lee, Thinning methodologies—a comprehensive survey. *IEEE Trans. Pattern Anal. Mach. Intell.* **14** (1992).
30. W. Abu-Ain, S. N. H. S. Abdullah, B. Bataineh, T. Abu-Ain, K. Omar, Skeletonization Algorithm for Binary Images. *Procedia Technol.* **11** (2013).

31. D. Jin, K. S. Iyer, C. Chen, E. A. Hoffman, P. K. Saha, A robust and efficient curve skeletonization algorithm for tree-like objects using minimum cost paths. *Pattern Recognit. Lett.* **76** (2016).
32. S. Tsukita, S. Yonemura, S. Tsukita, ERM (ezrin/radixin/moesin) family: From cytoskeleton to signal transduction. *Curr. Opin. Cell Biol.* **9** (1997).
33. A. L. Neisch, R. G. Fehon, Ezrin, Radixin and Moesin: Key regulators of membrane-cortex interactions and signaling. *Curr. Opin. Cell Biol.* **23** (2011).
34. D. Pore, N. Gupta, The ezrin-radixin-moesin family of proteins in the regulation of B-cell immune response. *Crit. Rev. Immunol.* **35** (2015).
35. M. Sainio, *et al.*, Neurofibromatosis 2 tumor suppressor protein colocalizes with ezrin and CD44 and associates with actin-containing cytoskeleton. *J. Cell Sci.* **110** (1997).
36. M. Arpin, M. Algrain, D. Louvard, Membrane-actin microfilament connections: an increasing diversity of players related to band 4.1. *Curr. Opin. Cell Biol.* **6** (1994).
37. T. A. Martin, G. Harrison, R. E. Mansel, W. G. Jiang, The role of the CD44/ezrin complex in cancer metastasis. *Crit. Rev. Oncol. Hematol.* **46** (2003).
38. K. Gowrishankar, *et al.*, Active remodeling of cortical actin regulates spatiotemporal organization of cell surface molecules. *Cell* **149** (2012).
39. S. Saha, *et al.*, Active emulsions in living cell membranes driven by contractile stresses and transbilayer coupling. *Proc. Natl. Acad. Sci. U. S. A.* **119**, e2123056119 (2022).
40. H. Ponta, L. Sherman, P. A. Herrlich, CD44: From adhesion molecules to signalling regulators. *Nat. Rev. Mol. Cell Biol.* (2003) https:/doi.org/10.1038/nrm1004.
41. P. Lajoie, *et al.*, Plasma membrane domain organization regulates EGFR signaling in tumor cells. *J. Cell Biol.* **179** (2007).
42. J. A. Torreno-Pina, *et al.*, Enhanced receptor-clathrin interactions induced by N-glycan-mediated membrane micropatterning. *Proc. Natl. Acad. Sci.* **111**, 11037–11042 (2014).
43. G. Muñoz-Gil, *et al.*, Stochastic particle unbinding modulates growth dynamics and size of transcription factor condensates in living cells. *Proc. Natl. Acad. Sci. U. S. A.* **119**, e2200667119 (2022).

Chapter 6

Pre-docking nanoplatforms of DC-SIGN, CD44 and Galectin 9 increases virus engagement in immature dendritic cells

DC-SIGN is pathogen-recognition transmembrane receptor exclusively expressed at the plasma membrane of immature dendritic cells (iDCs), an important sub-set of cells from the immune system. DC-SIGN is responsible for recognising multiple pathogens and viruses, including HIV-1 and SARS-CoV-2 amongst others. It is known that DC-SIGN interacts with multiple proteins at the plasma membrane, and previous work from our group and others have identified CD44 and Galectin-9 as main interaction partners. In this Chapter we have generated multi-colour high-density maps (HiDenMaps) to simultaneously monitor in real time the interactions between these three proteins, prior to virus engagement. Moreover, we succeeded on generating GFP-labelled HIV-1 and SARS-CoV-2 virus-like particles (VLPs) enabling us to generate for the first time four-colour HiDenMaps. Using this approach, we have studied interactions between DC-SIGN and the VLPs in space and time, while monitoring at the same time the influence of CD44 and Galectin-9 on viral capture. Our results show an increased binding success of HIV-1 and SARS-CoV-2 virus-like particles when binding to CD44/DCSIGN/Gal9 tripartite as compared to DC-SIGN alone (i.e., without their membrane partners). Moreover, using mock viruses, we demonstrate that this tripartite nanoplatform is important for increased capture of HIV-1 and SARS-CoV-2. Overall, our results suggest a potential generalised mechanism of virus capture being mediated by CD44/DCSIGN/Gal9 pre-docking nanoplatforms on iDCs.

This work has been published as **Nicolas Mateos**, Enric Gutiérrez-Martínez, Irene Carlon-Andres, Sergi Padilla-Parra, Maria F. Garcia-Parajo, and Juan A. Torreno-Pina, "Multicolour single molecule imaging reveals optimised virus capture by pre-docking receptor nanoplatforms", *in preparation*

6.1 Motivation

The immune system is responsible for the defence of the human body against pathogens (1) and is made out of two parts based on specificity and speed: the innate and the adaptive immunity. The innate immunity is the immediate response of the body against invading pathogens. Pathogens have conserved pathogen-associated molecular patterns (PAMPS) which are recognised by toll-like receptors (TLRs) present on the membrane of immune cells such as dendritic cells(2). The adaptive immunity occurs at later stages of infection but it is antigen-specific and it is orchestrated by T cells and B cells. Interestingly, both immune responses are connected through dendritic cells (3).

Dendritic cells (DCs) were discovered by Ralph Steinman in the 1970s(4–7) and led him to win the Nobel Prize in Physiology and Medicine in 2011. The main role of DCs is to capture pathogens and present them to T cells. DCs are present in the human body in mainly two states: immature and mature. Immature DCs (iDCs) patrol the peripheral tissue in search of pathogens and antigens. Following antigen recognition, iDCs get activated (maturing) and migrate to the lymph nodes where now mature DCs (mDCs) will present the antigens to T cells and initiate the adaptive response(3).

Besides TLRs, DCs are equipped with C-type lectins(8) such as the dendritic cell-specific intercellular adhesion molecule-3-grabbing non-integrin (DC-SIGN; CD209)(9). Lectin-type receptors recognise self-antigens and act as adhesion receptors(10). Nonetheless, they also bind to carbohydrate structures present on the membrane of multitude of viruses, bacteria, parasites and yeast. In fact, DC-SIGN is responsible for recognising HIV-1(11), hepatitis C virus(12), Ebola virus(13), severe acute respiratory syndrome (SARS) coronavirus(14, 15), candida albicans(16) or mycobacterium tuberculosis(17) amongst other pathogens. Notably, HIV is able to trigger a hijacking process of the DC thereby mediating a trans-infection process of T cells in the lymph nodes(11). Indeed, when HIV-1 binds to DC-SIGN via its glycoprotein gp120(18), rather than undergoing an internalisation and a degradation process, HIV-1 triggers a downstream signalling that induces the migration of iDCs towards the lymph nodes. Once at the lymph nodes, DCs mediate the productive trans-infection of T-cells in a DC-SIGN dependent manner.

DC-SIGN is a tetrameric transmembrane protein with a carbohydrate-recognition domain (CRD) at the C-terminal, a neck region formed by a seven-and-a-half tandem repeat of 23 amino acids, a single N-glycosylation site located at the N-terminal of the neck region, a transmembrane domain and a cytosolic tail(19, 20). The CRD is responsible for both the recognition of pathogens and for the binding to the adhesion molecules ICAM-3(10). The neck domain is responsible for the tetramerisation of DC-SIGN at the plasma membrane(21–23) inducing a multivalent binding to ligands via avidity(23). Moreover, the cytosolic tail contains recycling and internalisation motifs (19, 20).

In our lab and by using single molecule sensitive techniques and advanced super-resolution imaging, we have studied the spatiotemporal organisation of DC-SIGN on the cell membrane of iDCs. Early studies using electron microscopy and near-field scanning optical microscopy (NSOM), showed that the neck region of DC-SIGN regulates the formation of nanoclusters on the cell membrane of ~100nm in mean(24–27) and these nanoclusters were essential for trapping virus-size particles. Our lab also focused on the impact of the N-glycosylation motif of DC-SIGN on the spatiotemporal organisation of the receptor using single molecule and super-resolution microscopy(28). By using STED nanoscopy, it was shown that the N-glycosylation motif of DC-SIGN does not impact on its nanoclustering. Moreover, and by using high-density single particle tracking (HD-SPT), the meso-scale organisation of DC-SIGN and the potential role of the N-glycosylation motif was studied. HD-SPT showed that the diffusion of WT-DC-SIGN was confined into micron-sized patches. In contrast, the mutant lacking the N-glycosylation motif, N80A, showed less confinement at the meso-scale. Importantly, it was shown that these WT-DC-SIGN micron-sized patches were enriched with clathrin-coated pits (CPPs) thereby impacting on the receptor internalisation route(16, 28, 29). Indeed, abrogation of the galectin-network with lactose (25 mM for 2 days) induced a reduced colocalisation of DC-SIGN with CCPs on iDCs(28). Thus, revealing the importance of galectins in the spatiotemporal organisation of DC-SIGN.

Galectins are a family of soluble glycan-binding lectins(30) that are thought to cross-link glycoproteins at the plasma membrane by creating the so-called galectin lattice(31, 32). So far, 15 different galectins have been identified and classified into three major groups from the protein architecture point of view(33). First, the proto-type group includes those galectins with only one carbon recognition domain (CRD) and can act as monomers (Gal-5,-7,-10) or homodimers (Gal-1,-2,-11,-13,-14,-15). Second, the tandem-repeat group refers to galectins containing two homologous CRDs linked by a protein residue (Gal-4,-6,-8,-9,-12). Third, the chimeric group consists galectins with a CRD and a N-terminal domain which can polymerise (Gal-3)(34, 35). Galectins show different binding affinities to N-glycans on the plasma membrane of cells(36).

In the context of DC-SIGN, it was previously shown that Gal-9 was enriched on the DC-SIGN phagosome(37). Gal-9 is a tandem-repeat galectin, which means that it is formed by two homologous but not identical CRDs connected by a protein link. Because the CRDs are not identical, Gal-9 can cross-link different glycoproteins, and it has been shown to induce cell-signalling and even cell death (38, 39). Our Lab showed that removal of Gal-9 from the cell surface by means of lactose impaired DC-SIGN spatiotemporal organisation at the meso-scale and hampered virus-like particle internalisation(28). In addition, it has been also shown that cytosolic Gal-9 interacts with cortical actin and DC-SIGN, contributing to the regulation of DC function (40). Altogether, these finding strongly indicate that Gal-9 has the potential to influence the spatiotemporal organisation of DC-SIGN. However, direct visualisation of Gal-9 and DC-SIGN at the relevant spatiotemporal scales has not been reported yet.

In addition to Gal-9, CD44 has been also found at DC-SIGN phagosome, amongst other proteins(37). Moreover, it has been extensively reported that Gal-9 binds to CD44 inducing different cellular signalling responses (41–43) and that CD44 has the ability to connect the extracellular milieu with the intracellular actin network (44, 45). Using confocal microscopy, our lab previously showed that CD44, Gal-9 and DC-SIGN colocalise at the plasma membrane of iDCs(28). Furthermore, preliminary studies by means of dual-colour HD-SPT exploration maps of DC-SIGN and CD44 on iDCs showed that these receptors explore the space together, not fully colocalising but in contiguous patches, one next to the other. Interestingly, as we showed in Chapter 4, CD44 interacts with the cortical actin cytoskeleton(46) and independent work from the Grinstein group also showed that CD44 functions as a picket, affixing the cortical actin cytoskeleton to the cell membrane(47). Based on all these findings, it seems highly likely that CD44 plays an important role regulating the galectin-dependent spatiotemporal organisation of DC-SIGN.

One of the main goals of this thesis is to resolve the role of CD44 and galectins in the spatiotemporal organisation of DC-SIGN. Importantly, we aim at understanding how this spatiotemporal organisation affects the successful engagement of viral particles in iDCS. Although quite some research in the field of virology has been devoted to the study of viral infection by means of single virus tracking (SVT) (48–52), they have not resolved interactions of virus-like particles with their receptors in real-time.

In this Chapter, we introduce a novel methodology based on multi-colour HiDenMap, as described in Chapter 3, of DC-SIGN, CD44 and Galectin-9. We will develop a three-colour quantum dot labelling strategy of each individual membrane protein allowing the simultaneous characterisation of three components with high temporal and spatial resolution at the single molecule level. Furthermore, we will extend our methodology to a four-colour configuration by introducing single virus HiDenMap thereby combining HiDenMaps of membrane proteins with freely diffusing virus like particles in the medium. To show the biological significance of our approach, we will apply our methodology to study virus capture by DC-SIGN of HIV-1 and SARS-CoV-2. Moreover, by developing novel analysis algorithms, we will characterise how DC-SIGN, CD44 and Galectin-9 form pre-docking nanoplatforms on the cell membrane thereby inducing enhanced viral capture on iDCs. Overall, this chapter introduces a novel technological framework to study early viral capture events by a multi-component system on the cell membrane at the single molecule level.

6.2 Materials and Methods

6.2.1 **Primary cell culture**

Human immature dendritic cells (iDCs) were obtained from peripheral blood mononuclear cells (PBMC) from HIV-1-seronegative donors using a Ficoll-Hypaque gradient (Alere Technologies AS). The monocyte population was selected by adherence on a T75cm2 flask for 1 hour. iDCs were obtained by culturing the monocytes in complete RPMI with 1.000 IU/ml GM-CSF (granulocyte-macrophage colony-stimulating factor) and IL-4 (interleukin-4) both from R&D for 6 days. The medium was replaced every two days with fresh GM-CSF and IL-4. Experiments were performed at day 6 from the monocyte extraction.

6.2.2 **Antibodies and reagents**

Monoclonal mouse anti-human CD44 (Clone G44-26) and monoclonal mouse anti-CD209 (Clone DCN46) were obtained from BD Biosciences. Recombinant human Galectin-9 protein (Cat. number 9064-GA) was obtained from R&D systems. SARS-CoV-2 spike protein recognition binding domain (S-RBD) 9x His tag was kindly provided by Dr Jose Francisco Rodriguez Aguirre and Dr Cesar Augusto Santiago Hernandez (CNB, CSIC). SARS-CoV-2 Spike Protein (RBD) Chimeric Recombinant Rabbit Monoclonal Antibody (P05DHuRb) tagged with Alexa Fluor™ 647 was obtained from eBioscience. Streptavidin Quantum Dots (565, 605, 655 and 755) were obtained from Thermo Fisher scientific.

6.2.3 **Single Chain antibody generation**

Both anti-human CD209 and CD44 single chain antibodies were generated using a similar protocol. First, the full chain antibodies were dialysed using 10K dialysis devices (Thermo Scientific™ Slide-A-Lyzer™ MINI Dialysis Devices, 10K MWCO) against PBS for 8 hours at 4ºC. Second, we concentrate the dialysed full chain antibodies to a concentration of 1 mg/ml. Third, we reduce the antibodies using DTT (1,4-dithiotrheritol, Sigma Aldrich) at 1 mM. We let the mix reduce at room temperature for 1 hour rotating. Then, we proceed to dialyse overnight against PBS using the 10K dialysis devices at 4ºC. Fourth, we stabilise the broken sulphide-bonds with Iodoacetamide at 20 mM. We let the mix at room temperature for 1 hour rotating gently and we dialyse to remove excess iodoacetamide overnight at 4ºC. Figure 6.1 shows the electrophoresis gel for the single chain antibodies and the full chain antibodies as a control.

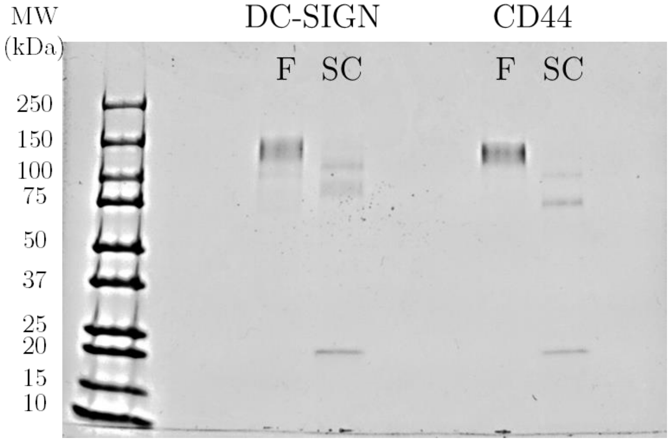

Figure 6.1 Electrophoresis gel showing for DC-SIGN and CD44 the bands for full-chain antibodies (F) and single-chain antibodies (SC).

6.2.4 Biotinylation and conjugation

We performed the biotinylation of single chain antibodies and rhGal9 with EZ-Link Sulfo-NHS-LC-Biotin (Thermo Fisher). We add a 20x mol excess of biotin and we let the mixture to shake for 1 hour in ice. Then, we dialyse using 10K units overnight at 4ºC to remove excess of non-reacting biotin. To generate the conjugation of single-chain/rhGal9 + QD, we mixed equal ratios of single-chain/rhGal9 and QDs and 5x excess of free biotin. To obtain a target concentration of 300 nM of stock conjugates, we first mixed 300 nM of QD with 1.5 µM biotin and then added 300 nM of single-chain/rhGal9.

6.2.5 Labelling strategy

To perform the single particle tracking experiments, we used conjugates of rhGal9/QD565, α-CD44/QD655 and α-DC-SIGN/QD705 at a concentration of 1 nM. For the HiDenMap experiments, we used conjugates of rhGal9/QD605, α-CD44/QD705 and α-DC-SIGN/QD655 at a concentration of 30 nM.

6.2.6 Pseudo-virus like particle generation

All the plasmids except the pr8ΔEnv.2 (obtained from addgene, Plasmid #12263) were kindly provided by Dr Sergi Padilla Parra and Dr Irene Carlon-Andres (KCL, London) as well as the protocol. Together with Dr Enric Gutierrez, we adapted the protocol in our lab as follows: 57 µL of Trans-IT reagent (Mirus) were added to 2 µg of pR8ΔEnv.2, 3 µg of Gag GFP, 1 µg of pcRev and 3 µg of BL4-3 to generate HIV VLPs as this plasmid expresses gp120 or 0.5 µg of SARS-CoV-2-Spike[D614G] to generate SARS-CoV-2 VLPs. To generate mock viruses, no plasmid generating the Env or the Spike protein was added. Then, we add the mixture to 1.9 mL of OPTIMEM (Gibco) and incubate for 15 min at room temperature. We add the mixture to 18 mL of DMEM with FBS and L-Glut and without antibiotics. We add the medium to HEK-293T cells at 80-90% confluency and we collect the supernatant at day 3. We first centrifuge briefly the supernatant (500 x g for 10 min) and filter the supernatant through a 0.45 µm filter. We concentrate the supernatant with Lenti-X concentrator (Takara) following the manufacturer’s protocol and resuspend it in RPMI. Finally, we aliquot the VLPs and freeze them using liquid nitrogen before storing them at minus 80ºC.

6.2.7 Sample preparation for SPT and HiDenMap experiments.

We plated ~50.000 cells on either glass coverslips (#1) coated with PLL (20 ng/ml) for control cells or on 35 mm Glass bottom dish with 10 mm micro-well (#1, Cellvis) also coated with PLL. We seeded the cells for at least 1 hour in RPMI without FBS, L-Gluy or antibiotics. The labelling strategy using the single chain-QDs was performed sequentially by diluting 1 µL of DC-SIGN/QD655 and 3 µL of CD44/QD705 in 46 µL of PBS with 6% BSA. We incubate the conjugates and the cells for 5 min. After washing 3 times in RPMI, we take 5 µL of rhGal9/QD605 and 45 µL of PBS diluted in 6% BSA and incubate for 5 min. Importantly and to avoid removing of the Gal-9 conjugate, we wash only once with RPMI. We then add RPMI to perform the imaging. For the experiments with VLPs (HIV, SARS-CoV-2 or mock) we added the VLPs defrosted and added 10 ng/ml of LPS. The mixture was added to the cells and imaged. The imaging is performed at 37ºC.

6.2.8 iDC response to S-RBD

To study the iDC response to S-RBD, we seeded 30.000 day 6 iDCs on Lab Tek 8-well plates (#1), which we previously coated with PLL (20 ng/ml). We led the cells adhere for 1 hour before starting any treatment. The conditions were either control (RPMI), S-RBD (50 nM in RPMI) and LPS (10 ng/ml in RPMI). After adding the medium with the different conditions, we fixed the cells using PFA 4% at either 10, 30, 60 or 90 min. We then labelled the samples with anti-human CD44 labelled with a secondary antibody tagged with AF488. We performed the confocal imaging in a Leica SP8 microscope making a Z-stack with a 100x objective.

6.2.9 Multi-colour SPT and generation of multi-colour HiDenMaps

Our strategy to resolve the interactions of DC-SIGN, Galectin-9 and CD44 at early stages of virus capture relies on the generation of multi-colour HiDenMaps by means of of HD-SPT. As mentioned in Chapter 3, HD-SPT provides high spatial (~20 nm) and temporal (30 frames/s) resolution at the single molecule level. Of crucial importance, the high labelling density required for multi-colour HiDenMaps allows the simultaneous localisation of a multi-component system at the single molecule level in living cells. This represents a step forward to other traditional techniques such as multi-colour SPT, where the probability of observing real time interactions between different components is quite low due to the high number of components (e.g., the expression level of membrane proteins) and the low labelling density required to reconstruct individual trajectories (typically 1-2 orders of magnitude lower as compared to HD-SPT, see also Chapter 3 or details regarding HD-SPT and HiDenMaps).

To optimise the design of the multi-colour single molecule setup, we took advantage of both the narrow fluorescence emission and broad excitation spectra of quantum dots (QDs) (Figure 6.2). We thus used QDs emitting at different spectral windows to label DC-SIGN, Gal-9 and CD44 (see also below). Moreover, the core of the virus-like particles (VLPs) was tagged with the green fluorescent protein (GFP). This exquisite combination of fluorescent emitters allowed simultaneous excitation of our multicomponent system using a single 488 nm laser line.

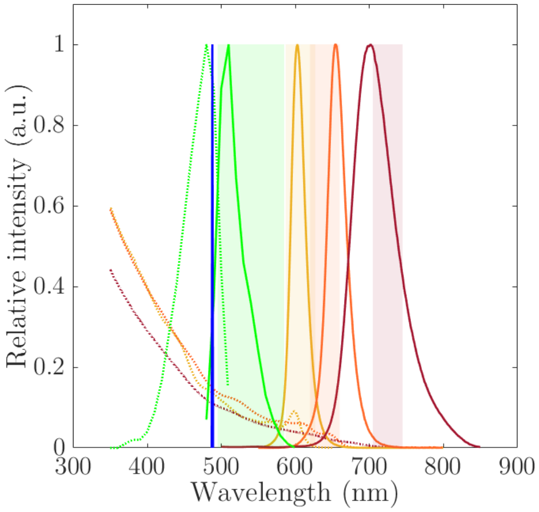

Figure 6.2 Excitation and emission spectra for GFP (green), QD605 (dark yellow), QD655 (orange) and QD705 (dark red). The excitation laser is drawn in blue and the band-pass filters are depicted by the shaded area. The green shaded area is the dichroic mirror with reflectance below 580 nm.

In order to immuno-label the proteins of interest DC-SIGN and CD44, specific single-chain antibodies were generated and biotinylated. Moreover, and in order to label Gal-9, recombinant human Gal-9 (rhGal9) was also biotinylated and conjugated with the corresponding QDs. In our experiments DC-SIGN was labelled with QD705 (SPT) or QD655 (HiDenMaps), CD44 with QD655 (SPT) or QD705 (HiDenMaps) and rhGal9 with QD565 (SPT) or QD605 (HiDenMap).

The optical setup is built around an inverted Nikon Ti-U microscope working under total internal reflection (TIR) illumination (Figure 6.3). The excitation light consists on a single diode-pumped solid-state 488 nm laser line which is circularly polarised using a quarter waveplate. The beam diameter is then increased using a telescope and ultimately focused at the back focal plane of a Nikon CFI APO TIRF 60x objective.

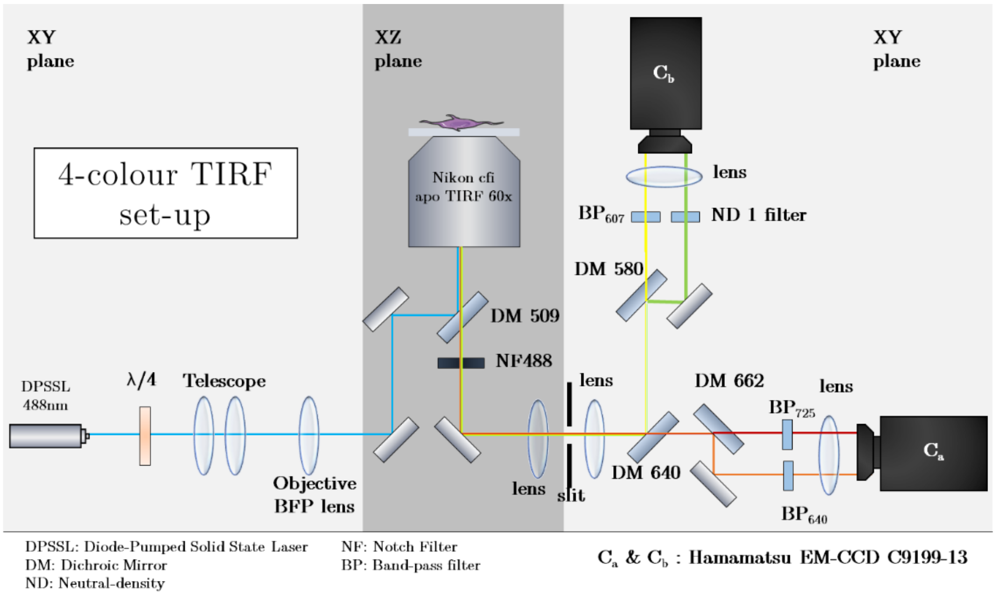

Figure 6.3 Schematics of our custom-built 4-colour TIRF inverted microscope. The sample is illuminated by a 488 nm laser line focused on the back focal plane of the objective. The fluorescence emission is collected through the objective and split into multiple optical paths using dichroic mirrors (DM) and filtered with band-pass filters. Each emission is focused on two different regions of an EM-CCD camera, leading to a four-colour detection scheme.

In order to obtain the TIR excitation, the beam is accurately shifted towards the edge of the objective using a mirror at the entrance of the inverted microscope. The emitted fluorescence light from the sample is collected through the same objective and the excitation light is filtered out using a notch-filter at 488nm. After creating the image using a slit, the emission light is split into two optical paths, each leading to a separate EM-CCD camera. Importantly, two images will be formed at each of the optical paths, obtaining a total of four simultaneously channels with different wavelengths. When single QDs or GFP-VLPs are placed on the set-up, the cross-talks between channels ranges from 5 to 20% in intensity. However, when all the QDs and GFP-VLPs are on the sample, then the intensity cross-talk becomes smaller and using proper thresholding in the particle detection, then the cross-detection is negligible.

Our analysis pipeline consists on generating four-colour HiDenMaps by localising single molecules at each frame of each channel and collapsing them all into a single image (Figure 6.4). In order to account for optical aberration due to differences in the optical paths of each channel, several images of

Tetraspeck™ beads visible in all the four channels were systematically acquired. By setting the channel corresponding to the GFP-labelled VLPs as the fixed channel, the affine transformation of the other three channels was defined. The affine transformation was then applied to all the localisations before collapsing them into a single image.

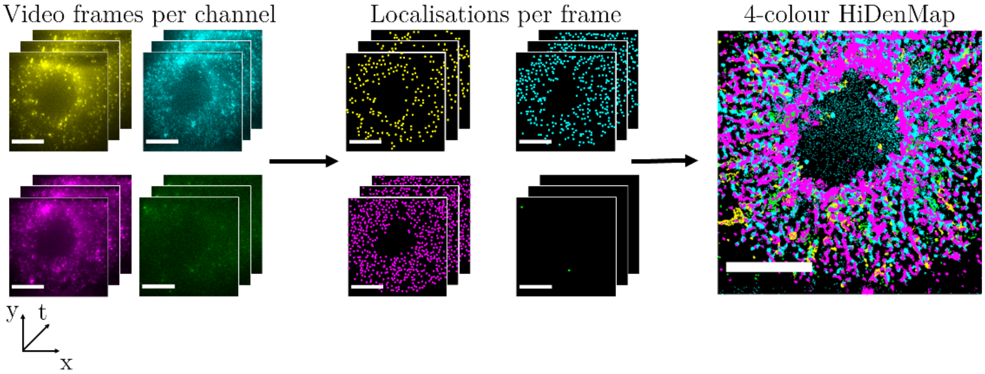

Figure 6.4 Schematics on how four-colours HiDenMaps are generated. From left to right: Video frames for each of the four channels. For each channel individual fluorescent molecules are localised at each frame of the video. Then, localisations per frame and channel are transformed using an affine transformation to correct the aberration of the optical paths and collapsed into a single image, the 4-colour HiDenMap. Scalebar: 10 µm.

6.2.10 Spatiotemporal autocorrelation decay

We took all the localisations of the HiDenMaps and applied a sliding time window, Δt, of 500 ms to temporally separate the localisations. The length of the window results from a compromise of having to accumulate sufficient localisations and still be short enough so that fast dynamics are not washed out. We then compute the autocorrelation curve as follows:

$$G_0\left(t_{lag} = m\Delta t\right) = \frac{1}{N-m} \sum_{i=1}^{N-m} \frac{< I(\Delta t_i) * I(\Delta t_i + m\Delta t) >}{< I(\Delta t_i) > \cdot < I(\Delta t_i + m\Delta t) >} \tag{6.1}$$

Here, $I(\Delta t_i)$ refers to the image of the i-th temporal window. To generate the images from localisations, we pixelated the space into 100 nm squared pixels and counted the number of localisations per pixel. We then normalised the curve to the first point ($t_{lag} = 0$ s). Finally, we fitted the decay curves from the second point onwards until $t_{\mathrm{lag}} = 50$ s. The fitting consists on a double exponential decay with a constant term:

$$F(t) = \tilde{A}_1 e^{-t/\tau_1} + \tilde{A}_2 e^{-t/\tau_2} + B \tag{6.2}$$

We performed the fitting in MATLAB's Curve Fitting Tool setting the bounds of $\widetilde{A_1}$, $\widetilde{A_2}$ and $B \in [0,1]$ and τ_1 and $\tau_2 \in [0,\infty)$. We chose '0.5' as the starting point for all the variables. The rest of parameters used for the fittings are summarised in the following table:

Table 6.1 Table summarizing the fitting options used in MATLAB

Algorithm	**Trust-Region**
Robust	On
Maximum iterations	10^5
Maximum number of evaluations	10^5
Minimum change in coefficients	10^{-8}
Maximum change in coefficients	10^{-2}
Termination tolerance on model value	10^{-16}
Termination tolerance on coefficient values	10^{-16}

Finally, once the fitting is performed, we rescaled the amplitudes of the exponential decays as follows:

$$A_1 = \frac{\widetilde{A}_1}{\widetilde{A}_1 + \widetilde{A}_2} \quad \& \, A_2 = \frac{\widetilde{A}_2}{\widetilde{A}_1 + \widetilde{A}_2} \tag{6.3}$$

6.2.11 **Multi-colour colocalisation algorithm**

We first took the VLP channel and run a DBSCAN algorithm (61), as described in Chapter 2, with parameters MinPts = 10 and $\varepsilon = 150$ nm to localise clusters of VLP localisations. With these settings, the algorithm will find events of VLPs that have visited the membrane for at least 10 frames. Moreover, at least 95% of the localisations for each defined cluster must have appeared at the membrane continuously as a function of time. Once the clusters are detected, we take each cluster of VLP localisations and define the visitation region of interest (ROI), which corresponds to the area visited by the virus. Then, we search for those localisations in the other three channels that explored the visitation ROI within the same time window that the VLP was on the membrane. If the three proteins visit the VLP area during the same time window, we then consider to have a true spatiotemporal colocalisation with the three proteins. If only one or two of the tripartite proteins visit the VLP area during the same time window, we then consider that the VLP colocalised with one or two proteins (denoted as “others” in the plots shown in Figure 6.13a and Figure 6.16a).

6.2.12 **Software**

For the single particle detection and to perform the linking of trajectories, we have used ImageJ’s FIJI plugin Trackmate (53, 54). For all the analysis of our data, we have used MATLAB R2020a.

6.3 Results

6.3.1 **Single molecule imaging of Gal-9 on the membrane of iDCs.**

To the best of our knowledge, no previous reports have documented the dynamics, nano- and the meso-scale organisation of Gal-9 on the surface of living cells. We thus used recombinant human Gal-9 (rhGal9) and first performed standard SPT experiments at low labelling conditions (1 nM) to investigate the dynamics of individual rhGal9 at the plasma membrane of iDCS. We labelled rhGal9 with streptavidin QD565 on living iDCs and performed imaging at a speed of 30 Hz. Representative trajectories showing the mobility of rhGal9 are presented in Figure 6.5a. A visual inspection of the trajectories reveals a large heterogeneity in the diffusion of rhGal9, ranging from fully immobile, restricted and highly mobile. To quantify the actual diffusion of rhGal9 we considered trajectories longer than 50 frames (>1.5 s) and calculated the apparent diffusion, $D_{1\text{-}4}$, of hundreds of individual trajectories from multiple cells following the approach explained in Chapter 2. The histogram of the $D_{1\text{-}4}$ values shows a bimodal distribution with a very slow population centred around $1.4 \cdot 10^{-3}$ µm^2/s and a faster population centred at ~ $2.2 \cdot 10^{-2}$ µm^2/s with a median value of $D_{1\text{-}4} = 1.9 \cdot 10^{-3}$ µm^2/s (Figure 6.5b).

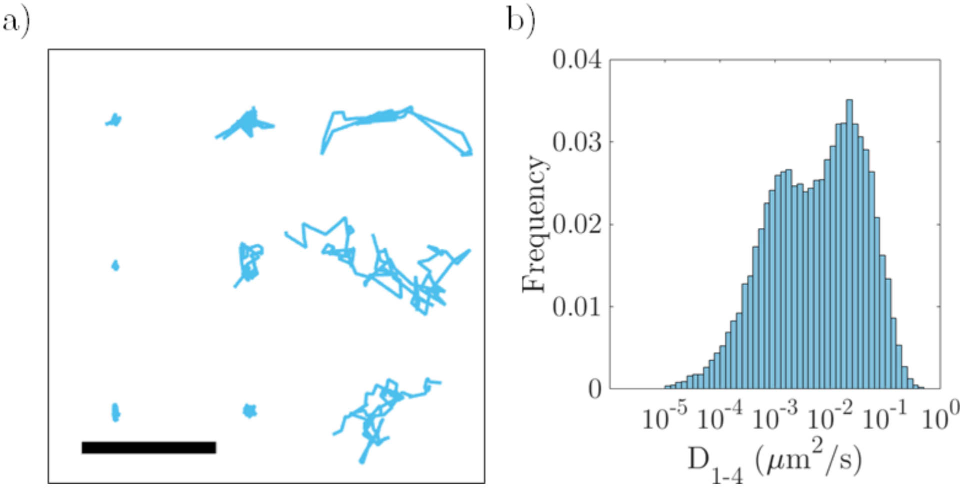

Figure 6.5 Single molecule dynamics for rhGal9 labelled with QD565 and imaged at 30 Hz. a) Representative single molecule trajectories of rhGal9. For the analysis we filtered the trajectories to be at least 50 points. b) Normalised semi-log distribution of $D_{1\text{-}4}$ values for rhGal9. The scalebar is 1µm.

We than performed HD-SPT experiments in order to generate HiDenMaps of rhGal9 at the surface of living iDCs. We labelled rhGal9 with QD605 for the HiDenMap experiments at a concentration of ~30 nM, and imaged at 30 HZ for 90 s.

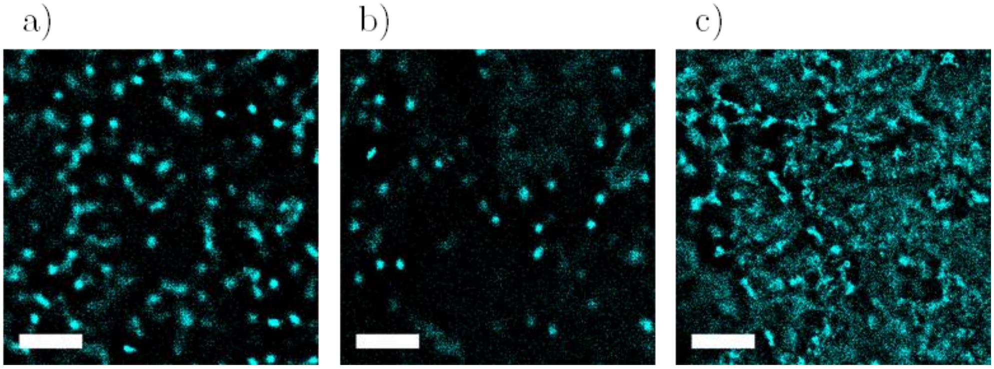

Figure 6.6 Representative HiDenMaps of rhGal9 labelled with QD605 and an integration time of 30 seconds. The number of localisations in each ROI are: 57.955 (a), 24.318 (b) and 111.140 (c). Each region of interest (ROI) corresponds to a different cell from a different donor taken on different dates. The scalebar is 2 µm.

Interestingly, the HiDenMap reveals a rather heterogeneous exploration of rhGal9 at the plasma membrane of iDCS with clearly defined hotspots enriched in localisations and other regions with more random-like localisations (Figure 6.6). These results indicate that over the course of imaging (30 s), a population of rhGal9 remains highly confined in regions around 100 nm, whereas other population of rhGal9 diffuses more freely and explores larger regions of the cell membrane. Moreover, we observed a large variability in rhGal9 mobility and spatiotemporal mapping of the cell membrane amongst different donors.

6.3.2 DC-SIGN, CD44 and Gal-9 interactions on the plasma membrane of iDCs.

To study the dynamics of single DC-SIGN and CD44 receptors by means of SPT, specific biotinylated single-chain antibodies conjugated with streptavidin QD705(for DC-SIGN) and QD655 (for CD44) were generated. Three-colour videos of DC-SIGN, CD44 and Gal-9 were recorded at 30 Hz and individual trajectories of the three different proteins were generated (Figure 6.5a for rhGal9 and Figure 6.7a,b for DC-SIGN and CD44 respectively). For each individual trajectory, the apparent diffusion, $D_{1\text{-}4}$, was extracted and compiled in a histogram. The distribution of $D_{1\text{-}4}$ values for both DC-SIGN and CD44 revealed a large spread, spanning several orders of magnitudes (Figure 6.7c,d), as expected for most transmembrane proteins. The median values obtained for both receptors are: $D_{1-4}^{DCSIGN} = 5.42 \cdot 10^{-2}\ \mu m^2/s$ and $D_{1-4}^{CD44} = 3.0 \cdot 10^{-2}\ \mu m^2/s$, which in in agreement with previously published data (28, 47, 55). Interestingly, these values are an order of magnitude faster than for rhGal9 (Figure 6.5)

Simultaneously to the experiments of SPT and HiDenMaps for rhGal9 we also studied the dynamics of DC-SIGN and CD44. We labelled DC-SIGN and CD44 using biotinylated single-chain antibodies conjugated with streptavidin QD705 (for DC-SIGN) and QD655 (for CD44) (Figure 6.7a,c). The apparent diffusion, $D_{1\text{-}4}$, distributions for DC-SIGN and CD44 reveal a small shoulder at slow diffusions and a bigger at faster diffusions (Figure 6.7b,d). The median values for these two proteins are which are an order of magnitude faster than for rhGal9 (Figure 6.5b).

To then enquire if there is any spatiotemporal relationship between these three different proteins, we generated multi-colour HiDenMaps. Fort this, DC-SIGN was labelled with QD655, CD44 with QD705 and rhGal9 with QD605, using all of them at a concentration of 30 nM. Three-colour videos were acquired at a frame rate of 30 Hz and localisations were accumulated for 90 seconds in total. The three-colour HiDenMaps revealed distinct patterns for the three proteins on the cell membrane but in close proximity to each other (Figure 6.8a). In fact, in the time window shown in Figure 6.8b (30 s), the three proteins show regions of confinement around ~200 nm together with a more diffusive pattern. Remarkably, these patterns are in close proximity to each other suggesting once more that the diffusion and spatial exploration of the three proteins on the cell membrane is highly coordinated.

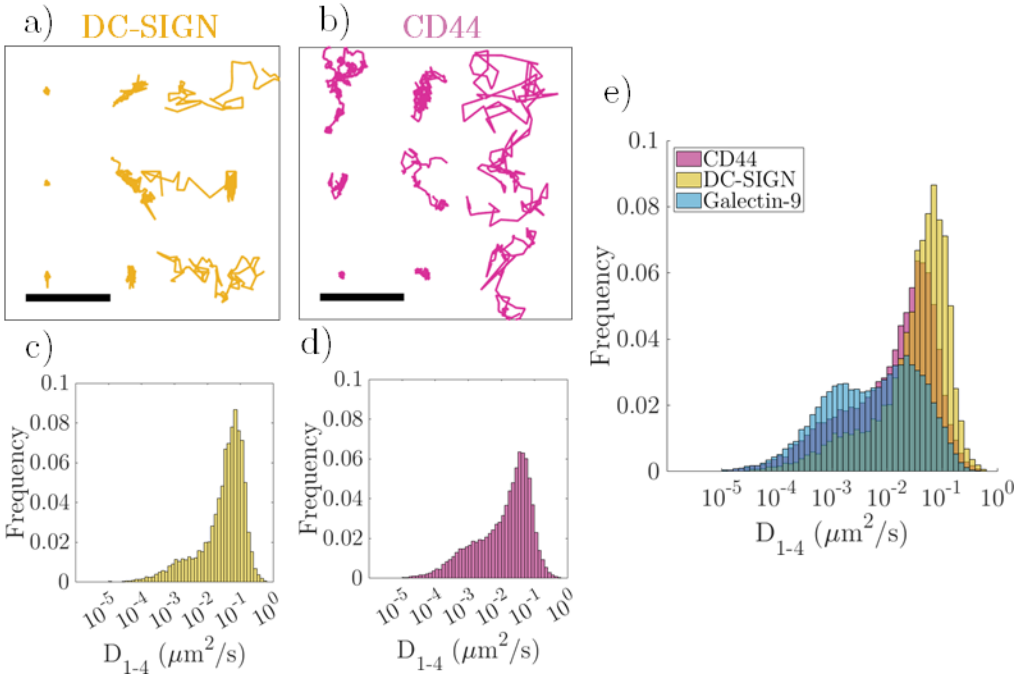

Figure 6.7 a) Representative single molecule trajectories of DC-SIGN labelled with streptavidin QD705. b) Representative single molecule trajectories of CD44 labelled with streptavidin QD655. c) Normalised semi-log distribution of D_{1-4} values for DC-SIGN. D) Normalised semi-log distribution of D_{1-4} values for CD44. e) Normalised semi-log distribution of D_{1-4} values for CD44, DC-SIGN and Gal-9. The scalebar is 1 µm.

In order to quantify a potential interaction between the three proteins at the mesoscale, the spatiotemporal autocorrelation decay for each HiDenMap was calculated (see Materials). Moreover, the different temporal scales of each

HiDenMap was extracted by performing a fitting with a double exponential function. Importantly, the autocorrelation was performed in time windows of 500 ms allowing a compromise between the number of localisations and an optimal high temporal resolution.

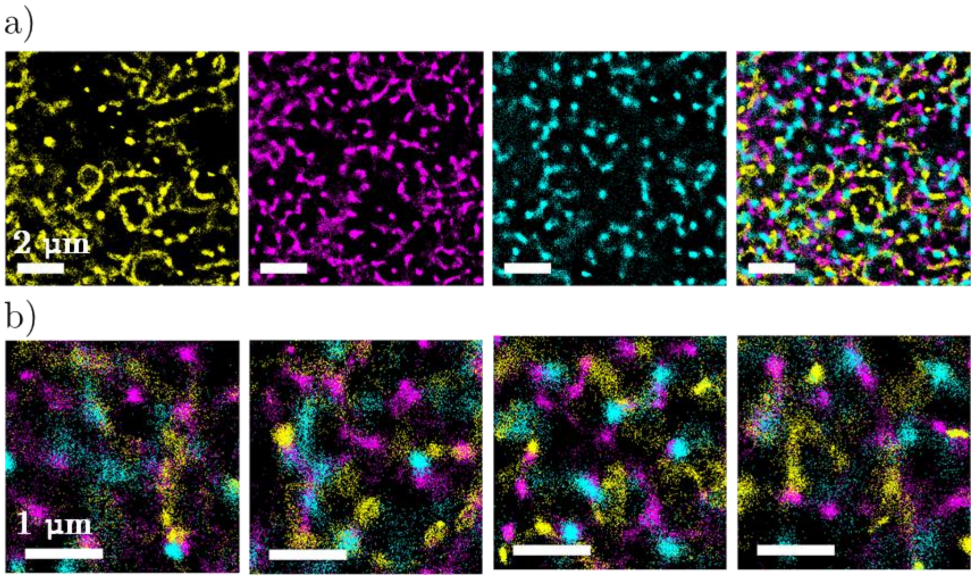

Figure 6.8 Representative 3-colour HiDenMaps with an integration time of 30 seconds. a) From left to right: DC-SIGN, CD44, rhGal9 and overlay of the three proteins. b) Zoom-in 3-by-3 µm ROIs of the same cell at different regions than for the top row.

From the autocorrelation analysis, two different time scales, a short decay, $\tau_1 \sim 3\ s$, and a long decay, $\tau_2 \sim 30\ s$, as well as the corresponding amplitudes, A_1 and A_2, respectively were extracted. Interestingly, the distributions of the time scales and the amplitudes from each different protein are not statistically different (Figure 6.9). This suggests that although the three proteins exhibit different diffusions at short time scales as observed by SPT, there is a persistent dynamic structure at the meso-scale inducing a preferred interaction between DC-SIGN, CD44 and Gal-9.

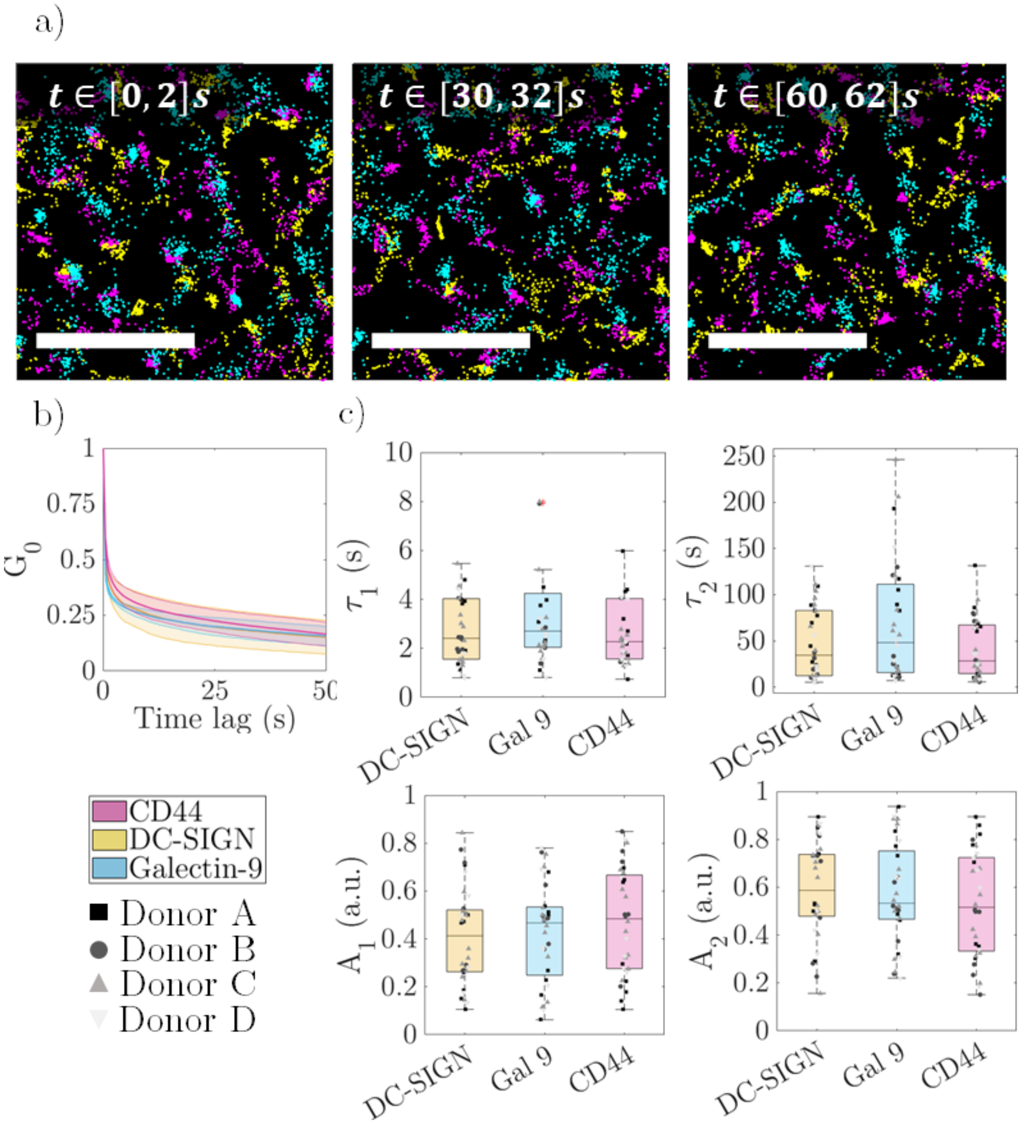

Figure 6.9 Temporal evolution of HiDenMaps. a) 2 seconds time windows of three-colour HiDenMaps at different observation times. b) Temporal autocorrelation decay for DC-SIGN, CD44 and rhGal9 with a ΔT of 500 ms. The weighted line corresponds to the mean between donors and the shaded area de standard deviation between donors. c) The parameters (A1, A2, τ1, τ2) fitted from the decays for DC-SIGN, CD44 and rhGal9. Each point in the scatter plot corresponds to a single cell. The Scalebar: 2 µm

6.3.3 Dynamic behaviour of GFP-tagged HIV VLPs at the plasma membrane of iDCs

After showing the successful implementation of the three-colour single molecule sensitive setup and the novel HiDenMap based analysis to unravel a meso-scale interaction between DC-SIGN, CD44 and rhGal9, there is an open question as to whether this pre-existing interaction could promote virus capture by DC-SIGN. To address this question, GFP-tagged HIV VLPs were introduced thereby expanding the experimental system into four colours. The three proteins of interest were labelled using QDs (DC-SIGN/QD655, CD44/QD705 and rhGal9/QD605) and the HIV-VLPs contained GFP proteins in the core.

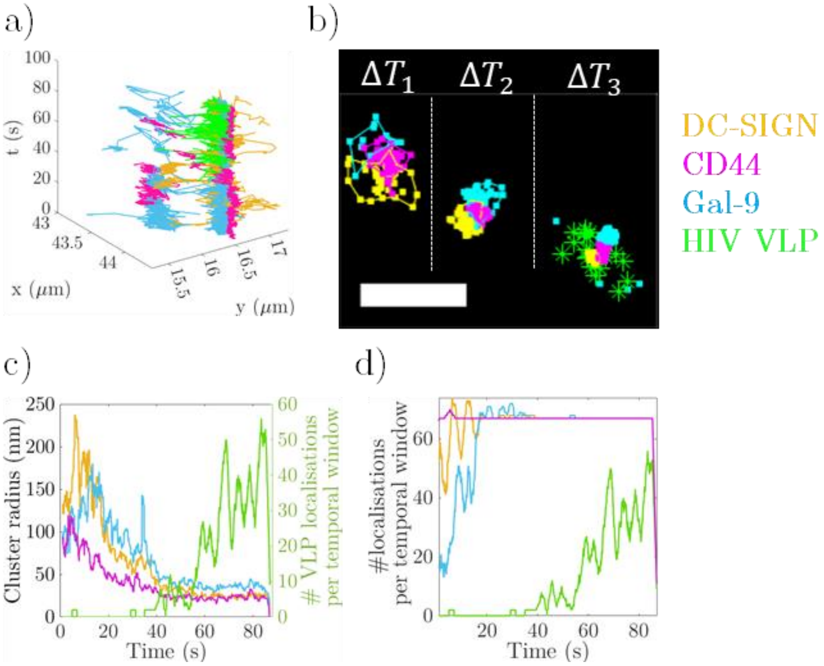

Figure 6.10 Single virus tracking and landing on the membrane, where it interacts with preestablished docking-platforms. a) SPT of the HIV-GFP VLP (green) and single molecules of DC-SIGN (yellow), CD44 (magenta) and rhGal9 (cyan). b) Cluster tracking of DC-SIGN (yellow), CD44 (magenta) and rhGal9 (cyan) while they diffuse together prior to HIV-GFP VLP (green) engagement. The three time-windows shown are: $\Delta T_1 \in [2,4]s, \Delta T_2 \in [25,27]s$ and $\Delta T_3 \in [70,72]s$. Scalebar is 500 nm. c) Quantification of cluster radius (left axis) and the number of VLP localisations per time-window (2 s time windows). d) Number of localisations per cluster and time-window for the three proteins and the VLP localisations per time-window (2 s time windows).

As a preliminary approach, SPT of the individual components was performed and their trajectories overlaid (Figure 6.10) showing a direct engagement of the VLP with a pre-formed docking platform of DC-SIGN, CD44 and Gal-9. Indeed, individual cluster tracking showed correlated diffusion of the three proteins prior to their encountering of the VLPs. Remarkably, there is a decrease in the cluster radius of the three components when engaging with the virus suggesting that the virus rearranges the spatiotemporal organisation of the docking platform at the nanoscale.

In order to extend this approach to a systematic analysis, four-colour HiDenMaps were generated from HD-SPT videos using time windows of 90 s at a frame rate of 30 Hz. Remarkably, by visually observing the obtained four-colour HiDenMaps, HIV VLPs appear to be engaged preferentially on hotspots where DC-SIGN/CD44 and Gal-9 colocalise (Figure 6.11). To rigorously quantify these observations, an algorithm based on a multi-colour DBSCAN analysis between the four components was developed (see Materials & Methods). This analysis showed that there is a significant enhanced (10-30%) colocalisation between DC-SIGN and the HIV VLP compared to a mock virus lacking the Env protein (from now on Δgp120 VLP, Methods) in three out of four donors (Figure 6.11b). A similar colocalisation degree was observed between CD44 and HIV VLP in two out of the four donors. As for Gal-9, there is a strong enhanced colocalisation (up to 60%) with HIV VLPs in all the donors. Remarkably, when analysing the four components together, there is an enhanced colocalisation (10-20%) of the three proteins and HIV VLPs compared to Δgp120 VLP in three out of the four donors (Figure 6.11b). Overall, our results reveal an enhanced interaction of HIV VLPs with the pre-docking nanoplatforms formed by DC-SIGN, CD44 and Gal-9.

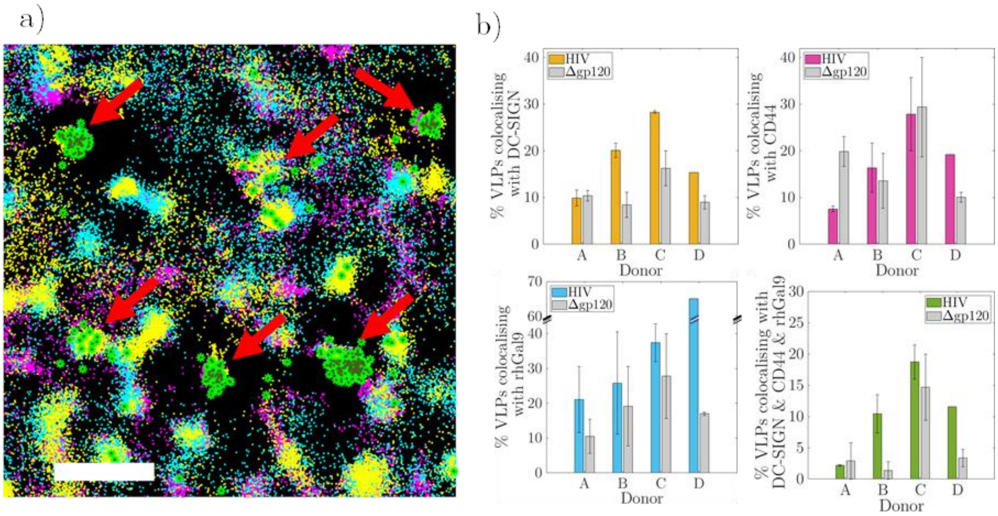

Figure 6.11 a) Representative 4-colour HiDenMap ROI with an observation time of 50 s and a frame rate of 30 Hz. The four channels correspond to DC-SIGN (yellow), CD44 (magenta), rhGal9 (cyan) and HIV-GFP VLP (green stars with dark dot, and the clusters are pointed with red arrows). b) Percentage of VLPs colocalising with at least DC-SIGN (top left), CD44 (top right), rhGal9 (bottom left) or with all three proteins (bottom right). Total number of HIV-GFP VLPs detected: 92 for donor A, 64 for donor B, 53 for donor C and 26 for donor D. Total number of gp120 VLPs detected: 106 for donor A, 88 for donor B, 52 for donor C and 216 for donor D. Number of cells analysed: 40 for donor A, 40 for donor B, 40 for donor C and 30 for donor D. The Scalebar: 1 µm.

We then addressed whether there is a functional consequence of this multi-component colocalisation. For this, the lateral behaviour of single viruses was analysed and correlated with their interaction probability with CD44, DC-SIGN and Gal-9. In other words, HIV VLPs HiDenMaps were generated and classified according to whether (I) the VLP disengaged from the plasma membrane during the acquisition time (vanishing); (II) the VLP transiently appeared (transient); (III) the VLP appeared and remained engaged (appearing); (IV) the VLP remained engaged (persistent). Figure 6.12 shows representative examples of these four different scenarios. Importantly and from the biological point of view, transient and vanishing VLPs were considered as unsuccessful engagements whereas appearing and persisting VLPs as successful. By correlating the dynamic engagement behaviour of the VLPs with the different colocalising membrane proteins, an increased successful engagement was found when the three different proteins (DC-SIGN, CD44 and Gal-9) colocalised together with the VLPs (Figure 6.13a). This trend was clearly found in two of the four donors

(donors C and D), while no significant differences were found for donor B. In addition, and for completeness, we also include data for donor A, in which viral engagement was unsuccessful. Importantly, gp120-VLPs showed a reduced engagement (vanishing or transient) compared to WT-VLPs even if they colocalised with DC-SIGN, CD44 and Gal-9. Thus, our data shows that colocalisation of HIV VLPs with DC-SIGN, CD44 and Gal-9 enhances the probability of a successful engagement of VLPs on the cell membrane of immature DCs.

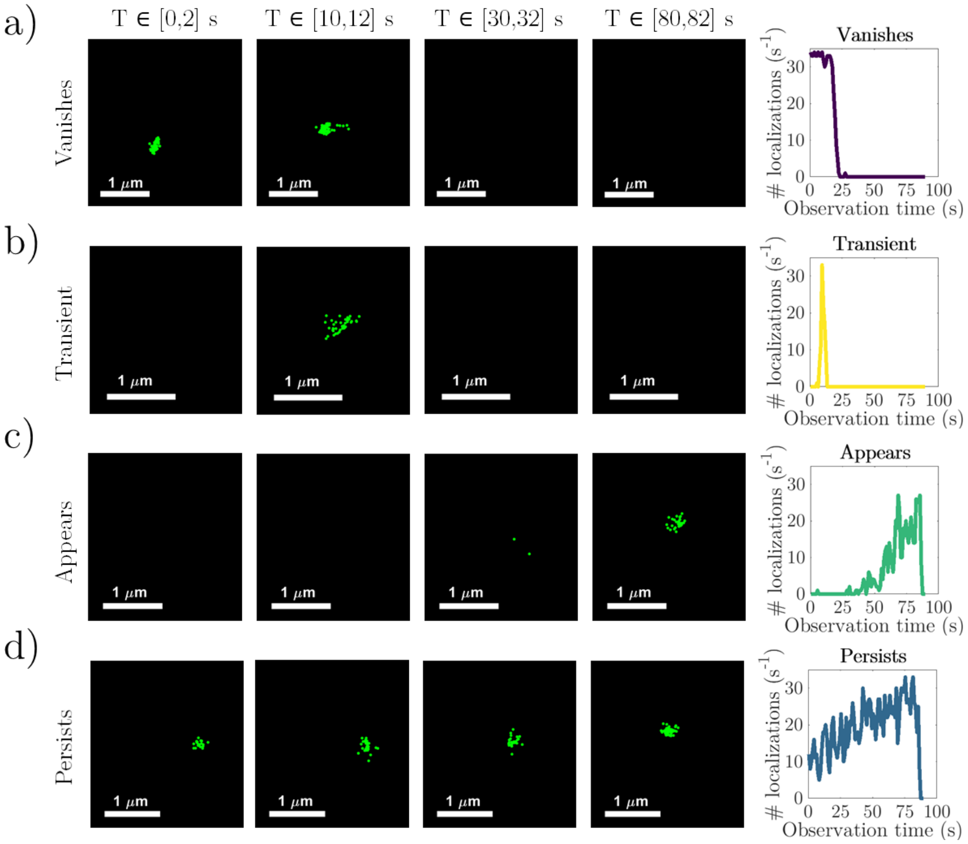

Figure 6.12 HiDenMaps revealed different engagement probabilities of HIV-GFP VLPs on the plasma membrane. Multiple ROIs display the localisations within a temporal window of 2 seconds. The last column shows the plot of localisations per second for the ROI on the same row. a) VLPs can vanish from the field of view due to unbinding or because the signal was too low to be detected. b) VLPs can show a transient behaviour, which means that the VLP arrives to the membrane but disengages and disappear. c) VLPs can appear on the field of view, which means

that the VLPs arrive at the plasma membrane and remain bound until the end of the acquisition time. d) VLPs can persist, which means that the VLP is visible throughout all the observation time (90 seconds). Scalebars: 1 µm.

Vanishing VLPs are those that either disengage from the plasma membrane and freely diffuse elsewhere or that because of the thresholding in the detection, we cannot detect them any longer. Photobleaching is discarded since we did tests at the same excitation conditions on HIV-GFP VLPs on glass and we were able to observe them for longer than the observation time. Transient VLPs are those that appear during the acquisition but leave the membrane after few seconds, thus not having a successful engagement with the membrane. Appearing VLPs are those that engage with the membrane during the acquisition and remain on the plasma membrane until the end of the observation time. Persistent VLPs are visible throughout the acquisition time. From a biological point of view, we classify the VLP engagement as successful (appearing and persistent) or unsuccessful (vanishing and transient).

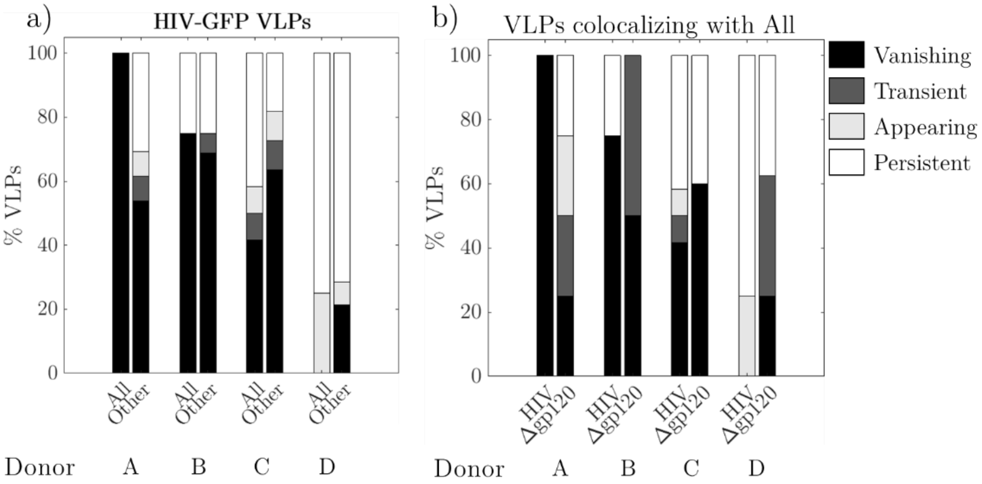

Figure 6.13 Dynamic engagement of individual HIV-GFP VLPs as function of the colocalising proteins. a) Percentage of HIV-GFP VLPs showing different engagement dynamics when they colocalise with all three proteins (DC-SIGN, CD44 and rhGal9) i.e., denoted as “All” in the plot; or with only a subset of the proteins, denoted as “Others”. b) Dynamic engagement for VLPs colocalising with all three proteins, for HIV-GFPs and the mutant Δgp120 VLPs. White and light grey bars correspond to successful engagement, while black and dark grey correspond to unsuccessful engagement. Total number of HIV-GFP VLPs detected: 92 for donor A, 64 for donor B, 53 for donor C and 26 for donor D. Total number of gp120 VLPs detected: 106 for donor A, 88 for donor B, 52 for donor C and 216 for donor D. Number of cells analysed: 40 for donor A, 40 for donor B, 40 for donor C and 30 for donor D.

6.3.4 SARS-CoV-2 and DC-SIGN

After having established with our novel methodology that the multi-component CD44/DC-SIGN/Gal-9 nanoplatforms indeed enhance HIV viral engagement on the cell membrane of iDCs, it remains to be elucidated whether our approach can be extended and generalised to other viruses. As such, and taking into consideration the global COVID-19 pandemics, we applied our experimental settings to SARS-CoV2 VLPs. It has been recently reported that DC-SIGN might indeed mediate SARS-CoV-2 viral binding even in the absence of the canonical receptor ACE-2 (14, 15, 56–59). Hence, we enquired whether SARS-CoV-2 virus capture could be enhanced by the presence of pre-interaction of DC-SIGN with CD44 and Gal-9.

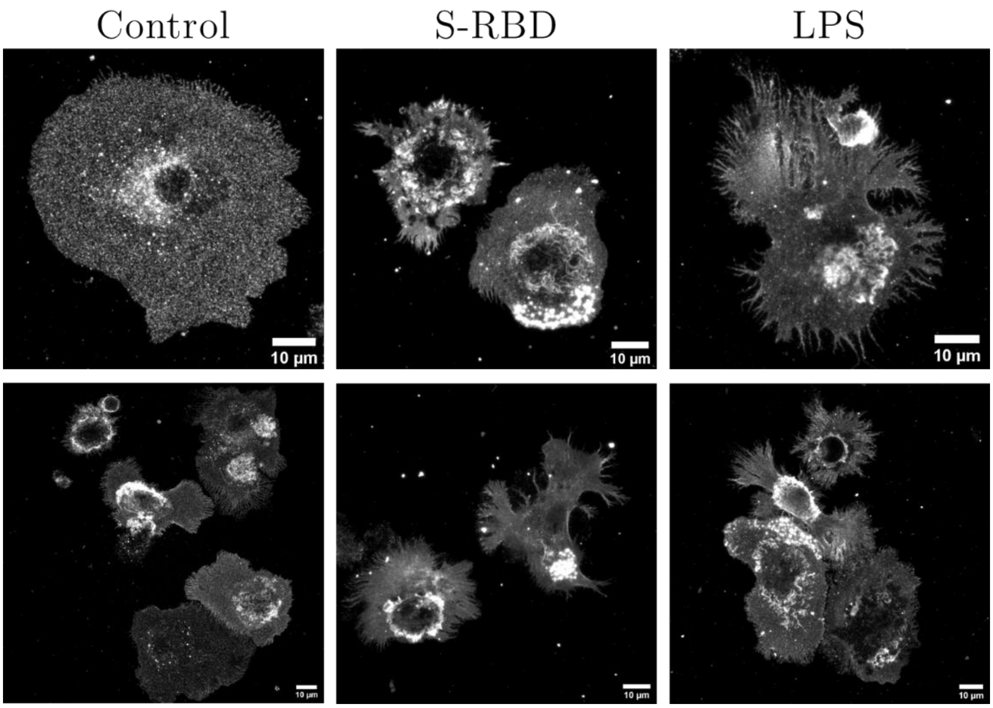

Figure 6.14 iDCs activation upon exposure to S-RBD for 90 min and membrane labelled with anti-CD44 (AF488). a) Control cells. b) Cells exposed with S-RBD (50 nM) during 90 min. c) Cells exposed with 10 ng/ml of LPS during 90 min. Scalebars: 10 µm.

As a first approach and to test whether SARS-CoV-2 could have an impact on iDC engagement and activation, iDCs were challenged with the soluble S-RBD spike protein. As a positive control for iDC activation, we also stimulated iDCs with the toll-like receptor 9 ligand LPS (Lipopolysaccharide, 10 ng/ml). Remarkably, after only 90 min of exposure to the soluble S-RBD spike protein, iDCs displayed an activation phenotype similar to that of LPS-treated iDCs (Figure 6.14).

In addition to iDC activation, we then asked whether SARS-CoV-2 VLPs could be preferentially engaged by the CD44/DC-SIGN/Gal-9 pre-docking nanoplatforms. In order to generate SARS-CoV-2 VLPs, a plasmid encoding the S-protein ([D614G] the Wuhan variant with a point mutation) was expressed using the HIV VLP backbone. The same mock virus without any receptor specific membrane protein, i.e., ΔSpike, was used as a negative control, in analogy to HIV VLP experiments. Using multi-colour HiDenMaps and DB-SCAN analysis as previously shown for HIV-VLPs, SARS-CoV-2 VLPs colocalised with DC-SIGN in 20% of the cases in the three donors analysed (Figure 6.15a). CD44 and Gal-9 also showed an enhanced colocalisation with SARS-CoV-2 VLPs in two of the three donors (Figure 6.15b,c). Remarkably, enhanced colocalisation of SARS-CoV-2 VLPs with the three proteins was observed in two of the three donors, as compared to experiments performed using Spike VLPs (Figure 6.15d). Thus, these results indicate that also in the case of SARS-CoV-2, pre-docking platforms formed by the tripartite proteins increase the capture of the virus.

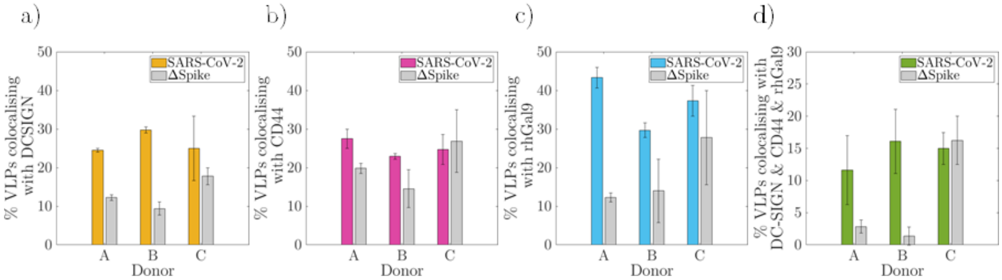

Figure 6.15 SARS-CoV-2 GFP VLPs show enhanced colocalisation with DC-SIGN (a), CD44 (b), rhGal9 (c) and with the three proteins (d). Note that the y-axis range is shorter in d, than for the previous plots. As a negative control we used the same Δgp120 VLPs which here we denote as ΔSpike. Total number of SARS-CoV-2-GFP VLPs detected: 132 for donor A, 74 for donor B and 87 for donor C. Total number of ΔSpike VLPs detected: 106 for donor A, 88 for donor B and 52 for donor C. Number of cells analysed: 40 for donor A, 40 for donor B and 40 for donor C.

Finally, the dynamic engagement behaviour of individual SARS-CoV-2 VLPs were also correlated with their colocalisation degree with CD44/DC-SIGN and Gal-9. SARS-CoV-2 VLPs colocalising with the three proteins showed enhanced membrane engagement as compared to a lower number of colocalising proteins (Figure 6.16a). Indeed, SARS-CoV-2 VLPs remained more efficiently engaged to the plasma membrane compared to mock viruses (Figure 6.16b). Overall, these results show that SARS-CoV-2 VLPs show enhanced engagement when binding to the multi-component CD44/DC-SIGN/Gal-9 pre-docking nanoplatforms.

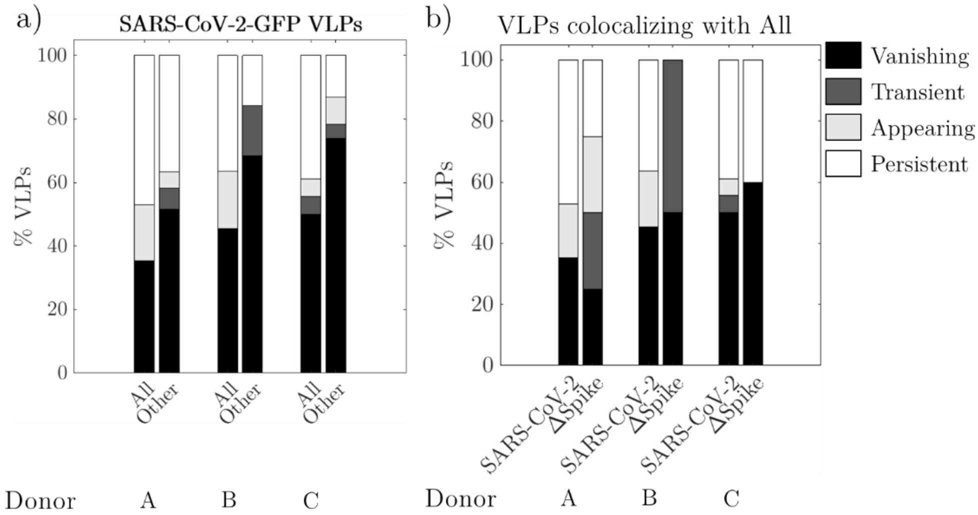

Figure 6.16 Dynamic engagement of individual SARS-CoV-2-GFP VLPs as function of the colocalising proteins. a) Percentage of SARS-CoV-2-GFP VLPs showing different engagement dynamics when they colocalise with all three proteins (DC-SIGN, CD44 and rhGal9) i.e., denoted as "All" in the plot; or with only a subset of the proteins, denoted as "Others". b) Dynamic engagement for VLPs colocalising with all three proteins, for SARS-CoV-2-GFP and the mutant ΔSpike VLPs. White and light grey bars correspond to successful engagement, while black and dark grey correspond to unsuccessful engagement. Total number of SARS-CoV-2-GFP VLPs detected: 132 for donor A, 74 for donor B and 87 for donor C. Total number of ΔSpike VLPs detected: 106 for donor A, 88 for donor B and 52 for donor C. Number of cells analysed: 40 for donor A, 40 for donor B and 40 for donor C.

6.4 Discussion

In this Chapter we have focused on resolving multi-component interactions of DC-SIGN with CD44 and Galectin-9 on the plasma membrane of iDCs and their impact on virus capture. We have established a novel multi-colour methodology that has allowed us to map in real time and with nanometric localisation accuracy interactions between four different molecular components, three of them being proteins located in the plasma membrane of living cells and a four-channel devoted to the dynamic visualisation of individual viruses and their interaction with the tripartite proteins. To the best of our knowledge, such powerful methodology has not been described before.

The galectin lattice has been proposed to compartmentalise glycoproteins at the plasma membrane of living cells by cross-linking them, regulating their diffusion and endocytosis. The roles of galectins have been widely studied and specially their effect in cell biology, cancer biology or immunity (31, 32, 39). However, to our knowledge, a direct visualisation of an intact galectin lattice has not yet been accomplished by means of microscopy. In order to tackle this, we have studied the single molecule dynamics of recombinant human Galectin-9 (rhGal9) using SPT on the plasma membrane of iDCs. Remarkably, we found that, although being a soluble protein, Gal-9 shows a stable 2-D diffusive behaviour on the cell membrane. Moreover, the distribution of diffusion coefficients is shifted towards lower values as compared to CD44 and DC-SIGN. This suggests that Gal-9 might be potentially connecting different diffusing membrane proteins on the cell membrane thereby effectively reducing their lateral mobility. Moreover, by applying HiDenMaps, we found a heterogeneous organisation of Gal-9 consisting on localised hotspots of around 200 nm in size and diffusive patterns supporting the concept that the Galectin lattice is indeed highly dynamic.

When studying the spatiotemporal organisation of DC-SIGN, Gal-9 and CD44 using SPT and HiDenMaps, we found that their dynamics are not correlated at the nanoscale. However, and remarkably, their meso-scale organisation shows a strong multi-component correlation as extracted from the autocorrelation analysis applied to the HiDenMaps. Importantly, the temporal scales retrieved from the analysis (~3 seconds and ~30 seconds) are consistent with the ones extracted in Chapter 5 suggesting that cortical actin might be the master regulator of the lateral behaviour of CD44, DC-SIGN and Gal-9 at the micron-scale. Indeed, CD44 has been suggested as a picket protein that links the underlying actin cytoskeleton and the extracellular milieu (47). In this chapter, we show that the galectin lattice adds a new organisation layer thereby linking DC-SIGN with CD44 at the meso-scale (28).

We wanted to further assess a potential functional outcome of the inter-connected meso-scale organisation of these three proteins. To tackle this, we extended the three-colour setup to a four-colour configuration where we introduced in the extra channel single virus HiDenMaps of VLPs. Remarkably, we found an enhanced colocalisation between HIV VLPs and CD44/DCSIGN/Gal-9 on three of the four donors tested. This interaction is gp120-specific, and thus DC-SIGN dependent, since mock viruses lacking the envelope protein gp120 showed reduced colocalisation with the tripartite proteins. This finding thus suggests that nanoclusters of CD44/DCSIGN/Gal-9 can act as viral pre-docking nanoplatforms on the cell membrane. Interestingly, this interaction could be further enhanced by the direct binding of Gal-9 to gp120 as it has been observed for Galectin-1 and Galectin-3 (60–62). We further expanded our single virus HiDenMap analysis by directly visualising the dynamic engagement of single viruses on the cell membrane in relation to their location with pre-formed nanoplatforms. We found an increased successful engagement of HIV VLPs when the viruses colocalised with the tripartite proteins indicating that pre-docking nanoplatforms of the three proteins promote a more efficient viral capture.

Finally, to show that our methodology can be applied to other viruses, we extended our multi-colour HiDenMap measurements to SARS-CoV-2 VLPs. Since it has been reported that DC-SIGN is a receptor for SARS-CoV-2 viruses (14, 15, 56–59), we hypothesised that SARS-CoV-2 capture could also be mediated by CD44/DCSIGN/Gal9 pre-docking nanoplatforms on iDCs. Indeed, our results show increased binding of SARS-CoV-2 viruses to the CD44/DCSIGN/Gal9 tripartite compared to mock viruses. This suggests a potential generalised mechanism of virus capture being mediated by CD44/DCSIGN/Gal9 pre-docking nanoplatforms on iDCs.

From the technological point of view, we have presented a novel generalised experimental and analysis framework that represents a step forward in the study of the spatiotemporal organisation of a multi-component system at the single molecule level. Our experimental approach offers the possibility to study the interaction between different components with high temporal and spatial resolution. We have applied this technique to follow the dynamics of individual viruses in combination with up to three receptors on the cell membrane but it can certainly be extended to other multi-component processes in the cell. As such, our experimental approach opens a new door in the quantitative study of dynamic processes at the nanometre scale, allowing multiplexing at the single molecule level.

6.5 References

1. J. Parkin, B. Cohen, An overview of the immune system. *Lancet* **357** (2001).
2. L. A. J. O'Neill, D. Golenbock, A. G. Bowie, The history of Toll-like receptors-redefining innate immunity. *Nat. Rev. Immunol.* **13** (2013).
3. J. Banchereau, R. M. Steinman, Dendritic cells and the control of immunity. *Nature* **392** (1998).
4. R. M. Steinman, Z. A. Cohn, Identification of a novel cell type in peripheral lymphoid organs of mice: I. Morphology, quantitation, tissue distribution. *J. Exp. Med.* **137** (1973).
5. R. M. Steinman, D. S. Lustig, Z. A. Cohn, Identification of a novel cell type in peripheral lymphoid organs of mice: III. Functional properties in vivo. *J. Exp. Med.* **139** (1974).
6. R. M. Steinman, Z. A. Cohn, Identification of a novel cell type in peripheral lymphoid organs of mice: II. Functional properties in vitro. *J. Exp. Med.* **139** (1974).
7. R. M. Steinman, G. Kaplan, M. D. Witmer, Z. A. Cohn, Identification of a novel cell type in peripheral lymphoid organs of mice: V. Purification of spleen dendritic cells, new surface markers, and maintenance in vitro*. *J. Exp. Med.* **149** (1979).
8. C. G. Figdor, Y. Van Kooyk, G. J. Adema, C-type lectin receptors on dendritic cells and langerhans cells. *Nat. Rev. Immunol.* **2** (2002).
9. T. B. H. Geijtenbeek, *et al.*, Identification of DC-SIGN, a novel dendritic cell-specific ICAM-3 receptor that supports primary immune responses. *Cell* **100** (2000).
10. Y. Van Kooyk, T. B. H. Geijtenbeek, DC-SIGN: Escape mechanism for

pathogens. *Nat. Rev. Immunol.* **3** (2003).

11. T. B. H. Geijtenbeek, *et al.*, DC-SIGN, a dendritic cell-specific HIV-1-binding protein that enhances trans-infection of T cells. *Cell* (2000) https:/doi.org/10.1016/S0092-8674(00)80694-7.
12. I. S. Ludwig, *et al.*, Hepatitis C Virus Targets DC-SIGN and L-SIGN To Escape Lysosomal Degradation. *J. Virol.* **78** (2004).
13. C. P. Alvarez, *et al.*, C-Type Lectins DC-SIGN and L-SIGN Mediate Cellular Entry by Ebola Virus in cis and in trans . *J. Virol.* (2002) https:/doi.org/10.1128/jvi.76.13.6841-6844.2002.
14. Z.-Y. Yang, *et al.*, pH-Dependent Entry of Severe Acute Respiratory Syndrome Coronavirus Is Mediated by the Spike Glycoprotein and Enhanced by Dendritic Cell Transfer through DC-SIGN. *J. Virol.* **78** (2004).
15. R. Amraei, *et al.*, CD209L/L-SIGN and CD209/DC-SIGN Act as Receptors for SARS-CoV-2. *ACS Cent. Sci.* **7** (2021).
16. A. Cambi, *et al.*, The C-type lectin DC-SIGN (CD209) is an antigen-uptake receptor for Candida albicans on dendritic cells. *Eur. J. Immunol.* (2003) https:/doi.org/10.1002/immu.200310029.
17. T. B. H. Geijtenbeek, *et al.*, Mycobacteria target DC-SIGN to suppress dendritic cell function. *J. Exp. Med.* **197** (2003).
18. B. M. Curtis, S. Scharnowske, A. J. Watson, Sequence and expression of a membrane-associated C-type lectin that exhibits CD4-independent binding of human immunodeficiency virus envelope glycoprotein gp120. *Proc. Natl. Acad. Sci. U. S. A.* **89** (1992).
19. H. Feinberg, D. A. Mitchell, K. Drickamer, W. I. Weis, Structural basis for selective recognition of oligosaccharides by DC-SIGN and DC-SIGNR. *Science (80-.).* **294** (2001).
20. D. A. Mitchell, A. J. Fadden, K. Drickamer, A novel mechanism of carbohydrate recognition by the C-type lectins DC-SIGN and DC-SIGNR. Subunit organization and binding to multivalent ligands. *J. Biol. Chem.* **276** (2001).
21. H. Feinberg, Y. Guo, D. A. Mitchell, K. Drickamer, W. I. Weis, Extended neck regions stabilize tetramers of the receptors DC-SIGN and DC-SIGNR. *J. Biol. Chem.* **280** (2005).
22. Q. D. Yu, *et al.*, Autonomous Tetramerization Domains in the Glycan-binding Receptors DC-SIGN and DC-SIGNR. *J. Mol. Biol.* **387** (2009).
23. S. Menon, *et al.*, Binding-site geometry and flexibility in DC-SIGN demonstrated with surface force measurements. *Proc. Natl. Acad. Sci. U. S. A.* **106** (2009).
24. A. Cambi, *et al.*, Microdomains of the C-type lectin DC-SIGN are portals for virus entry into dendritic cells. *J. Cell Biol.* **164** (2004).
25. M. Koopman, *et al.*, Near-field scanning optical microscopy in liquid for high resolution single molecule detection on dendritic cells. *FEBS Lett.* **573** (2004).

26. B. I. De Bakker, *et al.*, Nanoscale organization of the pathogen receptor DC-SIGN mapped by single-molecule high-resolution fluorescence microscopy. *ChemPhysChem* **8** (2007).

27. C. Manzo, *et al.*, The neck region of the C-type lectin DC-SIGN regulates its surface spatiotemporal organization and virus-binding capacity on antigen-presenting cells. *J. Biol. Chem.* **287** (2012).

28. J. A. Torreno-Pina, *et al.*, Enhanced receptor-clathrin interactions induced by N-glycan-mediated membrane micropatterning. *Proc. Natl. Acad. Sci.* **111**, 11037–11042 (2014).

29. A. Cambi, D. S. Lidke, D. J. Arndt-Jovin, C. G. Figdor, T. M. Jovin, Ligand-conjugated quantum dots monitor antigen uptake and processing by dendritic cells. *Nano Lett.* **7** (2007).

30. S. H. Barondes, *et al.*, Galectins: A family of animal β-galactoside-binding lectins. *Cell* **76** (1994).

31. O. B. Garner, L. G. Baum, Galectin-glycan lattices regulate cell-surface glycoprotein organization and signalling in *Biochemical Society Transactions*, (2008) https:/doi.org/10.1042/BST0361472.

32. I. R. Nabi, J. Shankar, J. W. Dennis, The galectin lattice at a glance. *J. Cell Sci.* (2015) https:/doi.org/10.1242/jcs.151159.

33. J. Hirabayashi, K. I. Kasai, The family of metazoan metal-independent β-galactoside-binding lectins: structure, function and molecular evolution. *Glycobiology* **3**, 297–304 (1993).

34. H. Leffler, S. Carlsson, M. Hedlund, Y. Qian, F. Poirier, Introduction to galectins. *Glycoconj. J.* **19** (2002).

35. D. Delacour, A. Koch, R. Jacob, The role of galectins in protein trafficking. *Traffic* **10** (2009).

36. J. Hirabayashi, *et al.*, Oligosaccharide specificity of galectins: A search by frontal affinity chromatography. *Biochim. Biophys. Acta - Gen. Subj.* **1572** (2002).

37. S. I. Buschow, *et al.*, Unraveling the human dendritic cell phagosome proteome by organellar enrichment ranking. *J. Proteomics* (2012) https:/doi.org/10.1016/j.jprot.2011.11.024.

38. S. Bi, L. A. Earl, L. Jacobs, L. G. Baum, Structural features of galectin-9 and galectin-1 that determine distinct T cell death pathways. *J. Biol. Chem.* **283** (2008).

39. L. A. Earl, S. Bi, L. G. Baum, Galectin multimerization and lattice formation are regulated by linker region structure. *Glycobiology* **21** (2011).

40. L. Q. Cano, *et al.*, Intracellular Galectin-9 Controls Dendritic Cell Function by Maintaining Plasma Membrane Rigidity Intracellular Galectin-9 Controls Dendritic Cell Function by Maintaining Plasma Membrane Rigidity. *ISCIENCE* **22**, 240–255 (2019).

41. R. Tanikawa, T. Tanikawa, M. Hirashima, A. Yamauchi, Y. Tanaka, Galectin-9 induces osteoblast differentiation through the CD44/Smad signaling pathway. *Biochem. Biophys. Res. Commun.* **394** (2010).
42. S. Katoh, *et al.*, Galectin-9 inhibits CD44-hyaluronan interaction and suppresses a murine model of allergic asthma. *Am. J. Respir. Crit. Care Med.* **176** (2007).
43. C. Wu, *et al.*, Galectin-9-CD44 interaction enhances stability and function of adaptive regulatory T cells. *Immunity* **41** (2014).
44. H. Ponta, L. Sherman, P. A. Herrlich, CD44: From adhesion molecules to signalling regulators. *Nat. Rev. Mol. Cell Biol.* (2003) https:/doi.org/10.1038/nrm1004.
45. P. Mrass, *et al.*, CD44 Mediates Successful Interstitial Navigation by Killer T Cells and Enables Efficient Antitumor Immunity. *Immunity* **29** (2008).
46. P. Sil, *et al.*, Dynamic actin-mediated nano-scale clustering of CD44 regulates its meso-scale organization at the plasma membrane. *Mol. Biol. Cell* (2020) https:/doi.org/10.1091/mbc.E18-11-0715.
47. S. A. Freeman, *et al.*, Transmembrane Pickets Connect Cyto- and Pericellular Skeletons Forming Barriers to Receptor Engagement. *Cell* **172**, 305-317.e10 (2018).
48. B. Brandenburg, X. Zhuang, Virus trafficking - Learning from single-virus tracking. *Nat. Rev. Microbiol.* **5** (2007).
49. T. Endreß, *et al.*, HIV-1-cellular interactions analyzed by single virus tracing. *Eur. Biophys. J.* **37** (2008).
50. S. L. Liu, *et al.*, Single-Virus Tracking: From Imaging Methodologies to Virological Applications. *Chem. Rev.* **120** (2020).
51. D. K. Cureton, C. E. Harbison, E. Cocucci, C. R. Parrish, T. Kirchhausen, Limited Transferrin Receptor Clustering Allows Rapid Diffusion of Canine Parvovirus into Clathrin Endocytic Structures. *J. Virol.* **86** (2012).
52. C. Johnson, J. Exell, Y. Lin, J. Aguilar, K. D. Welsher, Capturing the start point of the virus–cell interaction with high-speed 3D single-virus tracking. *Nat. Methods 2022*, 1–11 (2022).
53. J. Y. Tinevez, *et al.*, TrackMate: An open and extensible platform for single-particle tracking. *Methods* **115** (2017).
54. D. Ershov, *et al.*, TrackMate 7: integrating state-of-the-art segmentation algorithms into tracking pipelines. *Nat. Methods 2022 197* **19**, 829–832 (2022).
55. P. Sil, *et al.*, Dynamic actin-mediated nano-scale clustering of CD44 regulates its meso-scale organization at the plasma membrane. *Mol. Biol. Cell* **31**, 561–579 (2020).
56. N. Rahimi, C-type lectin CD209L/L-SIGN and CD209/DC-SIGN: Cell adhesion molecules turned to pathogen recognition receptors. *Biology (Basel).* **10** (2021).
57. A. Marzi, *et al.*, DC-SIGN and DC-SIGNR Interact with the Glycoprotein of Marburg Virus and the S Protein of Severe Acute Respiratory Syndrome

Coronavirus. *J. Virol.* **78** (2004).

58. D. P. Han, M. Lohani, M. W. Cho, Specific Asparagine-Linked Glycosylation Sites Are Critical for DC-SIGN- and L-SIGN-Mediated Severe Acute Respiratory Syndrome Coronavirus Entry. *J. Virol.* **81** (2007).
59. W. T. Soh, *et al.*, The N-terminal domain of spike glycoprotein mediates SARS-CoV-2 infection by associating with L-SIGN and DC-SIGN. *bioRxiv* (2020).
60. C. St-Pierre, *et al.*, Host-Soluble Galectin-1 Promotes HIV-1 Replication through a Direct Interaction with Glycans of Viral gp120 and Host CD4. *J. Virol.* **85** (2011).
61. S. Sato, M. Ouellet, C. St-Pierre, M. J. Tremblay, Glycans, galectins, and HIV-1 infection. *Ann. N. Y. Acad. Sci.* **1253** (2012).
62. C. N. Scanlan, J. Offer, N. Zitzmann, R. A. Dwek, Exploiting the defensive sugars of HIV-1 for drug and vaccine design. *Nature* **446** (2007).

Chapter 7

Conclusions and outlook

In this final chapter we draw some general conclusions of the thesis. The main aim of this PhD research has been to develop new quantitative methodologies and novel approaches that rely on single molecule imaging with the final goal of contributing to a deeper understanding on how molecules on the cell membrane organise in space and time to regulate cellular function. First, we shortly recapitulate our super-resolution studies where we have devised novel analysis tools to quantify the data. Second, we summarise the principle and main characteristics of our novel method called high-density maps (HiDenMaps) to quantify high-density single particle tracking data. Third, we summarise and discuss our studies on CD44 using HiDenMaps, namely, revealing its hierarchical and multi-scale temporal organisation mediated by the cortical actin cytoskeleton. Lastly, we highlight our research on virus capture by DC-SIGN in immature dendritic cells where we revealed the existence of pre-docking platforms of the DC-SIGN/CD44/Galectin-9 tripartite and their relevance for enhanced viral capture. We also provide some future perspectives on the use of HiDenMaps and potential improvements.

Understanding the spatiotemporal compartmentalisation of proteins in living cells at the nanoscale is crucial to elucidate their functions. A great deal of information has been obtained in the last years by the use of fluorescence-based super-resolution (SR) microscopy, or by the application of single particle tracking (SPT) approaches. Typically, these spatial (obtained via SR) and temporal (derived from SPT) studies are conducted separately due to technical limitations. Nevertheless, they provide different pieces of information that have greatly contributed to a wider understanding of molecular organisation and its dynamics. In this thesis, we have first shown some of the analyses approaches that we have developed to quantify SR data. SR microscopy is a great asset to study the spatial organisation of proteins and together with our algorithms and novel analyses have enabled us to gain further insights onto the organisation of different biomolecules: the pathogen recognition receptor Siglec-1 on mature dendritic cells, integrins and adaptor proteins in focal adhesions, the phosphatase PRL-3 and is role in clathrin mediated integrin endocytosis and RNA polymerase II (not shown in the thesis).

Unfortunately, SR microscopy techniques still suffer from poor temporal resolution, which hampers temporal studies of proteins. High-density single particle tracking (HD-SPT) has recently emerged as a powerful technique to bridge between SR-SMLM (super-resolution single molecule localisation microscopy) and SPT to investigate the spatiotemporal organisation of molecules(1–3). In this thesis, we have developed an approach to exploit HD-SPT without reconnecting trajectories to generate high-density maps (HiDenMaps) in just few seconds. HiDenMaps allow to study how molecules dynamically explore their environment from the nano- to the meso-scale. In Chapter 3, we stablished the technical requirements to generate faithful HiDenMaps using *in-silico* simulations of molecules diffusing in a Brownian motion fashion. We showed that proteins diffusing in a Brownian motion manner, such as proteins embedded on a lipid bilayer, render a homogeneous HiDenMap. On the contrary, CD44, a transmembrane protein that interacts with both the underlying cortical actin and components of the extracellular matrix (ECM), exhibits a highly inhomogeneous HiDenMap, diffusing in a meshwork-like pattern. Therefore, by simply collapsing the localisations into a single image as we have done to generate HiDenMaps, we can begin to ascertain heterogeneities on how molecules interact with their environment. Moreover, a key property of HiDenMaps is the temporal information encoded in the localisations and thus, by tuning the integration time of the HiDenMap we can probe the nanoscale and the mesoscale spatial organisation of the protein of interest. For instance, we have shown that by integrating during one second all the localisations from a HD-SPT experiment, we can obtain a HiDenMap of CD44 that contains similar information as to a STORM image of the same receptor. Both approaches have indeed revealed CD44 nanoclustering with comparable nanocluster sizes. Despite the biological mechanisms leading to the nanoclusters in STORM and HiDenMap (1 second integration) might be different, HiDenMaps provide additional and new dynamic information on the emergence of nanoclusters and their dynamic evolution in time and space.

We further showed that HiDenMaps is a methodology fully compatible with other live cell imaging techniques such as homo-Forster's resonance energy transfer (homo-FRET)(4). In a collaboration with Major's Lab at the National Centre for Biological Sciences (NCBS, Bangalore), we combined HIDenMaps with homo-FRET to further study CD44. Aside from its ability to interact with both the cortical actin cytoskeleton and with the extracellular milieu as described above, CD44 is especially interesting because it has been shown to act as a transmembrane picket compartmentalising other receptors at the plasma membrane of cells(5). Our joint research enabled us to build an understanding on the hierarchical organisation of CD44 at the plasma membrane of cells(6). Combining anisotropy measurements with homo-FRET and HiDenMaps we could directly ascertain that the nanoclusters measured by anisotropy corresponded to localisation hotspots in HiDenMaps. Moreover, these hotspots were enriched throughout a meshwork-like pattern. Interestingly, the lifetime of the hotspots (~ 3 seconds) corresponded well with the timescale of the transient confinements exhibited by single CD44 molecules(6). We also identified the actin cytoskeleton as being responsible for the transient confinement of the receptor. Thus, the receptor associates with actin-enriched regions transiently and unbinds to resume its diffusion until it finds another actin region to bind again. We believe that the localisation hotspots identified by the HiDenMaps correspond to the events in which CD44 binds to actin acting as a transmembrane picket as described by Freeman et al (5). Because the nanoclustering ability of CD44 is lost upon formin perturbation and the pattern revealed by HiDenMaps are affected by removing the cytosolic tail of the receptor and by formin perturbation, we concluded that the mesoscale spatiotemporal meshwork of CD44 indeed arises from its interactions with cortical actin. As a whole, our data support the picture of a tightly coupled actin-membrane composite where even proteins that do not directly couple to actin are impacted by the patterning of the underlying cortical actin meshwork(5, 7, 8).

Motivated by the actin-driven patterns revealed from CD44 HiDenMaps, we focused our efforts to develop novel algorithms to further analyse and quantify these patterns. These tools are described in detailed in Chapter 5 and summarised here. Using a new algorithm developed, which we call *Rivers*, we have been able to extract the patterns from the point-like data and use these patterns to filter the localisations in the HiDenMaps to perform a more segmented analysis. Because the patterns arise dynamically from multiple interactions of receptors with the underlying actin network, we analysed the temporal scales of such patterns. From the pattern dynamics, we found two distinct temporal scales, a short lived (~4 seconds) and a long lived (~ 30 s). Analysing also the dynamics outside the patterns, we found that the interactions outside the pattern are short lived and frequent. On the other hand, within the patterns the interactions are mostly long lived and more persistent. To further investigate the nature of long-lived persistent interactions in the pattern, we performed correlative HiDenMaps and SPT. We took advantage of photobleaching to reconnect trajectories at later stages of the acquisition of HiDenMaps where the effective labelling is dampened. Using standard SPT routines we then determined transient arrests of single CD44 molecules in the order of ~250 ms and correlated the transient confinement zones of single molecule trajectories with the localisation hotspots that appear in the HiDenMaps. Remarkably, we discovered that the hotspots in HiDenMaps are in fact built from multiple transient arrests of single molecules in the same region. These findings strengthen the hypothesis from Chapter 4, where we accounted the hotspots in the HiDenMaps as events where CD44 interacts with actin and acting as a transmembrane picket. A major finding of our work has been the measurement of three distinct temporal scales that regulate the spatiotemporal compartmentalisation of CD44, ranging from the nano- to the meso-scale.

Foreseeing the potential of using HiDenMaps to ascertain the interactions of single molecules with their environment and build analysis schemes that range from the nano-scale to the meso-scale, we further extended our methodology to study viral capture by cells of the immune system. In particular, we have focused on elucidating multi-component interactions of the pathogen recognition receptor DC-SIGN with CD44 and Galectin-9 and their role in virus capture. DC-SIGN is responsible for recognising a multitude of pathogens and viruses in immature dendritic cells (iDCs). DC-SIGN is a transmembrane receptor known to form nanoclusters that enhance the capture capability of trapping virus-sized particles (9). Preliminary studies from our group indicated that the spatiotemporal compartmentalisation of DC-SIGN at the plasma membrane of iDCs could be mediated by the interaction with CD44 and Galectin-9(10). Motivated by these earlier studies we implemented a multi-colour HiDenMap experimental scheme that enabled us to simultaneously follow the diffusion of these three different proteins as well as the virus (i.e., four colour scheme). We tagged the proteins using quantum dots and used GFP to tag HIV-1 and SARS-CoV-2 virus-like particles (VLPs). Using both SPT and HiDenMaps we found that while the diffusion of DC-SIGN, CD44 and Galectin-9 where different from each other, their mesoscale organisation showed a strong interaction with correlated temporal scales. The temporal scales retrieved from the global mesoscale dynamics match well with those measured in Chapter 5, suggesting that cortical actin might be the master regulator of the lateral behaviour of DC-SIGN, CD44 and Galectin-9 at the micron-scale. To assess the functional outcome of this inter-connected mesoscale organisation, we studied the interaction of VLPs with DC-SIGN while also tagging the other proteins. Trying to perform this study with standard SPT or even with HD-SPT approaches would be a huge struggle. Fortunately, using HiDenMaps we could determine where the interactions take place simply by overlaying the four individual HiDenMaps. Using this approach, we found an increased successful engagement of VLPs (both HIV-1 and SARS-CoV-2) when the viruses colocalised with the DC-SIGN/CD44/Galectin9 tripartite. Since HiDenMaps are so versatile, we could identify events where VLPs engaged with the plasma membrane at mid acquisition times and assess the spatial organisation of the tripartite prior the engagement. Remarkably, we revealed the existence of pre-docking nanoplatforms of the DC-SIGN/CD44/Galectin9 tripartite which promoted a more efficient viral capture. Thus, with our novel approach of multi-colour HiDenMaps we found a potential generalised mechanism of virus capture mediated by DC-SIGN/CD44/Galectin-9 pre-docking nanoplatforms on iDCS.

In summary, during the span of this thesis we have investigated the spatiotemporal organisation of multitude proteins mainly at the plasma membrane of cells. We have implemented novel algorithms to quantify super-resolution microscopy images to answer the biological questions regarding the spatial organisation of integrins, Siglec-1 and PRL-3. More importantly, the gross of this thesis has been devoted to the development of HiDenMaps to elucidate the spatiotemporal organisation of proteins at the plasma membrane of cells.

HiDenMaps is a simple concept but as we have shown, it is extremely powerful in the study of how molecules explore the space. Although in this thesis we have mainly focused on the plasma membrane of cells, HiDenMaps can be extended to other cellular contexts besides the plasma membrane. For instance, we have used HiDenMaps to study progesterone receptor (PR) transcription factor condensates in the nucleus of living cells(11). Indeed, using HiDenMaps we observed an accumulation of PR in nanoscale hotspots upon hormone treatment compared to the control in which no hotspots were visible. The emergence of these hotspots originate from the formation of PR condensates within the nucleus(11). Additionally, the multi-colour HiDenMap scheme herein presented has a huge potential to study interactions between multiple proteins simultaneously. As an example of a plausible application would be in the study of blocking antibodies for HIV-1 prevention, since we could label the antibodies, the proteins of interest and the viruses to see *in-situ* the real effect on blockage of the viral engagement. Moreover, we could study complex systems such as focal adhesions and obtain spatiotemporal information on the organisation of multiple integrin species and adaptor proteins as a function of substrate stiffness. Other possible applications could be the study of membrane contact sites, condensates within the nucleus,… The amount of possibilities on using

HiDenMaps to elucidate the spatiotemporal organisation of molecules in cells is almost infinite, we believe that we have contributed with a methodology that can make an impact in the field of biophysics. Indeed, because of its simplicity, HiDenMaps have the potential to be easily implemented in any analysis workflow in any lab.

However, HiDenMaps analysis still needss improvement in order to provide additional quantitative information. For instance, HD-SPT algorithms developed by Masson's lab provide energy potential maps and diffusivity maps which are extremely powerful(3, 12, 13). Since HiDenMaps do not rely on trajectory reconnection, this is currently beyond its capabilities. Moreover, for slow diffusing molecules ($D<10^{-4}$ µm^2/s) the time required to observe the full exploration of space is very long ($T_{obs} > 10^4$ s) which poses a major limitation in terms of acquisition. Currently, in the *Rivers* algorithm we use a 1st rank Voronoi tessellation to filter-out Brownian diffusing molecules. However, we use uniformly distributed localisations as a blank control to set the threshold on the Voronoi densities, which works well for fast diffusing molecules but not for slow diffusing molecules. Therefore, the next step to improve the *Rivers* algorithm is to find a better blank control that enables to improve the filter efficiency for slowly diffusing molecules. A possible direction that we have not yet exploited is to implement machine learning (ML) algorithms to further quantify the data obtained with HiDenMaps. First, we would investigate if ML algorithms could be used to filter the localisations in HiDenMaps instead of using our Voronoi tessellation algorithm. Second, working at slightly lower densities it would be interesting to investigate whether we could infer diffusivity maps without trajectory reconnection. Third, for multi-colour HiDenMaps it would be specially interesting to rely on ML algorithms because each channel would be considered as a layer and the localisations as nodes. Thus, we could seek for multi-layer connections to predict future interactions between the multiple proteins studied. So far, we have mostly developed analysis tools to investigate the spatiotemporal organisation of molecules at the plasma membrane that interact with the cortical actin network. Therefore, the next step is to continue developing algorithms to study intracellular processes such as in the nucleus, in the endoplasmic reticulum or the Golgi apparatus.

7.1 References

1. S. Manley, et al., High-density mapping of single-molecule trajectories with photoactivated localization microscopy. Nat. Methods (2008) https:/doi.org/10.1038/nmeth.1176.
2. J. B. Sibarita, High-density single-particle tracking: Quantifying molecule organization and dynamics at the nanoscale. Histochem. Cell Biol. (2014) https:/doi.org/10.1007/s00418-014-1214-1.
3. J. B. Masson, et al., Mapping the energy and diffusion landscapes of membrane proteins at the cell surface using high-density single-molecule imaging and bayesian inference: Application to the multiscale dynamics of glycine receptors in the neuronal membrane. Biophys. J. (2014) https:/doi.org/10.1016/j.bpj.2013.10.027.
4. S. Ghosh, S. Saha, D. Goswami, S. Bilgrami, S. Mayor, "Dynamic imaging of homo-FRET in live cells by fluorescence anisotropy microscopy" in Methods in Enzymology, (2012).
5. S. A. Freeman, et al., Transmembrane Pickets Connect Cyto- and Pericellular Skeletons Forming Barriers to Receptor Engagement. Cell 172, 305-317.e10 (2018).
6. P. Sil, et al., Dynamic actin-mediated nano-scale clustering of CD44 regulates its meso-scale organization at the plasma membrane. Mol. Biol. Cell 31, 561–579 (2020).
7. A. Kusumi, K. G. N. Suzuki, R. S. Kasai, K. Ritchie, T. K. Fujiwara, Hierarchical mesoscale domain organization of the plasma membrane. Trends Biochem. Sci. 36 (2011).
8. K. Murase, et al., Ultrafine membrane compartments for molecular diffusion as revealed by single molecule techniques. Biophys. J. 86 (2004).
9. C. Manzo, et al., The neck region of the C-type lectin DC-SIGN regulates its surface spatiotemporal organization and virus-binding capacity on antigen-presenting cells. J. Biol. Chem. 287 (2012).
10. J. A. Torreno-Pina, et al., Enhanced receptor-clathrin interactions induced by N-glycan-mediated membrane micropatterning. Proc. Natl. Acad. Sci. 111, 11037–11042 (2014).
11. G. Muñoz-Gil, et al., Stochastic particle unbinding modulates growth dynamics and size of transcription factor condensates in living cells. Proc. Natl. Acad. Sci. U. S. A. 119, e2200667119 (2022).
12. M. El Beheiry, et al., A Primer on the Bayesian Approach to High-Density Single-Molecule Trajectories Analysis. Biophys. J. 110 (2016).
13. M. El Beheiry, M. Dahan, J. B. Masson, InferenceMAP: Mapping of single-molecule dynamics with Bayesian inference. Nat. Methods (2015) https:/doi.org/10.1038/nmeth.3441.

Acknowledgements

Carrying out this PhD has been a long journey and it wouldn't have been possible without the help of many people. First, I would like to thank my supervisor Maria, for giving me the opportunity to complete the PhD in her Lab and giving me the freedom to wonder around the paths of data analysis. I also want to thank Juan, my co-supervisor, companion in long night experiments, always tough futbolin adversary and the best tennis partner to beat the Golgi team. To Carlo, for being an inspiration as a scientist and for all the hours of discussions. Felix, thanks for all the questions in the group meetings, the discussions and for the nice chats. Despite our rivalry in futbolin and tennis, it has been a great pleasure meeting you.

This work is also thanks to our collaborators, for their inputs, our joint experiments and discussions. Sergi Padilla and Irene Carlon, I'm very grateful for your help with the VLPs and discussions, because thanks to your help we could make Chapter 6 possible. Parijat, Sankarshan and Jitu, it has been a pleasure to learn from you and this PhD is tightly linked to our joint collaboration, thanks. Also, to the committee of my defence. Thank you, Ricardo Henriques for accepting being in the committee and for inspiring me with your work. Meeting you in MiFoBio in 2018 was truly enlightening. Also, thank you Pablo Loza, because I have bothered quite a bit your team when using the facility and for accepting being in the committee.

Pablo, thank you for everything. For being the best futbolin partner, for the morning chats in the cubicle, for the discussions and above all, for being a great friend. You truly mean a lot to me and to this thesis. Arturo, my adopted family with whom I have enjoyed so many beers, meals and chats, thanks. Sarah, thanks for being a great office mate, for the chats and for coming up with Matlab questions and new analyses so I had a plausible excuse to postpone checking the SPT trajectories. Nati, for the laughs and the soap opera episodes. The SMB group has grown a lot since I first joined, but everyone I have had the chance to meet (both past and present group members) have made a great impact on this phase of my life. Thank you Pamina, Maria Sanz, Lukas, Jessica,

Ediz, Roger, Jelena, Enric, Christian, Kyra and Morgan. Also, thanks to Javi and Joaquim, especially for the beers, the climbing and for being great friends.

I would also like to thank the Biolab crew: Merche, Angel and Maria M, for being there every time I needed something and for the nice chats during incubations. The SLN, and specially to Jordi because it has not been few times that I have come to annoy you about many things. Also, I would like to thank special people that have indeed made this experience a sweet journey. Jonas, despite you have tried to kick me out of the office so many times, here I remain till the end. To the futbolin gang, although most of you are already gone, it has been great to share so many coffee breaks.

The list of people that have contributed to me pursuing a PhD and motivated me during all my academic years is so long, but I would like to point-out few of them. Turgut, for taking me as a high-school student in your group and showing me the insights of research. To Christian Blum, for his mentorship during my MSc in Twente and for the chats about life we've had. And to Amin, Robert and Mireille from the BNP lab in Twente, because you made me see science differently and pushed me towards microscopy.

Finally, I want to thank my family and friends for the support and encouragement during these years. To my parents, Mònica and Miguel, because they always motivated me since my childhood to become a scientist. Last but not least, thank you Laia because this PhD wouldn't have been possible without you.

List of Publications

1. Parijat Sil†, **Nicolas Mateos†**, Sangeeta Nath, Sonja Buschow, Carlo Manzo, Kenichi G. N. Suzuki, Takahiro Fujiwara, Akihiro Kusumi, Maria F. Garcia-Parajo, and Satyajit Mayor, "Dynamic actin-mediated nano-scale clustering of CD44 regulates its meso-scale organization at the plasma membrane", *Molecular Biology of the Cell* **31**(7), 2020

2. Eva M. García-Cuesta, José Miguel Rodríguez-Frade, Sofía R. Gardeta, Gianluca D'Agostino, Pablo Martínez, Blanca Soler Palacios, Graciela, Tobias Wolf, **Nicolas Mateos**, Rosa Ayala-Bueno, César A. Santiago, Pilar Lucas, Lucia Llorente, Luis M. Allende, Luis Ignacio González-Granado, Noa Martín-Cófreces, Pedro Roda-Navarro, Federica Sallusto, Francisco Sánchez-Madrid, María F. García-Parajo, Laura Martínez-Muñoz, and Mario Mellado, "Altered CXCR4 dynamics at the cell membrane impairs directed cell migration in WHIM syndrome patients", *The Proceedings of the National Academy of Sciences* **119**(21), 2022

3. Gorka Muñoz-Gil, Catalina Romero-Aristizabal, **Nicolas Mateos**, Felix Campelo, Lara I. de Llobet Cucalon, Miguel Beato, Maciej Lewenstein, Maria F. Garcia-Parajo, and Juan A. Torreno-Pina, "Stochastic particle unbinding modulates growth dynamics and size of transcription factor condensates in living cells", *The Proceedings of the National Academy of Sciences* **119**(31), 2022

4. Enric Gutiérrez-Martínez, Susana Benet Garrab, **Nicolas Mateos**, Itziar Erkiziac, Jon Ander Nieto-Garai, Maier Lorizate, Carlo Manzo, Felix Campelo, Nuria Izquierdo-Useros, Javier Martinez-Picado, and Maria F. Garcia-Parajo, "Actin-regulated Siglec-1 nanoclustering influences HIV-1 capture and virus-containing compartment formation in dendritic cells", *eLife, second revision.*

5. **Nicolas Mateos†,** Parijat Sil†, Sankarshan Talluri, Satyajit Mayor, Carlo Manzo, and Maria F. Garcia-Parajo, "HiDenMaps: a biophysical tool to understand the interactions of single molecules with their environment", *in preparation.*

6. **Nicolas Mateos,** Enric Gutiérrez-Martínez, Irene Carlon-Andres, Sergi Padilla-Parra, Maria F. Garcia-Parajo, and Juan A. Torreno-Pina, “Multicolour single molecule imaging reveals optimised virus capture by pre-docking receptor nanoplatforms”, *in preparation*

7. Sarah Keary, **Nicolas Mateos**, Felix Campelo, and Maria F. Garcia-Parajo, “Differential activation and mesoscale organisation of integrin nanoclusters in focal adhesions”, *in preparation*

8. Pablo Lujan, Pablo Rios, **Nicolas Mateos**, Hans-Michael Müller, Christian Lüchtenborg, Timo Sachsenheimer, Britta Brügger, Maria F. Garcia-Parajo, Felix Campelo, Walter Nickel, and Maja Köhn, “Phosphatase of regenerating liver-3 enhances clathrin-mediated endocytosis by PI(4,5)P2 dephosphorylation”, *in preparation.*

9. Jofre Font-Mateu, Pol Sanllehí, Jesús Sot, Beatriz Abad, **Nicolas Mateos**, Juan A. Torreno-Pina, Roberto Ferrari, Roni H.G. Wright, Maria F. Garcia-Parajo, Jesús Joglar, Félix M. Goñi, Miguel Beato, “A progesterone derivative linked to a stable phospholipid activates breast cancer cell response without leaving the cell membrane”, *in preparation*

[†] Equally contributing authors